Study of stellar relics from the early Galaxy

A Thesis

Submitted For the Degree of

Doctor of Philosophy

in the Faculty of Science

by

Susmitha Rani Antony

Under the Supervision of

Prof. T. Sivarani

Indian Institute of Astrophysics

Bangalore

Joint Astronomy Programme

Department of Physics

Indian Institute of Science

BANGALORE – 560 012

July 2017

TO

My beloved parents..

"It has been said that astronomy is a humbling and character-building experience. There is perhaps no better demonstration of the folly of human conceits than this distant image of our tiny world. To me, it underscores our responsibility to deal more kindly with one another, and to preserve and cherish the pale blue dot, the only home we've ever known."

Carl Sagan, Pale Blue Dot

DECLARATION

I hereby declare that the work presented in this thesis titled, "Study of stellar relics from the early Galaxy" is the result of the investigations carried out by me under the supervision of Prof. T. Sivarani at Indian Institute of Astrophysics, Bangalore, India and Prof. Banibrata Mukhopadhyay at Indian Insitute of Science, Bangalore, Inida, under the auspices of the Joint Astronomy Programme of the Department of Physics, Indian Institute of Science. I further declare that this has not formed the basis for the award of any degree, diploma, membership, associateship or similar title of any University or Institution. Keeping with the general practice, due acknowledgements have been made wherever the work described is based on other investigations.

Dated: **Susmitha Rani Antony**

Department of Physics
Indian Insitute of Science
Bangalore-560012
India

ACKNOWLEDGEMENT

PhD is not an academic alone experience rather it is a journey through so many personal and emotional rises and falls. I owe my sincere gratitude to all the people who have been there to help me and to support me to complete this journey without much trouble.

First and foremost, I thank Sivarani for guiding me through the PhD period. Your positive attitude and enthusiasm towards each scientific projects were very inspiring to me through out the career. You were very considerate for the academic as well as personal problems. Your advices helped me a lot to look at problems with a different perspective. I thank you wholeheartedly for patiently guiding me and supporting me.

The supporting staffs, Pramod, Venkitesh, Gauri, Rahul, Kiran, Lekshmi and Prabhu at CREST and Kavalur were really helpful throughout the observing nights. Special thanks to Pramod, Venkitesh and Kiran for the wonderful time during the observations.

My stay in Bhaskara has given me amazing memories. I can't forget to mention the names of Arya da, Ramya chechi and Indu chechi for treating me like your younger sister and making me feel privileged. Thanks for the affection and care you have been giving me. Arun's constant motivations and positive attitude helped me a lot to be optimistic. Though you don't like to be thanked, I thank you for understanding me, advising me and generously helping me with academic and non-academic matters.

My involvement in Bhaskara committee, helped me to change the way I look at administrative matters. It taught me many things which I would not have learned

elsewhere. Thanks to Ramya chechi, Avijeet, Sam, Vaibhav, Arun Surya and Srinivasa Prasanna for the wonderful moments we shared in the committee.

Thanks to Avijeet, Ramya chechi and Sam for helping me with my comprehensive examination and sharing your valuable time to discuss the basics of the course work subjects.

Drisya chechi is another important person during my life at IIA who needs special mention. I enjoyed your company as a senior and as a friend. I could rush to you at any last minute with any worry and doubts. Thanks for being so close to me. A great thanks to Joice for several kind helps he has extended to me. You are a great human being with a compassionate heart. I will always remember your advices and kind words. Thanks for being there to help me whenever needed and listen to my worries. I will cherish being the beloved chechi of Nirmal and Honey. The immediate solutions and advices you had given me were not only useful for the life at IIA, but will also be useful throughout my life. Thanks for being by my side so many times. Thanks to Ambily and Sreejith for being there to help me out with the academic as well as non-academic matters. You have been kind whenever I hurried to you.

Annu was one of the best roommates I ever had in my life. The sync we had together made me feel very cozy. I will cherish the long discussions and thoughts we had.

Special mention to Devika for the sisterly affection. Your selfless and generous attitude I witnessed deeply touched me many times. Thanks to Chinthak for giving me the idea of going to Kavalur for writing thesis. I had my best working schedule there. I thank Jessy, Smitha, Drisya, Ramya and Indu for being the lovely chechis in my life. Thanks to Anand for the brotherly affection, the support and the care you gave me.

Thanks to Avrajit for being my beloved junior and Vidya and Arpita for my JAP batchmates. Be it academic or personal matters, you were there to help me without

any hesitation.

I thank Vineethettan, Ali,Pramod, Venki, Ajin, Prajwel, Rahna, Manpreet, Mayuresh, Sajal, Supriya, Sowmya, Sangeetha, Prasanna, Tanmoy, Shubham, Ramya, Sireesha, Prashanth, Roopasree, Amrita, Nancy, Pavana, Ruby, Prasanta, Priya, Priyanka, Sudip, Sandeep, Shejeela and Meenakshi,Dhanlal, Akanksha and Avinash for helping me to make memories.

I dedicate this thesis to my beloved parents, who taught me to be ambitious and hard working, who believed in me than in the society. Without you, I would not have dreamed and reached for the moon. Without you, my wings would not have got the strengths to fly higher and farther.

I am indebted to my sister, Resmitha for her constant motivation and help during my hard times. Though you are younger to me, you stood by me like an elder sister. Your words and support were really comforting. You are indeed the precious gift, that the God has ever gifted me.

My sincere thanks to Vivek for being an integral part of my life. Your perseverance surprised me quite a few times. I was amazed by the way you picked up and chased the life even if failure kicked you down. You were there whenever I needed even if we were fighting furiously. Your timely help and support helped me to complete this thesis on time. Thanks for being always there.

My aunts and uncles who were extending their support through prayer cannot be left unmentioned. Thanks for the prayers and comforting words. The acknowledgement will not be complete if I don't mention my mother in-law and Vineetha. Thanks for being so gentle and understanding.

Above all, I thank the God almighty for giving me an excellent opportunity to undertake this career and blessed me with so many wonderful people to love me, to care me, to protect me and to strengthen me.

LIST OF PUBLICATIONS

Journal Articles

* Abundance analysis of SDSS J134338.67+484426.6; an extremely metal- poor star from the MARVELS pre-survey , **A. Susmitha Rani**, Sivarani, T.; Beers, T. C.; Fleming, S.; Mahadevan, S.; Ge, J., 2016, MNRAS, 458, 2648

* Abundance analysis of a CEMP-no star in the Carina dwarf spheroidal galaxy, **A. Susmitha**, Koch, A.; Sivarani, T., 2017, (accepted in A&A) arXiv:1706.06599

Conference Proceedings

* Carbon abundances from SDSS globular clusters: exploring the origin in the large spread in [C/Fe] , Fiorenza, S. L.; Sivarani, T.; **Susmitha, A.**; Lee, Y. S.; Beers, T. C., 2013, mmSAI,84,208

* Carbon Abundances from SDSS Globular Clusters: Exploring the Ori- gin in the Large Spread in [C/Fe], Fiorenza, Stephanie; Sivarani, T.;**Antony, S.**; Lee, Y.; Beers, T. C., 2013, AAS, 221,250.26

* Mining the SDSS database to probe the imprints of the first stars of the Galaxy , **Rani Antony, Susmitha**; Sivarani, T., 2013, ASI conference series, 9,120.

ABSTRACT

The thesis, in general aims at studying the early history of the Milkyway through the chemical abundances of metal poor stars in the Halo and in the satellite galaxies of the Milkyway. Halo of a galaxy is one of the early structures that still remain pristine to probe the first low mass stars that formed during the first billion years after the Big Bang. According to the hierarchical galaxy formation models, Milky Way Halo could have formed by accretion of smaller satellite galaxies. Several hundreds of such small dwarf galaxies that did not merge to the Halo will be observable now. Low and high resolution, optical and NIR spectroscopic data are used to study the chemical abundances of metal poor stars both from the Galaxy and the satellite galaxies, to understand the common origin of them in the context of Galaxy formation. The details of each project undertaken during the period of the PhD is briefly described below.

- Chapter-1 includes, introduction of the following topics: metal poor stars, different classes metal poor stars based their origin and composition. Current understanding of the origin of satellite galaxies. Milkyway formation and its connection with the satellite galaxies.

- Chapter-2 includes observations, data analysis and methodology. We also discuss the stellar atmospheric models, radiative transfer codes, atomic and molecular data used in the analysis. Spectroscopic data analysis technique for low and high resolution spectroscopy is presented.

- Chapter 3 provides the details and results of slitless spectroscopic survey of

dwarf satellites of Milkyway using Himalayan Chandra Telescope and the follow up studies. Large photometric and spectroscopic surveys similar to SDSS have been successful in identifying faint galaxies around Milkyway. Most of the automated photometric searches, use over densities in the HESS diagrams, using a metal poor globular cluster color-magnitude diagrams as a representative population for the stars in these faint systems. They also pre-select the sample using various color cuts to avoid contamination from the foreground stars. Most of these methods identify very few RGB and AGB populations. RGB and AGB members are brighter and can be studied for its detailed chemical abundances, to derive clues of the early stellar population.

We initiated a slitless spectroscopic survey of 6 satellite galaxies using 2m Himalayan Chandra Telescope, India. We detected many new samples in these systems which fall in either RGB or HB group. This blind search and photometric preselection have been compared. Two of such bright metal poor stars identified are being followed up using Subaru. A proposal have been submitted for the same. The faint stars detected cannot be followed up using current facilities but are ideal candidates for upcoming large telescopes like TMT.

- Chapter 4 describes the abundance analysis of two CEMP stars from Carina dwarf spheroidal galaxy. Carbon-enhanced metal-poor (CEMP) stars bear important imprints of the early chemical enrichment of any stellar system. Plenty of CEMP stars are found in the Milkyway halo and their fraction increases with decreasing metallicity. But a very few CEMP stars are observed in the faint dwarf spheroidal (dSph) satellites. So we performed abundance analysis of two metal-poor carbon rich stars in the Carina dSph galaxy using high-resolution spectroscopic data obtained with the ESO/UVES instrument.

One of the stars (ALW-1) is showing enhancement in both heavy and light s-process elements thus classified as CEMP-s star .It is showing radial velocity variation indicating the presence of a binary AGB companion. The other star, ALW-8, show no enhancement in neutron capture elements thus classified as a CEMP-no star which is the first CEMP-no star detected in the Carina dwarf spheroidal galaxy. A moderate enhancement in yttrium is observed in this star indicating a weak r-process activity. Majority of elements detected in ALW-8 show similar abundance pattern of Carina's field star population as well as with CEMP stars in other dSph galaxies. The overall abundance pattern of ALW-8 confirms that the formation site for CEMP-no stars has been affected by both faint supernovae and/or fast rotating massive stars and by standard core collapse supernovae. It could also inferred that the mechanisms responsible for the heavy element production in CEMP-no stars are universal and act independent of the environment such as in the Galactic halo or in dSphs. The results have been published in Susmitha et al 2016, A&A accepted (arXiv:1706.06599).

- Chapter-5 describes the detailed abundance analysis of an Extremely Metal Poor stars (EMP) from the Milkyway halo. EMP stars are one of the subset of metal poor stars which preserve the chemical composition of first stars in their atmospheres. In order to understand the nature of first stars and the various nucleosynthetic mechanisms existed in the early universe, we initiated high resolution spectroscopic survey of extremely metal poor stars preselected from Multi-object Apache Point Observatory Radial Velocity Exoplanet Large-area Survey (MARVELS) spectroscopic pre-survey. One of the stars (SDSS J134338.67+484426.6) with an apparent magnitude V = 12.14, is

the lowest metallicity star found in the pre-survey, and is one of the only $\sim$20 known EMP stars that are this bright or brighter. Our high-resolution spectroscopic analysis of this star shows that this star is a subgiant with [Fe/H] = -3.42, having 'normal' carbon and no enhancement of neutron-capture abundances. Strontium is underabundant, [Sr/Fe] = -0.47, but the derived lower limit on [Sr/Ba] indicates that Sr is likely enhanced relative to Ba. This star belongs to the sparsely populated class of α-poor EMP stars that exhibit low ratios of [Mg/Fe], [Si/Fe], and [Ca/Fe] compared to typical halo stars at similar metallicity. An ISM with contributions from Pop III intermediate mass stars along with a later stage Pop II contributions with a low SFR can explain the abundance pattern seen in this star. The abundance analysis and the results of this star has been published in Susmitha & Sivarani et al 2016, MNRAS,458,2648.

- Chapter 6 discusses the HESP- TIRSPEC synergy of CEMP stars in the Milkyway halo. The large fraction of CEMP stars at lower metallicity indicates the physical mechanisms that causes production of carbon at earlier evolutionary stages of the Milkyway. High fraction might also indicate that the IMF in the earlier times included large number of intermediate to high mass stars than the present day. Abundance of carbon, nitrogen and oxygen play a crucial role in understanding the nature of the progenitors and origin of carbon in these stars. We studied four cool CEMP stars from the Milkyway halo, in optical high resolution and NIR medium resolution to derive the abundances of C,N and O using, C_2, CN, CH. [OI], and CO features. We compared the oxygen abundance derived from optical [OI] lines and CO band in the NIR and found reasonable match in the derived abundance. The CNO abundances

together with s-process element abundance and radial velocity monitoring in these four samples revealed that, they are having an AGB companion. The properties of the companion and possible origin of the C,N and O has been discussed in the chapter.

- Chapter 7 includes the conclusion and future plans.

Contents

[1]The results of detailed abundance analysis of the star ALW-8 from this chapter is accepted for publication in A&A, arXiv id:1706.06599

[2]The work presented in this Chapter is published as a paper (2016, MNRAS, 458, 2648)

List of Tables

List of Figures

Chapter 1

Introduction

The first three minutes after the big bang contributed the lightest elements to the universe. H, He and some traces of Li were formed at this first three minutes and they were distributed isotropically and uniformly across the universe. Small-scale density fluctuations prevailing in this primordial gas grew over time and created gas clumps which gradually evolved into gravitationally bound structures. These gravitationally bound structures merged to form bigger structures and collapsed to form the first stars in the universe. These first generation of stars also known as Pop III stars, were very massive due to the lack of metal lines to cool the contracting gas cloud and the higher Jeans mass required due to the high temperature of the collapsing cloud. So they evolved very fast and contributed their nucleosynthesized material to the inter stellar medium through supernova explosions. These first supernovae explosions contributed the first metal signatures to the early universe. Since Pop III star formation happened in the period of Dark Age of the universe, direct understanding about their formation and evolution is very difficult with observing facilities. Various simulations suggest that the first stars might had a very different

mass distribution and evolved differently compared to the later generation of stars.. Simulations also show that the formation of individual Pop III stars also affect the primordial star formation on larger scales. The ionizing flux from these massive stars destroys the H_2 within a larger region which is the main coolant in the absence of any metals and delays the star formation in other gas clumps within the vicinity which were collapsing under the gravity.

Simulations show that the first generation of galaxies were formed after the first star formation events. The characteristic mass of first star forming site has been figured out to be $\sim 10^6 M_\odot$ whereas the most probable site for the first galaxy formation is found to be within the atomic cooling halos of mass $\sim 10^8 M_\odot$ (Bromm and Yoshida, 2011, Bromm et al., 2009, and references therein). This indicates that the progenitors of the first galaxies needs to be pre-enriched by the Pop III stars' ejecta in order to provide the metal lines for atomic cooling. Hence, the mini halos which are the progenitors of the first galaxies, experienced Pop II star formation, which are the first low mass stars in the universe. These first galaxies evolve based on the age, metallicity, star formation rate and IMF of their stellar populations. Some of the first galaxies which are smaller in size evolved slower due to the shallow potential well to retain the gas from subsequent supernova explosions. Such galaxies may have left behind fossil records as well. The dwarf galaxies in the local universe are considered to be the fossils of the first galaxies which hosted the formation sites for the first low mass stars. So they are the ideal place to look for the origin and formation mechanism for the first low mass stars.

The Milkyway halo is another place where Pop II star were observed. The extremely metal poor stars detected in the Milkyway halo are considered to be the first low mass stars formed in the universe. So, studying them will provide insight into the nature of the first stars and the details of the first supernova explosions can be

understood.

Various theories have been put forward to explain the formation of the Milkyway halo and the Milkyway as such which are explained in the following section.

1.1 Galaxy formation models

There are three major theories which predicts, how a galaxy formation happened in the early universe; one explains a top-down formation process where as the other two explain the galaxy formation in a bottom-up scenario.

1.1.1 Monolithic Collapse model

This model gives top-down approach towards the galaxy formation. It suggests that the disk galaxies are formed from monolithic collapse of giant cloud of gas in the early universe. This was suggested by Olin Eggen, Donald Lynden-Bell and Allan Sandage (ELS) in 1962. According to ELS model, a giant cloud collapses and reaches equilibrium when the gravitational force is equal to the centrifugal force which is developed to conserve the angular momentum. At this point, matter near the center forms into a tight disk. This model explains that the halo stars and Globular Clusters are formed while the proto-galaxy was contracting and thus attained the eccentric orbits. Once the disk cools, the gas cloud can no longer remain as a single cloud. So, it fragments and stars are formed. If the halo stars were formed along with the galaxy, then they are also expected to be moving in the same direction. But stars with retrograde orbits have been observationally identified. This model could not explain the retrograde motion of the stars. This model also fails to explain the age spread in the Globular Clusters (GCs). According to this model, the age spread

should be less than 1 Gyr. But, age spread upto 3 Gyr has been observed among GCs.

1.1.2 Hierarchical clustering

This model is proposed by Searle and Zinn in 1972 and it states that larger structures are formed from the merging of smaller structures. They analysed data from Galactic Globular cluster(GGC) and found that no metallicity gradient was observed. They also found age spread in GCs indicating that the halo was built from independent low mass fragments over several billions of years. Recent cosmological simulations also suggest the hierarchical formation scenario, explained in detail in the next section.

1.1.3 ΛCDM model

ΛCDM model or lambda cold dark matter model is the widely accepted theory about the origin of the Universe. It is a modified form of the big bang theory. It assumes that most of the physical substance in the universe consists of dark matter, a material whose presence can only be detected by gravitational force and possibly by weak force. It also introduces the idea of dark energy which is responsible for the accelerating expansion of the universe.

According to this model, soon after the Big bang, the universe was intensely hot and substantially homogeneous and isotropic. As the universe began to cool, dark matter clumps started to condense and gas molecules were formed inside these clumps. These gas and dark matter clumps were attracted gravitationally to higher density regions and smaller halos were formed which are the representatives of the seeds of the first galaxies. First stars were formed in these smaller halos. Once they became

enough massive, they began to collapse under their own gravitational potential and grew into proto-galaxies. These proto-galaxies subsequently merged to form larger stellar systems and they eventually coalesce to form bigger galaxies. This process is called hierarchical merging.

Two types of merging are so far considered. major merging and minor merging. Major merging involve coalescing of two galaxies of comparable sizes to form a galaxy of completely different morphology. These major mergers can also trigger star formation. Galaxy simulations show that these major merging events are very rare and very few galaxies are involved in this major merging events. Minor merging involves the disruption of a dwarf galaxy by its massive companion through tidal interactions. These minor mergers are comparatively common and these mergers are still happening. These minor merger does not affect the center of the dwarf galaxies, so the remnants of these on-going events are present around the parent galaxies. The dwarf satellites around the Milkyway are considered to be the remnant of such minor merging events.

1.2 The Milkyway

The Milkyway is a spiral galaxy consisting of billions of stars. It has three general components: the halo, the bulge and the disk.

1.2.1 The Bulge

The spheroidal shaped central part of the Milkyway is called the bulge. It consists of gas and old stars. The age of the stars in the bulge are not known accurately due to the dust obscuration along the line of sight. An area in the sky which is relatively

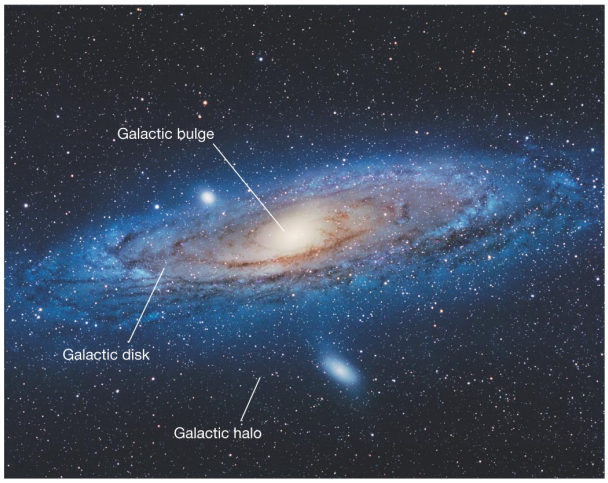

Figure 1.1: This is a schematic diagram of the Milkyway. The various components of Milkyway have been marked in the figure itself.
Image credits:http://pages.uoregon.edu/jimbrau/astr123/Notes/Chapter23.html

sparse in distribution of gas and dust is called as Baade's window. This spans around 2° in diameter through which the observations of the bulge is possible.

1.2.2 The disk

The disk of the galaxy is a flattened system consisting of young and intermediate stars having a coherent rotation about the galactic center. Density of the stars in the disk falls off exponentially, both in the radial and vertical directions. The position of the Sun is in the disk at 8.5 kpc away from the center of the galaxy. The disk also contains atomic and molecular gas and dust. It also contains several regions of star formation.
The disk has two components, thick disk and thin disk. The thin disk is composed of young stars where as thick disk hosts older stars and is considered to be formed

during the early stages of star formation.

1.2.3 The halo

The halo of the Milkyway is the outermost spherical part of the Milkyway consisting of old stars and Globular Clusters. The density of stars and Globular Clusters are sparse. The density of the visible matter of the halo is really low. The halo also consists of dark matter comprising 90% of the total mass.

1.3 The dichotomy of the Milkyway halo

The Milkyway halo was earlier considered to be single component consisting of stars sharing similar properties. But observations and analysis of the spatial density profiles of halo stars revealed that the halo is likely to have two components. with different radial distributions Miceli et al. (2008). Carollo et al. (2007) used a sample of over 20,000 stars to examine this dichotomy. They found that the halo consists of two components, inner halo and outer halo with different observed properties.

1.3.1 Inner halo

The inner halo component dominates the halo population at a distance upto 10-15 kpc. The stars in the inner halo are distributed in a non-spherical manner. The axis ratio of the distribution is inferred to be $\sim$0.6. The stars in the inner halo has a metallicity distribution peaking at [Fe/H]= -1.6 with tails extending to both higher and lower metallicities. These stars show a net prograde rotation around the center of the galaxy between 0 to 50 kms^{-1} and possess high orbital eccentricities.

1.3.2 Outer halo

The outer halo component of Milkyway starts around 15-20 kpc and possess a large fraction of older stars. The metallicity distribution function of the outer halo component peaks at [Fe/H]=-2.2 and have a spherical distribution of stars. The outer halo stars exhibit a net retrograde rotation (-40 to -70 kms^{-1}) about the centre of the Galaxy.

1.3.3 Origin of the dual nature of the Milkyway halo

The net retrograde rotation exhibited by the stars in the outer halo component of the Milkyway indicates that the formation of the outer halo is different from the inner halo component. Carollo et al. (2007) suggested that the outer halo component is formed from a dissipationless chaotic merging of smaller subsystems within an already existing dark matter halo. Before they fall farther into the inner part, these subsystems undergo tidal disruption in the outer part of the dark matter halo. The low luminosity dwarf galaxies surrounding the Milkyway is considered as the survivors from such tidal disruptions. If the masses of the subsystems were very low then none of them would have survived to the present day. In that sense, the outer halo might be assembled from low mass subsystems undergoing tidal disruptions. On the contrary, the inner halo is formed from dissipative merging of massive clumps followed by an adiabatic compression of the inner halo component to a more flattened disky structure. When the massive clumps merge radially, more number of stars obtain high-eccentricity orbits. Star formation in these massive clumps pushes the mean metallicity to higher values. The adiabatic compression of inner halo happens at this stage, resulting in a non spherical distribution of comparatively metal rich stars.

1.4 Stellar Streams and satellite galaxies of the Milky-way halo

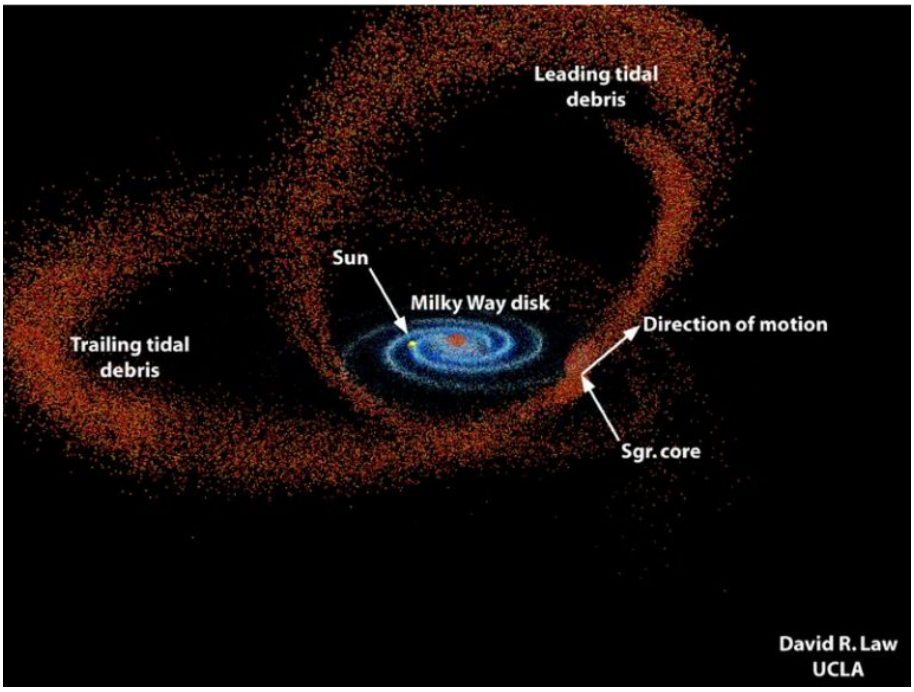

Figure 1.2: The stellar stream from the Sgr dwarf galaxy is shown in the diagram. Various parts of the stream is marked in the figure.
Image credit:https://astrobites.org/2017/06/20/galactic-archaeology-of-the-sagittarius-stream/

According to ΛCDM model, the Milkyway halo is considered to be formed from the tidal disruption and accretion of the small sub halos. It implies that there would be remnants of this interaction, either a stream of stars which are falling on to the Milkyway halo indicative of ongoing interaction or the core of the subhalos which were dense enough not to be fully disrupted due to the tidal interactions. The most

remarkable detection among them is the discovery of disrupting Sagittarius (Sgr) dwarf spheroidal galaxy (Ibata et al., 1995). Later Belokurov et al. (2006a), together with SDSS stars and M giants from Majewski et al. (2003), mapped the entirety of the Sgr stream which passes by the Galactic cap and returns to the Galactic plane thereby providing a probe for the shape of the Galactic halo. Belokurov et al. (2006a) also identified a field of streams near the north Galactic cap some of their progenitors are unknown. Orphan stream (Belokurov et al., 2007a) and Monoceros ring (Newberg et al., 2002, Yanny et al., 2003) are also some of the stellar streams detected from SDSS survey.

The other evidence of the hierarchical merging of subsystems is obtained from the plenty of dwarf galaxies around the Milkyway. There are around 30 of dwarf galaxies near to the Milkyway with different luminosities. They also found to be hosting stars of different metallcities. Most of the Milkyway satellites discovered till date are shown in the figure 1.3. Only a handful of satellite galaxies were known before the advent of large sky surveys. Among them Large Magellanic Cloud (LMC) and Small Magellanic Cloud (SMC) are the satellites which could be detected with the naked eye. Rest of the satellites were discovered based on the over densities in the spatial distribution of stars obtained through long exposures of the galaxy field. After the advent of SDSS, the number of low luminous satellites doubled which extended the faint end of the galaxy luminosity function. Since these galaxies are very faint, over densities in the Color Magnitude Diagram (CMD) of the co evolving population is used to detect them in the field of bright Galactic foreground stars. These satellite galaxies thus discovered are known as Ultra Faint Dwarfs (UFDs). Very recently, a few satellite galaxies were also discovered from the Dark energy survey. The stars in these galaxies show similar abundance pattern as that of the

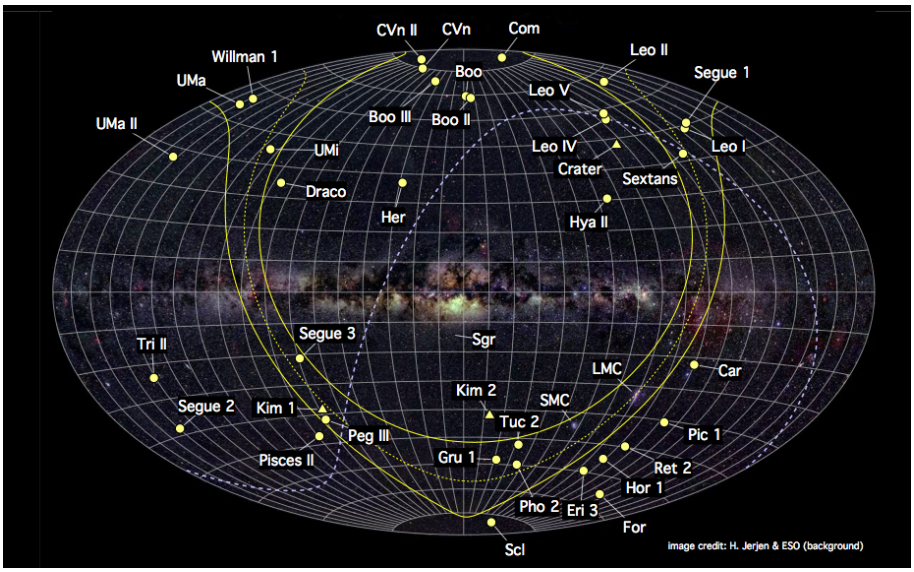

Figure 1.3: The known Milkyway satellite at a distance < 250 kpc. *Image credit:http://www.mso.anu.edu.au/ jerjen/SMS_mws.html* Figure copyright:Helmut Jerjen. Acknowledgment: Jerjen, H., 2010, PASA, 29, 383

stars in the halo indicative of their connection with the halo.

1.5 Nomenclature of Stars

In astronomy, any elements heavier than H and He are considered as metals. Other subsequent elements in the periodic table are resultant of stellar evolution. The term 'abundance' gives the measure of any element and it is usually represented in two ways

One is in the absolute scale relative to the number of hydrogen atoms

$$log\epsilon(A) = log_{10}(N_A/N_H) + 12.0$$

where A is the respective element.

The abundance can also be represented relative to the abundance of the element in sun which is represented as

$$[A/B] = log_{10}(N_A/N_B)_* - log_{10}(N_A/N_B)_\odot$$

where N_A and N_B represent the number of atoms of elements A and B.

For the case of stars, iron is considered as a proxy for the measure of metal content because of the excess nature of iron lines in the solar spectra and it is mentioned by the term metallicity often denoted as [Fe/H].

1.5.1 Metal poor stars

When a star has a lower abundance of iron compared to sun it is considered as a metal poor star. They are further classified based on the levels of metallicity (Table

Table 1.1: Table representing the nomenclature of metal poor stars. Adopted from Beers and Christlieb (2005)

[Fe/H]	Term	Acronym
$>$ +0.5	Super metal-rich	SMR
$\sim$0.0	solar	–
$<$ -2.0	Very metal-poor	VMP
$<$ -3.0	Extremely metal-poor	EMP
$<$ -4.0	Ultra metal-poor	UMP
$<$ -5.0	Hyper metal-poor	HMP
$<$ -6.0	Mega metal-poor	MMP

1.1) These metal poor stars also exhibit different chemical patterns apart from their scarcity in iron abundance. Majority of stars in the metal poor regime are showing enhancement in carbon in their atmospheres (explained in 1.5.3). Some stars show enhancement in r-process elements or s-process elements.

1.5.2 R-process and s-process rich stars

These are the stars which show enhancement in r-process or s-process elements in their spectra. Eu and Ba are the representative elements for distinguishing whether a star has r-process or s-process rich material on its surface. For a star, [Ba/Eu] $>$0.5 and [Ba/Fe] $>$ 1.0 indicates that the star has pure s-process enrichment whereas a star is considered to be purely r-process enriched then, [Ba/Eu]$<$0.0 and [Eu/Fe] $\geqslant$ 0.3 (Beers and Christlieb, 2005).

1.5.3 CEMP stars

Carbon enhanced metal poor (CEMP) stars are one of the major sub classes in the regime of metal poor stars. Any star whose metallicity is $\leqslant$ -2.0 and [C/Fe] $>$ +1.0 are considered to be CEMP star. During the evolution through red giant branch, the surface carbon abundance decreases as the carbon is consumed in the CN cycle to produce nitrogen and surface nitrogen abundance increases. So, for the case of star which has experienced first dredge up will show a lower carbon in their atmosphere than what it really has. In order to include this difference, Aoki et al. (2007) came up with the following criteria .

1) [C/Fe] $\geqslant$ 0.7 for stars with log ($L/L_{\odot}$) $<$2.3

2) [C/Fe] $\geqslant$ 3.0 - log ($L/L_{\odot}$) for stars with log($L/L_{\odot}$)$>$ 2.3

Carbon enhancement or carbonicity increases as we go lower in metallicity. According to (Beers and Christlieb, 2005, Lucatello et al., 2006) fraction of CEMP stars increases with decreasing metallicity and it becomes 100% beyond [Fe/H]$<$-5.0. Along with the enhancement in carbon, CEMP stars show peculiar abundance patterns. A large fraction of CEMP stars are observed with enhancement in neutron capture elements. They include both s-process and r-process elements. Based on the presence or absence of neutron capture elements, CEMP stars are further divided into CEMP-s stars, CEMP-r stars, CEMP-r/s stars and CEMP-no stars.

CEMP-s stars

CEMP stars which show enhancement in s-process elements are called as CEMP-s stars. According to Beers and Christlieb (2005), the criterion for a star to be CEMP-s is [Ba/Fe] $>$ +1.0, and [Ba/Eu] $>$ +0.5. CEMP stars so far observed are in the main sequence, turn off and red giant phase. In such a stage of evolutionary phase,

the stars cannot synthesize these s-process elements. Observations also revealed that CEMP star often comes with binarity. So, the most acceptable explanation for the enhanced s-process abundance is the mass accretion from the companion star which was once in AGB phase and now evolved to a white dwarf. S-process elements are produced in large quantities in AGB stars. Third dredge up brings out the s-process elements synthesized in the He-inter shell region and the same is transferred to the surface of presently observed CEMP-s star through some mass transfer mechanisms like, wind transfer and Roche lobe over flow. So, these CEMP -s stars thus reflect the abundance pattern and nucleosynthetic history of the companion AGB stars, not of the surrounding ISM.

CEMP-r stars

CEMP -r stars show enhancement in r-process elements. Eu is considered as the proxy for the r-process element abundance as they are easily available in the optical spectra of metal poor stars. Also, they are mainly produced in r-process elements in solar system materials. So the criteria for a CEMP star to fall in this category is [Eu/Fe] $>$ +1.0 and [Ba/Eu] $<$ 0.0 (Beers and Christlieb, 2005). The latter criteria is to distinguish it from stars which are abundant in both s and r-process elements because Eu is also produced in s-process. The only CEMP star which was categorized into this subgroup is CS22892-052 (Sneden et al., 2003) which shows a pure r-process abundance pattern. As major r-process production sites are supernovae explosions, the formation site for CEMP-r stars are considered to be r-process rich gas cloud which are pre enriched by supernovae.

CEMP -r/s stars

This is another classification of CEMP stars which shows enhancement in neutron capture elements, but the enhancement is neither from pure r-process nor from pure s-process elements. Instead, both are suspected to be contributing to the abundance pattern. According to Beers and Christlieb (2005), the criteria is $0.0 <$ [Ba/Eu] $<$ +0.5. Later, Jonsell et al. (2006) used the term CEMP -r+s to denote CEMP -r/s for stars with [Ba/Fe] > 1.0 and [Ba/ Eu] >0 or [Eu/Fe] > 1.0, considering the fact that all s-process and r-process enhanced stars are rich in carbon. Masseron et al. (2010) combined r and s and coined the term for CEMP -rs for stars [C/Fe] > 0.9 and [Eu/Fe] > 1.0 and [Ba/Eu] > 0 or [C/Fe] > 0.9 and [Ba/Fe] > 2.1. The origin of these stars are still in debate. These sub division of stars are also showing binarity and at low metallicity they are high in number (Barbuy et al., 2005, Jonsell et al., 2006, Masseron et al., 2010). The plausible explanation for this peculiar abundance pattern is that the star could be formed from a gas cloud which was pre enriched by r-process elements and an AGB companion transferred the s-process rich material to the surface of the presently observing star (Lugaro et al., 2012).

CEMP-no stars

Those CEMP stars which shows no enhancement in neutron capture elements by satisfying [Ba/Fe] < 0.0 are classified into this subcategory . CEMP-no stars are often found to be not associated with binaries. Hansen et al. (2016c) stated that CEMP-no stars are bonafide second generation stars which bears the remnants from first generation of stars. The frequency of CEMP-no stars increases with decreasing metallicity. At [Fe/H] $<$ -4.5, eight out of nine halo stars are CEMP -no stars making

them peculiar objects reflecting the abundance pattern of ISM. The abundance pattern shown by the CEMP-no stars can be matched with models of primordial faint supernovae that experienced mixing and fall-back thereby releasing small amount of iron but large amount of carbon and other light elements. Models of zero metallicity spin stars experienced mixing and mass loss due to their high rotational velocities also give a good agreement with the observed abundance pattern of CEMP-no stars. Chemical evolutionary studies could successfully derive the fraction of carbon enhanced to carbon normal stars in the assumption that faint supernovae dominated the early enrichment. This provides a link between CEMP-no stars and primordial faint supernovae.

1.6 Origin of chemical elements in the universe

Origin of chemical elements in the universe are through various mechanisms which are mentioned below:

1.6.1 Primordial nucleosynthesis

Primordial nucleosynthesis happens at the first three minutes of the Big Bang by combining the protons, neutrons and electrons. The elements created from primordial nucleosynthesis are ^{1}H, ^{2}H, ^{3}He, ^{4}He and traces of ^{7}Li. The other light nuclei (^{6}Li, ^{9}Be, ^{10}B and ^{11}B) found in the cosmos are produced by cosmic ray spallation in which the cosmic ray bombardment causes the fragmentation of the heavier nuclei in the ISM. Further nucleosynthetic process are stopped in the low density regime due to the lack of a stable nucleus with A $\geqslant$ 8. The rest of the elements found in

the universe are formed from stellar nucleosynthesis where the triple- alpha reaction tunnel the barrier the lack of A$\geqslant$8 nucleus. Here the star's interior acts as the production site via nuclear fusion reactions.

1.6.2 Stellar nucleosynthesis

The first step of stellar nucleosynthesis happens when hydrogen fuses to form helium. This ocuurs in two different ways depending on the density and temperature of the surroundings. Proton-Proton chain and CNO cycle are the two sets of reactions in which the hydrogen is fused to form helium via a series of reactions. Proton-Proton (PP) chain happens when the mass of the star is equal to or less than that of the Sun. This cycle occurs when the temperature of the surrounding is sufficient enough for the protons to overcome their Coulomb repulsion. PP chain is the dominant source of energy in these stars i.e; when the temperature of the surrounding is $\sim$4 x 10^6K.

CNO cycle happens when the stellar mass is 1.3 times massive than that of the Sun. Here, carbon, nitrogen and oxygen act as catalysts for the reaction to perform. CNO cycle is the dominant source of energy in stars massive than 1.3 times that of the Sun where the temperature of the surrounding is approximately 15 x 10^6K.

During stellar evolution, the relative proportion of nuclei forming will get altered. The convective episodes inside the star moves the material from the sites of CNO cycle to the surface. This alters the surface composition.

The helium produced inside the star accumulates in the core and when the temperature and pressure of the core becomes sufficient for the helium ignition to start, the alpha particles fuse to form carbon. This is called as triple alpha process. Some of the carbon nuclei fuse with another alpha particle to form oxygen. This happens at a

temperature of 10^8K. The Helium burning reaction releases one-tenth of the energy of the hydrogen burning phase and duration of this process is shorter. At the end of triple alpha process, carbon and oxygen is produced in equal amount.

In massive stars, following the triple alpha process, a series of reactions happens at the stellar interior by capturing alpha particles. Carbon burns to produce oxygen, neon and magnesium. Neon burning produces oxygen, magnesium and silicon and the reaction continues till the products reach upto iron. The figure 1.4 shows how the interior of a massive star at the end of stellar nucleosynthesis.

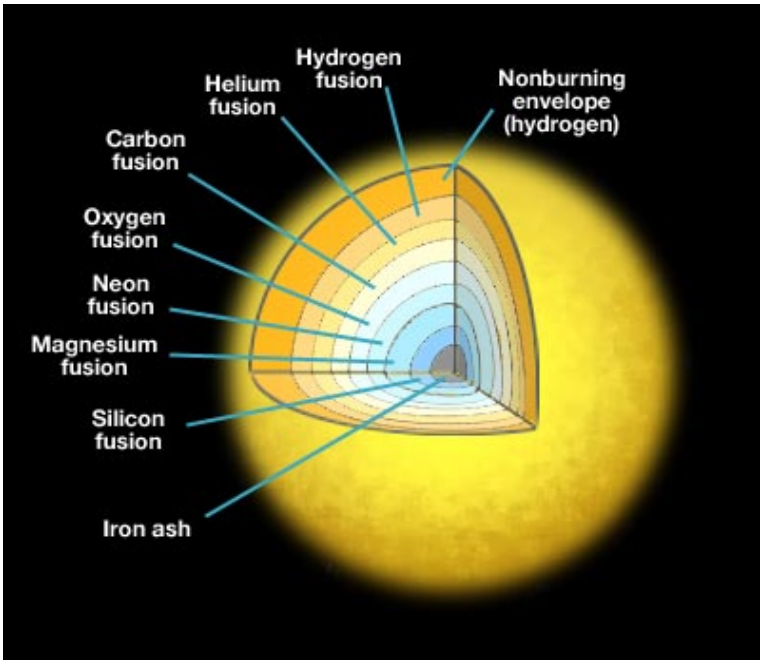

Figure 1.4: The schematic of the interior of a massive star when the core ash is iron. Image credit:*https://www.e-education.psu.edu/astro801/book/export/html/1824*

1.6.3 Neutron capture process

Presence of elements heavier than iron in the universe could not be explained by the conventional nucleosynthetic mechanisms like proton capture and alpha processes. The production upto iron involve charged particle interactions and electrostatic repulsion becomes significant as the proton number increases. At this stage , the repulsive forces hinder further production of heavy elements. But, neutron capture cross sections are larger for heavy elements compared to light elements which triggers the process and heavy elements (A $\geq$ 56) formation happens. Depending upon the neutron flux available for the nuclei, two types of neutron capture processes are available : Slow neutron capture (s-process) and rapid neutron capture process (r-process). When the nuclei captures neutrons, it becomes unstable and results in a beta decay which results in an increment in atomic number but with the same atomic mass. If the neutron flux available for the nuclei is low, the rate at which the neutron is being captured by the nuclei is lower than the beta decay time scale. Then, the unstable nuclei will undergo beta decay before it captures another nuclei. This process is called as s-process ('s' stands for slow). When the neutron flux is high (n $\sim 10^{22}$ to 10 ^{30} m^{-3}) the nuclei captures the neutrons at a rapid rate and the time taken for the successive neutron capture (10^{-3} - 10^{-4} s) is lower than the beta decay time scale. Since the beta decay always follows the neutron capture in s-process, the resulting elements always lie in the line of β stability where as r-process elements lie away from the line of β stability. The sources involving in the production of neutrons for s and r-processes are different. For s-process, the neutrons are produced in the He burning intershell region via

$$^{12}C(p,\gamma)^{13}C(\alpha,n)^{16}O$$

$$^{14}N(\alpha,\gamma)^{18}F(\beta,\nu)^{18}O(\alpha,\gamma)^{22}Ne(\alpha,n)^{25}Mg$$

The detailed nucleosynthetic conditions are explained in section 1.6.4. The neutron source for r-process element production is still an active field of research. The promising sites include core collapse supernovae, Neutron star - Neutron star (NS-NS) mergers and . Neutron Star - Black Hole (NS-BH) mergers. In type II supernova explosions, the heavy neutron flux is produced from the photo disintegration of nuclei due to the high photon density and extremely high temperature. Simulations of NS-NS mergers found that production of heavy r-process nuclei with A $\geq$ 130 are possible as the ejecta consists of extremely low electron fractions ($Y_e < 0.1$, i.e; almost pure neutrons).

1.6.4 AGB nucleosynthesis

S-process elements in AGB stars are formed at the He rich inter shell region. Sources for neutron flux required for the iron seed nuclei for the the production of s-process elements vary with the mass of AGB stars.‘ ^{22}Ne(α, n)^{25}Mg is the major source for high mass AGB stars (M $>$ 3M$\odot$) whereas low mass AGB stars (M $<$ 3M$\odot$), the major source is ^{13}C(α, n)^{16}O. In low mass stars, the temperature required for the ^{22}Ne(α, n)^{25}Mg cannot be attained in the He-rich intershell region. For the latter reaction, a lower temperature of $\sim 10^8$ is only needed for the ignition of ^{13}C which can be attained at the He- rich inter shell region (Gallino et al., 1998, Herwig, 2005). ^{12}C region in the intershell region captures hydrogen from the convective envelope during third dredge up and forms ^{13}C (Straniero et al., 1995). The ^{13}C burns through (α, n) reaction and releases neutron flux in the pocket and s-process occurs. During the next thermal pulse the s-process elements are taken in by the convective shell

and mixes all over. Third dredge up episodes convectively brings the newly synthesized s-process elements to the surface and alters the surface composition.
The s-process abundance pattern can be altered by changing metallicity, initial mass of AGB and the efficiency of ^{13}C pocket. Three peaks have been observed in the s-process abundance pattern peaking at Sr, Ba and Pb. The relative strength of the peaks changes with the decreasing metallicity. The more metal poor environment favors more neutrons to the seed nuclei resulting in shifting of the peak to the heavy s-process elements (towards Pb). A relative spread in the the s-process peak elements for a given metallicity is observed with a spread in the efficiency of ^{13}C pocket also.

AGB stars being the major production site of s-process nucleosynthesis, the s-process abundance pattern as well as the carbon abundance give details about the AGB nucleosynthesis and the efficiency of s-process production in lower metallicity.

1.7 Scope of the thesis

The thesis, in general aims at studying the early history of the Milkyway through the chemical abundances of metal poor stars in the Halo and in the satellite galaxies of the Milkyway. Halo of a galaxy is one of the early structures that still remain pristine to probe the first low mass stars that formed during the first billion years after the Big Bang. According to the hierarchical galaxy formation models, Milky Way Halo could have formed by accretion of smaller satellite galaxies. Several hundreds of such small dwarf galaxies that did not merge to the halo will be observable now. Low and high resolution, optical and NIR spectroscopic data are used to study

the chemical abundances of metal poor stars both from the Galaxy and the satellite galaxies, to understand the common origin of them in the context of Galaxy formation.

1.8 Overview of the thesis

Chapter-2 includes observations, data analysis and methodology. We also discuss the stellar atmospheric models, radiative transfer codes, atomic and molecular data used in the analysis. Spectroscopic data analysis technique for low and high resolution spectroscopy is presented.

Chapter-3 provides, details and results of the slitless spectroscopic survey of dwarf satellites of the Milkyway using Himalayan Chandra Telescope and the follow up studies of individual stars.

Chapter 4 explains the chemical analysis of two carbon enhanced metal poor stars from the Carina dwarf spheroidal galaxy.

Chapter-5 describes the high resolution follow up study of bright extremely metal poor (EMP) star (SDSS J134338.67+484426.6).

Chapter 6 discusses the HESP-TIRSPEC synergy for CNO abundance in the early galaxy using CEMP stars.

Chapter 7 contains the summary and future plans.

Chapter 2

Data acquisition and methodology

2.1 Introduction

Some of the basic parameters that characterize a star, are its luminosity, mass, radius, age and chemical composition. Some these parameters can be derived directly for stars that are part of an eclipsing binary system. For individual stars that are in the field the basic stellar parameters can be derived using fitting models to the observed colors, spectral energy distribution, line profiles, amount of polarization at different wavelengths and time variability. These different techniques are called, photometry, spectroscopy, polarimeter and astereoseismology. In photometry, total flux over a broad wavelength range is the intensity or the magnitude of the incoming radiation is measured over a broader wavelength range defined by the pass band of the filter used. In spectroscopy, the intensity is measured as a function of wavelength. Spectroscopy is considered to be a limiting case of photometry when the pass band is numerous in number. Polarimetry deals with the measurement of the degree and the direction of the linear polarization. These measurements can yield

enormous information on the object's nature, temperature, distance, age etc.

2.2 Spectroscopy

Among the various techniques mentioned above, spectroscopy is the most effective technique available for the detailed studies of stellar systems. It gives an understanding about the temperatures, compositions, luminosities, surface structures, line of sight velocities, binarity, masses, distance and ages. In spectroscopy, the incoming light collected by a telescope is fed into a spectrograph which decomposes the light into its constituent wavelengths using an optical element like prism, grating or a combination of prism and grating (grism). Finally, the dispersed spectra will be recorded by an appropriate detector like CCDs or IR arrays.

2.2.1 Spectrograph

The major components of a basic spectrograph are,

Slit : The entrance aperture at the focal plane of the telescope is called a slit and is used to limit the background noise and field and wavelength degeneracy. The spectral resolution increases with decreasing the slit width but there is a compromise of losing light when the slit width becomes narrower.

Collimator : The diverging beam coming out of the slit is made parallel using the collimator which will be then fed to the grating element. A collimator can be a lens, a mirror or a combination of both.

Grating element : The parallel beam from the collimator is dispersed into its constituent wavelengths using a prism, a grating or a combination of prism and grating called grism. A prism disperses the light more in the blue than in the red. Hence,

the redder portion of the spectrum will crowded. It works on the principle of refraction and is used in low resolution spectroscopic studies. A grating disperses the light using the principle of diffraction and the dispersed light is crowded in the bluer portion of the spectrum. The dispersion is nearly linear for the case of a grating. A grism is a combination of a transmission grating and a prism. A grism is designed in such a way that the diffraction angle of the transmission grating is cancelled by the refraction angle of the prism so that the dispersed beam will be in-line with the incoming beam. This design is ideal, in an instrument when one wants to facilitate both imaging and spectroscopy options without articulating the camera. In high resolution spectroscopic studies echelle grating are used as dispersion element, along with a cross disperser to separate the overlapping orders. **Camera** : The dispersed beam from the grating element is parallel. A camera is used to collect the beam and converge the beam so that the spectrum can be imaged on the detector. Usually a camera is either a lens or a mirror or a catadioptric system.

The performance of high resolution spectrograph is governed by its spectral resolution, efficiency and stability. Low resolution spectrograph is governed by efficiency and multiplexing capability.

$$Spectral\ resolution, R = \frac{\lambda}{\Delta\lambda}$$

$$Spectral\ dispersion = \frac{\delta\lambda}{\delta x}$$

where λ is the operating wavelength,

$\Delta\lambda$ is the smallest wavelength interval that can be resolved using the spectrograph,

$\delta\lambda$ is the change in wavelength over a distance δx along the spectrum.

This means the smaller the wavelength interval, the better is the resolution to resolve the spectral features.

2.2.2 Echelle spectrograph

Echelle spectrograph is a specially designed spectrograph to carry out high resolution studies. It disperses the light into two orthogonal directions using two dispersive elements resulting in a 2D spectrum of the object. The incident beam will be initially dispersed using a coarse-ruled (echelle) grating and then it will be cross- dispersed using a prism or a grating in the orthogonal direction. The echelle grating is coarse ruled grating and the groove shape is optimized in such a way that it results in high incident angle and high diffraction orders.

2.3 Facilities used in the study

2.3.1 Telescopes

Himalayan Chandra Telescope(HCT)

HCT is a 2.01-m optical-infrared telescope with an alt-azimuth mount, installed at Indian Astronomical Observatory (IAO), Hanle. It has a Ritchey-Chretien configuration with a primary mirror made of Corning Ultra Low-Expansion (ULE) ceramic to withstand a low temperature . The observatory site is located at an altitude of 4,500 m above the sea level. Low humidity, low temperature, low concentration of aerosols and less pollution along with the high altitude nature of the site help to have a better seeing. The telescope is remotely operated from CREST, Hosakote, through

a dedicated satellite link. The telescope is currently occupied with three science instruments which are mounted on the instrument mount cube at the cassegrain focus. The instruments are Hanle Faint Object Spectrograph and Camera (HFOSC), TIFR Near Infrared Spectrometer and Imager (TIRSPEC) and Hanle Echelle Spectrograph (HESP). Since these instruments are mounted on an instrument mount cube which has four side ports and one on-axis port, it is possible to switch from one instrument to another in one observing night itself.

ARC 3.5 m telescope

This telescope is located at Apache Point Observatory (APO), New Mexico, United States and is owned and operated by Astrophysical Research Consortium (ARC). It is a 3.5 m alt-azimuth mount telescope with Ritchey-Chretien configuration. This telescope has currently 7 main instruments operational, that are typically available in every night. The instruments are Echelle spectrograph, ARC Telescope Imaging Camera (ARCTIC), Dual Imaging Spectrograph (DIS), Optical Imaging Camera (SPIcam), Near Infrared Camera and Fabry-Perot Spectrometer (NICFPS), Near - Infrared spectrograph (TripleSpec) and high speed imaging camera (AGILE). The Echelle spectrograph is permanently mounted to the Nasmyth 1 (NA1) port of the telescope and AGILE is mounted at TR2 port of the telescope, while DIS , ARCTIC, TripleSpec , and SPIcam are mounted at Nasmyth 2 port (NA2).

ESO's Very Large Telescope

Very Large telescope (VLT) is the largest telescope in the Paranal observatory operated by European Southern Observatory It consists of four unit telescopes (UT) with main mirrors of 8.2-mm diameter and four movable auxiliary telescopes (AT)

with 1.8-m diameter. These telescopes can work together to form an interferometric array the 'ESO Very Large Telescope interferometer (VLTI) '. The Unit Telescopes (UT) named Antu, Kueyen, Melipal and Yepun can also work independently. In such cases, the light beam is sent towards either a Cassagrain focus or one of the two nasmyth focus stations where various instruments corresponding to different science cases are mounted.

2.3.2 Spectrographs and detectors

Hanle Echelle spectrograph (HESP)

HESP is a fibre-fed, high resolution, cross-dispersed near-Littrow echelle spectrograph mounted on the 2-m HCT telescope. Two resolution modes are available for this spectrograph. The high spectral resolution of R = 60,000 is achieved using sliced fibre inputs where as lower resolution, R = 30,000, echellegrams are achieved through unsliced fibre inputs. The spectrograph has a large wavelength coverage (350 - 1000nm) and it covers full spectrum with out any gap in the coverage and high throughput, based on a white pupil concept. It is developed, in collaboration with IRL (Industrial Research Lab, Kiwi Star), New Zealand. It has recently (September 2015) been installed on HCT. The instrument has four subsystems:

1. Cassegrain unit- attached to one of the side ports of the telescope which leads the light from the telescope to the spectrograph and the autoguider system.

2. Spectrograph unit - includes off-axis paraboloidal mirror collimator, an echelle grating, two thick prisms to disperse the spectra and f/2.7 camera. All these are mounted on an optical table located at the ground floor of the telescope building.

3. Calibration unit - possesses filters and calibration lamps (ThAr, ThArNe) and Halogen lamp for flat-fielding.

4. CCD detector system: It is a 4kx4k CCD system with a pixel size of 15.

ARC echelle spectrograph

The ARC Echelle Spectrograph (ARCES) is a high resolution, cross-dispersed visible light spectrograph mounted on the NA1 of the ARC 3.5m telescope. It covers the spectrum between 3200-10000Å in a single exposure on a 2048x2048 SITe CCD. The spectral coverage is limited by the the prism cross-disperser material on the blue side and the CCD sensitivity on the red side. The spectrograph provides a resolution (2.5 pixels) of R 31,500 (9km/sec) and is limited by the pixel size of the CCD. The spectrograph optics includes an off-axis paraboloidal (OAP) collimator, an echelle grating, two cross-dispersing prisms and and an f/2.7 Schmidt camera with achromatic corrector. The spectra are recorded in $\sim$120 orders that are distributed across the CCD chip. Longer wavelength orders are located at the bottom (low row numbers) of the chip, and shorter wavelength order are located at the top of the CCD (higher row numbers.)

UVES-FLAMES

UVES (UV-Visual echelle spectrograph) is a high resolution cross-dispersed echelle spectrograph of the VLT mounted on the Nasmyth B focus of Unit Telescope 2 (UT2, Kueyen). It is designed to operate within the wavelength range 300 nm-1100 nm. The incoming beam of light is branched and sent to either a blue arm (300-500 nm) or a red arm(420-1100 nm). These two arms can either operate separately or in parallel with the help of a dichroic beam splitter. The typical resolving power

is 40,000 when 1" slit is used and higher resolving powers can be achieved (upto 110,000) when narrower slits are implemented.

FLAMES is a multi-object, intermediate high resolution spectrograph of the VLT, mounted at the Nasmyth A platform of UT2. It has three main components which includes fibre positioner; a medium-high resolution optical spectrograph, GIRAFFE; a link to the UVES spectrograph (to the red arm) through 8 fibers of 1 arcsec entrance aperture.
though UVES is dsigned to work in long slit mode, fibre mode is possible when combined with FLAMES where 6 to 8 fibres can be fed to the Red Arm of the UVES. Three standard set up are possible for this combination of UVES and FLAMES with central wavelength of 520 , 580 and 860 nm with a resolving power of 47,000. for fainter objects, additional fibres are available for recording the sky contribution. for the 580 nm central set up, an additional fibre is available for calibration for obtaining simultaneous ThAr spectra.

HFOSC

Hanle Faint Object Spectrograph Camera (HFOSC) is an optical imager cum spectrograph mounted on 2-m HCT, built in collaboration with the Copenhagen University Observatory. The spectrograph covers a wavelength range of 350-990 nm and have a set of 11 grisms with a resolution ranging from 150 to 4500. This instrument is a focal reducer type instrument, this characteristic helps to get a wider field of view. It is mounted on the on-axis port of the instrument mount cube of HCT. The detector used with this instrument is a CCD with 2048 x 4096 pixels with each pixel is having a size of 15 x 15 microns. We have extensively used Grism 7 of the

HFOSC for our studies. It covers a wavelength of 3800-6840 Å with an instrument resolution of 1330.

TIRSPEC

TIFR Near Infrared Spectrometer and Imager (TIRSPEC) is mounted on 2-m Himalayan Chandra Telescope (HCT). It covers a wavelength range of from 1 to 2.5 micron with a resolution $\sim$1200 and can be used for near-infrared medium resolution spectroscopy as well as imaging. TIRSPEC was developed in collaboration with Mauna Kea Infrared (MKIR), Hawaii. Single order mode covers 1.02-1.20 microns (Y order), 1.21-1.48 microns (J order), 1.49-1.78 microns (H order) and 2.04-2.35 microns (K order). Apart from the single order mode, it also has cross disperse modes which provides simultaneous wavelength coverage of 1.02-1.49 microns (YJ) and also 1.50-2.45 microns (HK). In this instrument the detector array is 1024x1024 Hawaii-1 array.

2.4 Observation

Observations of our target stars were carried out using the above facilities during the alloted nights. The observed spectrum of target stars will have contributions from the atmosphere as well as the instrument response. The contributions from the instrument response can be rectified or removed using additional calibration frames which are observed along with the targets. Those frames include bias frames, flat frames and dark frames. Bias frames are taken to remove the thermal noise from the target frames. A set of bias frames are to taken ($\sim$ 10 frames) These bias frames are averaged and a master bias is generated. This is used to remove the pedestal

counts due to the bias voltage. Dark frames are taken to remove the thermal noise generated in a CCD as a function of temperature and exposure time. The exposure time required for a dark frame is identical to the target frame (since dark counts are nonlinear) but with the camera shutter closed in order not to let any light enter the CCD.Usually optical CCDs are kept in a diwar which is cooled by a constant supply of liquid nitrogen to reduce the thermal electrons considerably and most often such corrections are not needed for CCDs. Flat frames are used to remove the variations in the pixel to pixel sensitivity variation of the detector. These frames are taken by exposing the camera to a uniformly illuminated field and any variations in the counts give the information about the variations in the sensitivity. These flat frames are bias subtracted and dark corrected before proceeding for averaging. A master flat is generated from averaged flat frames. This master flat is normalized and divided from the target frames to correct for the variation which is called as flat-fielding.

Apart from these frames, wavelength calibration frames and standard star exposures are taken along with the target observation. Wavelength calibration frames are arc lamp spectra which are used to map the pixels positions to wavelength values using the arc emission lines. Usual arc lamps are Fe-Ar, Th-Ar and Fe-Ne. Calibration spectra are taken soon after the target observation without altering the instrument set up.

Molecules in the earth atmosphere generates some absorption features in the spectra which are known as telluric lines. Telluric spectra contaminates the source spectra beyond 6000 Å . These lines can be removed by dividing it with a normalized hot star spectra, that will have few stellar atmospheric atomic lines. Standard star spectra are also used to do the flux calibration.

2.4.1 Medium resolution NIR spectroscopy

The NIR spectroscopic images are reduced using a semi-automated pipeline developed by Ninan et al. (2014) The pipeline codes are written in Python using standard modules like astropy, numpy, matplotlib and PyRAF. The first part of the reduction which includes dark subtraction, intelligent pixel masking and slope fitting, is performed at the end of every observation night. The dark subtracted spectra is inspected manually to choose the good frames and those frames are combined to get a better SNR spectrum. Flat correction and bad pixel interpolation is applied on the combined images. Spectral extraction and wavelength calibration is performed using standard PyRAF tasks. Once the wavelength calibrated spectra is obtained, telluric correction needs to be applied since NIR spectra contains many telluric lines. Telluric correction is done by dividing the object spectra with the spectrum of a telluric standard whose NIR spectrum is taken at nearby airmass soon before or after the object observation. This correction also removes the instrument response and the fringes in the K band spectra.

2.5 Data analysis

Once the stellar spectrum is extracted and calibrated, the stellar atmospheric parameters (Effective temperature, log g, metallicity and microturbulent velocity) and the abundance of various elements can be derived either by equivalent width analysis or by spectrum synthesis method. The abundance of various elements as well as the precision in stellar age determination from the evolutionary tracks solely depend on the input set of stellar parameters. So it is essential to derive these parameters correctly before undergoing any detailed analysis.

2.5.1 Equivalent width

The strength of a spectral line is often referred by the term $equivalent\ width$, and it is defined as the width in angstroms of a rectangular box whose height is equal to the height of the continuum and whose area is equal to the integrated area of the spectral line. Mathematically it can be expressed as

$$W_\lambda = \int_{\lambda_1}^{\lambda_2} \frac{F_{\lambda c} - F_\lambda}{F_{\lambda c}}\, d\lambda$$

where $F_{\lambda c}$ represent the flux at the continuum and F_λ represent the flux at the wavelength λ. The quantity $(F_{\lambda c} - F_\lambda)/F_{\lambda c}$ is referred to as the depth of the spectral line.

2.5.2 Linelist

Analysis of an astronomical spectrum solely depend on information from the spectral features. Each spectral feature is characterized by the wavelength, the energies of lower and upper atomic levels and atomic transition probabilities or their oscillator strengths. A linelist is a compilation of these informations which include the precise wavelengths, oscillator strengths or transition probabilities and excitation potential. In this study the linelist have been compiled from VALD, NIST and KURUCZ database with the latest available gf values.

2.5.3 Stellar atmosphere

Stellar atmosphere is the outermost visible region of the star which we can observe, measure and analyze includes plenty of information.Through this atmosphere the photons escape from the most opaque region to the highly transparent region of

space. This is the region which produces the stellar spectrum. Theoretical model of the stellar atmosphere is needed for the studies of many of the properties like physical conditions, chemical compositions. The details of the chemical nature is encoded in the spectra.

Effective temperature

Effective temperature of the star is the surface temperature of the black body which emits equal amount of radiation as that of the star. The effective temperature is calculated using Stefan-Boltzmann law

$$L = 4\pi R^2 \sigma T_{eff}^4$$

where L is the stellar luminosity, R is the radius of the star, σ is the Stefan-Boltzmann constant = 5.6705x10^{-5} erg cm^{-2} K^{-4} s^{-1} and T$_{eff}$ is the effective temperature. Effective temperature of the given star can be calculated using photometric colors using various techniques mentioned in Alonso et al. (1996) and Alonso et al. (1999). or from excitation potential equilibrium.

Surface gravity

The surface gravity of a star is the acceleration experienced by any particle on its surface. It is usually expressed in logarithmic values denoted by log g. It has a unit of cms^{-2}. The evolved stellar populations have a lower value for surface gravity. It is also a measure of pressure in the photosphere. Higher the value of surface gravity, larger will be the collision rate for species in the photosphere which results in broadening of spectral lines. The surface gravity can be estimated by fitting the stellar evolutionary tracks/isochrones or from the ionization equilibrium between

neutral and singly ionized line of any species (usually iron). Another way is to fit the Mg triplet near 5172 Å whose wings are dependent on the change in the gravity.

Micro-turbulent velocity

The particle in the photosphere has a non zero velocity and this velocity has contributions from both thermal and non thermal ways. The non thermal component of particle velocity is the micro-turbulent velocity. It is denoted as ξ and expressed in units of kms^{-2}. This non thermal component of particle velocity is due to the small scale turbulent motion in the photosphere. The size of the turbulent element is as small as the mean free path of photons. Microturbulence broadens the spectra features and it greatly affects the strong lines than the weak lines.

Metallicity

In the case of stars, the metallicity is represented with the abundance of iron because plenty of iron lines are present in the solar spectrum. So metallicity is quantified by the term [Fe/H].

2.5.4 Modeling stellar atmosphere

In order to model the stellar atmosphere, various assumptions have been used.

(1) Plane-parallel

Though the stars are perfect spheres, the photosphere is thin ($\Delta R/R << 1$) enough to assume a plane parallel geometry.

(2) The stellar atmosphere is in steady state

(3) The stellar atmosphere is homogeneous - we ignore granules, spicules, cells,

spots, magnetic fields etc.

(4) The energy flux is constant with depth. The energy is generated far below the atmosphere and is merely transferred through the atmosphere. it is represented by,

$$flux = \sigma T_{eff}^4$$

where σ = 5.6704x10^{-5} erg cm$^{-2}s^{-1}K^{-4}$.

(5) The layers of the atmosphere do not have any relative motion in the normal direction so no net acceleration for the atmosphere. Hence the pressure balances the gravity.

$$\rho \frac{\mathrm{d}^2 r}{\mathrm{d}t^2} = -\rho g + \frac{\mathrm{d}P}{\mathrm{d}r} = 0$$

where ρ is density and g is acceleration due to gravity and is given by

$$g = \frac{GM_\star}{R_\star^2}$$

where $M_\star$ and $R_\star$ represent the mass and radius of the star respectively.

(6) The abundance of elements in the atmosphere is assumed to be constant and specific.

Incorporating these assumptions, The model generated is a large table with set of numbers representing the variation of temperature, pressure and other properties of the gas with depth below the stellar surface.

Model atmosphere- ATLAS9 models

ATLAS9 models are grid of stellar atmospheric models developed by Castelli and Kurucz (2004) using ATLAS9 program (Kurucz, 1993) in which line opacity is treated by making use of a set of pre-calculated tabulated opacity data called as Opacity Distribution Functions (ODF). These ATLAS9 models have 72 plane parallel layers from $\log\tau_{Ross}$ =−6.875 to +2.00 at steps of $\Delta\log\tau_{Ross}$ =0.125. Each layer has multiple columns in which the first column is the mass depth. The subsequent columns are the temperature, in kelvins, of the layer, the gas pressure, the electron density, the Rosseland mean absorption coefficient, the radiation pressure, the microturbulent velocity in meters/second, the amount of flux transported by convection, the convective velocity and the sound velocity.

Solar abundances from Grevesse and Sauval (1998) is used to compute the models. All these models are computed by keeping the convective option on while the overshooting option is off. For all the models, the mixing-length convection with l/H_p =1.25 is assumed.

We have used ATLAS9 models for all our studies.

2.5.5 Turbospectrum

TURBOSPECTRUM (Plez, 2012) is a set of codes used to generate synthetic stellar spectra. It is an enhanced version of "Spectrum" program package originally developed at Uppsala observatory(Alvarez and Plez, 1998, Plez et al., 1992, 1993). It evaluates continuous opacities and solution for the radiative transfer equations through opacity sampling technique. The input data and routines of this code has a high overlap with SOSMARCS routines (Plez et al., 1992). SOSMARCS routines are meant to especially generate stellar atmospheric models for cool star that are

hydrostatic, line-blanketed, spherically symmetric, flux constant, LTE with mixing length description of convection. It focuses on a full Opacity Sampling (OS) treatment of all opacities with 10912 sampling points between 990 to 125000 Å.
TURBOSPECTRUM can handle millions of lines in a reasonable amount of time. Synthetic spectra of desired models can be generated using TURBOSPECTRUM code with models input to it. Radiative transfer equations are calculated based on the input parameters.

2.6 Derivation of stellar parameters

The stellar parameters, temperature, log g, metallicity and micro turbulent velocity, can be determined by the following ways.

2.6.1 Equivalent width analysis

Unblended individual spectral lines have been identified from the target spectra and equivalent width have been measured using the IRAF task **splot** which fits a Gaussian to the profile with the width at the half flux point. Equivalent width have been measured for three times to minimize the error in measurement and the median of the three values have been taken as the final value of equivalent width. These equivalent widths are input to the stellar synthetic spectrum generation codes to generate the abundance values based on the input equivalent widths.
In order to calculate the stellar parameters, abundance of Fe is used in general because of the availability of large number of Fe lines in the optical spectra. Stellar parameters are calculated by iteratively changing the input model parameters to satisfy certain conditions. The trend between Abundance of Fe I vs (W_λ/λ) is minimized

to derive the microturbulent velocity (ξ). The abundance trend is sensitive to the changes in ξ. The lines of different strengths are affected differently by ξ, weaker lines are least affected whereas the stronger lines are heavily affected. The adopted value of ξ is where the abundance is independent of the equivalent width. The effective temperature (T_{eff}) is set when the Fe abundance is independent of the lower excitation potential (LEP) of the selected lines. The population in various energy levels are dependent on the excitation temperature and at excitation equilibrium, the temperature dependency is lifted and the trend in the Fe I abundance vs LEP is zero or minimized. The surface gravity (log g) is constrained in such a way that for the chosen T_{eff} and ξ, the abundance from the Fe I and Fe II has to be same. The metallicity of the star is obtained from the abundance of Fe when the T_{eff}, log g and ξ is fixed.

2.6.2 Spectrum synthesis method

For the case of medium resolution spectra, the stellar atmospheric parameters cannot be determined from the equivalent width analysis. Instead, spectrum synthesis method is used. A grid of synthetic spectra is generated using radiative transfer codes and model atmospheres from different combinations of stellar atmospheric parameters. The generated grid of spectra is matched with the observed spectrum. The χ^2 minimization technique is employed to find the best fit model parameters, in which the difference between the observed flux vector O and the synthetic flux vector S is minimized as functions of T_{eff}, log g, metallicity using a reduced χ^2 criterion, which is given by

$$\chi^2/DOF = \sum_{i=1}^{m+1}(O_i - S_i)^2/\sigma_i^2$$

where σ_i is the error in flux in the ith pixel and DOF is the number of degrees of freedom.

2.7 Radial velocities

The radial velocity of objects used in this study are determined by cross-correlating the observed spectrum against a template synthetic spectrum. The synthetic spectrum is generated using the stellar parameters of the star. The IDL routine (from the idlutils repository), crosscor.pro is used for the cross-correlation. In the routine, both the spectra are interpolated to an equally spaced common set of logarithmic wavelength points, which means a Doppler shift is identical to a constant shift in the x-dimension. Both the spectra are continuum normalized prior to the cross-correlation. A Gaussian is fitted to the peak of the cross-correlation function to accurately determine the best spectral shift. Finally, the shift and the errors are converted to velocity units. The radial velocity thus obtained needs to be corrected for the motion of the observer in the direction of the observation which is called the heliocentric radial velocity correction. The components of the observer's motion corrected, are those due to the Earth's rotation (diurnal velocity), the motion of the Earth's center about the Earth-Moon barycenter (lunar velocity), the motion of the Earth-Moon barycenter about the center of the Sun (annual velocity), and the motion of the Sun (solar velocity) relative to some specified standard of rest. The IRAF task **rvcorrect** is used for computing these corrections. The radial velocities mentioned in the study are the velocity values corrected for these motions and represented as

V_{helio}.

For the case of medium resolution spectra taken using HCT, the movement of telescope from one elevation to another results in a systemic shift in the spectral features. The systemic shift is measured and it is found as -30km/s to +30km/s throughout the night. The shift are corrected using the atmospheric lines present in the spectra.

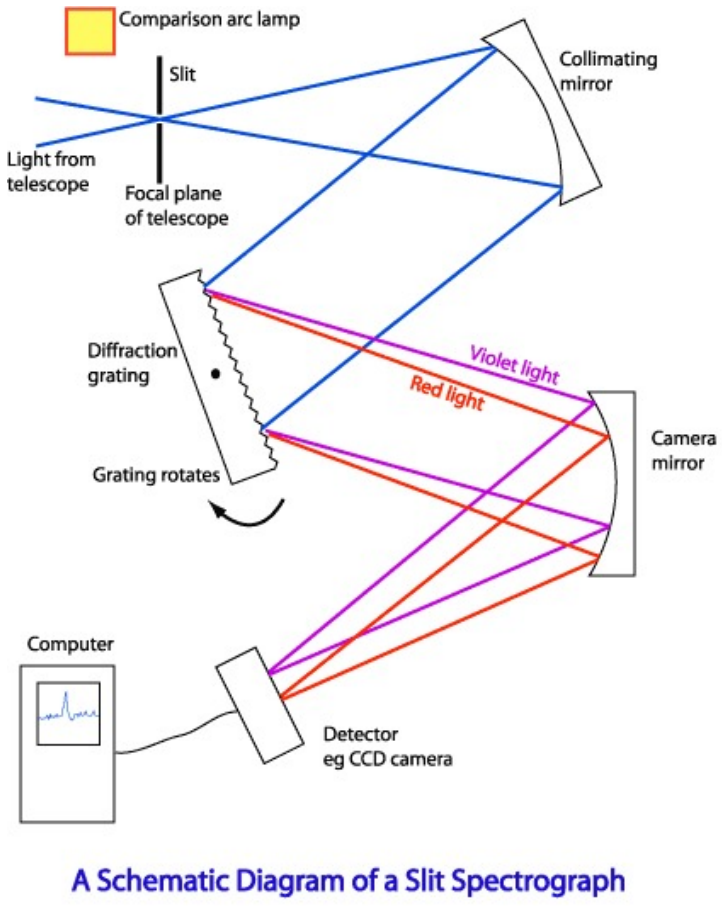

Figure 2.1: *Credit: James B. Kaler, in "Stars and their Spectra," Cambridge University Press, 1989*

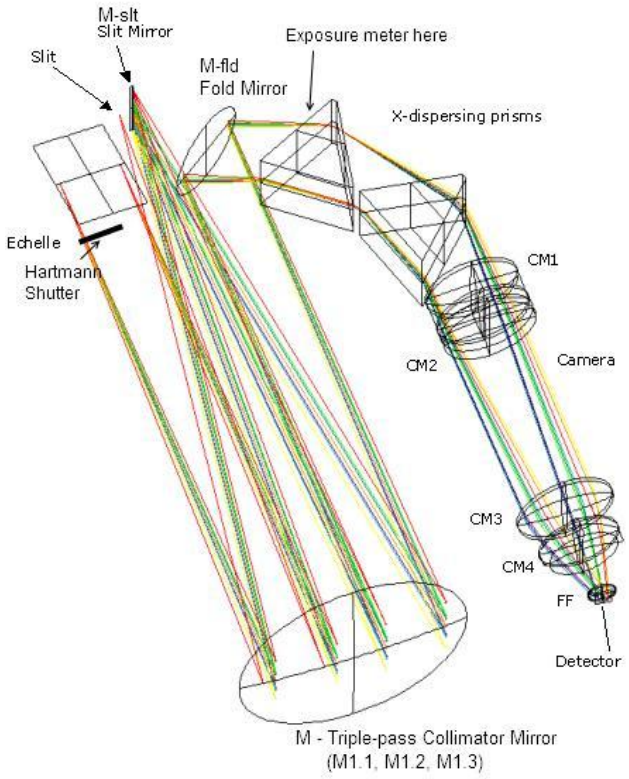

Figure 2.2: This is the ray diagram of HESP. The components have been marked in the figure itself. image creidt:iiap.res.in

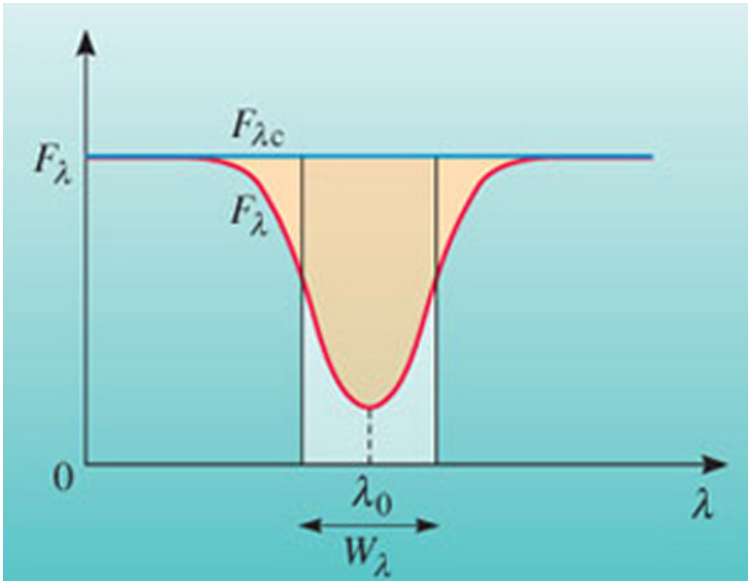

Figure 2.3: Equivalent width of an absorption line (red). The continuum level is represented by the term $F_{\lambda c}$ (blue). The equivalent width, W_λ, the width in angstroms of the rectangular box whose height is equal to the height of the continuum and whose area is equal to the integrated area of the spectral line. It is a measure of the strength of the line, higher the value of equivalent width, stronger the line is. (*credits: http://www.open.edu/openlearn/science-maths-technology/science/physics-and-astronomy/overview-active-galaxies/content-section-8.4)*

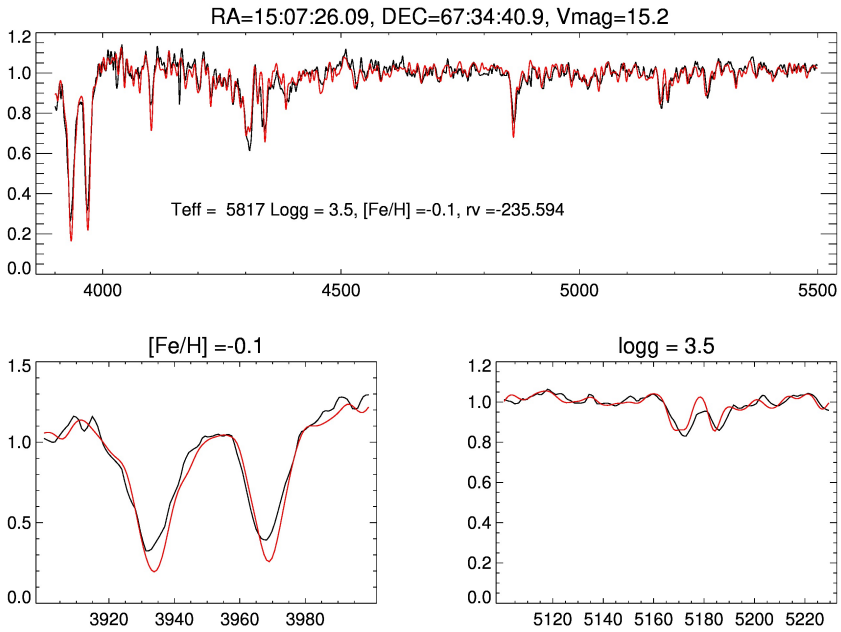

Figure 2.4: This figure shows how the stellar parameters have been derived by spectrum synthesis method for a medium resolution spectrum. This is the spectrum of a star observed with HCT-HFOSC.

Chapter 3

Slitless spectroscopic survey of dwarf satellites of Milkyway

3.1 Introduction

The Milkyway Halo has been a search place for metal-poor stars in order to understand the chemical enrichment of the early Galaxy. Metal poor stars are formed from a medium pre enriched by first generation of stars formed in the universe. Since, they are low mass stars, they preserve the chemical abundance of natal molecular cloud from which they formed, in their atmospheres. Various surveys have discovered metal poor stars of diverse chemical nature, with different metallicity ranging upto most metal poor ([Fe/H]=-7.2) star from the Milkyway halo (Aoki et al., 2007, Barklem et al., 2005, Beers and Christlieb, 2005, Keller et al., 2014, Lai et al., 2008). Chemical tagging of these stars help to reveal how our Galaxy have chemically evolved over billions of years. In order to directly observe star formation at these very early epochs, we need to wait until the upcoming facilities (e.g. JWST

and the large telescopes). However, metal poor stars can still shed some light on the early star formation history and various astrophysical mechanisms involved in the formation and evolution.

In order to study such old metal poor population among the Galactic population, Halo could be an ideal place. Since halo is one of the oldest structure (formed around almost similar time as the central regions of the Galaxy)of the Galaxy and remains pristine compared to the other components of the Galaxy. the Milkyway halo was considered as single component with stars sharing common properties, formed through monolithic collapse(Eggen et al., 1962). But subsequent studies revealed that the halo comprises of two spatially overlapping components, an inner and an outer halo (Carollo et al., 2007, 2010). Stars in these two components exhibit different spatial morphology and different rotational velocities around the Galaxy. (Carollo et al., 2007) showed that MDF of these two halo components also peak at different metallicities. The difference in the spatial density profiles, stellar metallicities and stellar orbits indicate that the formation scenario of the outer halo is entirely different from that of the inner halo.

(Searle and Zinn, 1978b) suggested hierarchical merging of protogalactic fragments as possible scenario of Galactic halo formation. Among these, hierarchical merging model received more attention as it matches well with the predictions of ΛCDM cosmology which proposes that the bigger structures in the universe are formed from the subsequent merging of mini-haloes formed against the cosmological expansion. Numerical simulations based on ΛCDM cosmology predict that the stars in the halos of the Milkyway sized galaxies are stellar remnants from a large number of sub haloes that were disrupted by the tidal interactions with their parent galaxies. These smaller haloes are considered to be formed during earlier

times and are denser (Navarro et al., 1997). So the remnant of the progenitors and the smaller satellites of the bigger haloes would still be present(Diemand et al., 2008). One can consider the low luminosity satellites of Milkyway are remnants of such interactions. SDSS has discovered many low luminosity dwarf galaxies around Milkyway(Belokurov et al., 2006b, 2007b, 2009, Walsh et al., 2007, Willman et al., 2005, Zucker et al., 2006a,b) known as ultra faint dwarfs (UFDs) extending the faint end of the galaxy luminosity function. Among the dwarf satellites discovered, Coma Berenices, Segue I, Segue II and Bootes II are found to be on the projected plane of the Sagittarius Stream. These satellites are also have velocities similar to stream membership implying that they are once associated with the Saggitarius dwarf. These faint galaxies are very metal poor and probably hosted the first stars of the universe. The current observations show that they might have had only one episode of star formation. There are no extended star formation observed in these galaxies (Frebel and Bromm, 2012). The star formation was probably stopped due to the reionization of the Universe (Brown et al., 2012, 2014). According to Kirby et al. (2011) the dwarf spheroidal galaxies follow the luminosity and stellar metallicity of galaxies. But UFDs like Segue II, Segue I, Willman I were observed to be showing a higher value in [Fe/H] than predicted by the luminosity metallicity relationship. This might indicate that these faint satellites of Milkyway are remnants of tidally stripped galaxies, that were hundred times more luminous before the tidal interactions.

Since these satellite galaxies are very faint, identifying them in the presence of bright Galactic stars is difficult. So most of the automated search using large photometric surveys use over densities in the color-magnitude diagrams (called the HESS diagrams). These methods assume a color-magnitude diagram that are similar to that the of metal-poor globular clusters to search for over density of co-evolving

population. Various color and magnitude cuts are used to avoid the contamination from fore-ground stars. Membership based on photometry alone needs very deep photometry in order to reach the main sequence luminosities. However, the main sequence stars are too faint to be useful for spectroscopic followup with the current 8-10m telescopes, in order to derive metallicities, and kinematics. Spectroscopic followup of bright candidates have resulted in a handful of (10-50) membership stars for each of these galaxies. These studies reported very few RGB and AGB populations. Many of the UFDs show small spread in the metallicity. These results could biased due to the photometric preselection techniques used or these systems would have really experienced only one shot of star formation. In order to understand this situation, spectroscopy of every target in the field could be ideal. This will use spectroscopic luminosity and the radial velocity to decide the membership. However this is expensive on the telescope time. This may be partly possible by a slitless survey where the spectra of all the stars in the field are obtained in single observation. Such observations, can provide information on the stellar metallicity, stellar velocity dispersion thereby to understand the dark matter and the chemical evolution of these systems.

This chapter explains the details of a sliteslss spectroscopic survey to detect the missing stars/populations in these satellite galaxies. Section 2 describes the observation, section 3 explains the various methods for reduction, section 4 describes the details of the stellar parameters and section 5 gives the details of the follow up long slit spectroscopy. Section 6 and the subsequent sections discuss the results of the survey and the details of the members identified.

3.2 Observation

One of the main aim of this study is to search for evolved stellar populations in these satellite galaxies, due to the medium size (2m) aperture of telescope, we won't be able to reach the faint unevolved population. The satellite galaxies of the Milkyway that are considered includes both ultra faint dwarfs and dwarf spheroidals and their distance and position information are collected from literature. The magnitudes of RGB, HB and AGB populations are calculated from this distance information using the magnitude and distance relation. The absolute magnitudes of Arcturus (for RGB), and that of HB stars in globular cluster 47 Tucane and a typical M_v of a carbon star (AGB, Mv=-2.0) were adopted to put in the magnitude distance relation and the magnitudes of these stars at the distance of each satellite galaxies have been calculated. The calculated values and the details of satellite galaxies which can be probed by HCT are given in Table 3.1. AN uncertainity of 2 magnitude is adopted to account for the uncertainty in the metallicity of the stellar populations in these satellite galaxies. These satellite galaxies are close enough to resolve the individual

Table 3.1: Satellite galaxies of MW and their literature details

name	RA	DEC	distance (kpc)	RGB,HB, AGB
Ursa Major II (UMa II)	08:51:30	+63:07 :48	30	17.0, 18.4, 14.55
Segue II	02:19:16	20:10:31	35	17.4, 18.7, 14.9
Segue I	10:07:04	+16:04:55	23	16.5, 17.8, 14.0
Segue III	21:21:31	+19:07:02	16	15.7, 17.0, 12.2
Bootes II	13:58:00	12:51:00	42	17.8, 19.1, 15.2
Bootes III	13:57:00	26:48:00	46	18.0, 19.3, 15.5

stars in them. Hence, spectra of individual object might be possible. This can be achieved either by multi-object spectroscopy or slitless spectroscopy of the field. We use 2m HCT grism spectroscopy without any slit in the path. Slitless spectroscopy gives many spectra in single observation. Slitless spectroscopy of a field covering 30' x 30', centered around the satellite galaxy field was performed using Grism, Gr#7 (wavelength coverage is 3800-6840 Å and an instrument resolution of 1330) of HFOSC. Gr7 has been used through out this study because it covers the blue region including Ca H & K and Mg triplet around 5172 Å and Hα line. These wavelength regions are very useful to derive the stellar metallicities,log g and radial velocities. Since the field of View of HCT is 10'x 10', each satellite galaxy field was tiled into 10'x10' frames and observations were performed. Each tiled field was observed for 1hour, with three 20 minutes exposures in the slitless mode. Splitting the exposure has helped to probe fainter stars without saturating the brighter stars in the field. An example of typical UFD tiled field is shown in the figure 3.1. Imaging mode is chosen to do the slitless spectroscopy, so full 2kx2k size of HFOSC CCD is utilized for the study. After each slitless spectroscopy exposure, an image of the same field is taken to get the star position in the field which is needed to do an accurate wavelength calibration. Sky flats were taken in the beginning as well as at the end of each nights. FeAr calibration spectra was taken with a long slit which covers the full pixels along the spatial axis with an exposure time of 120 sec.

3.3 Reduction

Each tile has multiple frames of observation. These were median combined to have a good signal to noise ratio. The combine from is subtracted it from the imaging frame of the respective field to find the reference for the mid point of the spectral

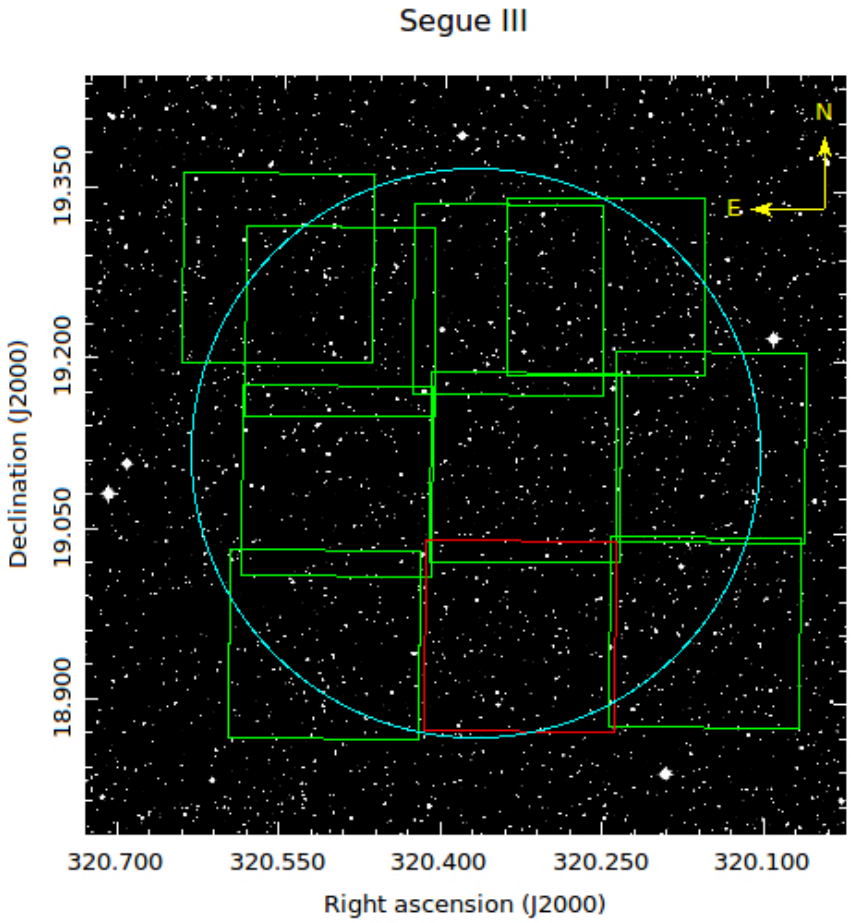

Figure 3.1: An example of tiling of each satellite galaxy field. The cyan circle represents the 30'x30' field and each green boxes represent a tile of 10'x10' size. The red tile represents one of such tile whose image as well as the slitless image is given in figure 3.2

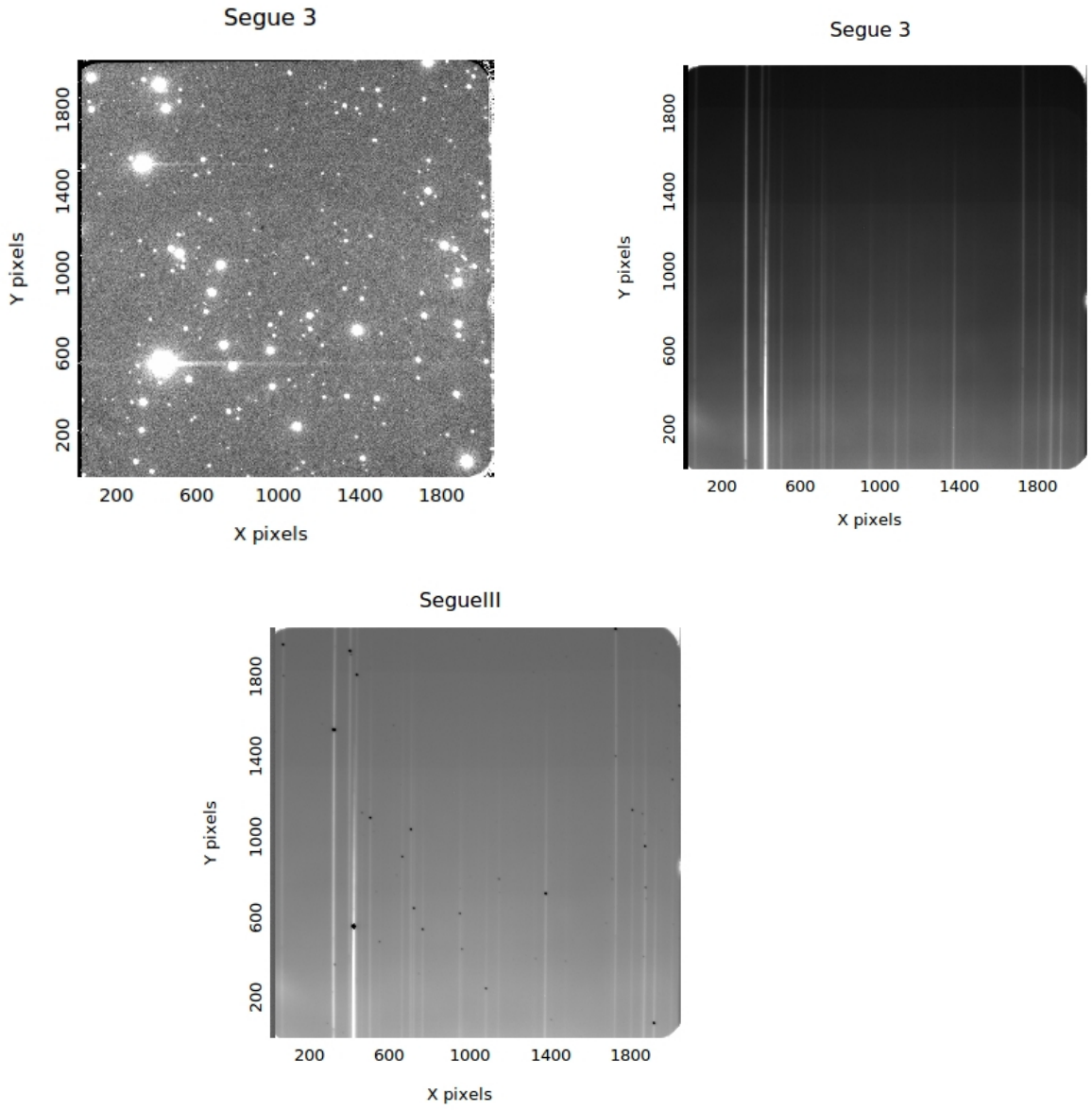

Figure 3.2: One of the field of Segue 3 is given here. The field image, the slitless image and the image when the field image is subtracted from the slitless image are shown here. The black dot in the lower most image is the zero point of each spectrum formed in the slitless field.

order. An example spectrum is given in the figure 3.2. Bias subtraction and flat fielding have been performed on these frames using standard IRAF routines. The next step is to convert the pixel scale to the wavelength scale which can be achieved by wavelength calibration using FeAr arc lamps. The solution of conventional one dimensional wavelength calibration in a long slit spectra is only a function of position along the dispersion axis. Here for the case of slitless frame, a two dimensional wavelength calibration approach is required. So the solution has to be function of both the dispersion and slit (spatial) axes. So, in order to do the wavelength calibration, the lamp spectrum has been calibrated along both the dispersion axis and slit axis. This has been achieved by the tasks ”identify” and ”fitcoords” in the IRAF tasks. The task ”identify” first identifies FeAr emission lines along the dispersion axis and the task ”reidentify” uses the identified features from ”identify” to find same features at different points along the slit. "fitcoords", another task in IRAF, gives a 2D fit dispersion solution. Thus the solution is a function of both the slit position and the wavelength. Once the lamp has been calibrated, the dispersion solution needs to be applied to the 2D science frame. This has been performed by the IRAF task ”transform” which transform the input spectra from the pixel scale to the wavelength scale. The 2D slitless frame thus obtained has wavelength information in each point. Individual spectra were extracted using ”apall” which includes aperture extraction and tracing. A similar technique has been implemented in extracting the spectral features of an extended galaxy in (Bagchi et al., 2014).

The dispersion solution derived here is a function of wavelength and the slit position. But the lamp exposures were taken using a slit which is fixed at a position which is equal to the 1024^{th} pixel on the CCD. It means that the spectra are wavelength calibrated assuming that the stars are placed on the slit but at different positions along the spatial axis . The original scenario is that, the stars are distributed randomly

on the frame. This difference in the star position and the position of the slit in the dispersion axis can cause a shift in the spectral features. This shift can be rectified by obtaining the position of the star in the 2D frame. This can be achieved from the image frame taken with the slitless frames. Once the difference is obtained, it can be converted to the wavelength scale by multiplying it with the degree of dispersion. This value is applied to the spectra to correct for the position. Examples of such extracted spectra is given in figures 3.3 and 3.4 The extracted spectra are normalized using a semi automated IDL routine.

3.4 Stellar parameters

The normalized spectra is then carefully inspected for the presence of any peculiar features. In order to get the RA and DEC of all the stars in the field, http://nova.astrometry.net/ is used. Based on this information, the SDSS colors of the objects have been obtained and the effective temperature of the objects have been derived from $g-i$ color using Infra red Flux Method

$$\theta = (a_0 + a_1 * X + a_2 * X^2 + a_3 * X^3 + a_4 * X * [Fe/H] + a_5 [Fe/H] + a_6 * [Fe/H]^2)$$

$$T_{eff} = 5040/\theta$$

where, X is g-i color and a_0 = 0.6787, a_1=0.3116, a2=0.0573, a_3=-0.0406, a_4=-0.0163, a_5=-0.0021, and a_6=-0.0003 for log $g \geq$ 3.7, while a_0=0.6919, a_1=0.3091, a_2=0.0688, a_3=-0.0428, a_4=-0.0078, a_5=-0.0086, and a_6=-0.0042 for log $g <$ 3.7.
Since previous information of log g and metallicity were not available for any of the objects, the temperature estimates will have a dependency due to the assumed log$g$ and metallicity. So various log g and metallicity have been assumed to derive

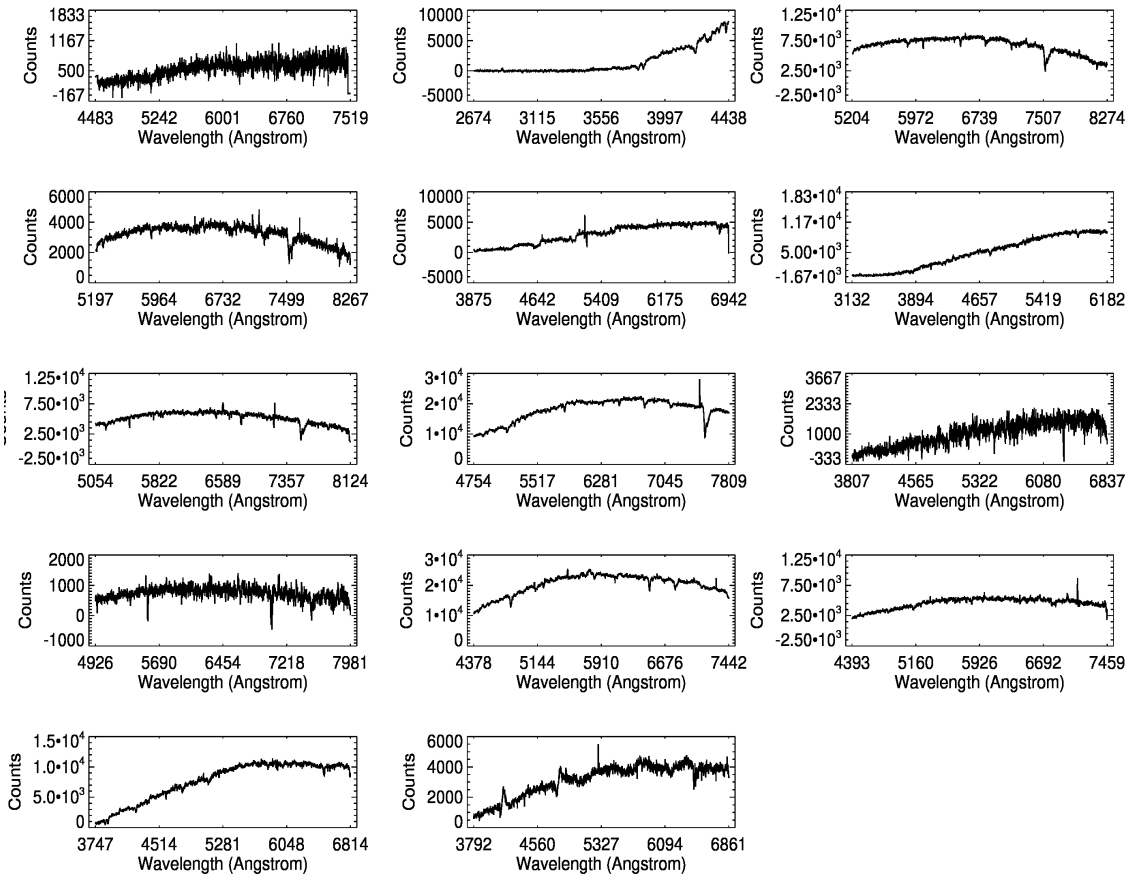

Figure 3.3: The slitless spectra of all the stars in one tile. This tile belongs to the UMa II field. 9 such tiles have observed in the field of UMa II which gave a total of 98 spectra including the stars from the Milkyway halo and the satellite galaxy.

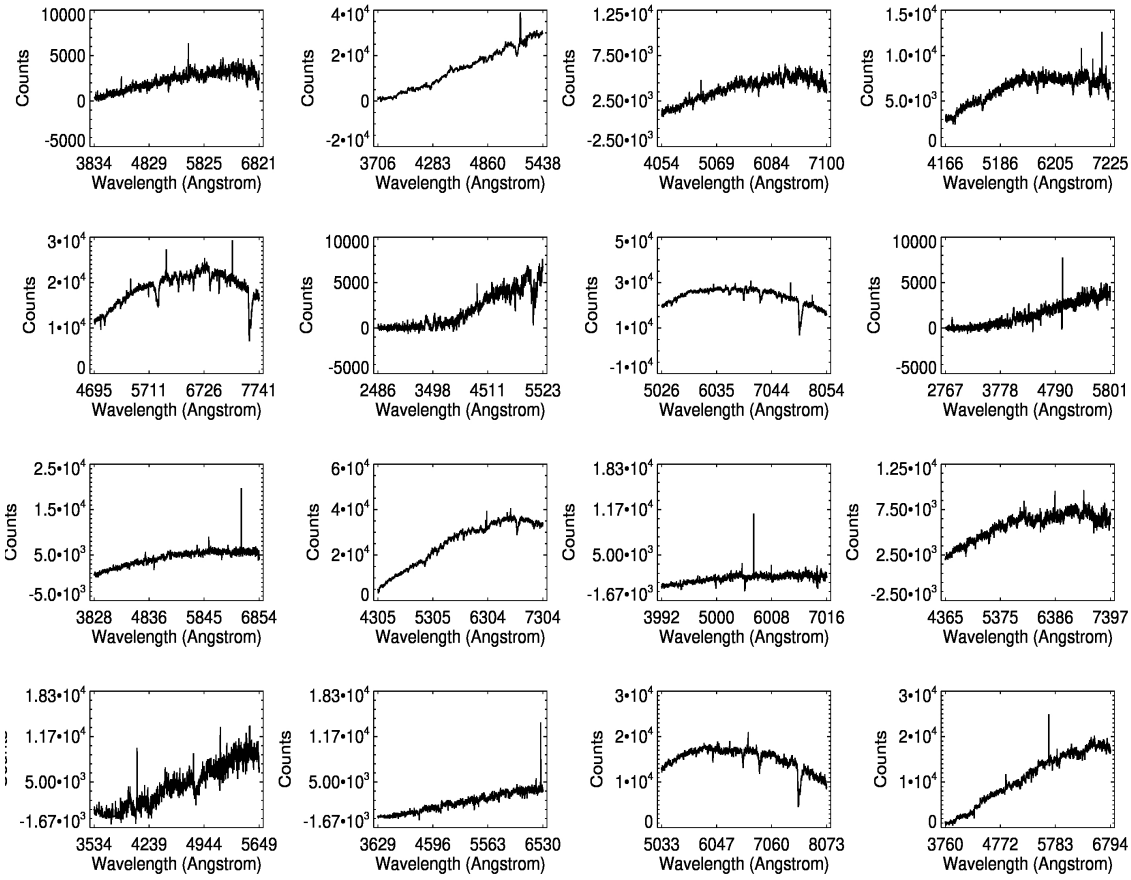

Figure 3.4: The slitless spectra of all the stars in one tile. This tile is observed from the field of Segue III. 9 tiles from the field of Segue III have been observed which gave 160 spectra including stars from foreground contamination.

the temperature and the uncertainty in deriving the temperature was found to be not exceeding beyond 250K. Considering the low resolution nature of the spectra, this uncertainty in temperature will not affect the candidacy of the sample. So the effective temperature of all the stars in each field is derived by assuming a a metallicity of -2.0 and a log g of 3.0.

Log g and metallicity of the samples are derived by fitting the observed spectra with a grid of synthetic spectra. The grid is generated by fixing the temperature using colors and varying the log g value from 0.0 to +4.5 in an initial step size of 0.5 then refined to 0.1 and [Fe/H] changed from 0.0 to -3.5. with an initial step size of of 0.25 then refined to 0.1. Once the stellar parameters are derived, the absolute magnitude of all the objects are derived based on the distance information and they are placed on the isochrones (Pietrinferni et al., 2006) of different ages. Together with the stellar parameters and brightness information candidates from the survey is separated out from the foreground stars. A few of the slitless spectra is given in the figure 3.5. These are followed up using long slit spectroscopy to derive the radial velocity and to better constrain their stellar parameters.

3.5 Follow up long slit spectroscopy

The selected candidates are followed up using longslit spectroscopy in which the medium resolution (R= 1880) spectra of the samples have been taken with HCT-HFOSC using Gr7 which covered a wavelength of 3900- 6880 Å . FeAr lamp spectra and halogen flats were taken with the similar observation set up. The long slit spectra of these samples are bias subtracted, flat fielded, extracted and wavelength calibrated using standard reduction technique which has been explained in detail in the chapter 2. Radial velocities were estimated using calibration spectra and telluric lines in

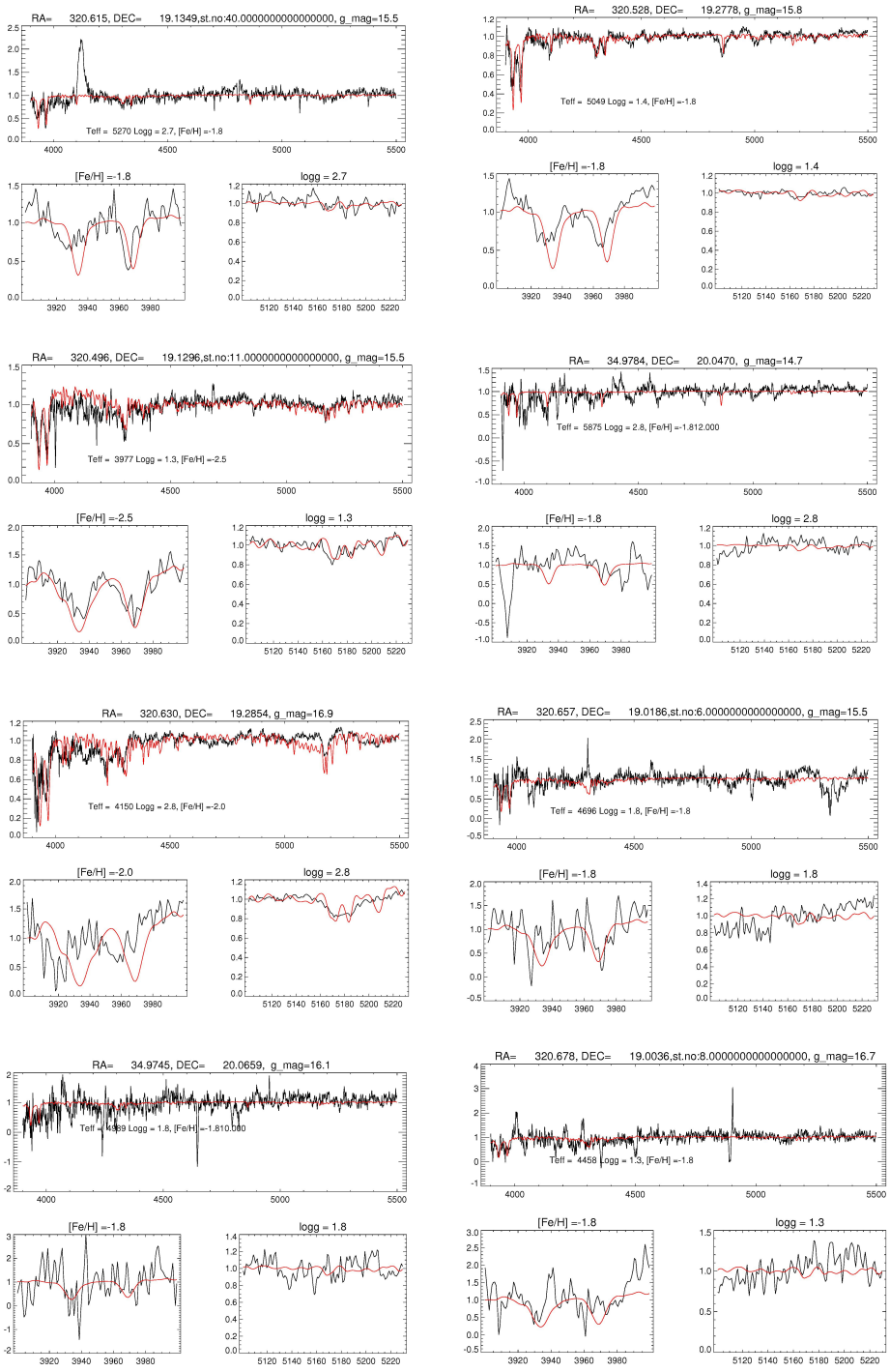

Figure 3.5: A few of the spectra extracted from the slitless field is given here. The red fit is synthetic spectrum corresponding to the model parameter. The stellar parameters are labelled in the figure.

the spectra. The calibrated spectra are then normalized using an IDL routine and then fitted with various stellar models to accurately determine the stellar parameters and the best synthetic fit model parameters were taken. 11 members have been discovered whose membership have been confirmed using the radial velocity value and the stellar parameters. The spectra and the best synthetic fit of the members are given in the Figure 3.15d. The details of all the candidates which are followed up using longslit spectroscopy is given in the Table 3.2

3.6 Results

Six satellite galaxies of milkyway have been studied using slitless spectroscopy and the based on the stellar parameters and brightness information, the candidates have been sorted out which were followed up using longslit spectroscopy. Nine new members have been discovered in the field of Segue 2 and Ursa Major II. We have also compiled a list of likely members of these satellite galaxies which needs to be followed up using long slit. Log of observed fields are given in table **??**. A detailed discussion on the members discovered in the field of UMa II and Segue 2 is given in the following sections.

3.6.1 Ursa Major II

Ursa major II has been identified as a dwarf satellite of the Milkyway by Zucker et al. (2006a) with an $M_v \sim$ -3.8 whose location in the sky is given in table 3.2 The distance to this UFD is 30$\pm$5 kpc and has a half light radius ranging from 50 to 120 pc. UMa II appears to be elongated with an ellipticity of $\sim$ 0.5. (Belokurov et al., 2007a, Fellhauer et al., 2007) indicates that UMA II could be a progenitor of

Satellite galaxies	Observed area	Number of spectra from slitless	Number of possible candidates	Number of stars followed up	Members
Segue III	30’ x 30’	160	20	3	0
Segue II	20’x 20’	67	25	3	2
Ursa Major II	25’x 30’	98	43	13	9
Segue I	10’x10’	16	9	1	0
Bootes II	10’x 10’	19	3	3	0
Bootes III	10’x10’	17	6	0	0

the stellar stream 'Orphan stream'. The abundance and kinematic studies of UMa II

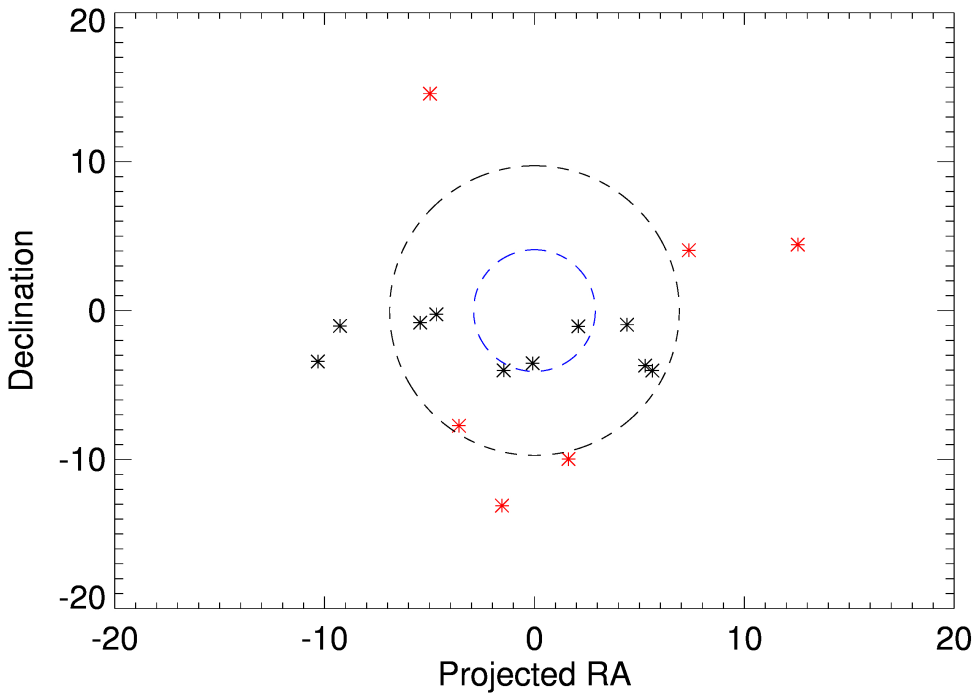

Figure 3.6: The position of the confirmed members from this survey is placed in the RA and Dec plane. The value in the X-axis is the projected RA value. The red points are the confirmed members from this survey and the black points are the members from Martin et al. (2007). The two circles represent the half light radii suggested by Zucker et al. (2006a) due to their elliptical shape.

revealed the fact that the system is undergoing a process of disruption (Simon and Geha, 2007).

Martin et al. (2007) discovered nine members in this dwarf galaxy (none of them are brighter than SDSS g_{mag} =*19.0*) and found that the members identified do not show any clear radial velocity peak. Simon and Geha (2007) identified 20 new members

in this dwarf galaxy with a velocity dispersion of 8.2 $\pm$ 1.6 kms^{-1}. Frebel et al. (2010b) has discovered CEMP stars in the field of UMa II which are the most metal poor stars identified in this system till date.

In our survey, we identified 6 new candidates at the brighter side of UMa II using radial velocity. We have also identified two interesting candidate in the field of Ursa Major II, a CEMP star and another one is a VMP star with carbon depletion and possible nitrogen enhancement. Due to high elevation of the this field for the HCT latitude, is available for observations for longer time. This enabled follow up of more objects in the field. All the samples in the field which are followed up using longslit are mentioned in the table in the appendix of this chapter.The radial velocity and the metallicity has been plotted for all the samples in the field (3.7)and it shows a clear distinction from the non-members. The histogram of all the samples (**??**)show that the members have a spread in their radial velocity and no clear RV peak is visible as suggested by Martin et al. (2007). Though the samples are less in number, this agrees with the earlier studies.

3.6.2 Segue 2

Segue 2 has been discovered by Belokurov et al. (2009) from Sloan Extension for Galactic Understanding and Exploration (SEGUE) imaging survey as overdensities in the field. It has a half light radius $\sim$30 pc and an absolute magnitude M_v =-2.5($\sim$900 $L_\odot$). According to Belokurov et al. (2009) the mean radial velocity of the members is -40 kms^{-1} with a velocity dispersion $3.4^{+2/5}_{-1/2}$ kms^{-1} which is indicative of the presence of dark matter. If the dark matter was not present the velocity dispersion would have been 0.5 kms^{-1}.

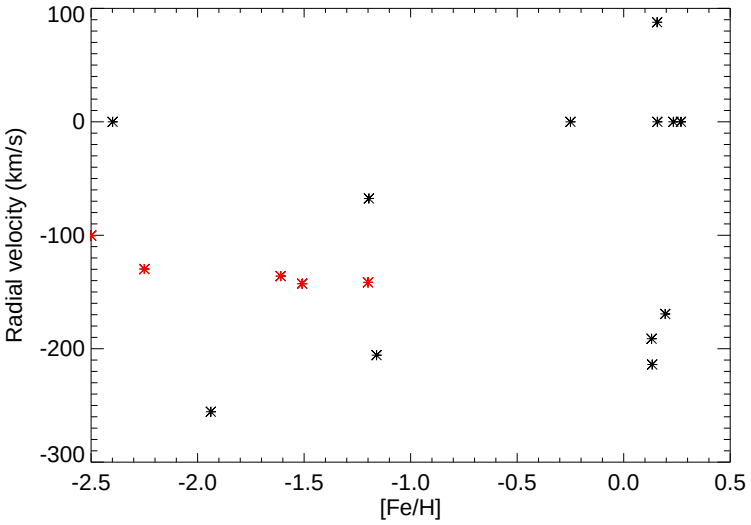

Figure 3.7: The metallicity of the all the samples in the UMa II field which are followed up using longslit spectroscopy is plotted against radial velocity.There is a clear distinction in the non candidates and presumed candidates. The red ones are candidates confirmed from their radial velocity values.

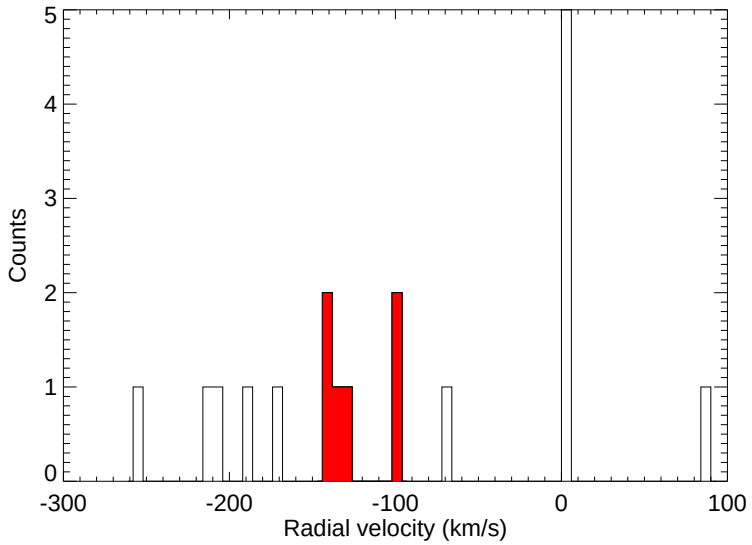

Figure 3.8: The histogram in radial velocity of the samples are plotted here. The filled ones corresponds to the most promising members in the UMa II field

Kirby et al. (2013) confirmed 25 more members in Segue 2 through spectroscopy. They found that there is a wide dispersion in the metallicity of the stars in Segue 2 ([Fe/H] from -2.85 to -1.33) and classified it as a dwarf galaxy because of the metallicity spread. The mean metallicity of Segue 2 is found to be -2.22$\pm$0.13 Kirby et al. (2013) which is higher than the value suggested by the luminosity metallicity relationship (Kirby et al., 2011) ([Fe/H]=-2.83). This could either be due to the tidal stripping or due to the presence of a metallicity floor galaxy formation (bottom panel of the figure-9 in Kirby et al. (2013)). In this study, we have found 3 new members in Segue 2 dwarf galaxy from their radial velocity value and the luminosity. The metallicity of these stars -1.81, -1.62 and -1.75. Though they are slightly metal rich than the mean metallicity of the stars in Segue 2, they fall well within the metallicity spread reported by Kirby et al. (2013). If we consider the mean metallicity of all the members in this dwarf galaxy, these samples have added an additional 0.1 dex

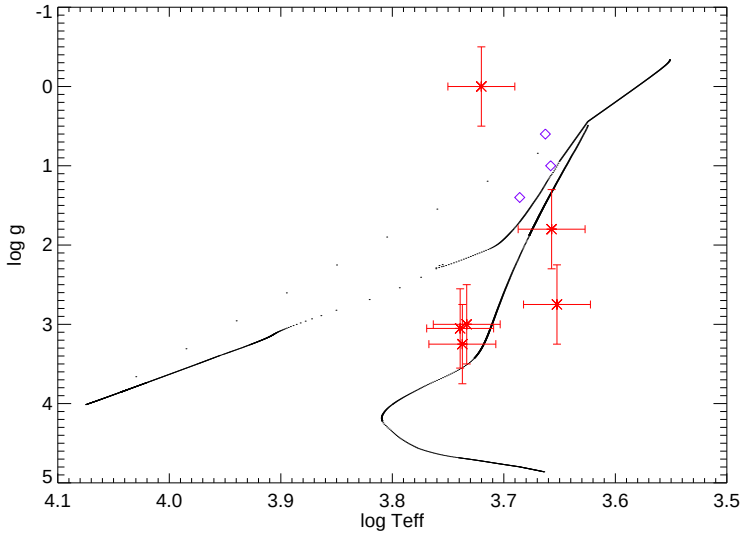

Figure 3.9: The figure corresponds to the most promising members selected from radial velocity value. The UMa II members from this study are shown in red asterisks. The UMa II candidates from Frebel et al. (2010b) is shown as violet diamonds. The isochrone is obtained from BASTI stellar isochrones with age is 13 Gyr.

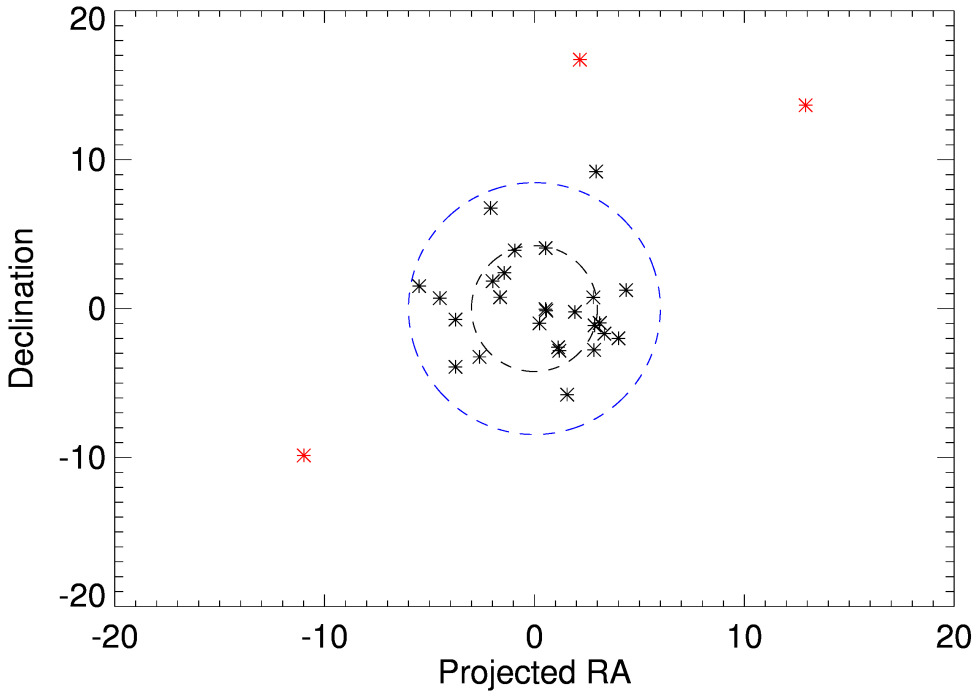

Figure 3.10: The plot corresponds to the confirmed objects in the field(red points). The black circle corresponds to the r_h whereas the outer circle corresponds to the $2r_h$. The black points are from Kirby et al. (2013).

towards the metal rich side but this value falls within the error quoted for the mean abundance.

3.6.3 Segue 1, Segue 3, Bootes 2 and Bootes 3

Segue 1

Segue 1 is an ultra faint dwarf galaxy discovered by Belokurov et al. (2007b) from over densities in the field with an absolute luminosity of $M_v \sim -3 \pm 0.6$ with a tail associated to it. Segue 1 is also found to be superposed on the leading arm of the Sagittarius stream which was the reason by Belokurov et al. (2007b) to identify Segue 1 as a globular cluster associated with the stream. Later Martin et al. (2008) revised the luminosity to $M_v = -1.5^{+0.6}_{-0.8}$ also explained the tidal tails as the Poisson scatter of few brighter stars in this system . It is situated at a distance of 23$\pm$2 kpc having a half light radius of 30 pc.

Geha et al. (2009) performed spectroscopy of 24 stars in the Segue 1 and found that Segue 1 is metal poor and dark matter dominated an with internal velocity of 4.3 ± 1.2 kms-1. A large spread in metallicity of Δ [Fe/H] > 0.8 dex have been reported from five of the seven stars (Frebel et al., 2014, Norris et al., 2010a,b). Segue 1 was found not to host stars with intermediate metallicities $-3<$[Fe/H]< -2. Webster et al. (2016) explained that it could be due to a supernovae feedback that stopped further star formation. They also explain the spread in metallicity could either be due to star formation at the interface of two colliding supernovae remnants or it being the first galaxy that experienced only single burst of star formation lasted ≤ 50 Myr and inefficient mixing.

10'x10' field of Segue 1 was observed and spectra of sixteen stars were obtained

from the slitless observations. The spectra were fitted with synthetic models and derived their stellar parameters and luminosity information. Among the sixteen spectra, nine were found to be satisfying the criteria to be the member of the dwarf satellites. Out of the nine stars, three stars were followed up using long slit and none of them turn out to be the members of Segue 1. This could probably due to the lesser sample of stars we have dealt with and the magnitude limit of this survey and the low intrinsic luminosity of the Segue 1.

Segue 3

Segue 3 has been identified as a faint star cluster (Mv $\sim$ -1.2) as overdensities in the SEGUE imaging catalog (Belokurov et al., 2010). The galaxy is situated at a distance of $\sim$ 17 kpc with a half light radius of $\sim$ 3pc. The low dispersion in velocity (1.2 ± 2.6 kms-1) and low dispersion and high average value of metallicity (from isochrone fitting) makes it a faint star cluster with no significant dark matter content. The extreme low luminosity Segue 3 is explained by the tidal disruption events suggested by the discovery 11 members of stars at a distance more than three half light radii from the center of Segue 3 (Fadely et al., 2011). These make it a strong candidate for studying the dynamical evolution due to tidal shocks and disruption events.

We observed 30'30' field of Segue 3 in order to find the details of tidal disruption. We have obtained 160 spectra of all the stars in the field. Out of these stars, 20 stars were found to be satisfying the membership criteria as explained in 3.4. out of these 20 stars, three stars were followed up and neither of them found to be members. This low fraction of likely membership (20 out of 160) is due to the large fraction of foreground stars in the field. Another reason could be the magnitude limit of HCT

(Vmag=17). brighter foreground stars also hinder probing the fainter stars in the field, this reduces the probability of detection of low luminosity stars.

Bootes II and Bootes III

Bootes II and Bootes III are at distances 42 kpc and 46kpc respectively (Grillmair, 2009, Walsh et al., 2008). We have observed these two UFDs through slitless spectroscopy. We could not find confirmed candidates in this field. It could possibly due to the small area we covered. Carlin et al. (2009) suggested that Bootes II is in a process of a complete tidal disruption, so it is possible for the objects to be present away from the center of the galaxy, but we cannot confirm it until we identify the objects.

3.7 Interesting candidates in the field of UMa II

Two interesting candidates have been identified in the field of UMa II. Both the stars are metal poor and enhanced with carbon or nitrogen. Their stellar parameters were derived from spectrum synthesis method and both the objects are found to be in the evolved population. Both the members are confirmed to be the member of UMa II through their radial velocity value.

3.7.1 CEMP star in the field of UMa II

HSS_0852+6311 is a bright star (V_{mag}=14.8) in the field of UMa II, easily identified in the field due to its prominent C_2 bands (refer figure 3.11). The stellar parameters of this objects are T_{eff}=5250K, log$g$=0.0, and [Fe/H]=$-$2.25. The spectrum is fitted for various values of carbon abundance and the best fit value found to be [C/Fe]=

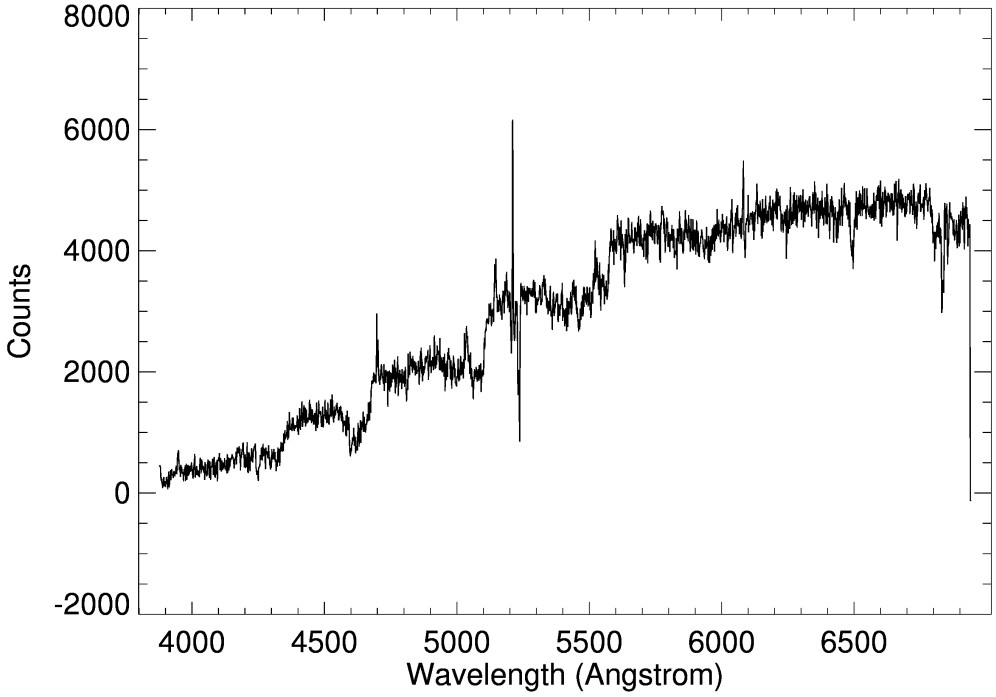

Figure 3.11: The slitless spectrum corresponding to the CEMP star in the field of UMa II .

3.25, which makes the star the most carbon rich in the field of UMa II. Though the metallicity makes the star to be placed in the metal rich end of CEMP stars reported from UMa II (Frebel et al., 2010b), the carbon abundance is really high among the reported carbon enhanced stars. Since the object show a high carbon abundance, nitrogen abundance can be measured from the CN features which are present in the spectrum. Obtaining the N abundance from the CN feature at 3880 Å is really difficult as the region is very noisy. So other CN features after 5635 region is used for obtaining the nitrogen abundance and the value obtained to be [N/Fe]= +2.25. This gives a [C/N]=+1.1. Apart from the C_2 bands, the star also show prominent Ba feature at 4934 Å . This indicate that the star is enhanced in s-process elements. The s-process enhancement along with the carbon can be explained in two ways. It could be due to either from the Third Dredge up (TDU) episodes the star underwent or from a binary companion which was once its AGB phase dredged up the s-process and carbon rich materials to the surface via TDU episodes and then transferred the mass to the binary companion which is the presently observing star. Considering the evolutionary phase of the star, TDU would have happened in this star itself causing the origin of s-process and carbon to be intrinsic in nature. But the star also show radial velocity variation from two epochs of observation, so external pollution is also possible for the carbon and s-process rich materials to be brought to the surface of the star.

Tc and ^{93}Nb are ideal probes to differentiate the intrinsic and extrinsic origin of carbon and other elements. ^{93}Nb is the product of radioactive decay of ^{93}Zr over a time scale of 1.5 Myr, which is rather fast compared to the time scale for a binary mass transfer. If the carbon star is intrinsic in nature, it would show enhanced Tc and Zr but very little Nb, whereas extrinsic carbon stars show enhanced Nb but depletions in Zr and Tc, at levels of [Zr/Nb] $\sim$ 0 (Ivans et al., 2005). But these

lines can only be detected in the high resolution observations of the objects. So high resolution observations are required for the detailed analysis of the object and nature of its companion star.

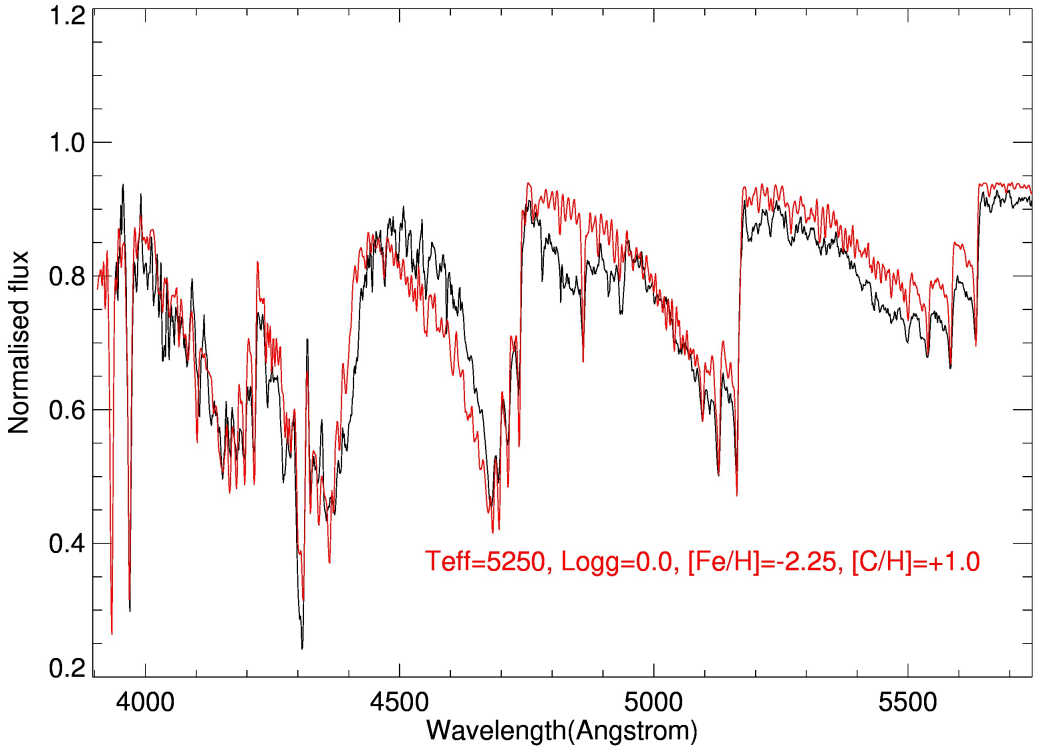

Figure 3.12: The CEMP star detected in the UMa II field. The best fit is shown here along with the model parameters.

3.7.2 VMP star in the field of UMa II with nitrogen enhancement

HSS_0852+6305 is identified as a VMP star in the field of UMa II with a metallicity of -2.5 which show nitrogen enhancement. The model parameters were derived using the spectrum synthesis method as explained in the chapter 2 and found to be a cool star (T_{eff} = 4541K) which is in an RGB phase. The synthesized spectrum

showed a poor fit CH-Gband region for solar carbon ratio (3.14). So the carbon was iteratively changed and fitted the region for the best fit gave a sub solar value for the carbon ([C/Fe]=-1.5). Another crucial element, Nitrogen, whose abundance can be derived using either the CN feature at 3880 or NH feature at 3330 Å . In any of the cases, the HCT spectrum cannot be precisely used for deriving the nitrogen abundance, as the 3330 feature is not covered and the CN feature at 3880 Å was very noisy. Though, being in the noisy part of the spectrum, 3880 CN feature was synthesized to get a cursory details of the nitrogen abundance. An enhancement in nitrogen is found [N/Fe]=0.6) giving a [C/N] ratio of -2.1. This satisfies the criterion required for the star to be NEMP as suggested by Johnson et al. (2007)([N/Fe]$>$0.5 and [C/N]< -0.5). The spectrum was also checked for any traces of Ba as a representative element of neutron capture nucleosynthesis. The Ba II line at 4934 Å is not detected in this spectrum which indicate that the s-process elements are underabundant.

This star was also reported by Frebel et al. (2010b), but nitrogen enhanced nature of the star was not mentioned in their study. The reported stellar parameters and the carbon abundance Frebel et al. (2010b), are matching within errors with the analysis in this study. According to Frebel et al. (2010b), the star show a depleted neutron capture elements ($[s/\mathrm{Fe}] < 0$), this supports the non-detection of Ba line in the spectrum.

The common origin of nitrogen in the early universe is the very metal poor AGB stars of intermediate mass to massive stars which underwent hot bottom burning (HBB) During HBB, the carbon produced during the dredge up of helium -burning products are predicted to be converted to nitrogen by CN cycling at the bottom of the convective envelope. The surface abundance of carbon and nitrogen in such

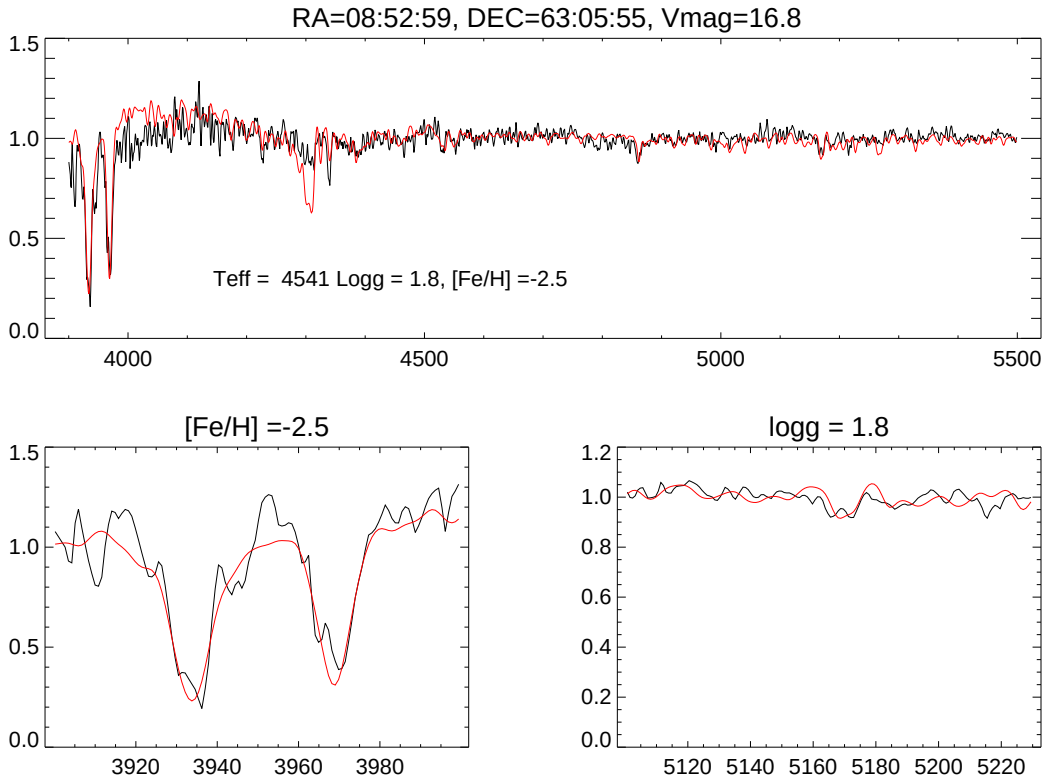

Figure 3.13: VMP star detected in the UMa II field with nitrogen enhancement. The poor fit of CH G band is visible in the spectral fitting.

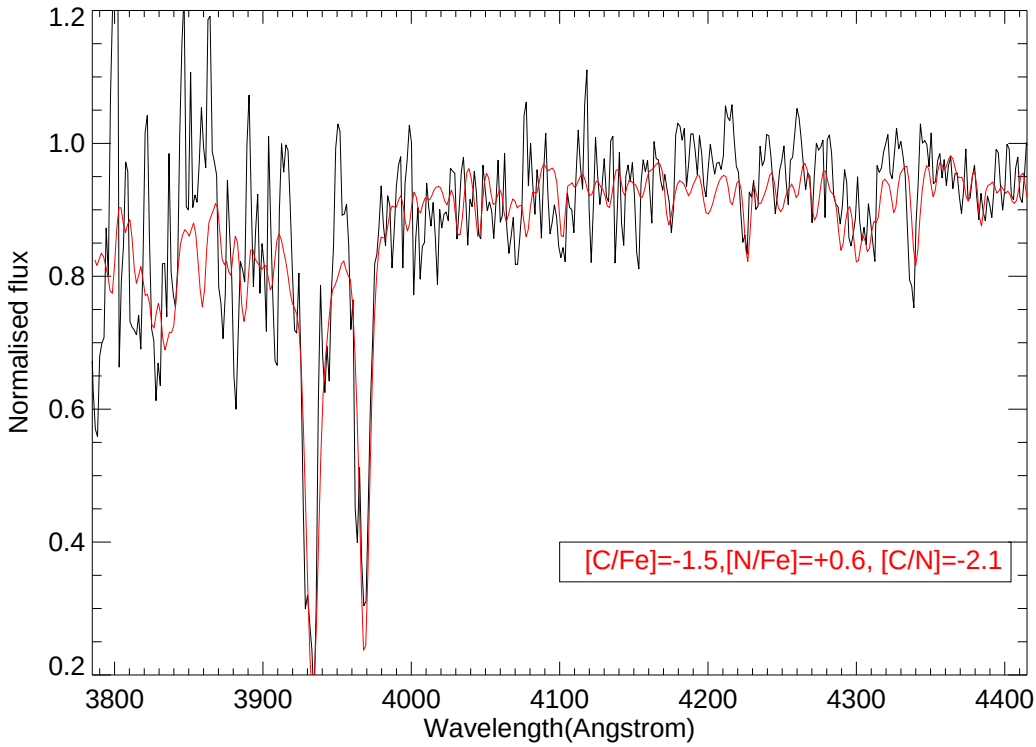

Figure 3.14: The VMP star with nitrogen enhancement is refitted with iterated carbon and nitrogen value is shown here. The best fit is the red spectrum and the final carbon and nitrogen value adopted for the best fit synthetic spectrum is shown in the figure.

AGB stars approach [N/C]$\sim$2 at the CN equilibrium. Detailed AGB evolution models (Karakas and Lattanzio, 2007, Karakas, 2010) indicate that metallicity is crucial factor which determines the mass required for the HBB to occur. A mass $\geq 5M_{\odot}$ is required at solar metallicity while in low metallicity, significant lower masses are only needed for the HBB to set in (at [Fe/H]= -2.3, mass $\approx$3 $M_{\odot}$)

Another possibility is that, the star in the RGB phase must have undergone first dredge up and the carbon would have been be depleted by CN cycling and thus enhancing the nitrogen. In such a case the isotopic ratio of carbon would also have reduced due to the mixing and CN cycling $^{12}C/^{13}C$ ratio is a very good diagnostic to understand the degree of mixing in the envelope. Unfortunately, the study which is reported here include low resolution observations covering 3900-6880 Å and $^{12}C/^{13}C$ ratio cannot be determined from this spectral range. Frebel et al. (2010b) also report that the star show a radial velocity variation, which support the idea of AGB contributing to the nitrogen enhancement. But, the depleted carbon value with no traces of s-process elements might indicate the AGB companion is of intermediate mass that went through HBB.

The radial velocity variation together with the depleted carbon value and the absence of neutron capture elements make it difficult to constrain the origin of nitrogen in this star. High resolution observations of the object in the bluer wavelengths is required to explain the origin of nitrogen enhancement thereby to constrain the origin of elements.

3.8 Conclusion

The fields of each satellite galaxy mentioned in table 1 has been studied using slitless spectroscopy. The possible candidates are being followed up using long slit

spectroscopy. Based on the obtained medium resolution data, the candidacy of 9 objects have been confirmed. The objects could not be followed up in high resolution using HCT because of its faintness. Two of the members which are peculiar in their chemical pattern (carbon enhanced and nitrogen enhanced) were proposed for follow up observations using larger telescope. All the candidates confirmed for their membership are found to be outside the half light radius. This indicate that the satellite galaxies have undergone tidal disruption events. There might still be members present which could not be probed out by our survey. We will further study the potential candidates by combining the recent deeper survey and GAIA to refine the candidacy.

3.9 APPENDIX

RA	DEC	T_{eff}	Logg	[Fe/H]	hrv	field	Membership
hh:mm:ss	dd:mm:ss	K	cms^{-1}	dex	kms^{-1}		
02:18:29.30	20:00:38.38	4291	2.950	-1.89	-64.097	Segue II	yes
02:18:55.54	19:58:07.95	4584	3.534	-1.987	-8.87	Segue II	no
02:19:14.00	20:27:34.00	4724	2.750	0.108	-85.24	Segue II	no
02:19:14.45	20:09:51.60	3915	4.545	-2.236	-40.70	Segue II	no
02:19:16.20	20:13:07.73	5505	3.539	-2.010	-158.67	Segue II	no
02:19:25.32	20:27:12.70	5367	3.00	-1.624	-50.863	Segue II	yes
02:19:34.23	20:05:38.38	5320	3.247	-1.422	20.07	Segue II	no
02:20:11.23	20:24:09.30	5090	2.750	-1.750	-31.841	Segue II	yes
08:50:45.62	63:22:22.03	4491	2.90	-2.500	-100.24	UMa II	yes
08:50:32.33	63:12:15.8	5435	2.750	0.158	0.00	UMa II	no
08:50:39.53	63:09:5.43	4372	2.687	-2.399	0.00	UMa II	no
08:50:41.60	62:57:33.8	5159	2.750	0.195	-169.34	UMa II	no
08:50:45.62	63:22:22.03	4481	3.087	-2.468	0.00	UMa II	no
08:50:53.3	63:19:40.1	4387	2.750	0.157	87.74	UMa II	no
08:50:58.34	63:00:4.12	5460	2.802	-1.61	-135.967	UMa II	yes
08:51:6.89	63:01:57.16	5428	2.750	-1.160	-205.71	UMa II	no
08:51:16.44	62:54:42.43	4758	3.000	-1.196	-67.57	UMa II	no
08:51:19.09	62:59:7.64	4818	3.379	-1.938	-255.57	UMa II	no
08:51:20.28	63:12:4.59	4974	2.750	0.131	-191.17	UMa II	no
08:51:35.52	62:58:39.19	3757	0.000	-0.250	0.00	UMa II	no
08:51:44.25	62:57:49.99	5485	3.052	-1.509	-142.676	UMa II	yes
08:52:18.39	62:57:34.99	4976	2.750	0.233	0.00	UMa II	no

08:52:25.35	63:00:6.47	5174	2.750	0.269	0.00	UMa II	no
08:52:30.02	63:03:24.7	4992	2.750	0.134	-213.92	UMa II	no
08:52:35.2	63:11:51	5250	0.0	-2.25	-129.8	UMa II C*	yes
08:52:59.00	63:05:55.00	4541	1.8	-2.5	-100.3	UMa II	yes
08:53:21.21	63:12:13.97	5411	3.000	-1.159	-141.518	UMa II	yes
10:06:18.27	15:52:52.3	5633	2.750	0.314	-47.76	Segue 1	no
10:06:46.58	15:58:04.99	5917	2.750	0.152	-61.84	Segue 1	no
10:07:43.82	15:52:18.73	5291	3.250	-1.250	36.75	Segue 1	no
13:58:37.46	12:44:49.78	4441	2.750	0.500	-69.65	Bootes II	no
13:57:57.11	12:52:13.8	3402	2.750	-2.500	31.00	Bootes II	no
21:22:3.36	19:19:26.67	4897	2.750	0.339	94.2	Segue 3	no
21:22:37.8	19:01:08.2	3974	2.750	-0.046	59.17	Segue 3	no

Figure 3.15: The best model fit for stars in different satellite galaxies. Their stellar parameters derived are mentioned in the plot

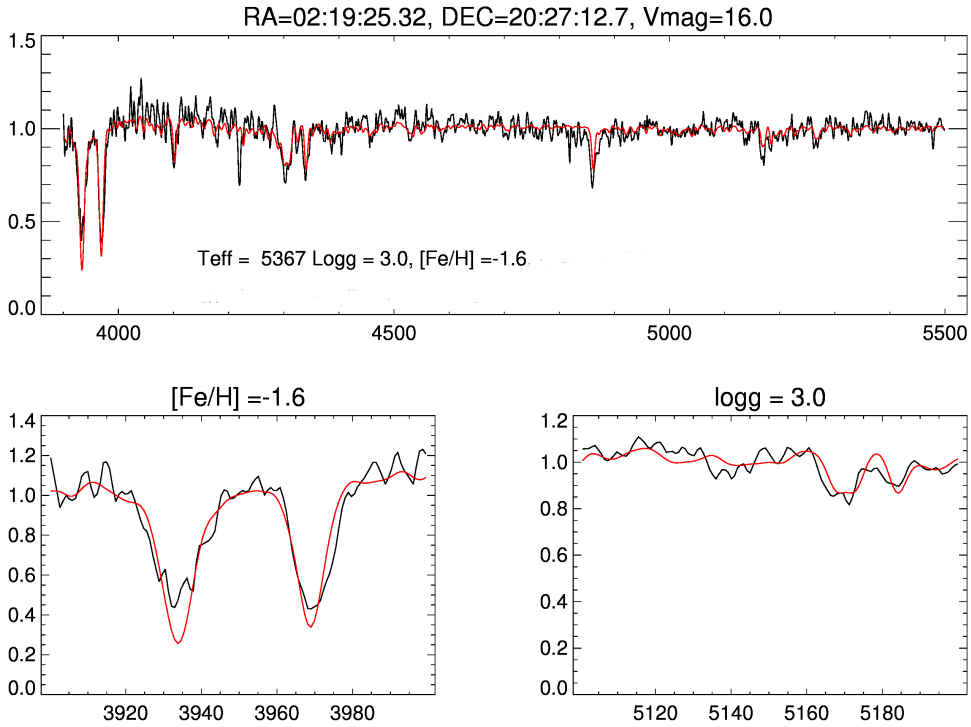

(a) A star from Segue II dwarf galaxy.

(b) Star from Segue II dwarf satellite galaxy

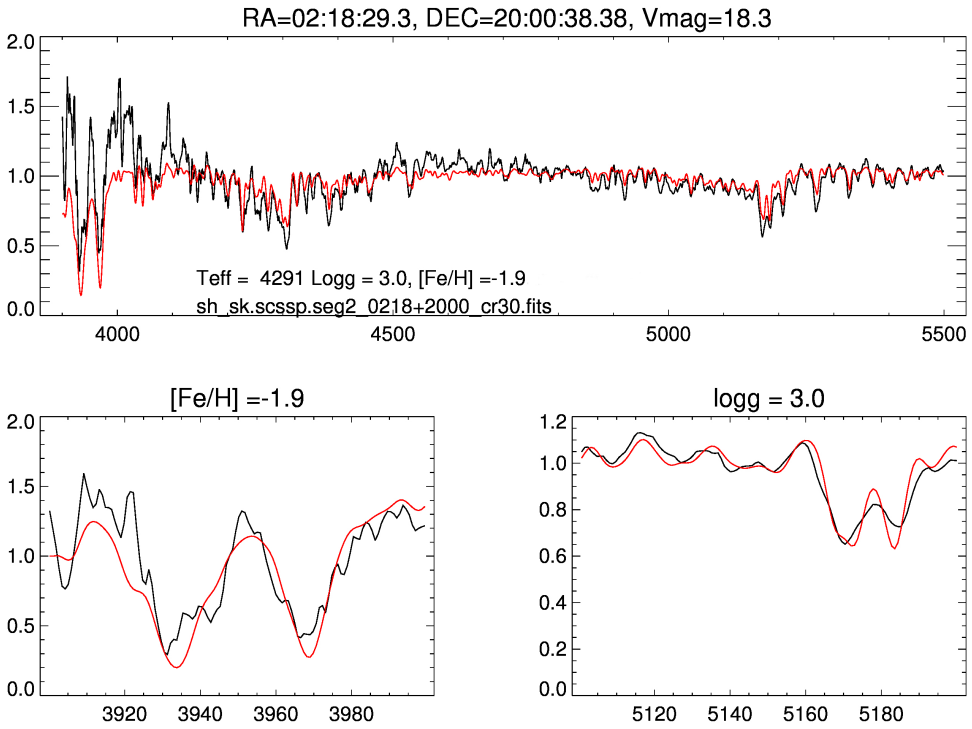

(c) Star from Segue II dwarf satellite galaxy

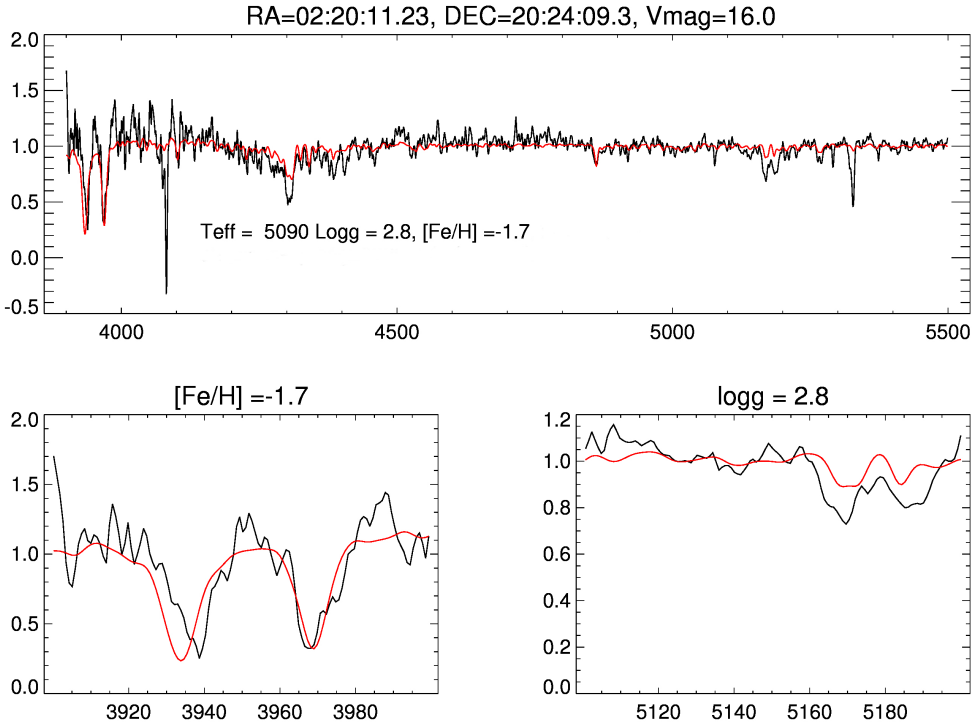

(d) Star from Ursa Major II dwarf satellite galaxy

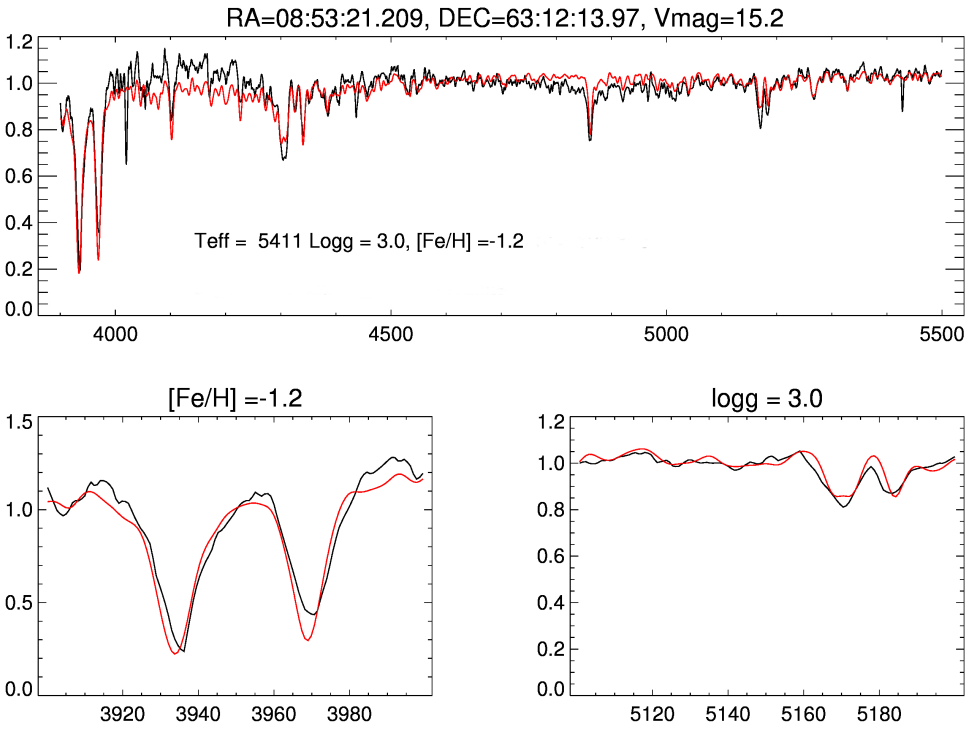

(e) Star from Ursa Major II dwarf satellite galaxy

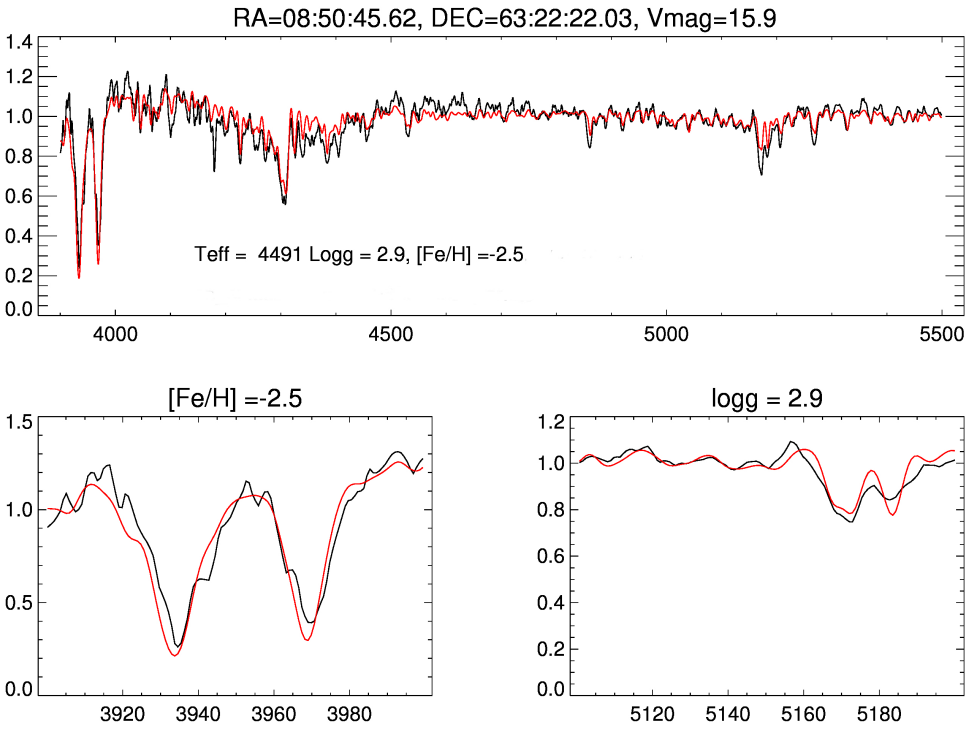

(f) Star from Ursa Major II dwarf satellite galaxy

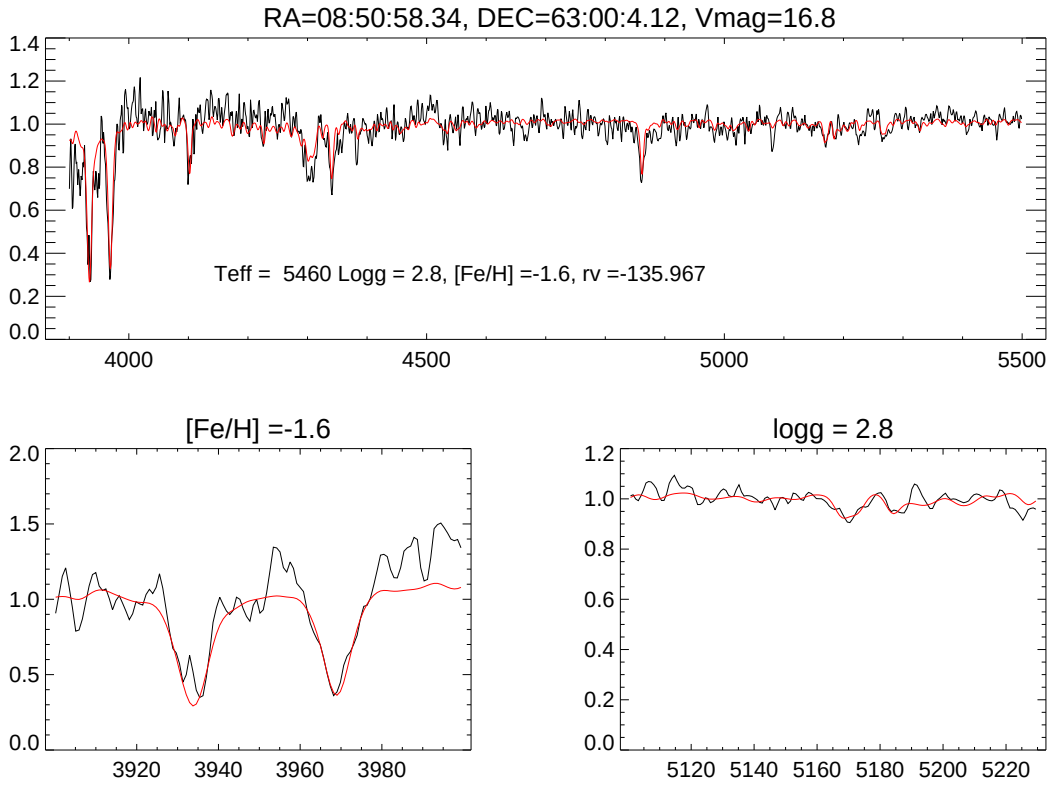

(g) Star from Ursa Major II dwarf satellite galaxy

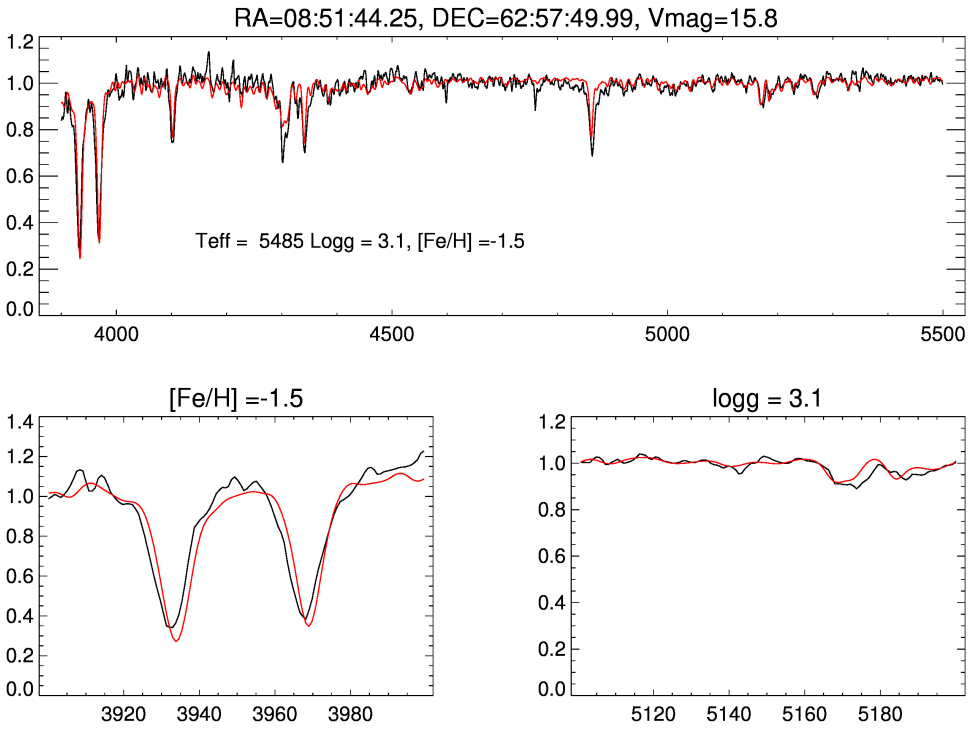

Chapter 4

CEMP stars from Carina dwarf spheroidal galaxy[1]

4.1 Introduction

Observational studies of metal-poor stars in the Milky Way (MW) and other nearby galaxies reveal that the early Universe has experienced various nucleosynthetic mechanisms. The diverse chemical composition these stars preserve in their photosphere is the result of such nucleosynthetic mechanisms and detailed studies of their abundances yield information about the nature of their progenitors and how the latter contributed to the interstellar medium (ISM) through various (explosive) mechanisms. The diversity in the stellar chemical properties becomes more important and unique as the metallicity of the stars decreases.

Metal-poor stars in the MW have been extensively studied and classified into

[1]The results of detailed abundance analysis of the star ALW-8 from this chapter is accepted for publication in A&A, arXiv id:1706.06599

different groups based on their metallicity, with further distinctions based on the abundance of certain key elements (e.g., Aoki et al., 2007, Beers and Christlieb, 2005). Amongst these, Carbon-enhanced metal-poor (CEMP) stars (defined by [Fe/H] < -2.0 and [C/Fe] $>$0.7) are of great interest since the origin of the carbon overabundance is versatile and closely related to the formation and enrichment history of the host stellar system (Aoki et al., 2007, Bonifacio et al., 2015, Carollo et al., 2014, Hansen et al., 2016b, Koch et al., 2016, Lee et al., 2017, Masseron et al., 2010). These stars are primarily categorized based on the presence and absence of neutron capture elements as CEMP-s, CEMP-r, or CEMP-r/s, versus CEMP-no, respectively. Amongst these sub classes, CEMP-s stars with their strong enhancements in s-process elements are mainly found to be members of a binary system (Aoki et al., 2007, Hansen et al., 2016d, Starkenburg et al., 2014). This favors the idea that their carbon-enhancement is due to mass transfer from a companion, which was once in its Asymptotic Giant Branch (AGB) phase and has since faded into a white dwarf. Thus, the carbon- and s-process-rich material had been accreted onto the surface of the presently observed star, which does not necessarily reflect the properties of the genuine ISM from which it was born.

CEMP-no stars, on the other hand, are often found not to be associated with binaries (according to Hansen et al. (2016c), 4 out of 24 stars in the radial velocity monitoring show binarity) and, as such, their abundance patterns are those imprinted by the ISM. Hansen et al. (2016c) stated that CEMP-no stars are *bona fide* second generation stars, bearing the primordial remnants of enrichment from an early generation of stars. The frequency of CEMP-no stars increases with decreasing metallicity, and below an [Fe/H] of approximately -3.5 dex almost all C-rich stars are of the CEMP-no class (Bonifacio et al., 2015, Hansen et al., 2016b). The

abundance pattern observed in CEMP-no stars matches well with models of primordial faint Supernovae (SNe) that experienced mixing and fall-back, and models of zero-metallicity-spin stars having high rotational velocity (e.g., Ishigaki et al., 2014, Kobayashi et al., 2011, Meynet et al., 2006, Umeda and Nomoto, 2003). In this regard, Yoon et al. (2016) and Hansen et al. (2016b) suggest that probably more than one class of first-generation progenitors is required to account for the abundance patterns of CEMP-no stars.

Recent studies have uncovered several carbon-rich stars in dwarf spheroidals (dSph) and ultra faint dwarf satellites around the MW (Frebel et al., 2010b, Ji et al., 2016a, Lai et al., 2011, Norris et al., 2010a). Broadly consistent with the properties of CEMP stars in the Galactic halo, these objects were found across the entire metallicity range down to [Fe/H]~-3.5 dex and as metal rich as -2.0 dex and above, with varying C-enhancements from moderate values of [C/Fe]$\sim$0.5 up to 2.3 dex, and drawn from the CEMP-no and CEMP-s subclasses. Moreover, these stars have now been found and analyzed in detail in the more luminous dSphs such as Sculptor and Sextans (Honda et al., 2011, Salgado et al., 2016, Skúladóttir et al., 2015). Here, the latter works stand out in that they provide the first carbon-rich stars within the metal-rich tails of the galaxies' metallicity distributions (at [Fe/H]=-2 and -1 dex). Even though all of the more luminous dSphs contain old stellar populations (Grebel, 1997), none of them appear to show any CEMP population in the extremely metal-poor regime below -2 dex, owing to the shift in the metallicity distribution function towards the metal-rich side with increasing galaxy luminosity (Kirby et al., 2011, Salvadori et al., 2015).

Amongst the classical dSphs, Carina is of special interest because of its unusual, episodic star formation history, where each of the stellar populations has also experienced distinct chemical enrichment (Koch et al., 2008, Monelli et al., 2003, Mould

and Aaronson, 1983, Smecker-Hane et al., 1994, Tolstoy et al., 2003). Azzopardi et al. (1986, hereafter ALW) detected ten carbon-rich (CH- and C-) stars in Carina. Two of those (ALW-6 and ALW-7) were analyzed by Abia et al. (2008), with a particular focus on the origin of the s-process elements in these stars. At [Fe/H]=-1.8 to -2 dex and [Ba/Fe]$>$1.9 dex, both qualify as CEMP-s stars, where mass transfer of processed material acted as the source of the abundance enhancements. Conversely, no CEMP-no stars have been identified in Carina to date.

In this chapter, the abundance analysis of the first CEMP-no star in Carina (ALW-8), and a CEMP-s star from ALW -sample (ALW-1) are being discussed. This chapter is organized as follows: In Section 2, the observations and data for the stars have been summarized, in Sect. 3 detailed abundance analysis of both the stars and in Sect. 4, the results are presented.

4.2 Observation and Data reduction

The data were obtained in the course of the ESO Large Programme 171.B-0520 (PI: G. F. Gilmore) that aimed at studying the kinematic and chemical characteristics of Local Group dSphs (Koch et al., 2006, 2008). Along with high-resolution ($R\sim$40000) spectra of ten red giants that were observed with the Ultraviolet and Visual Echelle Spectrograph (UVES) at the ESO/VLT in multi-object mode, two of the targets turned out to be carbon-rich stars as was obvious from their strong molecular bands. Coincidentally, these were part of the ALW sample, namely ALW-1 and ALW-8. The C-rich nature of ALW-8 was also noted by Venn et al. (2012), but discarded from their further analysis. The observations covered a spectral range of 4700-6800 Å with the central wavelength at 5800 ÅṪhe overall set up of 1" fibre aperture and the chosen CCD binning of 1x1 pixels provided a resolving power of

$\sim$ 47000.

The data were reduced using standard UVES pipeline (Modigliani et al., 2004) implemented in the MIDAS [2] environment. The standard reduction steps like bias subtraction, division by a master flat field, obtaining spectral orders from fibre flat-field frames, wavelength solutions from calibration exposures of Th-Ar lamp and extraction of the target spectra have been performed. Sky subtraction has been performed on this final extracted, wavelength calibrated spectra using the sky spectrum taken along with the target spectrum using a dedicated fibre set up. The spectral orders of the final spectrum is merged and the individual exposures are shifted to the helio centric standard of rest and coadded. Each individual exposures have given a weightage of its S/N before coadding. The final S/N of the final spectrum thus achieved is approximately 20 per pixel. Fig. 4.1 shows the location of the stars in a colour magnitude diagram with photometry taken from the ESO Imaging Survey (Nonino et al., 1999), and their general properties are listed in Table 4.1

4.2.1 Radial velocity and binarity

In order to correct for the shift in spectral lines, the spectra of both stars have been cross-correlated against a synthetic spectrum generated on the initial assumptions of temperature, surface gravity, and the mean metallicity of Carina (Koch et al., 2006). The resulting heliocentric velocity of ALW-8 of 223.3$\pm$1.0 km s^{-1} is not only in excellent agreement with Carina's systemic velocity, but also agree well with the values of these stars found by Walker et al. (2009).

[2]The European Southern Observatory Munich Image Data Analysis System (ESO-MIDAS) is developed and maintained by the European Southern Observatory

Table 4.1: Photometric, kinematic, and atmospheric parameters of the target stars

Property	ALW-1	ALW-8	Reference[a]
α (J2000.0)	06:41:08.58	06:41:46.27	1
δ (J2000.0)	$-$50:47:50.1	$-$50:58:55.9	1
V	17.68	17.88	2
I	16.33	16.41	2
J	15.235	15.465	3
H	14.557	14.778	3
K	14.295	14.509	3
E(B$-$V)	0.053	0.064	4
v_{HC} [km s^{-1}]	226.2 / 256.2[b]	223.3	5
T_{eff} [K]	4100	4150	5
$\log g$	0.25	1.00	5
ξ [km s^{-1}]	2.0	2.3	5
[Fe/H]	~ -2.8	-2.5	5
C/O	8	1.5	5
^{12}C/^{13}C	100	9	5

[a]References: 1: ALW; 2: Walker et al. (2009); 3: 2MASS (Cutri et al., 2003); 4: Schlegel et al. (1998a); 5: This work.

[b]Radial velocity from the two epochs of observations.

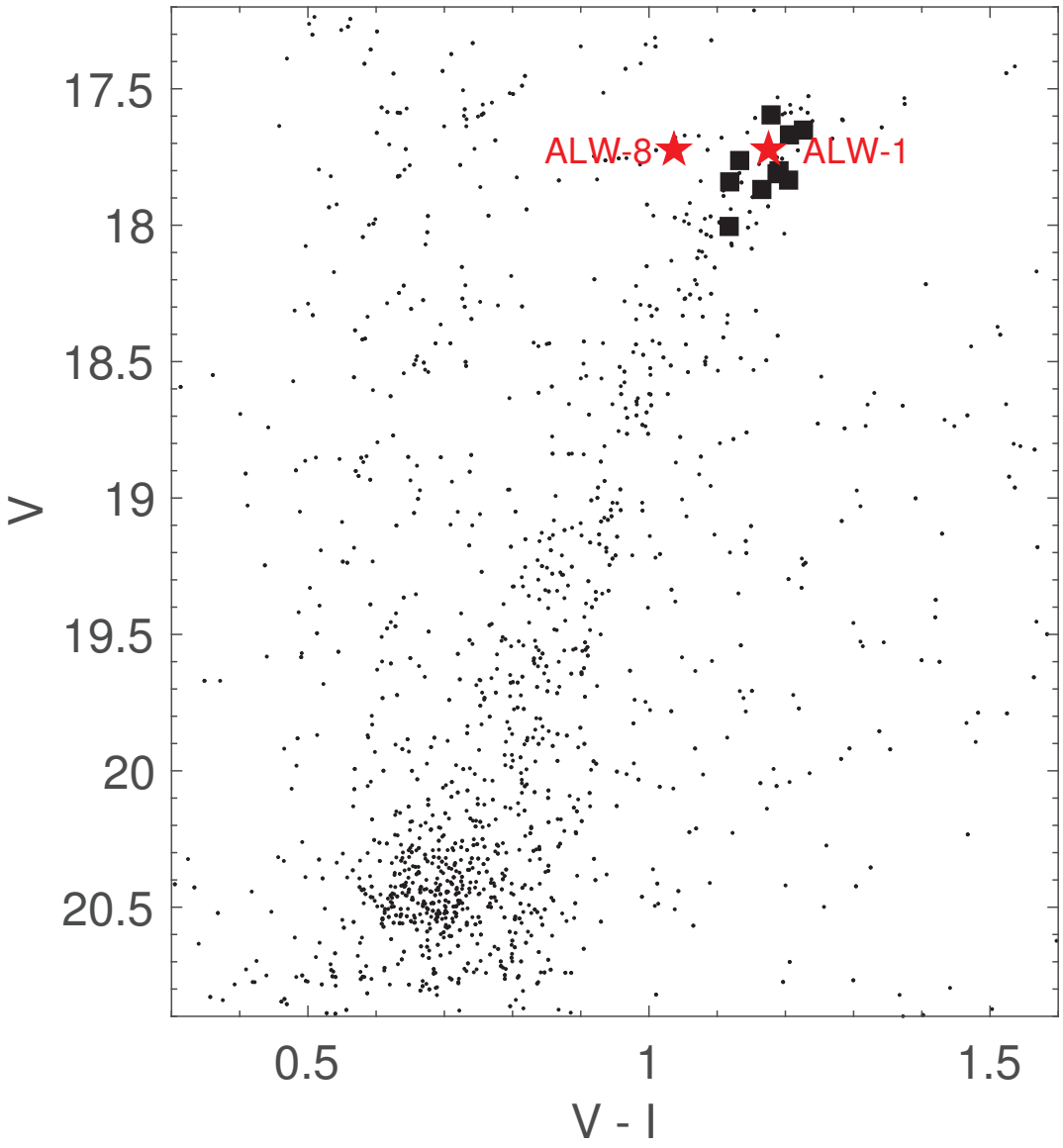

Figure 4.1: Upper colour magnitude diagram of Carina's central 10arcsec, using photometry from the ESO Imaging Survey. Stars shown as black squares are the red giant targets of Koch et al. (2008), while the filled red star symbols indicate the carbon stars from the present work.

For ALW-1, the spectrum used in this study is a resultant of coadding of individual spectra taken at two different runs separated by 60 days. The cross correlation analysis of the co-added spectrum of ALW-1 showed a double peak, separated by 30km s^{-1}, with a ratio of $\sim$ 0.7. This double peak nature of CCF is either due to the presence of a spectroscopic binary star or from the radial velocity variation of the star which would not have been taken into account while co-adding the spectra. (refer figure 4.2). The two spectra were taken with a separation of 60days. Thus, it could be that the object show RV variation due to an unseen companion and shift is not accounted in the co-added spectra. Unfortunately,the data archive of ESO does not bear the original tapes. The shift is around 30km/s over a 60days as seen in the cross correlation peak is rather large. Data from Walker et al. (2009, and 2017, private communication) and T.T. Hansen (2017, private communication) has been used to resolve the actual cause of the double peak. Their data did not show any such features of double peaks in the cross-correlation rather indicated significant radial velocity variations. Hence, is it is likely ALW-1 is likely a part of a unseen binary system. We consider this analysis is still worthwhile, to probe the nucleosynthesis of the unseen close companion on the current CEMP star.

4.3 Abundance analysis

The spectral synthesis code TURBOSPECTRUM developed by Plez (2012). has been used through out the work. To this end, the final stellar atmospheric model from a grid of model photospheres (Mészáros et al., 2012) has been interpolated in which the ATLAS9 and MARCS codes were modified with an updated H_2O linelist and with a wide range of carbon- and α-element enhancements. Local thermodynamic equilibrium (LTE) has been assumed for all species.

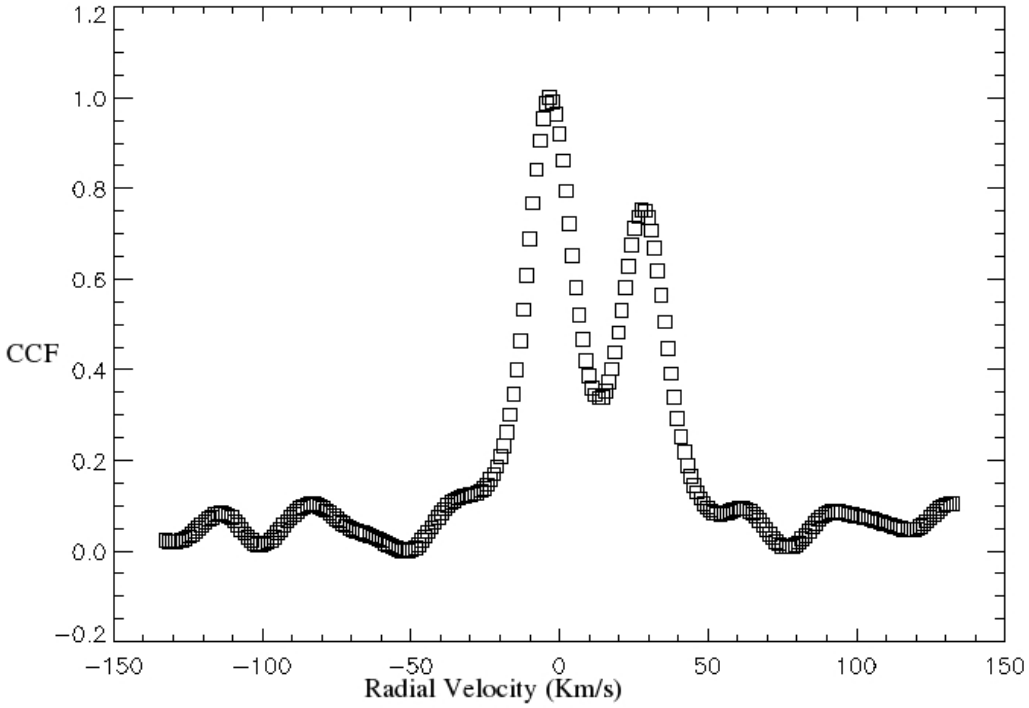

Figure 4.2: The plot obtained after cross correlating the spectrum of ALW-1 and the template synthetic spectrum. The double peak is clearly visible in the spectrum.

The Solar abundances from Asplund et al. (2009) has been adopted and Solar isotopic ratios were used for all the elements unless noted otherwise (see Sect. 4.3.). Line lists for atomic lines were assembled from the VALD database Kupka et al. (1999) and details are given in Table 4.3. Hyperfine structure (HFS) has been accounted for for Li, Sc, Ba, and Eu, although the corrections were negligible in the latter two cases. Finally, for the relevant molecules, the CH line list compiled by T. Masseron (private communication) and CN data from Plez and Cohen (2005) were employed.

4.3.1 ALW-1: Spectral synthesis

The spectrum of ALW-1 is similar to that of a double line spectroscopic binary in which each stellar feature have two components. In this spectrum, each absorption feature has two contributions: one bluer component called as primary, is due to the contribution from earlier observation while the redder component called as secondary, which is from the observation after 60 days. Due to the two components in the spectra, the normalized continuum levels of the spectrum will also have unequal contributions. Deriving the chemical abundance from such a spectrum is hampered by each spectral feature having contributions from either component. Moreover, this CEMP star is a cool star having a high carbon-abundance so that most of the lines are blended with strong carbon bands. Thus, abundance analysis for this star is done by exclusively using spectral synthesis, where each bluer and redder component of the spectrum has been synthesized individually. These were then combined using the appropriate veiling factor (Koch et al., 2011, Preston, 1994, Thompson et al., 2008); as suggested by the relative strength of the CCF peaks (Fig.4.2), the veiling has been adopted as 1:0.7, i.e., where the secondary component contributes $\sim$40%

to the overall flux. A portion of the spectrum is indicated in Fig.4.3.

4.3.2 ALW-8: Equivalent-width measurements

The spectrum of ALW-8 also shows a wealth of molecular features that contaminate the atomic lines. This severely hindered the measurements of precise equivalent widths (EWs) for a large number of lines. To this end, analysis has been constrained to such few lines that are devoid of contributions from molecular bands . In order to identify such unblended lines, the full spectral range has been synthesized using the representative carbon, nitrogen, and oxygen abundances, and checked for those lines that remained free from molecular features. In practice, EWs were measured by fitting Gaussian profiles to the features using IRAF's *splot* task. The uncertainties in the measurements were determined via the revised Cayrel formula (Battaglia et al., 2008, Cayrel de Strobel and Spite, 1988). The final linelist is given in table 4.3 in the appendix of this chapter.

4.3.3 Stellar parameters

ALW-1

As an initial guess for the effective temperature, photometry of ALW-1 in different passbands are employed from the literature (Table 4.1) and the empirical color-$T_{\rm eff}$ relations of Alonso et al. (1999). The temperature thus derived are 3980 K, 4120 K and 4000 K from J−K, J−H and V−K colours respectively. In the following, the value based on the (V−K) colour of 4000 K was adopted because of the large separation of the wavelengths of the bands involved and less influences of molecular carbon features than that on the other passbands. Using this value as input, a grid of

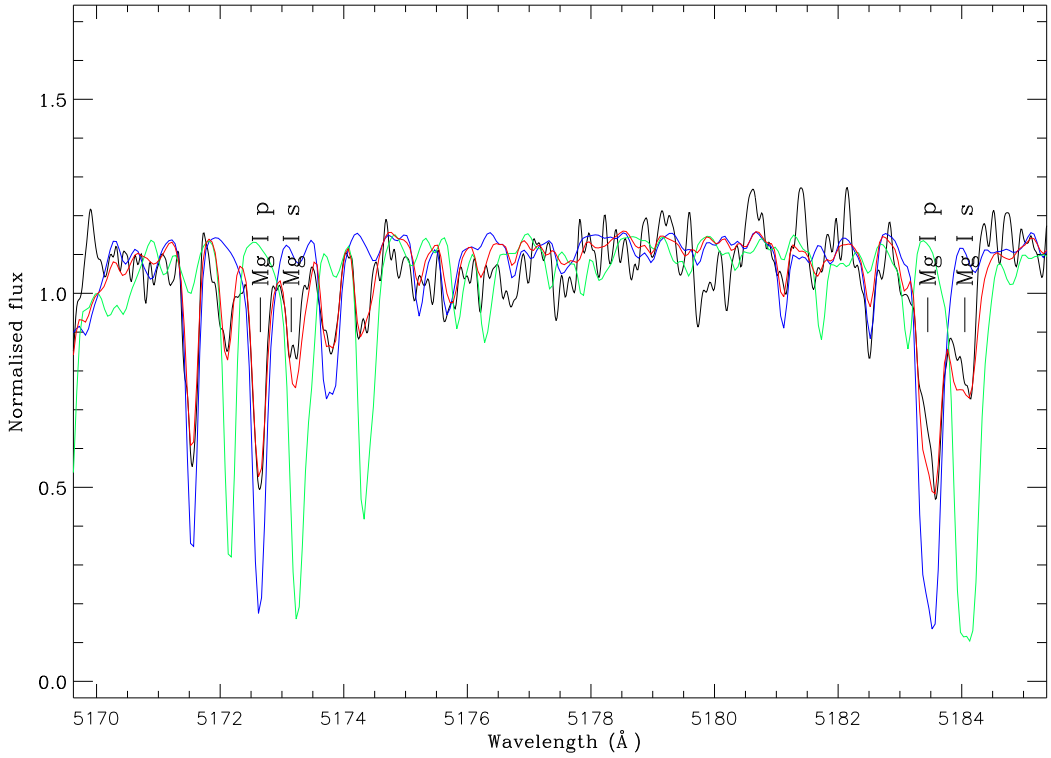

Figure 4.3: Observed spectrum of ALW-1 near the Mg I triplet lines (black line); overplotted are synthetic spectra computed with the best-fit stellar parameters (refer section 4.3.3). Blue and green spectra show individual plot of the primary and secondary components, respectively, while the red line corresponds to the final spectrum after Doppler-shifting and co-adding of the two spectra, weighted by the appropriate veiling. Mg-lines due to the primary and secondary have been marked as 'p' and 's' respectively.

synthetic spectra were created to represent either of the spectral component. These were combined as elaborated above, i.e., by using a veiling factor of 70%, and used to fit the region at 5160 - 5190 Å which includes the Mg triplet lines around 5170Å in a least-squares sense in order to constrain the star's surface gravity and metallicity. Furthermore, spectra were synthesized with various levels of carbon enhancements in which log ϵ(C) has been varied from +6.42 to 7.52 in steps of 0.2 dex. The best result was obtained from ($T_{\rm eff}$, log g) = (4100 K, 0.25). and with a metallicity of -2.8 dex. The typical uncertainties in the parameters, as determined from the goodness of the fit, are $\pm$ 250 K and $\pm$0.5 dex. The process has been iteratively performed by including oxygen abundance and isotopic ratio and the values quoted in table 4.1 were obtained from the best fit. The [C/Fe] thus obtained is 1.30 quoted in the table 4.2. Table 4.1 lists the best stellar parameters obtained in this way and in Figure 4.4, the region around the Mg triplet lines and C_2 band that was used in the parameter derivation is shown.

The spectrum of ALW-1 is rich in molecular features and the derivation of stellar parameters from the equivalent width analysis will be erroneous. So stellar parameters and other elemental abundance were derived by solely depending on spectral synthesis method. The metallicity is also derived by fitting the Fe lines in the overall spectrum and the value is chosen in such a way that most of the iron lines are matching with the chosen metallicity value, at -2.8. The microturbulent velocity (ξ)was fixed at 2.0 km s^{-1} throughout the analysis because a similar ξ is reported for red giant stars in Carina having temperature and log g similar to ALW-1 (Shetrone et al., 2003).

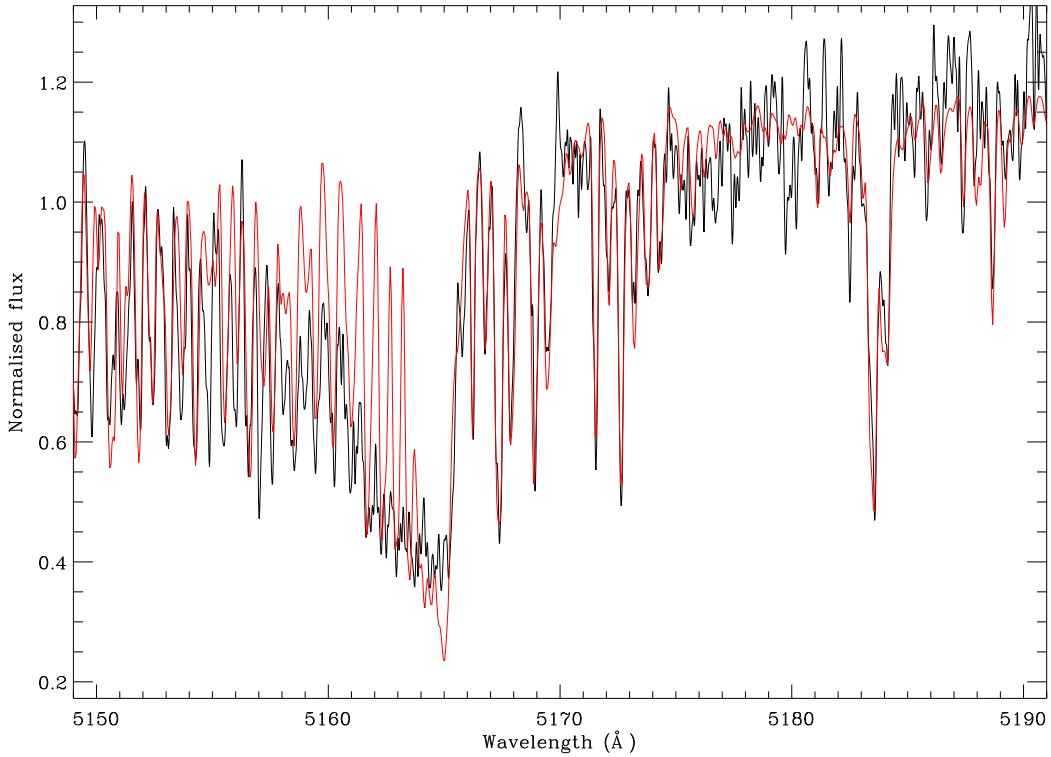

Figure 4.4: The Mg triplet region of ALW-1 (black line) is plotted together with the best-fit synthetic spectrum (red). A veiling factor of $\sim 70\,\%$ is used for the spectrum of the successive observation to obtain the final spectrum shown in red.

ALW-8

The effective temperature of ALW-8 has been estimated using various color indices from the literature (Table 4.1), and using the color-transformation of Alonso et al. (1999). To this end, an initial metallicity of -2.5 dex and a reddening of E(B$-$V) = 0.064 (Schlegel et al., 1998a) were adopted. At $T_{\rm eff}$=(4150$\pm$40 K, 4200$\pm$170 K, 4240$\pm$125 K) from the V$-$K, J$-$H, and J$-$K colors, respectively, all photometric values are in very good agreement within the errors. In the following,the value from

the V−K color of 4150±40 K is adopted as the stellar temperature. Given the broad color range spanned by this index, this is the most reliable indicator, and it also corresponds to the error-weighted mean of all values above. This also yielded a flat trend of abundance of Fe I lines with excitation potential. By demanding that the slope of the iron abundances from the neutral lines with excitation potential do not change by more than one standard deviation of the Fe i line abundances, an error of 100 K was placed on the spectroscopic temperature.

The surface gravity, $\log g$ was derived by fitting a grid of synthetic spectra to the Mg triplet lines around 5170 Å, where the temperature derived above was adopted as the model's $T_{\rm eff}$. The best-fit model thus found is indicated in Fig. 2. Acceptable fits, in particular accounting for the Mg triplet's wings, were still obtained within variations of $\pm$0.25 dex, which was adopted as the error on the $\log g$ determination. Finally, the microturbulent velocity, ξ, was set by removing any trend of the abundance from the Fe i lines with the reduced width, $\log$(EW/λ). The resulting value was found to be ξ= 2.3 km s^{-1} with an error of 0.2 km s^{-1}, as determined by the point where the Fe i abundance did not change by more than 1σ. While fixing the surface gravity, the C-abundance was iteratively changed from log ϵ(C)= 6.42 to log ϵ(C) = 8.02 in steps of 0.2 dex to converge on the best-fit parameters. All stellar parameters obtained in this way are listed in Table 4.1.

4.3.4 Abundance errors

For the case of ALW-1, the contribution of the continuum of one spectra to the continuum of the other spectra significantly affects the abundance estimate. Though the veiling factor has been derived with atmost care, the low signal to ratio also affects the abundance estimates. So large uncertainty values are adopted for the

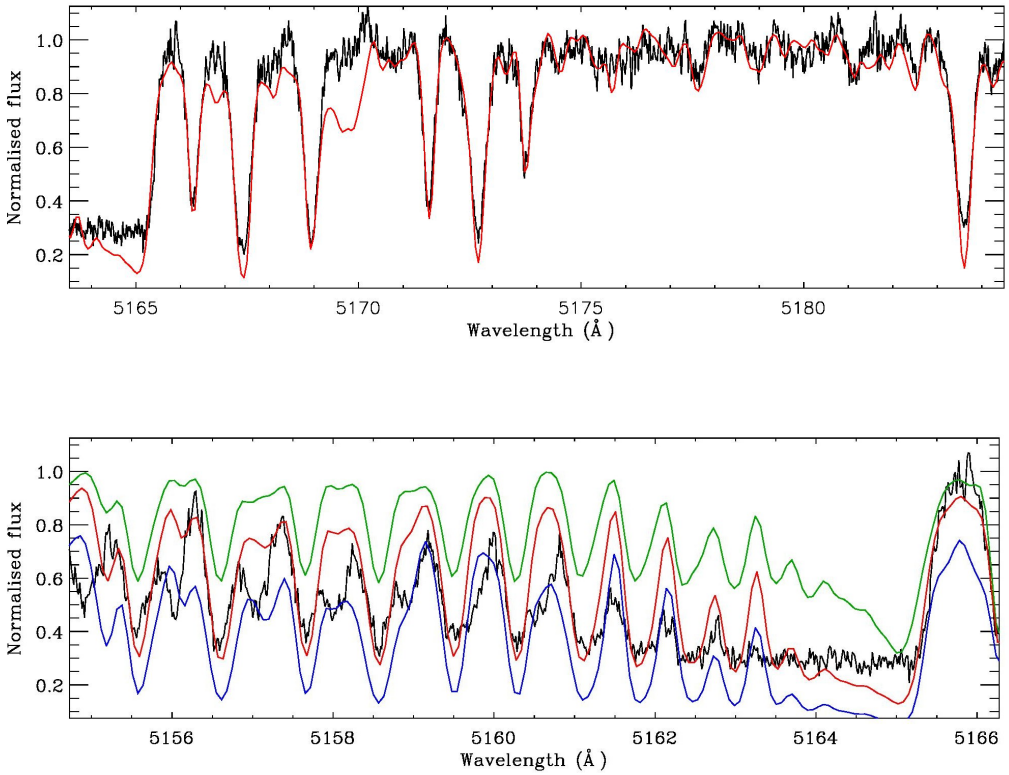

Figure 4.5: Top panel: Region of the Mg I triplet in ALW-8 (black line). The best-fit synthetic spectrum is plotted in red. The additional feature at 5170Å is due to the chosen carbon abundance. Bottom panel: Synthesis of the C_2-band in ALW-8. The best-fit spectrum is shown in red ([C/Fe]=+1.39), while the blue and green lines have been computed for carbon abundances that differ by $\pm$0.2 dex.

abundance analysis and stellar parameters.

For the case of ALW-8 , in order to quantify the statistical error due to contributions from uncertainties in EWs and atomic parameters, I list in Table 4.2, the 1σ line-to-line scatter, $\sigma_{\log \epsilon}$ and the number of lines on which each element's abundance was based. For those few cases, where the abundance could only be derived from less than three lines, this random error was adopted as 0.10 as an empirical, conservative upper limit. For the abundances derived via spectrum synthesis, the quoted abundance uncertainty was determined via the goodness of the least-squares fit.

Systematic errors for abundances in ALW-8 were derived by computing new models, where each stellar parameter ($T_{\rm eff}$, $\log g$, ξ) was varied by a fixed amount ($\pm$100 K, $\pm$0.25 dex, $\pm$0.2 km s^{-1}), and from those, new abundances were computed in an identical manner as before. The resulting line-to-line change upon these parameter variations is listed in Table **??**, and the combined effect was determined by adding the contributions in quadrature. These systematic uncertainties are listed in the last column of Table 4.2.

4.4 Abundance results

All abundance results for ALW-1 and AW-8 are listed in Table 4.2, together with the adopted Solar values from Asplund et al. (2009).

4.4.1 AlW-1

The abundance of each element for ALW-1 has been calculated separately from both the components of each spectral feature in the spectra and a weighted average is

Table 4.2: Abundance results.

Species	log $\epsilon_\odot$	ALW-1			ALW-8				
		log ϵ	[X/Fe]	Error	log ϵ	[X/Fe]	$\sigma_{log\epsilon}$	N	σ_{sys}^{tot}
Li i	1.05	0.28	2.03	syn	0.00	1.45	0.30	syn	0.32
C (C_2)	8.43	6.93	1.30	syn	7.32	1.39	0.20	syn	0.15
N (CN)	7.83	6.42	1.39	syn	6.92	1.59	0.30	syn	0.14
O i	8.69	6.03	0.14	syn	7.08	0.89	0.30	syn	0.10
Na i	6.24	2.66	−0.78	syn	$4.62_{\rm NLTE}$	$0.88_{\rm NLTE}$	0.12	2	0.09
Mg i	7.60	...	...	...	5.40	0.30	...	1	0.13
Ca i	6.34	...	...	...	4.26	0.42	0.27	5	0.13
Sc ii	3.15	...	...	...	1.17	0.52	0.09	3	0.16
Ti i	4.95	1.96	...	0.7	2.75	0.30	0.37	7	0.18
Ti ii	4.95	...	...	...	2.85	0.40	0.15	3	0.16
Cr i	5.64	...	...	...	2.94	−0.20	0.29	5	0.16
Mn i	5.43	...	...	...	2.63	−0.30	0.10	2	0.19
Fe i	7.50	4.7	0.0	syn	5.00	0.00	0.12	11	0.12
Fe ii	7.50	4.75	0.05	syn	4.99	0.01	0.10	2	0.19
Ni i	6.22	...	...	...	3.56	−0.16	0.15	3	0.11
Zn i	4.56	...	...	...	2.24	0.18	...	1	0.12
Y ii	2.21	0.30	0.89	syn	0.00	0.29	...	syn	0.11
Zr ii	2.58	0.41	0.63	syn	<0.50	<0.42	...	syn	0.42
Ba ii	2.18	1.84	2.46	syn	−0.86	−0.55	...	syn	0.19
La ii	1.10	1.46	3.16	syn	...	...	...	...	...
Ce ii	1.58	0.20	1.42	syn	...	...	...	...	...
Nd ii	1.42	0.10	1.48	syn	...	...	...	...	...
Eu i	0.52	−0.43	1.85	syn	< -1.50	<0.48	...	syn	0.86

taken for the final reported value in table 4.2. A large error has been included considering difficulty in placing the continuum due to contribution of each spectrum on others and the difficulty on decomposing the individual spectra due to contribution of each spectrum on others. All the abundance is calculated based on the spectral synthesis and an error of 0.7 is taken as the representative error in abundance measurements unless the error is explicitly mentioned.

Lithium

Though the Li I 6707Å resonance line could be detected in the spectrum of ALW-1, it is highly blended with CN-features. Its abundance was thus derived by spectral synthesis and due to the strong blending, a large error of 1.0 dex is placed for the quoted abundance Moreover, the low value of A(Li) = 0.28 is in line with the depleted Li-abundances in such metal-poor evolved stars (e.g., Hansen et al., 2016a, Lind et al., 2009). Fig. 4.6 shows the best-fit spectrum of this line.

Carbon, Nitrogen, Oxygen, and ^{12}C/^{13}C ratio

The abundance of C is determined by fitting both the C_2 region at 5164 and 5635 Å . At its low metallicity of -2.8 dex and the high carbon enhancement in excess of one dex, the ALW-1 clearly qualifies as a CEMP star (Beers and Christlieb, 2005).

Nitrogen abundances of ALW-1 was derived by fitting the region of 6200–6700 Å as the commonly used CN lines at $\sim$8000Å are not covered by the UVES spectra. As a result, a high [N/Fe] ratio of 1.39$\pm$0.2 dex is also found in the analysis.

The oxygen abundance was derived from synthesis of the [O I] lines at 6300 Å and 6363 Å. This region has effect of CN molecular features. So any change in the carbon and nitrogen abundance would result in the change in the oxygen abundance.

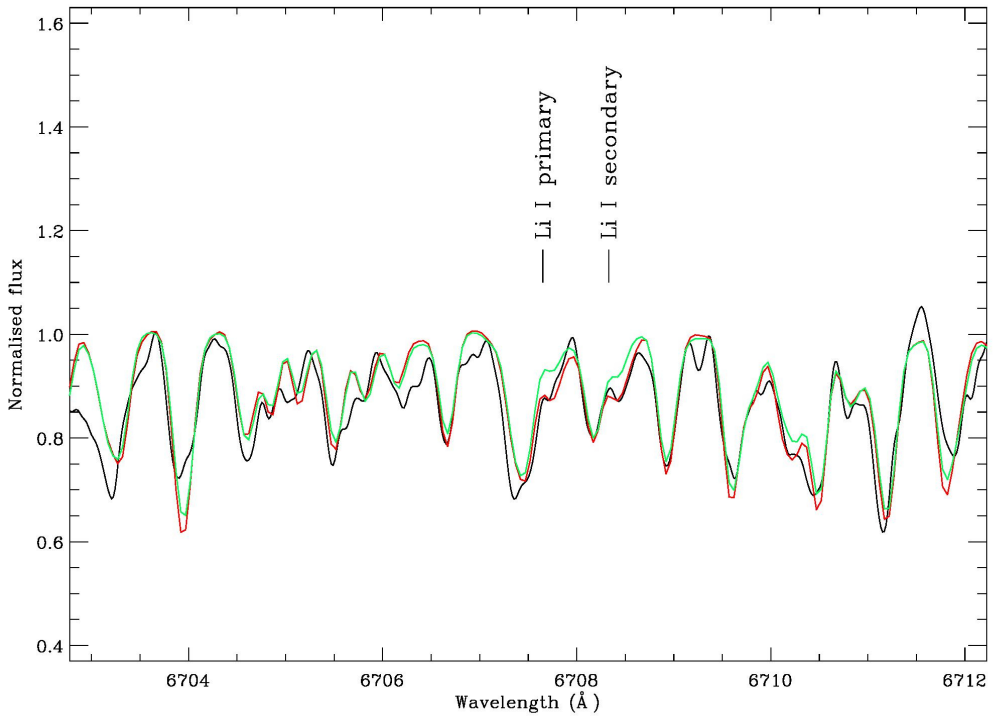

Figure 4.6: For ALW-1, Li I resonance line at 6707 Å have been fitted with the synthetic spectra and the best fit is shown here. Green spectrum corresponds to the fit when no atomic lines are included while synthesis. Red fit corresponds to the synthesis included both molecular and atomic features. Large contribution of CN features to the region is evident in the fit.

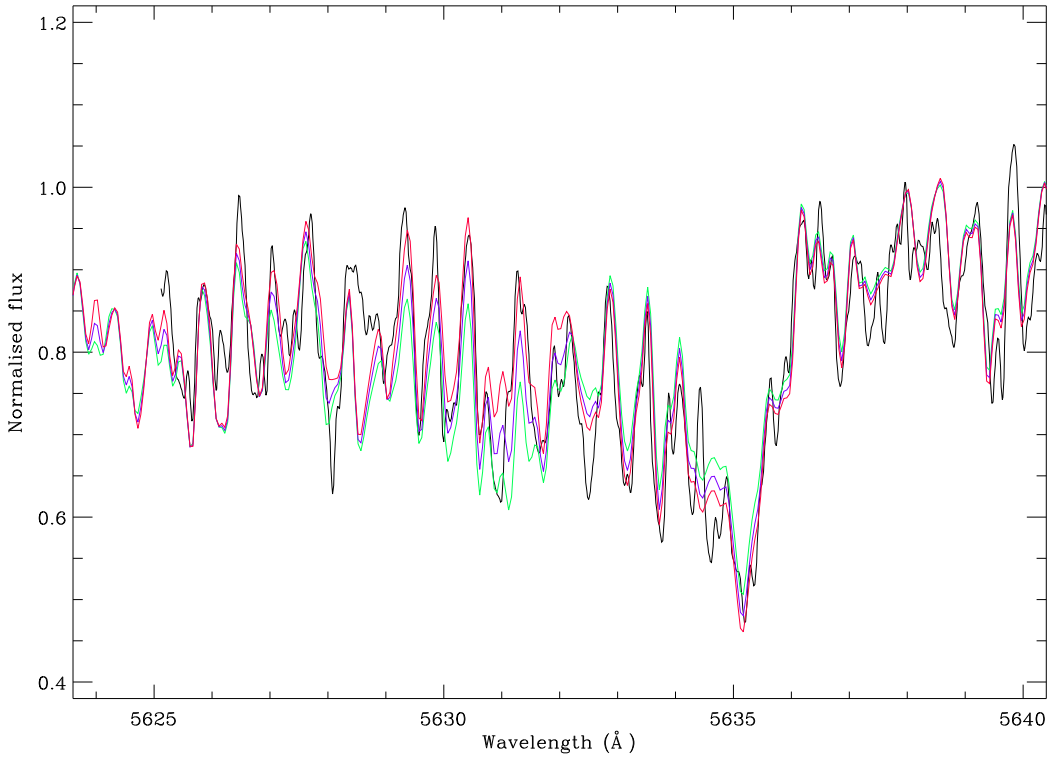

Figure 4.7: 5635 Å region has been fitted for ALW-1 with various values of $^{12}C/^{13}C$ ratio to derive the $^{12}C/^{13}C$ ratio. The best fit is shown in the magenta color which corresponds to a ratio of $\sim$ 100. Blue fit corresponds to a ratio of $\sim$ 20 where as green corresponds to 10.

So carbon and nitrogen abundance were estimated from C_2 and then CN features and oxygen abundance is measured after fixing the value of C and N. This contribute to a large error to the reported oxygen abundance which is quoted in the table 4.2

Na and Ti

Na abundance is derived by synthesizing D_1 and D_2 lines using various values of Na. Since the region has contributions from CN features, the C and N abundance from the C_2 and CN features have been included and final abundance of Na has been found out. According to Gratton et al. (1999) cool giants are expected to have larger NLTE. Then for the case of ALW-1 the abundance will be even lower if the NLTE correction is considered.

Ti abundance also has been derived by synthesizing available clean Ti lines in the spectrum. and the value is given in the table 4.2

Neutron-capture elements: Y, Zr, Ba, La, Ce, Nd, Eu

The strongest and most reliable features of most heavy elements are in the blue part of the spectrum, which is strongly affected by blending (Hansen et al., 2015), even more so in the C-rich stars of this study. Accordingly, larger error bars were assigned to the abundances of these elements.

The Ba-lines at 5853 and 6141 are very strong, while the the 4937Å-line was severely affected by blends and thus was ignored in this analysis. The resulting Ba abundance from the former two lines is [Ba/Fe] = 2.46, which implies that the system is strongly s-process enhanced. The best fit spectrum of both features is shown in Fig.4.8.

Several other heavy element features were fitted over the wavelength range of

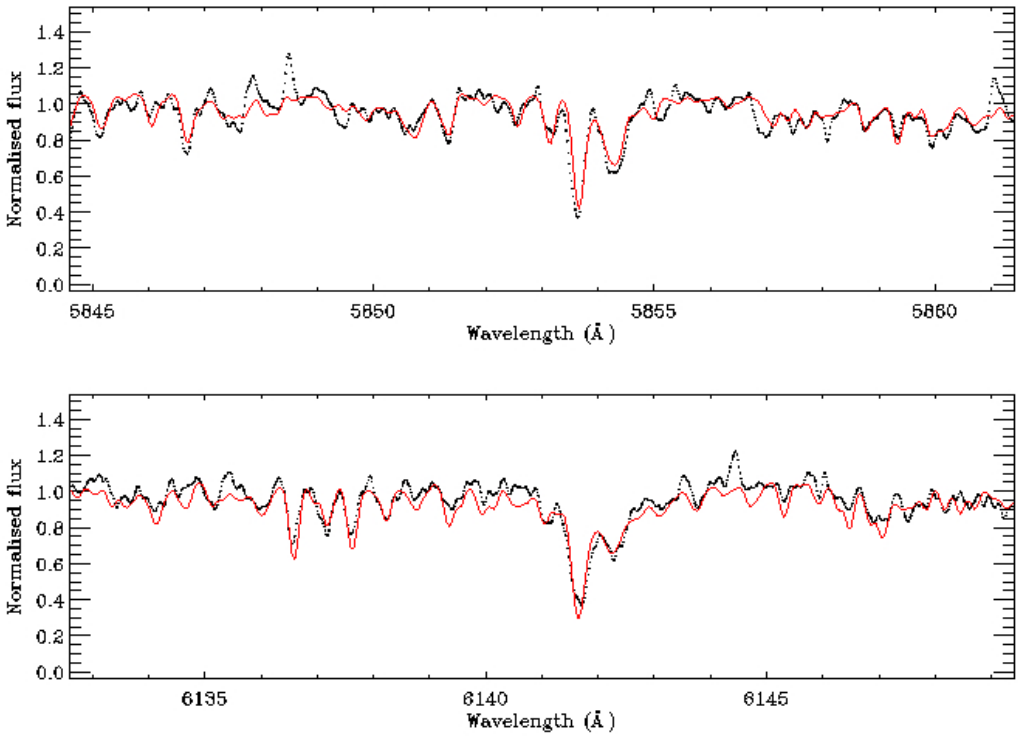

Figure 4.8: Ba-lines at 5853 and 6141 Å in ALW-1 (black lines) with the best-fit synthetic spectrum shown in red. The corresponding [Ba/Fe] ratio is 2.46.

4800–5000Å, including Zr, La, Ce, and Nd; additionally, yttrium abundances were derived from the two lines at 5200 and 5204Å. An estimate of the Eu abundance of ALW-1 could be derived from the Eu II line at 6645 Å and the abundance is [Eu/Fe]=1.85

4.4.2 ALW-8

In Fig. 4.9, the abundance results of ALW-8 are compared to literature measurements in the Galactic disks (Battistini and Bensby, 2016, Bensby et al., 2014, Koch and Edvardsson, 2002) and halo (Roederer et al., 2014a), where the data for C-normal stars in Carina (Fabrizio et al., 2015, Koch et al., 2008, Venn et al., 2012), other C-rich stars in MW dSph satellites, including Carina's ALW-6 and -7 (Abia et al., 2008), and the sparse available data from a few ultra faint galaxies (Frebel et al., 2010b, Geisler et al., 2005, Honda et al., 2011, Ji et al., 2016a,b, Norris et al., 2010b, Salgado et al., 2016, Skúladóttir et al., 2015). were also included. Here the Galactic data have not been preselected to show exclusively CEMP stars, but they are, rather, representative of the metal-poor MW field population. Similarly, for the faint dSphs, only those stars that have several key elements derived from high-resolution spectra are shown, while the overall detection rate of carbon excesses from low-resolution spectra without further chemical follow-up is larger (e.g., Lai et al., 2011). Moreover, a few of the CEMP-stars in the faintest dSphs often fall within the CEMP category by a margin of their [C/Fe] ratio (Aoki et al., 2007).

Iron

Many iron lines are severely blended with CN and C_2 molecular features, but 11 blend-free Fe i lines were detected in the spectra and the EWs were measured for

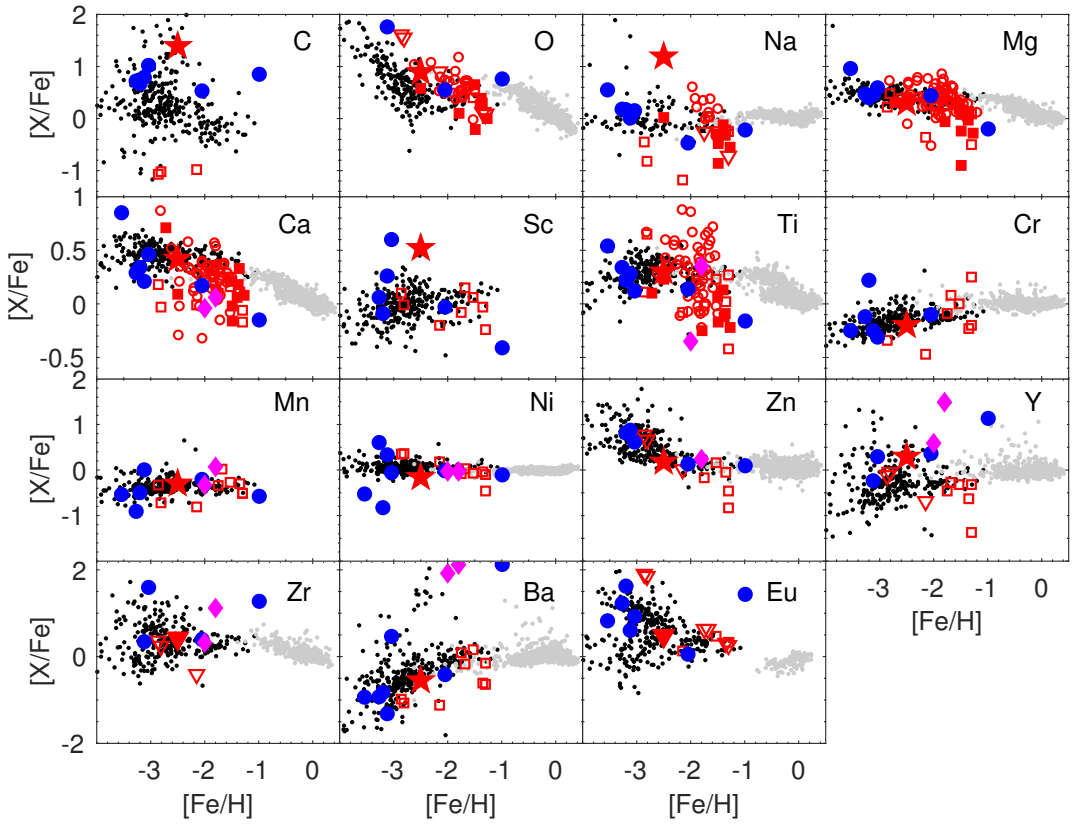

Figure 4.9: Abundance ratios for ALW-8 (red star symbol and, for the case of upper limits, filled red triangles) in comparison with MW and dSph samples from the literature. Data are from Roederer et al. (2014a) for halo stars (black dots); Bensby et al. (2014) for disk stars (gray points), except for Zr (Battistini and Bensby, 2016) and Eu (Koch and Edvardsson, 2002). Carina field star abundances were taken from Koch et al. (2008, filled red squares); Venn et al. (2012, open red squares); and Fabrizio et al. (2015, open red circles), while open red triangles indicate upper limits from these studies. Blue points designate C-rich stars in luminous and ultra faint dSphs (Frebel et al., 2010b, Geisler et al., 2005, Honda et al., 2011, Ji et al., 2016a,b, Norris et al., 2010b, Salgado et al., 2016, Skúladóttir et al., 2015). Finally, the CEMP-s stars in Carina from Abia et al. (2008) are shown as magenta diamonds.

those.. In addition, the full spectral range was synthesized in its entirety in order to assess the accuracy of the abundance analysis and the influence of such blending. As a result, the values from the EW analysis and spectral synthesis are in excellent agreement. the Fe-abundance of ALW-8 is derived to be [Fe/H] = -2.50 ± 0.04.

The covered spectral range also allowed for the abundance measurements from two unblended Fe ii lines. The resulting abundance from these lines indicates an excellent ionization equilibrium in that [Fe i/ii]=0.01$\pm$0.13, which also renders the surface gravities from the synthetic grid fitting reliable.

Carbon, Nitrogen, Oxygen, and ^{12}C/^{13}C ratio

The carbon abundance of this star has been derived by fitting the C_2 molecular band heads at 5164 Å and 5635 Å (Fig. 4.5). Both features yielded the same abundance of log $\epsilon(C)$ = 7.3$\pm$0.2 dex. The isotopic ratio ^{12}C/^{13}C was derived by fitting the ^{13}C contribution to the band at 5634 Å, resulting in a ratio of 9, which is consistent with other CEMP-no stars (Aoki et al., 2007, Sivarani et al., 2006). The equilibrium ratio for CNO-cycled material is $\sim$4 and the value in ALW-8, resulting from the production of ^{13}C in the CN cycle, indicates a high level of processing, in line with the evolved nature of this star (Charbonnel et al., 1998, Gratton et al., 2000). Since the strong CN band at 4215 Å is not covered by this spectrum, so CN lines in the wavelength range from 5635–6700Å is used by iteratively changing the nitrogen abundance of the synthetic spectra by 0.2 dex and fitting this entire spectral region. This yielded a best-fit value of [N/Fe]=1.6.

Finally, the oxygen abundance of ALW-8 was derived by using the [O I] lines at 6300, 6363 Å (Fig. 4.10). Since these lines are blended with CN features, a slight change in the nitrogen abundance affects the derived oxygen abundance. Thus, the

carbon abundance was first fixed to be the value obtained above from the C_2 band, after which the oxygen and nitrogen abundances were iteratively adjusted to fit the [O I] lines, without affecting other CN features. The resulting O-abundance from both lines differs by 0.3 dex owing to the iterative process involving both N and O, and this difference is adopted as the final uncertainty on the reported nitrogen and oxygen abundances.

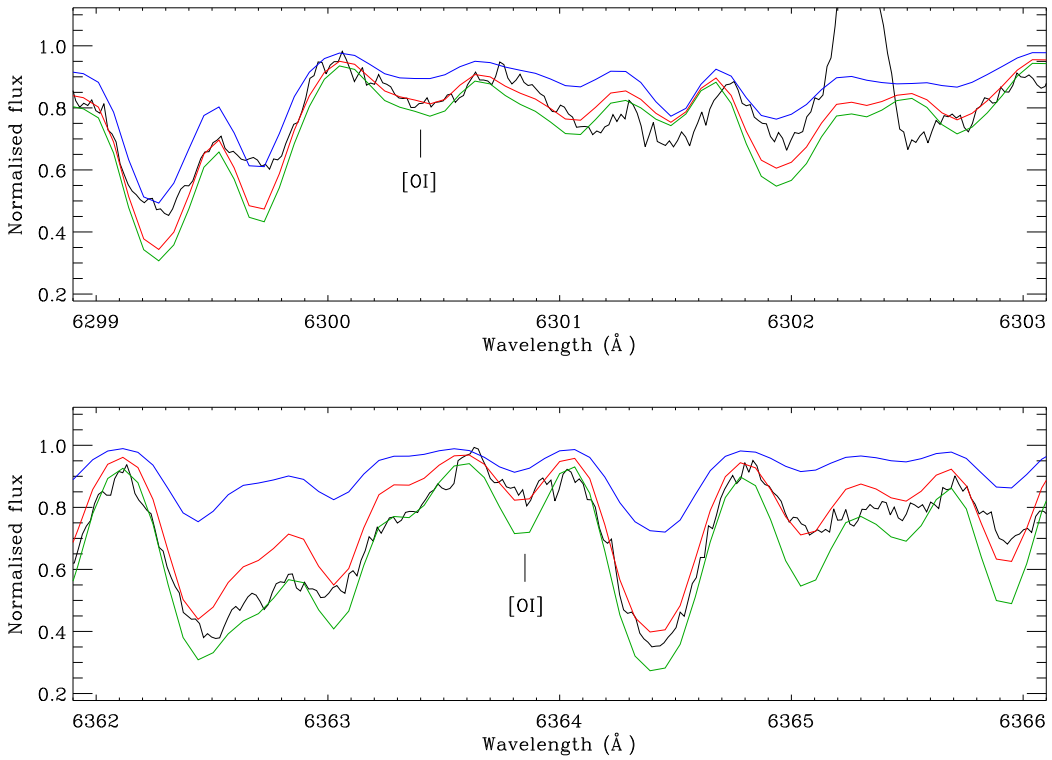

Figure 4.10: Regions around the [O I] lines in ALW-8. The best spectrum (red) was computed with log ϵ(O)=6.93 (top panel) and log ϵ(O)=7.23 (bottom panel), respectively. The green and blue lines indicate syntheses corresponding to the range of uncertainty of $\pm$0.3 dex in oxygen abundance. The poor fitting of CN features around [OI] comes solely from the change in the oxygen abundance.

Lithium

The Li-abundance for the star was determined by synthesizing the resonance doublet at 6707 Å which yielded A(Li)=0.0. Due to the presence of prominent CN bands in this region, affecting the continuum placement, a fitting uncertainty of 0.3 dex has been assigned to this result. The low value for A(Li) is found to be consistent with the star being an evolved giant, in which Li is easily destroyed at the high interior temperatures that it is exposed to due to the convective mixing of material (e.g., Gratton et al., 2000, Lind et al., 2009, Skúladóttir et al., 2015). In contrast, unevolved CEMP stars show Li-abundances that are lower than the standard plateau value of 2.2 dex (Bonifacio et al., 2015, Masseron et al., 2012, Sbordone et al., 2010a, Spite and Spite, 1982).

α-elements: Mg, Ca, and Ti

Clean lines of Mg, Ca, and Ti are available in the spectrum of ALW-8 and the abundances of the respective elements have been determined from their EWs. The Mg I triplet lines at 5172 Å and 5183 Å are very strong (at EWs $>$300 mÅ) and saturated; conversely, the line at 5711Å is strongly blended with molecular features and thus unusable for an abundance determination. Hence, the measurement of the Mg-abundance in this study is based on the unblended line at 5528 Å at moderate strength (120 mÅ), resulting in a [Mg/Fe] ratio of 0.3 dex.

A poor mixing has been found between Carina's old and intermediate-age populations in terms of their Mg abundances (Koch et al., 2008, Lemasle et al., 2012, Shetrone et al., 2003, Venn et al., 2012). Here, older stars with systematically lower Fe abundances show depleted [Mg/Fe] ratios, whereas the intermediate-age population is more strongly enhanced in Fe and the α-element Mg. This left Venn et al.

(2012) to conclude that the second phase of star formation in Carina occurred out of gas that was already pre-enriched in the α-elements. Moreover, the gas out of which the older stars formed was inhomogeneously mixed itself, leading to a broad spread in the [Mg/Fe] ratios at low metallicities. At its low [Fe/H] and the elevated [Mg/Fe], ALW-8 is clearly part of Carina's old population.

Five Ca i lines have been used to determine a halo-like [Ca/Fe] ratio of 0.42 dex, while, for Ti, eight and three neutral and ionized lines were clean and detectable, respectively. These indicate that ionization balance is matched very well within the uncertainties, at [Ti i/ii]=0.10$\pm$0.18 dex. No Si lines are present in the available range of the spectrum.

The straight average of the three α-elements amounts to an enhancement of [α/Fe] = 0.36 dex. Even though the trends indicating the poor mixing between the components is less pronounced in the other α-abundances, there is still considerable spread in Ca and in particular Ti (Fabrizio et al., 2015). ALW-8 behaves rather halo-like in its enhancements. While this overlap is also seen for several of the CEMP stars in other dSphs, two of these stand out clearly. One is the most metal-poor of these objects, (the CEMP-no star in Segue 1; Norris et al., 2010b), which is α-enhanced to almost one dex. Secondly, the most metal-rich C-rich star in Sculptor, at -1 dex (Geisler et al., 2005), shows subsolar [α/Fe] ratios; although it has been noted that it represents the typical [α/Fe] ratio of stars at similar metallicity in Sculptor. Also the CEMP-s stars ALW-6 and -7 are towards the low-α tail of Carina's distribution. The fact that ALW-8 and the majority of the other C-stars follow the overall trends in the α-elements very well is not surprising, since the nucleosynthesis of the α-elements is decoupled from the channels responsible for the C-overabundances.

Odd-Z elements: Na and Sc

Since the Na D lines are too strong (EW $\sim$ 300 mÅ) for a meaningful abundance analysis, weaker absorption lines at 5682 and 5688 Åhas been used for Na abundance determination. NLTE corrections from Lind et al. (2011) have been incorporated and the resulting NLTE [Na/Fe] ratio is high, at 0.9 dex, skimming the upper distribution of halo stars and Carina stars. Fabrizio et al. (2015) found that a correlation between Na and O in their Carina stars matched well with that in MW halo field stars, supporting the similarity between the chemical enrichment history of the MW halo and Carina stars (Geisler et al., 2007, Idiart and Thévenin, 2000). Unfortunately, no Na abundances were derived for the old stars in their sample. While, at first glance, the correlation noted by Fabrizio et al. (2015) appears to be driven by a single, low-Na, low-O star, the very high Na and O abundances in ALW-8 provide a unique match to this trend at the other extreme, bolstering the presence of this correlation beyond the intermediate-age population. This suggests that, apart from an O-enhancement in the CNO processing that this star experienced, the gas out of which it formed was already strongly pre-enriched in O and Na via previous Type-II SNe events.

No lines of Al and K could be measured in the spectrum and all available V-lines are too heavily blended with molecular features to infer any abundance.

The Sc-abundance measured from three generally strong and unblended lines yields a high [Sc/Fe] ratio of 0.52$\pm$0.05 dex, which is significantly larger than in halo-, Carina-, and CEMP-stars at similar metallicity. These reference samples typically fall within $\pm$0.2 dex of the Solar value. One exception is the CEMP-s star

S15-19 in the Sextans dSph (Honda et al., 2011), which, however, shows neutron-capture element patterns that are fully consistent with the AGB mass-transfer scenario, and no explanation of the high Sc/Fe ratio was offered. Moreover, the horizontal branch star CS 29497-030 in the sample of Roederer et al. (2014a), at the same [Fe/H], shares almost identical abundances of all the light elements in common, while its neutron-capture elements are highly enhanced, classifying that object as a CEMP-r/s star. A high Sc ratio could be indicative of a high-energy SN event and/or a high electron fraction in the nucleosynthetic environment (Tominaga et al., 2007). However, there is little evidence for this acting in the neutron-capture element patterns seen in ALW-8 (Sect 4.8). Furthermore, the NLTE corrections for Sc in warmer stars are still largely unknown, hampering a detailed model comparison to pin down the origin of the Sc overenhancement (Hansen et al., 2011).

Fe-peak elements: Cr, Mn, Ni

As the Fe-peak elements are co-produced with iron and their nucleosynthesis is decoupled from that in charge of the carbon-enrichment and heavy element patterns in the CEMP stars, the [Cr/Fe], [Mn/Fe], and [Ni/Fe] ratios bear little surprise. ALW-8 is fully compatible with the (low-scatter) trends in the MW halo and those seen in other CEMP stars of either class, as well as with the abundances found in Carina stars, albeit their larger scatter. Th Cr and Mn abundances reported here are not corrected for NLTE effects, but it is noted that these would have no impact on the normality of ALW-8 in this abundance space.

Neutron-capture elements: Zn, Y, Zr, Ba, Eu

The [Zn/Fe] ratio in ALW-8 and other CEMP stars is compatible with those in metal-poor halo stars, showing little scatter in the samples. Furthermore, there is no systematic difference to be seen between CEMP-no and -s stars, which is to be expected as Zn is not significantly affected by s-process nucleosynthesis (Kobayashi et al., 2006, Timmes et al., 1995). However, C-normal stars in Carina show a large scatter towards intermediate metallicities, where their low-Zn and Fe-peak abundances indicate a lack of hypernovae, that is, energetic SNe that would lead to an overproduction of those elements (see also Hanke et al., 2017). Amongst the first-peak n-capture elements, only Y and Zr abundances could be determined. For Y, we employed the lines at 5200 and 5206 Å (Fig. 4.11). While the latter feature is blended with a Cr I line, it can still be used for an abundance estimate, though with a larger error bar. As a result, an elevated [Y/Fe] ratio of 0.3 dex is found, which still overlaps with halo stars owing to the large scatter found in that MW component. Unblended Zr lines could not be detected in the spectrum and an upper limit is placed on the Zr abundance by synthesizing the lines at 6127 and 6134 Å, which are blended with CN bands; this yields an upper limit of [Zr/Fe] $<$0.42. Barium is the only heavy neutron-capture element with several strong lines present in the spectrum. Four Ba II lines were detected in the spectrum of ALW-8 at 4934.1, 5853.7, 6141.7, and 6496.9 Å. However, the reddest of these lines is too blended with molecular feature to be considered in this analysis. The remaining three lines yield a depleted value of [Ba/Fe]=$-0.55\pm$0.20 that is in line with other metal-poor stars in Carina and the Galactic halo. The [Ba/Fe] ratio shows a distinct bifurcation over a broad range in metallicity and both ALW stars in Carina studied by Abia et al. (2008) fall on the high-Ba band that is made up of CEMP-s stars in binaries.

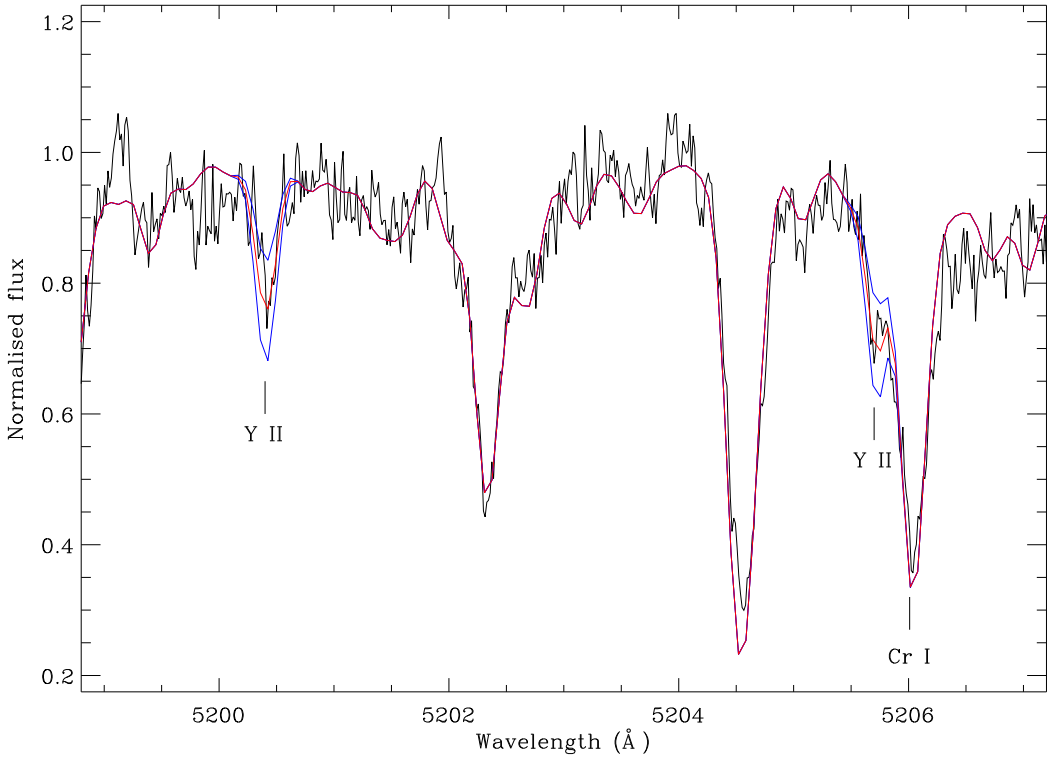

Figure 4.11: Spectrum of ALW-8 around the Y ii lines at $\lambda\lambda$5200, 5206Å (black line), illustrating the spectral fitting. The best synthetic spectrum using [Y/Fe] = 0.26 is plotted as a red line. The spectra shown in blue differ by $\pm$ 0.3 from the best-fit value.

The weak Eu-line at 6645 Å is blended with CN molecular features and only an upper limit of [Eu/Fe] $<$0.43 could be derived from spectral synthesis.

4.5 Origin of elements in ALW-1

ALW-1 is categoised into CEMP-s star due to the enhancement in carbon and s-process elements. The enhancement in carbon along with the s-process elements can be the result of either an intrinsic or extrinsic nature of the carbon star. These elements are either synthesized inside the star and brought to the surface via multiple third dredge up (TDU) episodes (intrinsic) or the were accreted on the present star from an AGB companion in which the carbon and s-process materials are brought to the surface by TDU episodes which later transferred to the presently observing star through any mass transfer mechanism (extrinsic). But observations show that this star has a high radial velocity variation (refer table 4.1). So the possible origin of carbon and s-process elements has an extrinsic nature that is from the companion AGB star from which the mass would be transferred to ALW-1 through any mass transfer mechanism like wind transfer or Roche - Lobe over flow or wind-assisted Roche-lobe overflow (WRLOF). But since only two epoch of observations are available for ALW-1 and from this , it is not possible to constrain which mass transfer mechanism was responsible for the mass transfer.

ALW 1 is also enhanced in nitrogen to similar levels as in carbon and has a [C/N] ratio of Solar to slightly subsolar. This indicates that the star is unaffected by internal mixing during stellar evolution (Hansen et al., 2016b, Spite et al., 2005).

This star also shows enhancement in heavy s-process elements (hs: Ba, La, and Ce) when compared to the lighter s-process elements (ls: Y, Zr). [hs/ls] ratio has

been calculated for ALW-1 and value coming to be 1.59. It indicates that the companion AGB star has a low metallicity value. At lower metallicities heavy s-process elements are produced more than the light s-process elements. It is because neutron flux required for the production of s-process elements per seed nuclei increases with reducing the metallicity. This favors the production of heavy s-process elements compared to light s-process elements. The [hs/ls] ratio of ALW-1 is high when compared to Galactic AGB stars whereas similar [hs/ls] ratios are reported in dwarf spheroidals (Abia et al., 2008, de Laverny et al., 2006). [hs/ls] ratio for carbon stars are plotted in figure 4.12. Apart from an enhancement in s-process elements, ALW-1 also show an enhancement in r-process element (Eu). At the resulting [Ba/Eu] ratio of 0.61 $\pm$ 0.7, ALW-1 lies at the border to the CEMP-r/s regime (Beers and Christlieb, 2005, Masseron et al., 2010). The origin of r-process elements in CEMP-rs are still uncertain. Not many CEMP-rs stars have been detected. But it is observed that, at low metallicities, the frequency of CEMP-r/s stars increases and also found to be members of binary systems (Hansen et al., 2016b,d) This put constrains on the formation scenario of these system of stars. According to Vanhala and Cameron (1998) the explosion of massive stars favor the formation of binaries, which in turn aid the stars to be having the imprints of first massive stars. Cohen et al. (2003) have recommended a delayed r-process pollution to the CEMP-s stars making it CEMP-r/s stars. The AGB companion pollutes the star with its s-process rich material. When the AGB turns into a white dwarf and if it is O-Ne-Mg white dwarf it accrets the matter back from the secondary thereby turning into a neutron star. The neutrino driven wind to the secondary star favors the r-process production and turn the star to be a CEMP-rs. XMM Newton observations of Carina dSph (Ramsay and Wu, 2006) brought out a few soft x-ray sources in the field and presumed to be the candidates of the dwarf spheroidal. One of such source is in the close vicinity of ALW-1 which

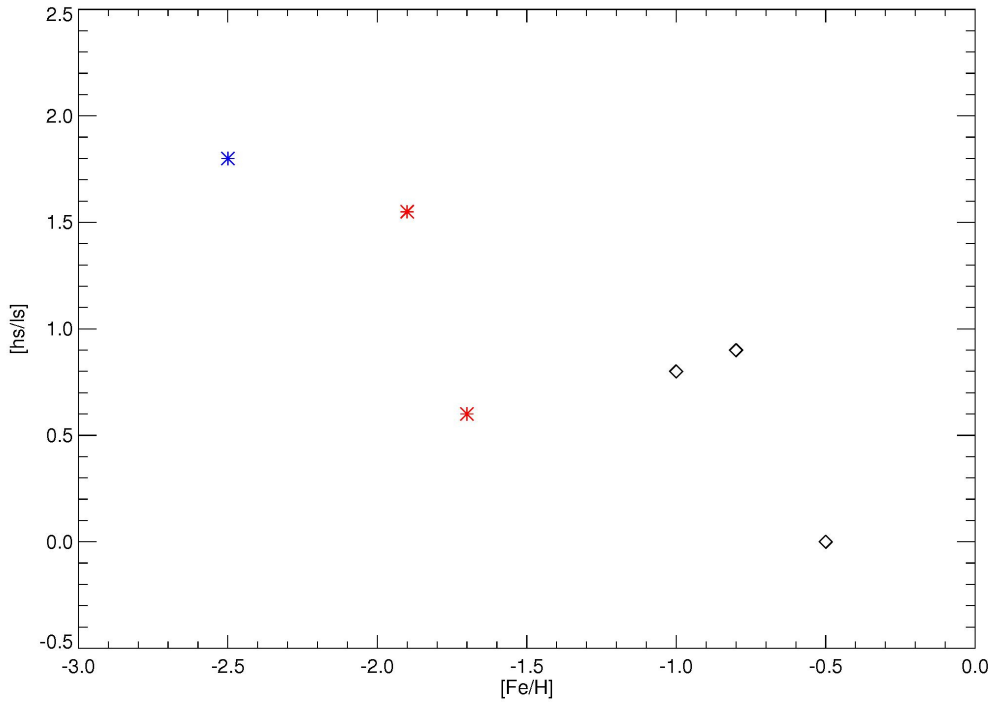

Figure 4.12: The [hs/ls] ratio for the carbon stars in dwarf spheroidals have been plotted here. Open diamonds indicate the samples from de laverny et al 2006 and red asterisk are the stars from Abia et al 2008. Blue asterisk indicate the [hs/ls] of ALW-1 star. An error of 0.7 dex has been adopted for the quoted value.

makes the star more interesting for further follow up to have a detailed identification of r-process elements as well for a radial velocity follow up.

4.6 On the origin of elements in ALW-8

The abundance analysis of ALW-8 revealed that this CEMP star is enhanced in carbon as well as nitrogen. Considering its evolutionary phase, its ^{12}C/^{13}C ratio, and the depleted Li abundance give a sense that this star has undergone first dredge up (FDU). Nitrogen is the result of a CN cycle acting during the FDU. In this case, the original carbon in the star must have been even higher than what is measured now. Based on its low subsolar [Ba/Fe] ratio and considering the lack of any strong r-process enhancement, ALW-8 can be unambiguously classified as a CEMP-no star (Beers and Christlieb, 2005). A mild enhancement is seen in the light neutron capture element Y, which suggests the presence of a weak r-process activity. Thus, in the following, the origin of the enhancements seen in different element tracers in ALW-8. is further investigated.

4.6.1 Origin of carbon

The strong C-enhancement of ALW-8 unambiguously confirms its nature as a CEMP star. ALW-8 is in the RGB phase where the primordial carbon abundance has been reduced due to the CN cycling and the presently observed abundance will be lower. While the moderate [C/N] ratio of -0.2 dex alone would suggest that its surface composition has not been significantly altered by internal mixing during stellar evolution (Hansen et al., 2016b, Spite et al., 2005), other tracers of mixing paint a different picture. Amongst these are the strong depletion in lithium and the carbon

isotopic ratio, where Spite et al. (2006) suggest an upper limit of $^{12}C/^{13}C < 10$ as a proxy for effective deep mixing.

To further assess the impact of such processes, the corrections of Placco et al. (2014) have been taken into consideration, which account for the evolutionary status of C- and N-rich stars. As these model calculations indicate, the surface composition of stars like ALW-8 has not been altered by more than $\sim$0.2 over the course of its evolution. Since, during the hot CNO cycles, N is strongly enhanced at the expense of lowering the carbon abundance, the high [C/Fe] we found in ALW-8 must have been a relic of external processes that enhanced the primordial gas to the observed high levels.

Carbon in CEMP-no stars can have several origins (e.g., Skúladóttir et al. 2015 , for a comprehensive overview). While the possibility of mass transfer from a AGB binary companion cannot be ruled out from a dynamical standpoint due to the single-epoch observations, the lack of significant s-process material renders this unlikely; in fact, the majority of CEMP-no stars are not related to any binary mechanisms (Hansen et al., 2016c). The high value of carbon in CEMP-no stars can be the result of primordial, low- or zero-metallicity faint SNe that underwent mixing and fall-back mechanisms (Umeda and Nomoto, 2003). Alternative enrichers can be fast rotating massive stars (Meynet et al., 2006). However, both polluters produce excess abundances of N and O that are not produced to that extent in regular-energy SNe II. Indeed, nitrogen and oxygen measurements of ALW-8 indicate a strong enrichment in those elements, which, however, is more likely to be a consequence of the CNO cycling and mixing that the star experienced. Another piece of evidence against faint SNe being the sole producer of the high C is that they tend to have very low yields of the odd-Z Fe-peak elements such as Mn, which shows a regular, non-depleted value in ALW-8.

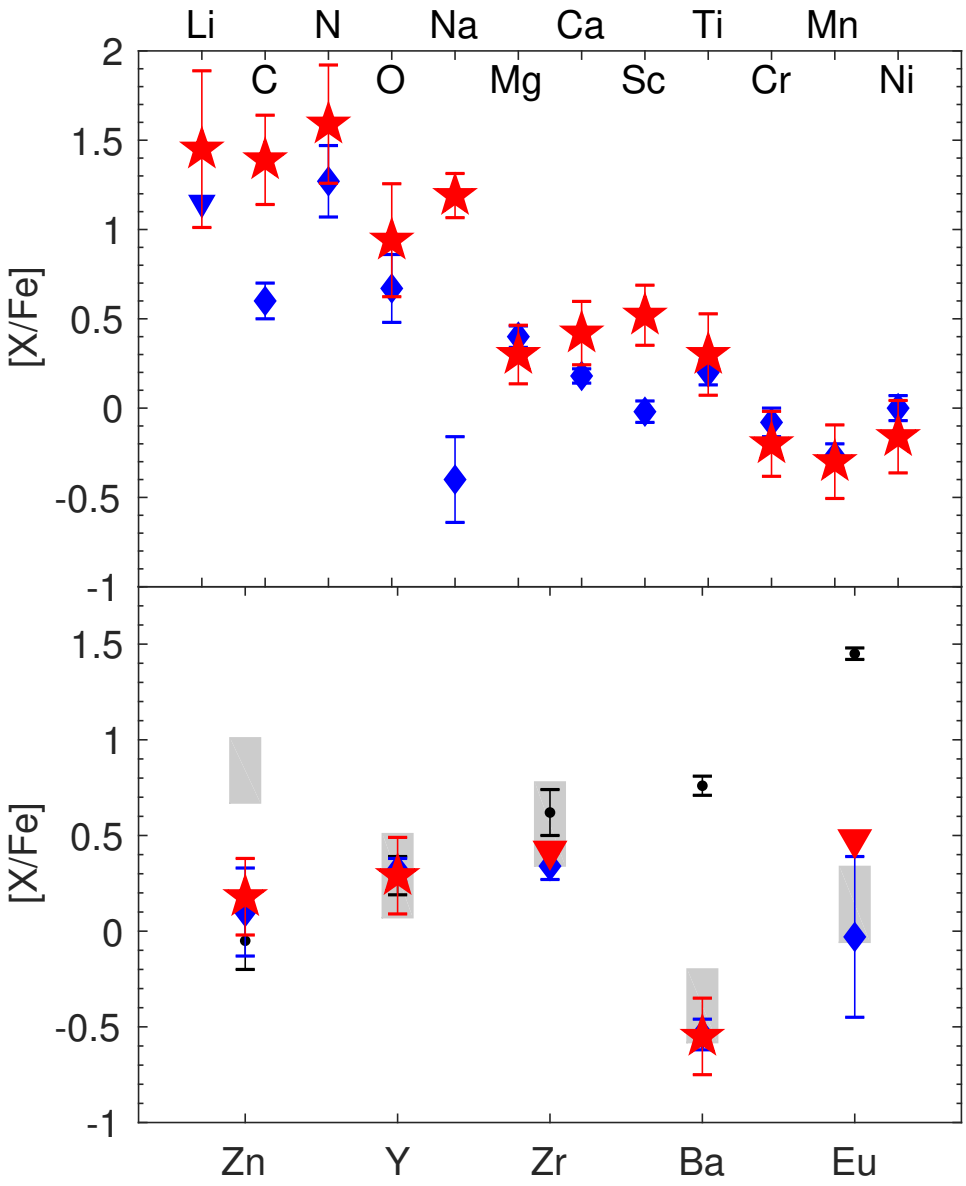

Figure 4.13: Chemical element patterns for ALW-8 (red symbols) are shown for the lighter elements (top panel) and the neutron-capture element abundances (bottom panel). For comparison, the CEMP-no star in the Sculptor dSph (Skúladóttir et al., 2015, blue diamonds), and the weak and main r-process stars HD 122563 (Honda et al., 2006, gray shades) and CS 22892-052 (Sneden et al., 2003, black dots) were overplotted. Here, all stars were placed on the same Solar scale. All ratios for the heavier elements were normalized to Y.

The very similar abundance pattern of the CEMP-no star in the Sculptor dSph (Fig. 4.13) prompted Skúladóttir et al. (2015) to propose that a mix of faint and regular SNe II is required to reproduce the high C without invoking any of the peculiarities present in the faint SNe models. The regular pattern observed in the α-elements and the high Na abundance seen in ALW-8 agrees with such a scenario and it can be concluded that Carina has also experienced some degree of enrichment by faint SNe that was, however, diluted with yields from SNe II. Overall, a very good agreement of the [α/Fe] and Fe-peak abundance ratios between the Sculptor star and Carina CEMP-no star are noted (top panel of Fig. 4.13).

4.6.2 Origin of neutron-capture elements

At metallicities as low as ALW's [Fe/H] of -2.5 dex, the main source of the n-capture elements is r-process nucleosynthesis without major contributions from the s-process in AGB stars (Simmerer et al., 2004, Sneden et al., 2008). Generally, the ratio of first-to-second peak n-capture elements, such as [Y/Ba], is systematically lower in dSphs than in MW halo, owing to their low star forming efficiency (Fig. 14 in Tolstoy et al. 2009). The opposite is seen in ALW-8, which exhibits a high [Y/Ba] of 0.84 dex, which is otherwise seen in metal-poor halo stars below around -2.7 dex and also in the two most metal-poor Carina stars of Venn et al. (2012) as well as in two other dSph CEMP stars. This reflects significant departures from the abundance patterns that are governed by the main r-process in that the first-peak elements (such as Sr, Y, Zr) are systematically enhanced with respect to the heavier ones (Z$>$56). Such trends prompted the need for an additional source of these elements via a weak r- or weak s-process (e.g., Arcones and Montes, 2011, Honda et al., 2006, Travaglio et al., 2004). Also in ALW-8, only a low upper limit could be derived for Eu, which

serves as a tracer for main r-process.

Thus, in Fig. 4.13 (bottom panel), we place ALW-8 in the context of the n-capture processes by comparing the heavier element pattern to those in two metal-poor halo stars: HD 122563 ([Fe/H]= -2.82, [C/Fe]= -0.47) (Honda et al., 2006, Spite et al., 2005), which shows an archetypical weak r-process pattern, and CS 22892-052 ([Fe/H]= -3.12, [C/Fe]= 0.89) (Sneden et al., 2003, black dots) as a contender for enrichment via the main r-process. All these reference stars have been normalized to the abundance of Y in ALW-8 in Fig. 4.13. It becomes immediately clear that the low Ba and Eu abundances are incompatible with an overproduction in the standard r-process. The scaled abundance ratio of Zn for HD 122563 deviates from the other stars shown here, while it is noted that the absolute [Zn/Fe] ratios of these stars are consistent with one another. Thus, Zn appears comparably low; its origin rather lies in complete Si-burning with possible contributions from a weak s-process (Timmes et al., 1995, Travaglio et al., 2004, Venn et al., 2012). It is noted that the upper limit for Zr coincides with the lower error bound in HD 122563, while it should be produced in equal amounts to Y by the weak r-process. Ideally, an enhanced Sr abundance is expected from this process as well, but no Sr-feature fell within our spectral range.

An alternative source of the excess in light n-capture elements is a weak s-process in fast rotating massive stars (Frischknecht et al., 2016). This scenario predicts an additional overproduction of O accompanying the enhancement in C, Sr,Y, and Zr. Indeed, the [O/Fe] of 0.89 in ALW-8 is high, and also for HD 122563, a strongly elevated [O/Fe] ratio between 0.6 and 1.1 dex has been reported (Afşar et al., 2016, Barbuy et al., 2003). Given the low number of elements that was measured in ALW-8 beyond $Z > 30$, it cannot be unambiguously concluded which of

the processes ultimately led to the observed abundances and whether O was predominantly enhanced internally in the CNO processing or already imprinted in the gas alongside with the primordial carbon from earlier generations of faint SNe and/or fast rotators.

4.7 Conclusion

Two carbon enhanced metal poor stars from Carina dwarf spheroidal have been studied in this chapter. ALW-1 is the third CEMP-s star which is being reported from Carina where as ALW-8 is the first CEMP-no star to be reported in the Carina dSph galaxy. ALW-1 also show enhancement in heavy s-process elements compared to light s-process indicating that the binary companion is metal poor in nature. Because of the poor signal to noise ratio and the difficulty in placing the continuum, in ALW-1, the abundance of crucial elements could only be derived. The results are restricted to the reporting of the abundance measurements.

The overall abundance pattern of ALW-8 suggests that the star was born from a medium that was enriched by a mixture of faint SNe and/or fast rotating massive stars, and low-metallicity SNe II. The gas from which it formed had only undergone poor mixing. Moreover, the neutron-capture elements in ALW-8 are in excellent agreement with the only CEMP-no star in the Sculptor dSph and the weak-r process star HD 122563. This suggests that, whichever process was responsible for the heavy element production must be an ubiquitous source to pollute the CEMP-no stars, acting independently of the environment, such as in the halo or in dSphs.

While a wealth of CEMP-no stars is known in the MW halo, the absolute number of such stars identified in nearby dSph and ultra-faint dSph satellites is low. Amongst these is the most iron-poor and most carbon-rich star in the Segue 1 dSph

([Fe/H] = −3.5, [C/Fe] = 2.3; Norris et al. 2010b). While more iron-poor extragalactic stars exist in dSphs (Frebel et al., 2010a, Tafelmeyer et al., 2010), none of these are carbon-rich. On the other hand, the fraction of CEMP stars in the halo and in metal-poor dSph galaxies is known to significantly increase with decreasing metallicity, which has been interpreted as being due to the shift in the mean metallicity from lower to higher values as the luminosity of the galaxy increases (Salvadori et al., 2015).

Finally, the CEMP-no subclass is of particular interest as their fraction is largest in the outer Galactic halo, while CEMP-s stars prevail in its inner, in-situ component (Carollo et al., 2014). This finding provides an immediate connection to the CEMP population in dSphs owing to the accretion origin of the outer halo (e.g., Bullock and Johnston, 2005, Carollo et al., 2007, Cooper et al., 2013, Searle and Zinn, 1978a). As a consequence, the CEMP-no fraction in the Galactic satellites should be large and any additional candidate in this category is significant not only for nucleosynthetic considerations, but also for constraining the halo formation scenarios.

appendix

Table 4.3: Line list for the EW analysis, abundance and abundance uncertainties to 1 σ scatter in the stellar parameters for ALW-8.

Element	λ (Å)	χ (eV)	log(gf)	EW (mÅ)	A(x)	δ T $\pm$100 K	δ log g $\pm$0.25 dex	$\delta\xi$ $\pm$0.2 km s^{-1}
Li I	6707.70	0.00	0.17	syn	0.00	$\pm$0.30	$\mp$0.10	$\pm$0.01
O I	6300.31	0.00	−9.82	syn	6.93	$\mp$0.10	$\mp$0.03	$\pm$0.01
O I	6363.78	0.02	−10.30	syn	7.23	$\mp$0.10	$\mp$0.03	$\pm$0.01

Table 4.3 – continued from previous page

Element	λ (Å)	χ (eV)	log(gf)	EW (mÅ)	A(x)	δ T $\pm$100 K	δ log g $\pm$0.25 dex	$\delta\xi$ $\pm$0.2 km s^{-1}
Na I	5682.63	2.09	−0.70	58	4.84	$\mp$0.03	$\pm$0.07	$\mp$0.02
Na I	5688.21	2.09	−0.45	82	4.91	$\mp$0.02	$\pm$0.09	$\mp$0.03
Mg I	5528.40	4.34	−0.62	120	5.57	$\mp$0.00	$\pm$0.11	$\mp$0.06
Ca I	5261.70	2.52	−0.59	67	4.51	$\mp$0.04	$\pm$0.08	$\mp$0.04
Ca I	5588.75	2.53	0.31	100	4.07	$\mp$0.02	$\pm$0.10	$\mp$0.07
Ca I	5594.46	2.52	0.05	102	4.36	$\mp$0.02	$\pm$0.10	$\mp$0.08
Ca I	6102.72	1.88	−0.86	85	4.05	$\mp$0.06	$\pm$0.09	$\mp$0.04
Ca I	6122.22	1.89	−0.38	167	4.66	$\mp$0.05	$\pm$0.15	$\mp$0.09
Sc II	5526.79	1.77	0.02	100	1.27	$\pm$0.00	$\mp$0.13	$\mp$0.08
Sc II	5657.90	1.51	−0.60	70	1.08	$\mp$0.02	$\mp$0.16	$\mp$0.04
Sc II	5684.20	1.51	−1.07	55	1.15	$\mp$0.03	$\mp$0.16	$\mp$0.02
Ti I	4981.73	0.85	0.50	180	3.26	$\mp$0.11	$\pm$0.14	$\mp$0.15
Ti I	4999.50	0.83	0.25	95	2.14	$\mp$0.11	$\pm$0.10	$\mp$0.07
Ti I	5020.03	0.84	−0.41	84	2.66	$\mp$0.12	$\pm$0.10	$\mp$0.05
Ti I	5024.84	0.82	−0.60	47	2.30	$\mp$0.14	$\pm$0.08	$\mp$0.02
Ti I	5036.46	1.44	0.13	60	2.63	$\mp$0.11	$\pm$0.09	$\mp$0.03
Ti I	5173.74	0.00	−1.11	135	2.83	$\mp$0.15	$\pm$0.08	$\mp$0.12
Ti I	5210.38	0.05	−0.88	120	2.44	$\mp$0.15	$\pm$0.09	$\mp$0.09
Ti II	4865.61	1.12	−2.67	51	2.78	$\mp$0.04	$\mp$0.15	$\mp$0.02
Ti II	5336.77	1.58	−1.63	97	3.01	$\mp$0.00	$\mp$0.14	$\mp$0.08
Ti II	6491.56	2.05	−1.79	33	2.74	$\mp$0.02	$\mp$0.17	$\mp$0.01

Table 4.3 – continued from previous page

Element	λ (Å)	χ (eV)	log(gf)	EW (mÅ)	A(x)	δ T $\pm$100 K	δ log g $\pm$0.25 dex	$\delta\xi$ $\pm$0.2 km s^{-1}
Cr I	5247.57	0.96	−1.64	66	2.99	$\mp$0.12	$\pm$0.09	$\mp$0.03
Cr I	5296.69	0.98	−1.40	95	3.18	$\mp$0.11	$\pm$0.10	$\mp$0.07
Cr I	5345.80	1.00	−0.98	139	3.44	$\mp$0.10	$\pm$0.11	$\mp$0.12
Cr I	5348.31	1.00	−1.29	64	2.66	$\mp$0.12	$\pm$0.09	$\mp$0.03
Cr I	5409.77	1.03	−0.72	120	2.91	$\mp$0.10	$\pm$0.10	$\mp$0.10
Mn I	5394.68	0.00	−3.50	70	2.61	$\mp$0.18	$\pm$0.06	$\mp$0.03
Mn I	5432.55	0.00	−3.79	54	2.70	$\mp$0.18	$\pm$0.06	$\mp$0.02
Fe I	4891.49	2.85	−0.11	160	4.81	$\mp$0.04	$\pm$0.14	$\mp$0.11
Fe I	4966.09	3.32	−0.87	94	5.22	$\mp$0.04	$\pm$0.07	$\mp$0.08
Fe I	5001.86	3.88	0.01	88	5.01	$\mp$0.02	$\pm$0.06	$\mp$0.07
Fe I	5194.94	1.55	−2.08	156	4.90	$\mp$0.09	$\pm$0.06	$\mp$0.16
Fe I	5195.47	4.21	−0.08	57	5.05	$\mp$0.04	$\pm$0.04	$\mp$0.03
Fe I	5215.18	3.27	−0.87	100	5.17	$\mp$0.04	$\pm$0.07	$\mp$0.08
Fe I	5225.53	0.11	−4.78	128	4.97	$\mp$0.15	$\pm$0.01	$\mp$0.12
Fe I	5242.49	3.63	−0.96	50	5.04	$\mp$0.06	$\pm$0.03	$\mp$0.02
Fe I	5307.36	1.61	−2.98	93	4.84	$\mp$0.11	$\pm$0.04	$\mp$0.07
Fe I	5586.76	3.36	−0.12	133	4.97	$\mp$0.03	$\pm$0.09	$\mp$0.10
Fe I	6546.24	2.76	−1.53	103	4.97	$\mp$0.08	$\pm$0.02	$\mp$0.07
Fe II	5197.58	3.23	−2.09	55	5.03	$\pm$0.05	$\mp$0.18	$\mp$0.03
Fe II	5234.63	3.22	−2.23	45	4.96	$\pm$0.04	$\mp$0.18	$\mp$0.02
Ni I	4980.17	3.60	0.00	95	4.62	$\mp$0.01	$\pm$0.04	$\mp$0.08

Table 4.3 – continued from previous page

Element	λ (Å)	χ (eV)	log(gf)	EW (mÅ)	A(x)	δ T $\pm$100 K	δ log g $\pm$0.25 dex	$\delta\xi$ $\pm$0.2 km s^{-1}
Ni I	5424.64	1.95	-2.77	85	4.84	$\mp$0.08	$\pm$0.00	$\mp$0.06
Ni I	6108.11	1.67	-2.45	52	3.59	$\mp$0.11	$\mp$0.01	$\mp$0.02
Ni I	6314.65	1.92	-1.77	62	3.39	$\mp$0.10	$\mp$0.01	$\mp$0.03
Ni I	6643.63	1.67	-2.30	75	3.69	$\mp$0.11	$\mp$0.01	$\mp$0.04
Zn I	4810.53	4.07	-0.13	30	2.19	$\pm$0.02	$\mp$0.12	$\mp$0.01
Y II	5200.41	0.99	-0.57	syn	0.00	$\pm$0.05	$\pm$0.10	$\pm$0.01
Y II	5205.73	1.03	-0.34	syn	0.00	$\pm$0.05	$\pm$0.10	$\pm$0.01
Zr II	6127.48	0.15	-1.06	syn	$<$0.50	$\pm$0.30	$\mp$0.30	$\pm$0.01
Zr II	6134.59	0.00	-1.28	syn	$<$0.50	$\pm$0.30	$\mp$0.30	$\pm$0.01
Ba II	4934.08	0.00	-0.15	syn	-1.20	$\pm$0.10	$\pm$0.10	$\mp$0.01
Ba II	5853.68	0.60	-0.91	syn	-0.50	$\pm$0.15	$\pm$0.20	$\mp$0.10
Ba II	6141.73	0.70	-0.03	syn	-0.90	$\pm$0.10	$\pm$0.10	$\mp$0.10
Eu II	6645.09	1.38	0.12	syn	< -1.50	$\pm$0.70	$\pm$0.50	$\pm$0.01

Chapter 5

Abundance analysis of SDSS J134338.67+484426.6; an extremely metal-poor star from the SDSS-MARVELS pre-survey[1]

5.1 Introduction

Extremely metal-poor (EMP; [Fe/H]$<$ -3.0) stars were formed during the very early phases of our Galaxy's evolution, and thus carry the chemical imprints of the first generations of supernovae that exploded in the Galaxy (Bromm et al., 2003, Kobayashi et al., 2006). Detailed abundance analysis of such stars constrain the nuclear processes and nucleosynthesis sites which were prevalent during early galaxy evolution, and can be used to explore predictions of Galactic chemical-evolution models

[1]The work presented in this Chapter is published as a paper (2016, MNRAS, 458, 2648)

(Hansen et al., 2014).

EMP stars exhibit a variety of distinct abundance patterns (for detailed reviews see Beers and Christlieb 2005, Frebel and Norris 2015). High-resolution spectroscopic surveys using 8-10 m class telescopes have revealed a number of interesting trends in the abundance ratios of these stars (Barklem et al., 2005, Cayrel et al., 2004, Lai et al., 2008, Roederer et al., 2014b, Yong et al., 2013). For example, François et al. (2007) showed that there exists a large scatter in the [n-capture/Fe] ratios for stars with [Fe/H] < -2.5, while the α-elements and iron-peak elements exhibit a surprisingly uniform behavior. These authors also showed that the light n-capture element abundances (e.g., Sr) are anti-correlated with the abundances of heavier species such as Ba, suggesting the operation of the so-called Light Element Primary Process (LEPP) among some stars of extremely low metallicity (Montes et al., 2007). As these trends were derived from samples of stars that did not exhibit other anomalies in their abundance ratios, they may be representative of the well-mixed ISM abundance at these metallicities. Similar results have been observed in other well-mixed environments, such as globular-cluster stars (Otsuki et al., 2006).

Though majority of the EMP stars in the halo and nearby dwarf galaxies show uniform abundance in their α elements, a few exhibit abnormally low abundance value compared to the the mean halo α abundance (Aoki et al., 2009, Carney et al., 1997, Cohen et al., 2013, King, 1997, Kirby and Cohen, 2012, Lai et al., 2009, Tafelmeyer et al., 2010). RecentlyCaffau et al. (2013) identified a class of α-poor EMP stars, several of which exhibit low carbon abundances (see also Cohen et al. (2013), and references therein).

Kobayashi et al. (2014) showed that α-poor EMP stars can be naturally explained

by the nucleosynthesis yields of core-collapse supernovae, i.e., 13 - 25 $M_{\odot}$ supernovae or hypernovae, but pointed out that detailed abundances of additional iron-peak elements, which are not available for most of this subset of EMP stars, are required to better constrain the models.

According to Ivans et al. (2003), the low α abundance exhibited by their samples are due to the the larger contribution of SNIa yields over the pre existing SNeII ejecta. But EMP stars might have formed much earlier than the onset of SNIa. So it is less likely that the EMP stars are affected by the SNe Ia yields unless they belong to a system where the star formation rate is very low and the mixing is highly inhomogeneous so as to keep the gas cloud metal poor until the onset of Sne Ia .

In this chapter I discuss the high-resolution spectroscopic follow-up observations of a newly identified EMP star, SDSS J134338.67+484426.6 (hereafter, SDSS J1343+4844) that may shed additional light on the nature of early nucleosynthesis in the Galaxy, in particular for stars that do not exhibit other abundance anomalies (such as carbon over-abundances) that are commonly found for EMP stars. Since SDSS J1343+4844 is bright compared to many of the known EMP stars, particularly among the rare α-poor sub-class, it also presents an ideal target for future high-resolution studies capable of deriving detailed isotopic ratios, which can be used to better constrain the SNe models.

5.2 Observation and data reduction

SDSS J1343+4844 was identified as a likely metal-poor star from the SDSS-III-MARVELS (Multi-object APO Radial Velocity Exoplanet Large-area Survey; Ge et al. 2008) pre-survey spectroscopy using the SDSS legacy spectrographs (Gunn et al., 2006). The pre-survey was used for selecting suitable bright dwarfs for planet

searches, in the magnitude range $9 < V < 13$ and with spectral types from late F to K. MARVELS pre-survey plates were reduced using a slightly modified version (NOCVS:v5_3_23) of the IDLSPEC2D pipeline. Stellar atmospheric parameters were estimated using the n-SSPP pipeline, a modified version of the SEGUE Stellar Parameter Pipeline (SSPP; Lee et al. 2008, see also Beers et al. 2014 for a description of the use of the n-SSPP). Based on the pipeline procedures and visual inspection, SDSS J1343+4844 was identified as carbon-normal extremely metal-poor star, with a metallicity [Fe/H] < -3.0.

Figure 5.1 shows the metallicity distribution of the complete set of MARVELS pre-survey stars; these stars clearly exhibit peak metallicities arising from the thin-disk and thick-disk components of the Galaxy. As is clear from inspection of this figure, metal-poor stars are quite rare in the sample, due to the low Galactic latitude of the pre-survey area. Among the MARVELS pre-survey spectroscopic spectra (N $\sim$ 20000), SDSS J1343+4844 was the only star found with metallicity [Fe/H] $<$ -3.0.

Follow up high-resolution ($R \sim 30000$) spectroscopic observations of SDSS J1343+4844 were obtained with the ARC Echelle Spectrograph on the 3.5 m telescope at Apache Point Observatory (APO) and the High resolution Spectrograph (HRS) on the Hobby-Eberly 9.2-m telescope (HET). Multi-epoch low-resolution ($R \sim 1300$) spectra were also obtained using the Hanle Faint Object Spectrograph Camera (HFOSC) at the 2 m Himalayan Chandra Telescope (HCT). The spectral resolution, wavelength coverage, and the signal-to-noise ratios of the available spectra are listed in Table 5.1.

The APO pipeline-reduced high-resolution spectrum exhibited slightly lower equivalent widths compared to the HET data. Hence I manually re-reduced the data using IRAF, in order to ensure proper background subtraction, and found a better

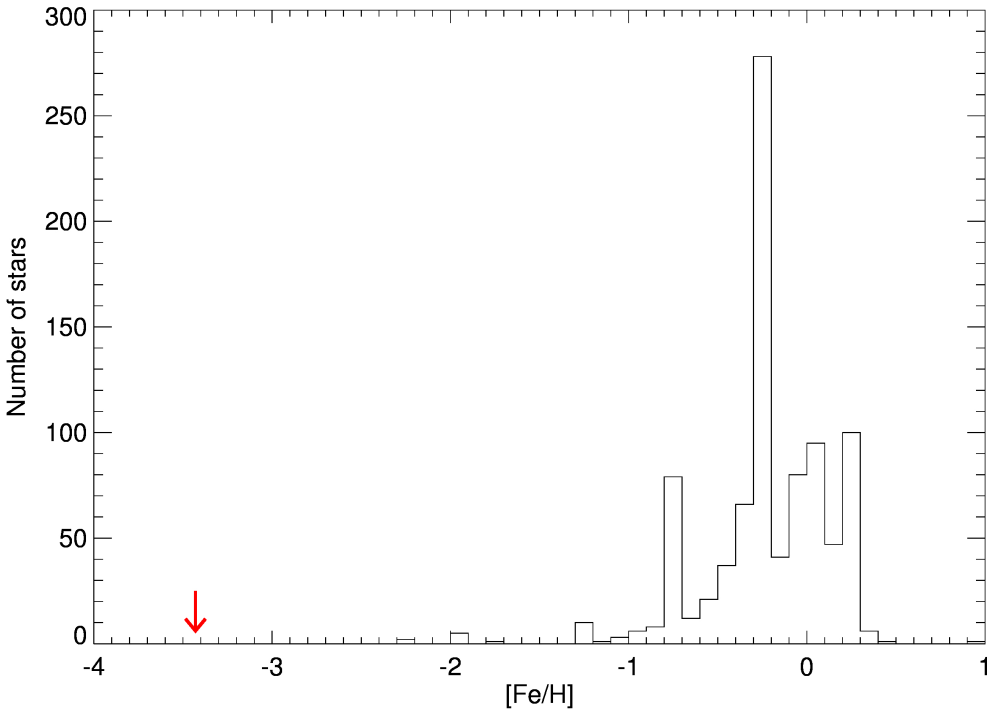

Figure 5.1: Metallicity distribution of the MARVELS pre-survey stars. The two strong peaks correspond to the expected metallicities of the Galactic thin and thick disks.

match between the equivalent widths of the APO and HET datasets in the overlapping wavelength regions (see Figure 5.2). The equivalent widths for individual species are listed in the table in the appendix.

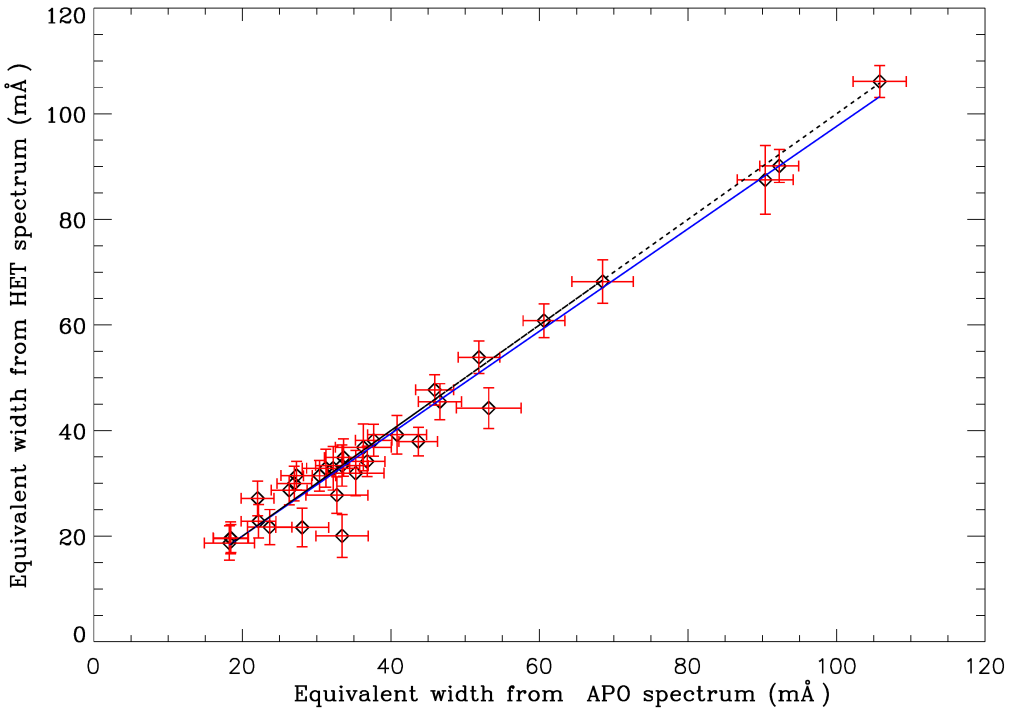

Figure 5.2: Comparison of measured equivalent widths of the spectral lines from the high-resolution APO and HET spectra. The solid line is a fit to these measurements; the dashed line is the one-to-one line.

Table 5.1: Details of observations and radial velocities of SDSS J1343+4844 using various telescope/spectrograph combinations

Date	MJD	Telescope-Spectrograph	Resolving Power	λ coverage (Å)	SNR*	RV (km/s)
2009-01-14	54845.48138	SDSS-premarvels	2000	3800 - 9200	58.17	-114.7 ± 3.8
2009-03-20	54910.23972	APO-ARCES	31500	3373 - 10240	59.67	-123.2 ± 9.2
2012-04-23	56040.15483	HET-HRS	30000	4376 - 7838	58.29	-106.1 ± 4.0
2013-06-05	56448.84183	HCT-HFOSC	1330	3800 - 6840	132.87	-248.6 ± 10.4
2014-05-28	56805.84180	HCT-HFOSC	1330	3800 - 6840	155.89	-219.3 ± 10.9
2014-06-25	56833.91528	HCT-HFOSC	1330	3800 - 6840	140.94	-241.0 ± 10.9
2014-07-31	56869.67394	HCT-HFOSC	1330	3800 - 6840	135.79	-269.7 ± 10.9

* SNR is calculated at 5000 Å.

5.3 Radial velocities

Radial velocities were calculated based on six epochs of high- and low-resolution data taken over a span of five years. A cross-correlation analysis was performed, using the best-matching synthetic template that represents the stellar parameters and the chemical abundances of SDSS J1343+4844, as derived below, and degraded to match the spectral resolution of each observation. These observed velocities were then corrected for Earth's motion; the resultant heliocentric radial velocities are presented in Table 5.1.

A stability analysis of the HCT-HFOSC spectrograph was performed in order to estimate realistic errors for the derived radial velocities of this star. For this purpose, calibration exposures of FeAr, taken during the course of an entire night, were used. One of the lamp exposures was taken as a reference and relative radial velocities were derived. Although drifts in the calibration spectra for which the telescope position did not change are less than 2 km/sec, a large systematic shift of the spectra was noticed for a number of different telescope pointings; ranging from -30 km/s to $+30$ km/s. The systemic shift in the spectra due to the changing telescope position has been corrected using the prominent [OI] skylines at 5577.34, 6300.3, 6363.8 Å . The median of the shifts calculated from these lines was taken and corrected all the spectra observed with HCT accordingly.

The software package RVLIN has been used, provided by Wright and Howard (2009), which is a set of IDL routines to fit Keplerian orbits to the radial velocity data, and find the period of the radial-velocity variation. The radial-velocity measurements exhibit a variation with a period of 592 days; the best fit for is shown in Figure 5.3. Although the data are insufficient to derive the mass ratio of the binary

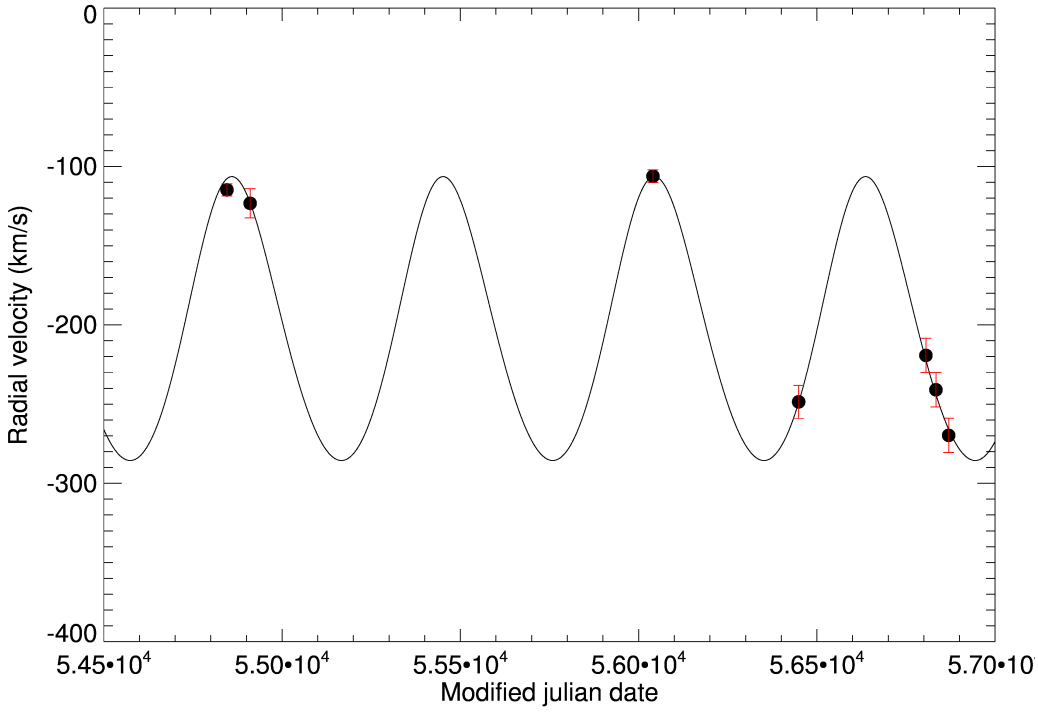

Figure 5.3: Variation of radial velocity with the MJD. The black dots represent the observed points and the black line indicates the best fit corresponding to a period of 592 days.

system, the binary nature appears to be clear. Additional radial-velocity monitoring of this system would be useful to check on the derived period, given the sparse coverage of the proposed orbit at present.

5.4 Stellar parameters

Both low- and high-resolution spectroscopic data were used for deriving estimates of the effective temperature, log g, and metallicity for SDSS J1343+4844 as described below, so that these determinations might be compared with one another.

Stellar temperature estimates were derived making use, in part, of various available photometric datasets. The photometric colours and errors are listed in Table 5.3. A reddening estimation (E(B-V) = 0.009) from the Schlegel et al. dust maps (Schlegel et al., 1998b) was used. Optical (APASS; Henden et al. 2015) and NIR (2MASS; Cutri et al. 2003) photometric data were used to derive effective temperature estimates, based on the Alonso relations (Alonso et al., 1996, 1999) assuming a dwarf classification for a metallicity [Fe/H] = -3.0 (Table 5.2).

VOSA (http://svo2.cab.inta-csic.es/), the online SED fitter, is also used to derive the temperature, by using all of the available photometry (optical, 2MASS, and WISE, Wright et al. 2010). A Bayesian fit using the ATLAS-NOVER-NEWODF model yielded a best-fit value of T_{eff} = 5750 K.

the H_β line wings of the APO and HET spectra were fitted for various temperatures. The red wing of H_β in the APO spectrum lies close to the edge of the order, so it was not considered in the fitting. The best-fit synthetic spectrum in this region, along with the observed spectra from APO and HET, are shown in Figure 5.4.

The derived temperature from the n-SSPP pipeline is 6161 K, which clearly deviates from the rest of the estimates. This is due, in part, to the fact that the

Table 5.2: Photometric data of SDSS J1343+4844

	B	V	J	H	K_s	W1	W2	W3	W4
Magnitude	12.685	12.147	11.031	10.675	10.609	10.566	10.563	10.56	8.808
error	0.041	0.039	0.022	0.028	0.022	0.023	0.020	0.081	... *

* The error is not available in the catalog.

flux calibration of the MARVELS pre-selection spectrum is not accurate, as these plug-plates were observed during twilight at high airmass. So,T_{eff} is re-derived using only the normalized SDSS spectrum, obtaining T_{eff} = 5832 K. An effective temperature of 5620 K was derived using the high-resolution spectra, employing the excitation equilibrium for the derived abundances using Fe I lines (see the upper panel of the Figure 5.5).

Finally, T_{eff} is also derived from the V-K colour, where the K_s magnitude is used instead of the K magnitude (the difference between the two magnitudes is $K_s - K = -0.0003$, which yields no difference in the derived temperature); T_{eff} thus obtained is 5671 K. This estimate differs from the temperature obtained based on the excitation equilibrium approach by only 50 K, which is adopted for the subsequent analysis.

Several different methods have been employed for the estimation of surface gravity of SDSS J1343+4844, including the ionization equilibrium of Fe I and Fe II lines, isochrone fitting, and the best-fit of the Mg I wings. Only four Fe II lines were detected in the spectra (see upper panel of Figure 5.5), and derived log g = 3.44. Theoretical isochrones (Demarque et al., 2004) for an age range of 11-13 Gyr (see Figure 5.6) have been fitted by assuming a temperature of 5620 K. There are two

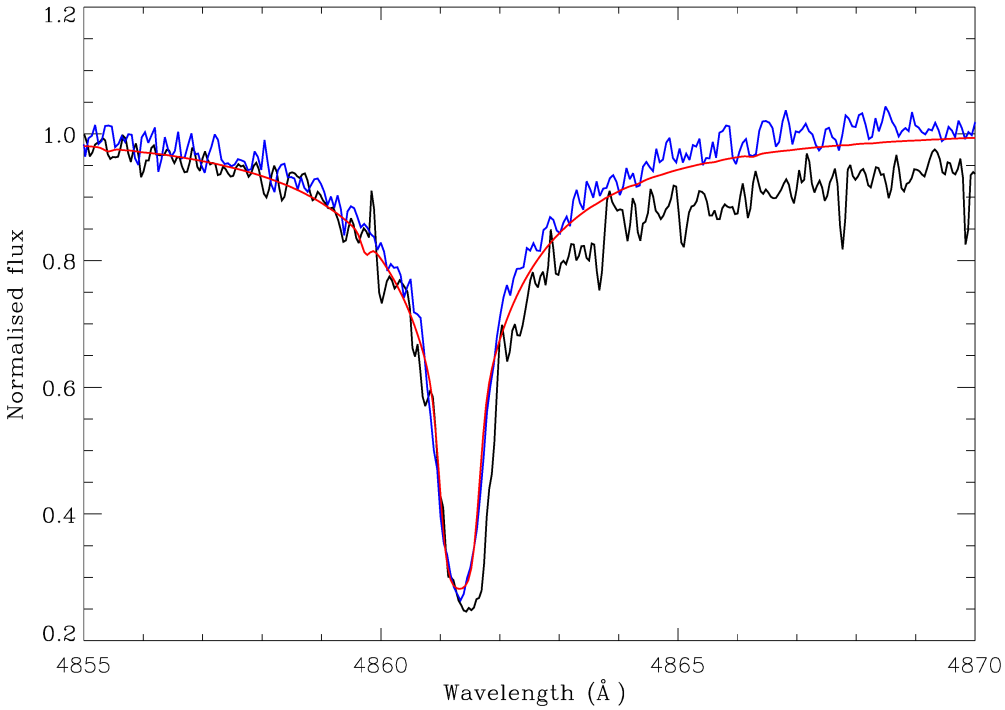

Figure 5.4: The H_β region from the APO spectrum (black), the HET spectrum (violet), and the synthesized spectrum (red) are shown. The best fit corresponds to T_{eff} = 5620 K. The red wing of the APO spectrum falls at the edge of the echelle orders, so only the blue wing is considered for the fit.

Table 5.3: The temperature derived from various methods

Colour	T_{eff} (K) (for Dwarf)
B−V = 0.538 ± 0.057	5618 ± 130
V−K = 1.538 ± 0.044	5671 ± 37
J−H = 0.356 ± 0.036	5444 ± 144
J−K = 0.422 ± 0.031	5394 ± 144
SED fitting	5750
SSPP	6161
SDSS normalized spectra	5832
High resolution spectra - Excitation equilibrium	5620

possibilities – the star could be a dwarf (log $g \sim 4.7$) or a subgiant (log $g \sim 3.4$). Mg I lines were also fitted for both the APO and HET spectra at λ5167 Å, λ5172 Å, and λ5183 Å for various values of log g, and obtained a value of log g = 3.4 (Figure 5.7). log g= 3.4 has been adopted, a value that is consistent with all three methods.

The microturbulent velocity (ξ) of the star is derived using 68 Fe I lines, by adjusting the input microturbulence value in such a way that the weak and strong Fe I lines give the same abundances (see lower panel of Figure 5.5). The adopted stellar atmospheric parameters are listed in Table 5.4.

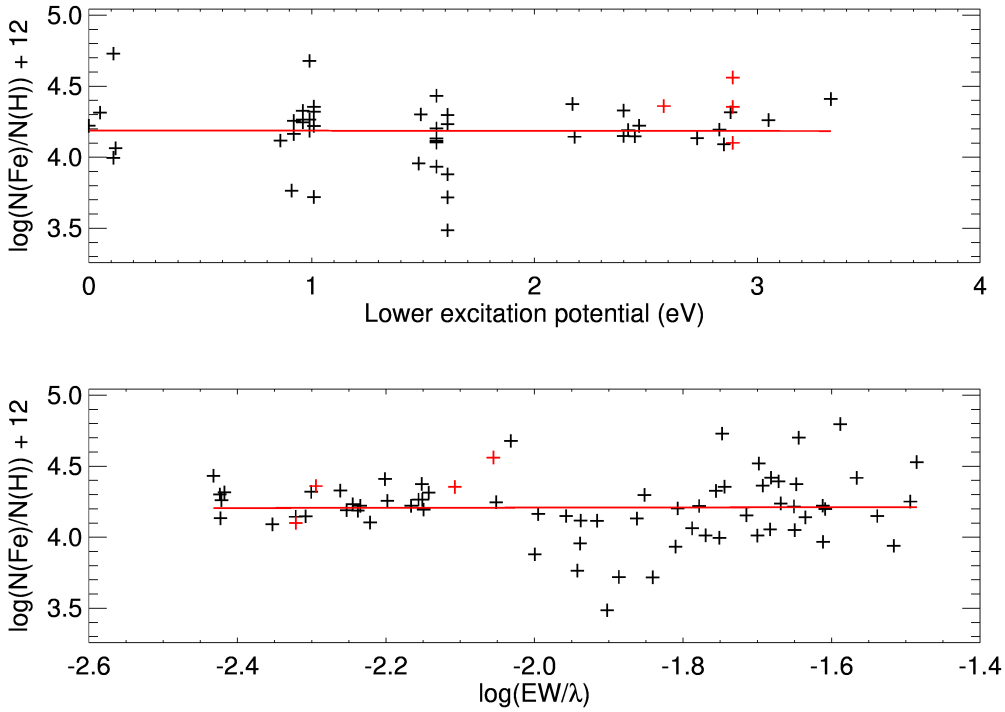

Figure 5.5: The upper panel indicates the abundance trend for T_{eff} = 5620 K, log g =3.44, ξ =1.35 km/s. The red crosses indicate Fe II lines, while the black crosses are Fe I lines. The lower panel indicates the derived Fe abundance as a function of the respective line strengths. In both cases the solid line indicates the best fit.

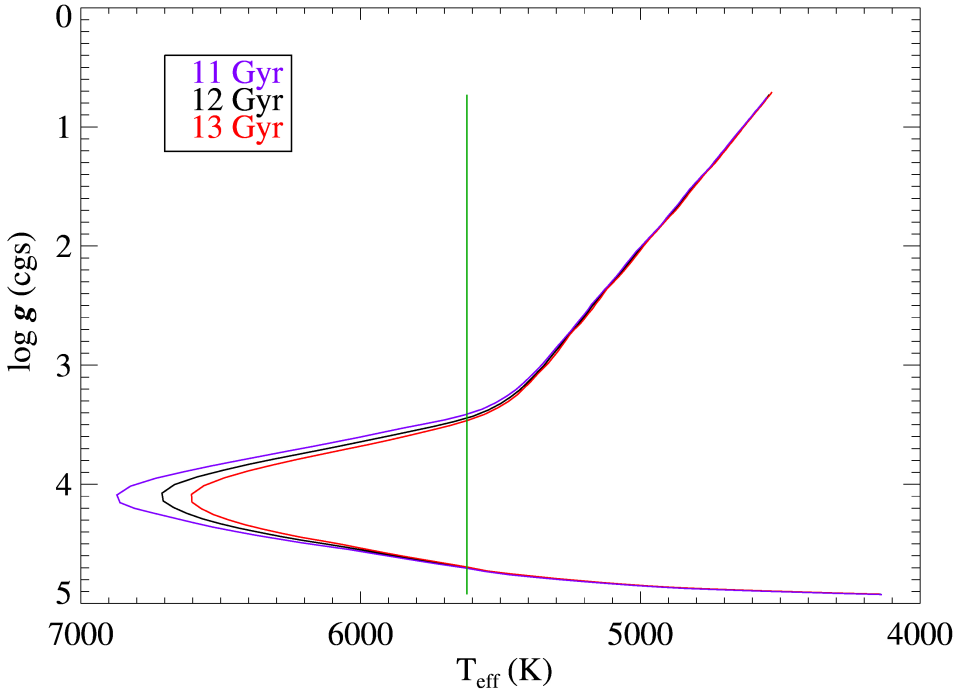

Figure 5.6: Theoretical isochrones from Demarque et al. (2004) for different ages; the black line corresponds to an age of 12 Gyr, whereas the violet and red lines correspond to 11 Gyr and 13 Gyr, respectively. [Fe/H] = 3.5 and [α/Fe] = 0.0 have been assumed for isochrone generation. The log g values are taken where the temperature lines intersects the isochrones. For the adopted T_{eff} = (5620 K), indicated by the vertical green line, two possible log g values (log g = 4.7,3.4) were found.

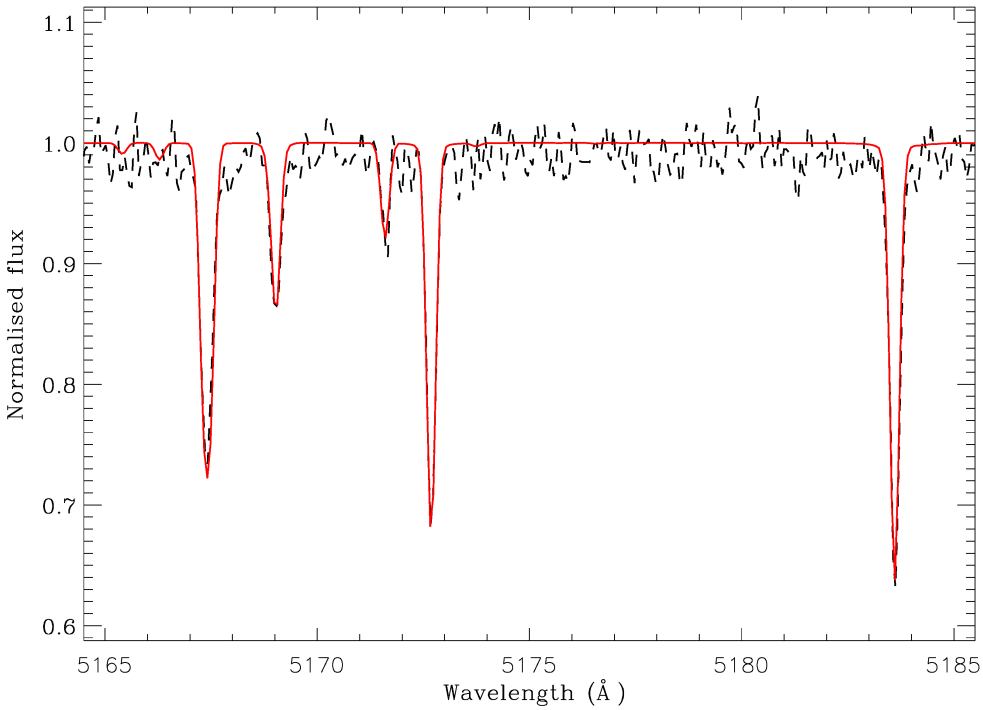

Figure 5.7: High-resolution HET spectrum in the region of the Mg I triplet. The black dashed line indicates the HET spectrum, while the red solid line indicates the synthetic spectrum with parameters corresponding to T_{eff} = 5620 K, log g = 3.4. and [Fe/H] = -3.33.

Table 5.4: The adopted stellar parameters for SDSS J1343+4844

T_{eff} (K)	log$g$ (cgs)	ξ (km/s)	[Fe/H]
5620	3.44	1.35	-3.33

5.4.1 Abundance analysis

ATLAS9 NEWODF (Castelli and Kurucz, 2004) model atmospheres without convective overshoot have been used through out this study. The main abundance-analysis results come from the APO spectrum, since it covers a broader wavelength region. In the overlapping regions of both the APO and HET spectra, a final abundance value is derived using a weighted average of abundances from both spectra. For the H_β and Mg fitting, the HET spectrum is primarily used because these lines are fall at the edge of the echelle orders, and in such cases continuum normalization was better accomplished from the HET spectrum. Only those lines with equivalent widths less than 100 mÅ were considered for the abundance analysis, since they are on the linear part of the curve of growth, and are relatively insensitive to the choice of microturbulence.

The solar abundance from Grevesse and Sauval (1998) has been adopted; solar isotopic fractions were used for all the elements. I used the CH and CN molecular line list compiled by Plez et al. (2005), and the NH and C_2 molecular-line lists from the Kurucz database. The atomic data for the other lines comes from the Vienna Atomic Line Database (VALD). The line lists used are the same as in Cui et al. (2013). Version 12 of turbospectrum code was employed for spectrum synthesis and abundance analysis (Alvarez and Plez, 1998, Plez, 2012).

Table 5.5: Elemental abundance determinations for SDSS J1343+4844

Species	N_{lines}	A(X)	Solar	[X/H]	[X/Fe]	σ^*
CH	...	5.62	8.52	-2.9	$+0.43$	synth
Na I	2	2.33	6.33	-4.00	$-0.67^{\S}$	0.01
Mg I	5	4.31	7.58	-3.27	$+0.06$	0.11
Al I	2	3.33	6.47	-3.14	$+0.19^{\S}$	0.07
Si I	1	4.30	7.55	-3.25	$+0.08$	...
S I	...	<5.64	7.33	< -1.69	$< +1.64^{\dagger}$	synth
Ca I	3	3.24	6.36	-3.12	$+0.21$	0.03
Sc II	1	-0.01	3.17	-3.18	$+0.15$	...
Ti II	12	1.73	5.02	-3.29	$+0.04$	0.23
Cr II	3	2.29	5.67	-3.38	-0.05	0.00
Mn I	2	1.81	5.39	-3.58	-0.25	0.1
Fe I	68	4.17	7.50	-3.33	0.00	0.22
Ni I	3	3.08	6.25	-3.17	$+0.16$	0.01
Sr II	2	-0.90	2.97	-3.87	-0.54	0.14
Ba II	...	$<$ -1.83	2.13	< -3.96	$< -0.63^{\dagger}$	synth

§ Represents the values after applying the NLTE corrections.

† Denotes the abundance values from the synthesis.

* The errors quoted are random errors.

5.5 Abundances

5.5.1 Carbon, Nitrogen, and Oxygen

There is only a weak CH G-band present in the spectra of SDSS J1343+4844. The carbon abundance was derived by fitting the bandhead region with synthetic spectra iteratively, and adopting the value that yields the best match to the observed spectra. A step size of 0.3 dex has been chosen because no visible change in the spectral features was found for smaller step sizes. The best match is shown in Figure 5.8. The APO spectrum is very noisy in the G-band region, and the HET spectrum did not cover this wavelength. So, the low-resolution HCT spectra have been used to derive the carbon abundance from the CH G-band region. Neutral C,N, and O lines were not detected, due to the lower abundance and low temperatures. As is clear from inspection of Figure 5.8, the fit is not particularly good, so the reported value should be considered provisional. However, it is also obvious that SDSS J1343+4844 is not enhanced in carbon, which would have resulted in a much larger CH G-band.

5.5.2 The α-elements

Magnesium lines at 3838 Å and 5172 Å are detected in the spectra. Only two lines of the triplet at 5172 Å and one clean line in the 3838 Å region were used to determine the abundance. The derived [Mg/Fe] ratio is close to solar ([Mg/Fe] = +0.06); it is not enhanced as often found for halo stars. The silicon line at 3905 Å is used for the abundance estimate; the result is also close to solar, [Si/Fe] = $+0.08$. The titanium abundance also has a solar ratio, with no enhancement ([Ti/Fe] = +0.04), unlike most metal-poor stars. The S I lines at 9212 Å and 9237 Å could not be detected thus only derived an upper limit for sulphur. The Ca abundance was derived from

the three prominent Ca I lines at 4226.73 Å, 4302.53 Å and 4434.96 Å; they indicate a slightly enhanced [Ca/Fe] ratio ($+0.21$).

Overall, the α-element enhancement for SDSS J1343+4844 ([α/Fe] $\sim$+0.1) is lower than for typical halo stars in the Galaxy ([α/Fe] $\sim +0.4$). Non-LTE effects on the Mg and Ca abundances for EMP stars were investigated by Mashonkina et al. (2007), Andrievsky et al. (2010), and Spite et al. (2012). The non-LTE corrections for Mg are +0.1 to +0.3 dex. Hence, the Mg abundance ratios could be systematically higher than those derived by LTE analysis in this study. However, most of the Mg abundances results that are available for EMP stars are also based on an LTE analysis, and exhibit higher [Mg/Fe] abundance ratios relative to SDSS J1343+4844. The Ca I 4226 Å line is affected by NLTE effects, compared to other subordinate lines. These lines are very weak in our spectra, however they show consistent values with the abundances derived from Ca I 4226 Å.

5.5.3 The odd-Z elements

The sodium abundance is derived from the Na D_1 and D_2 resonance lines at 5890 Å and 5896 Å, and the abundance of aluminium is derived using the resonance doublet at 3944 Å and 3961.5 Å. These resonance lines are very sensitive to NLTE effects. The NLTE corrections to the abundance are -0.30 dex for Na (Baumueller et al., 1998) and $+0.65$ dex for Al (Baumueller and Gehren, 1997).

After the NLTE corrections are applied, the derived abundances for this star are in good agreement with the values found for other EMP stars (Cayrel et al., 2004, Lai et al., 2008).

5.5.4 The iron-peak elements

Iron abundances are derived from 68 Fe I and 4 Fe II lines. The abundance derived from the Fe I and Fe II lines show a difference of ~ 0.2 dex, which is in agreement with the NLTE effects explored by Asplund (2005). Among the iron-peak elements, Mn, Cr, and Ni were detected. The abundance of Mn was derived from the resonance Mn triplet at 4030 Å. The spectral line at 4034.4 Å was not used in the abundance analysis, since it is affected by a bad pixel. The abundance of scandium is based on one line at 4246.8 Å, and is found to be similar to other EMP stars. The observed abundance of Cr and Mn are similar to other EMP stars. The [Cr/Mn] ratio at the metallicity of SDSS J1343+4844 is in agreement with the [Cr/Mn] ratio obtained for EMP stars by Cayrel et al. (2004). The abundance ratio derived for Ni, using two lines (3783.5 Å and 3858.29 Å) is [Ni/Fe] = $+0.16$, which is also similar to the sample from Cayrel et al. (2004).

Figure 5.9 shows a comparison of abundances for SDSS J1343+4844 compared to the mean abundances of EMP giants and dwarfs. The iron-peak elements agree with the mean EMP abundances of these elements.

5.5.5 The neutron-capture elements

The neutron-capture elements in SDSS J1343+4844 are under-abundant relative to the solar values.

Resonance lines of strontium Sr II 4077 Å and 4215 Å are detected in the spectra; both the lines exhibit under-abundances with respect to the solar ratio ([Sr/Fe] = -0.54). No strong barium lines were detected, thus an upper limit for the abundance of Ba is estimated in SDSS J1343+4844 by fitting the Ba II resonance lines at 4554 Å and 4934 Å, incorporating the hyperfine splitting by McWilliam et al. (1995)

and assuming a solar isotopic composition. The upper limit derived for Ba is [Ba/Fe] < -0.66, also quite low.

5.6 Discussion and conclusions

5.6.1 Mean ISM abundance below [Fe/H] < -3.0

Metal-poor stars with enhanced/peculiar abundances in certain key elements help to identify the nuclear processes and astrophysical sites of their production. However, it is also interesting to study objects that do not exhibit such enhancements, since they may represent the mean ISM abundances at those epochs. This will help to understand the frequency of the nuclear sites that produce the peculiar abundance enhancements. SDSS J1343+4844 does not exhibit enhancement of the C, N, and O abundances, indicating that there was no internal CN processing, which is consistent with its evolutionary stage as a subgiant. Spite et al. (2006) and Bonifacio et al. (2009) show that the mean [C/Fe] abundance ratios in unmixed giants and dwarfs are about [C/Fe] = +0.19 and [C/Fe] = +0.45, respectively. The SAGA compilation (Suda et al., 2008) and Figure 2 of Bonifacio et al. (2009) also show that the carbon abundance ratios in the carbon-normal EMP stars are slightly enhanced with respect to the solar ratio. SDSS J1343+4844 has [C/Fe] = $+0.43$, based on the low-resolution spectrum, consistent with these EMP stars.

SDSS J1343+4844 also follows similar abundance patterns as that of the EMP dwarfs and giants for the Fe-peak elements and n-capture elements. Strontium abundance ratios for EMP dwarfs and giants are between [Sr/Fe] = -0.6 and [Sr/Fe] = -0.1 at metallicities of [Fe/H] = -3.0 (Andrievsky et al., 2011), which is again similar in SDSS J1343+4844. The upper limit for Ba abundance of SDSS J1343+4844

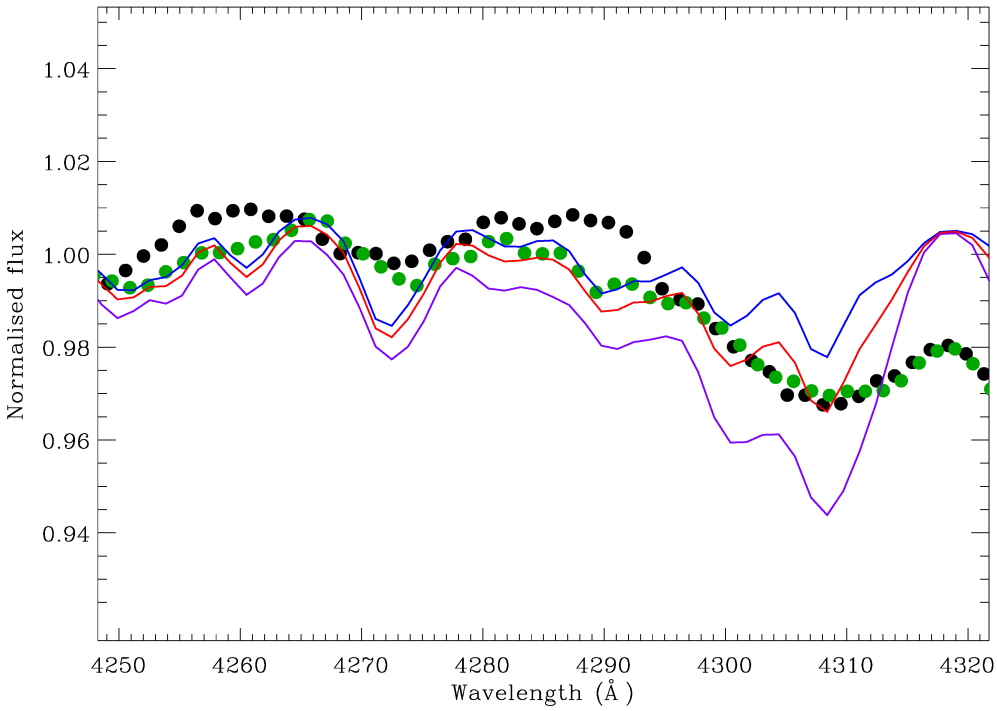

Figure 5.8: The CH G-band at 4300 Å fitted for various values of carbon abundance. The red line indicates the best fit, where the absolute carbon abundance used is log ϵ = 5.62. A step size of 0.3 dex has been used from the best-fit value, represented by the blue and violet colours. The observed HCT spectra are plotted in black and green colours. The G-band feature is not particularly well-fit, but it is clearly weak. The 4271 feature in the synthetic spectra is the Fe I line. It is poorly fitted because the observed spectra is of low resolution.

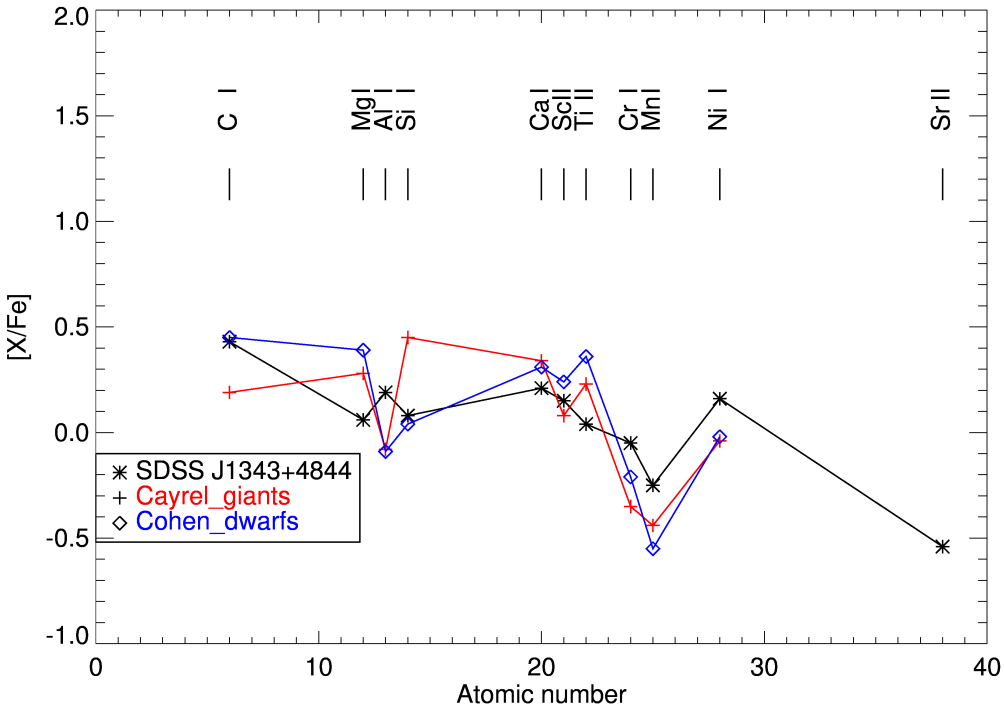

Figure 5.9: Elemental abundance for SDSS J1343+4844, compared with samples available from Cayrel et al. (2004) and Cohen et al. (2004). The red crosses indicate the mean elemental abundances from the Cayrel sample and the open diamonds represent the mean abundance values of the Cohen sample (EMP stars). The black asterisks represent the abundances of SDSS J1343+4844.

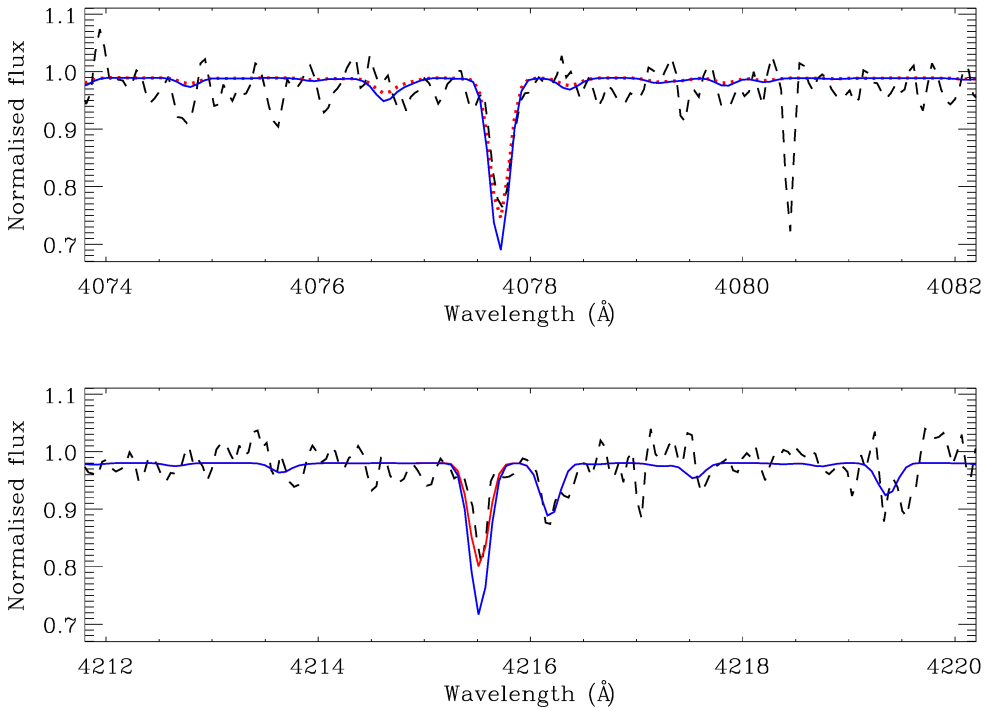

Figure 5.10: The Sr II lines at 4077 Å and 4216 Å are shown. The APO spectrum is plotted as a black dashed line, and the synthesized spectrum is plotted as a solid red line. The abundance value derived from the equivalent-width analysis is used for the synthetic spectrum. The blue solid line indicates the synthesized spectrum for [Sr/Fe]=0.

([Ba/Fe] $<$ -0.63) lies well within the average Ba abundances of EMP stars having normal carbon abundance at the same metallicity (Cohen et al. 2013; [Ba/Fe] ~ -0.6). During the early epochs of chemical evolution most AGB stars would not have had time to contribute to the ISM (Kobayashi et al., 2014). They contribute significantly only after z = 1.8 (roughly [Fe/H] > -2.4). Hence the n-capture elements seen in SDSS J1343+4844 has likely had contributions from massive stars. Recent chemical-evolution models find neutron-star mergers to be major contributor to the r-process (Vangioni et al., 2015). If one assumes Ba and Sr have purely r-process origin at these metallicities, then the increase in [Sr/Ba] ratio cannot be completely explained by the r-process alone. An additional mechanism, perhaps the LEPP, might be operating at metallicities [Fe/H] < -3.0.

5.6.2 Low α-element stars at [Fe/H] < -3.0

In spite of having similar elemental abundances compared with the mean abundances of EMP stars, SDSS J1343+4844 belongs to a rare class of carbon-normal EMP stars that exhibit low α-element abundances.

Different burning stages in the intermediate mass to massive stars produce α elements and they are ejected to ISM mainly due to SNe II explosions. Majority of EMP samples in the halo as well as dwarf galaxies share a common pattern for these α elements. Nevertheless, there have been studies which reported EMP α-poor population in the halo and the nearby dSphs. Such stars, though they are very few among the co existing stars, clearly points towards a different astrophysical sites and inefficient mixing mechanism. The schematic diagram 5.11 clearly specifies that SDSS J1343+4844 is a peculiar rare one which shows a different formation history compared to the normal population.

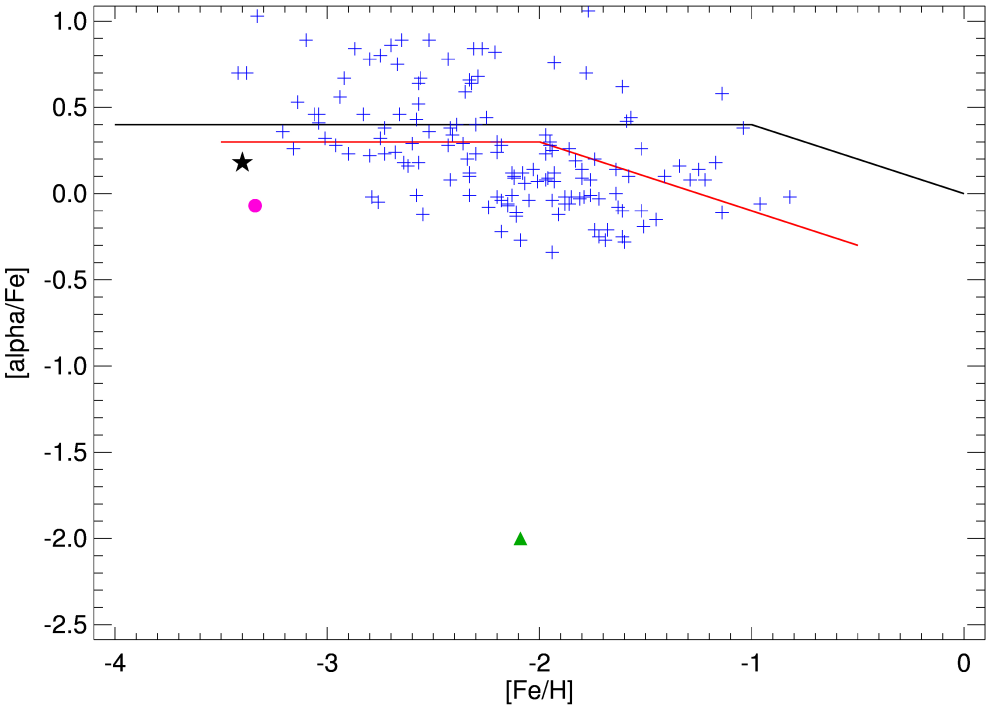

Figure 5.11: α-elemental abundance for SDSS J1343+4844(black star), compared with samples available from Ivans et al. (2003) (green filled triangle),Vargas et al. (2013) (the blue crosses),Caffau et al. (2013) (magenta filled circle). The black line is the schematic representation of the mean α abundance of the milkyway halo, thick disk and thin disk. The red line is the schematic representation of mean α abundance of the dwarf spheroidal galaxy.

Low α-element abundances might indicate a low star-formation rate, similar to that found for many dwarf spheroidal galaxies. If this star belongs to the rare population which represent low star forming inhomogeniously mixed systems, then SDSS J1343+4844 could be younger than other EMP stars, which are α-element enhanced at the same metallicity. The similarity of carbon and n-capture elements with other EMP stars, in spite of the low α-element abundance, might indicate that the objects that contributed to the enrichment of the mean ISM carbon and strontium at metallicities below [Fe/H] < -3.0 are universal; these progenitors could be among the first Pop III stars. Vangioni (2012) explores the possibility of intermediate-mass Pop III stars as a source of C and N enrichment. These intermediate-mass stars can also produce weak s-process elements through operation of the ^{22}Ne(α,n)^{25}Mg neutron source, due to the thermal pulses occurring at hotter temperature (Gallino et al., 2000). Gallino et al. (2000) found that this reaction could form enough Sr-Y-Zr, however it does do not produce much Ba, which is the expected trend for [Sr/Ba] in EMP stars.

5.6.3 Lithium depletion and binarity

The lithium line at 6707 Å is not detected in SDSS J1343+4844. The derived upper limit agrees with the declining lithium abundance trend seen below metallicities [Fe/H] < -3.0 (Sbordone et al., 2010b). There are two possibilities for the depletion of lithium: binary mass transfer and binary-induced mixing, or mixing due to the evolutionary status of the object as a subgiant. Detection of a radial-velocity variation with no peculiar chemical composition support the idea of binary-induced mixing. Most short-period binaries were found to have preserved lithium, possibly due to tidal locking. However long-period binaries with periods of few hundred

days seem to have depleted lithium abundances (Ryan and Deliyannis, 1995), which could be the case for SDSS J1343+4844.

5.6.4 Conclusions

LTE abundances for SDSS J1343+4844, a bright EMP star identified during the MARVELS pre-survey has been derived. The abundance pattern for most elements in this star are similar to other carbon-normal EMP stars, except for the low α-element abundance and the apparent depletion of lithium. The depletion of lithium could be understood in terms of binary-induced mixing or additional convection, as the object is a subgiant. Low α-element abundance, along with the agreement of the observed ratios of the carbon abundances and heavy elements with the mean EMP value is not so easy to understand. Though I propose the star could be formed a different system where the star formation rate is low and the medium remained unmixed until the onset of SNe Ia, and migrated to our galaxy through merging scenario, more samples are needed to further constrain the argument and need better models for a detailed explanation to the physical processes existed in the early universe. Also Contributions from Pop III intermediate-mass stars, along with later Pop II contributions with a low star-formation rate (similar to dwarf spheroidal galaxies), may explain the abundance patterns seen in SDSS J1343+4844.

Appendix

Table 5.6: Atomic data and derived abundances for SDSS J1343+4844. Errors due to δ T, δ log g and $\delta\xi$ are added in quadrature

Element	λ	χ	log(gf)	Equivalent width	A(x)	abund δ T	abund δ log g	abund $\delta\xi$	σ
	()	(eV)		(m)		$\pm$ (250 K)	$\pm$ (0.5)	$\pm$0.2 km/s	$\pm$
Na I	5889.951	0.000	0.112	52.80	2.65	-0.200	0.024	0.019	0.202
Na I	5895.924	0.000	-0.191	33.70	2.62	-0.193	0.010	0.009	0.193
Mg I	3829.355	2.710	-0.207	89.30	4.31	-0.213	0.113	0.057	0.248
*Mg I	3832.304	2.710	0.146	126.20	4.55	-0.271	0.217	0.048	0.350
*Mg I	3838.290	2.710	0.415	151.00	4.53	-0.281	0.235	0.033	0.368
Mg I	5172.684	2.710	-0.380	90.10	4.29	-0.229	0.117	0.047	0.261
Mg I	5183.604	2.720	-0.158	106.10	4.33	-0.254	0.164	0.051	0.307
Al I	3944.006	0.000	-0.640	48.20	2.61	-0.221	0.017	0.021	0.223
Al I	3961.520	0.010	-0.340	72.00	2.75	-0.236	0.062	0.047	0.248
Si I	3905.523	1.910	-1.090	92.10	4.49	-0.259	0.104	0.070	0.288
Ca I	4226.728	0.000	0.240	104.70	3.19	-0.310	0.181	0.086	0.369
Ca I	4302.528	1.900	0.183	18.20	3.27	-0.154	0.000	0.007	0.154
Ca I	4434.957	1.890	0.066	14.40	3.24	-0.155	-0.003	0.005	0.155
*Ca I	4454.779	1.900	0.260	13.30	3.02	-0.154	-0.004	0.004	0.154
*Ca I	6162.173	1.900	-0.090	13.90	3.31	-0.161	0.007	0.005	0.161
Sc II	4246.822	0.310	0.240	40.00	-0.01	-0.154	-0.158	0.025	0.222
Ti II	3757.688	1.570	-0.460	33.90	2.33	-0.096	-0.164	0.021	0.191
Ti II	3759.296	0.610	0.270	105.10	2.28	-0.224	0.036	0.093	0.245
Ti II	3761.323	0.570	0.170	75.00	1.66	-0.167	-0.075	0.109	0.213
Ti II	3913.468	1.120	-0.410	46.70	2.06	-0.119	-0.153	0.038	0.198
Ti II	4290.219	1.160	-0.930	14.10	1.79	-0.114	-0.169	0.006	0.204
Ti II	4300.049	1.180	-0.490	21.40	1.60	-0.114	-0.167	0.010	0.202
Ti II	4395.033	1.080	-0.510	36.80	1.86	-0.121	-0.160	0.022	0.202

Table 5.6 – continued from previous page

Element	λ	χ	log(gf)	Equivalent width	A(x)	abund δ T	abund δ log g	abund $\delta\xi$	σ
		(eV)		m	dex	$\pm$ 250 K	$\pm$ 0.5	$\pm$ 0.2 km/s	$\pm$
Ti II	4443.794	1.080	-0.700	20.00	1.65	-0.119	-0.168	0.009	0.206
Ti II	4468.507	1.130	-0.600	33.40	1.92	-0.119	-0.162	0.018	0.202
Ti II	4501.273	1.120	-0.760	32.90	2.05	-0.120	-0.162	0.018	0.202
Ti II	4533.969	1.240	-0.540	27.80	1.84	-0.114	-0.165	0.014	0.201
Ti II	4549.617	1.580	-0.220	32.80	1.99	-0.100	-0.162	0.018	0.191
Cr I	4254.332	0.000	-0.110	52.30	2.29	-0.273	0.024	0.054	0.279
Cr I	4274.796	0.000	-0.230	49.20	2.34	-0.271	0.019	0.046	0.276
*Cr I	4289.716	0.000	-0.360	17.40	1.72	-0.264	0.000	0.008	0.264
Mn I	4030.753	0.000	-0.480	37.30	1.71	-0.287	0.004	0.028	0.288
Mn I	4033.062	0.000	-0.620	39.30	1.90	-0.287	0.005	0.032	0.289
Fe I	3719.935	0.000	-0.431	113.30	3.94	-0.416	0.244	0.096	0.492
Fe I	3748.262	0.110	-1.016	92.30	4.20	-0.372	0.176	0.140	0.435
Fe I	3758.233	0.960	-0.030	122.90	4.53	-0.374	0.242	0.069	0.451
Fe I	3763.789	0.990	-0.240	84.30	4.05	-0.315	0.137	0.129	0.367
Fe I	3767.192	1.010	-0.390	78.20	4.06	-0.300	0.110	0.128	0.344
Fe I	3787.880	1.010	-0.860	49.20	3.72	-0.264	0.013	0.054	0.270
Fe I	3795.002	0.990	-0.761	79.00	4.42	-0.303	0.112	0.128	0.347
Fe I	3812.965	0.960	-1.047	66.90	4.33	-0.284	0.065	0.109	0.311
Fe I	3815.840	1.480	0.240	103.60	4.42	-0.334	0.206	0.093	0.403
Fe I	3820.425	0.860	0.120	122.50	4.25	-0.372	0.231	0.070	0.443
Fe I	3825.881	0.910	-0.040	93.60	3.97	-0.334	0.167	0.120	0.392
Fe I	3840.438	0.990	-0.510	82.40	4.24	-0.309	0.123	0.127	0.356
Fe I	3841.048	1.610	-0.045	74.10	4.15	-0.273	0.099	0.112	0.311
Fe I	3849.967	1.010	-0.970	69.40	4.36	-0.284	0.067	0.111	0.312
Fe I	3856.372	0.050	-1.290	86.20	4.22	-0.357	0.142	0.148	0.412
Fe I	3859.911	0.000	-0.710	111.70	4.15	-0.414	0.236	0.103	0.488

Table 5.6 – continued from previous page

Element	λ	χ	log(gf)	Equivalent width	A(x)	abund δ T	abund δ log g	abund $\delta\xi$	σ
		(eV)		m	dex	$\pm$ 250 K	$\pm$ 0.5	$\pm$ 0.2 km/s	$\pm$
Fe I	3865.523	1.010	-0.980	64.40	4.22	-0.277	0.049	0.098	0.298
Fe I	3872.501	0.990	-0.928	77.60	4.52	-0.299	0.102	0.126	0.340
Fe I	3886.282	0.050	-1.080	95.00	4.22	-0.379	0.181	0.139	0.442
Fe I	3887.048	0.910	-1.144	44.40	3.77	-0.267	0.005	0.042	0.270
Fe I	3895.656	0.110	-1.670	88.40	4.70	-0.361	0.152	0.146	0.418
Fe I	3899.707	0.090	-1.530	83.10	4.39	-0.348	0.125	0.147	0.398
Fe I	3906.480	0.110	-2.243	69.90	4.73	-0.320	0.064	0.124	0.349
Fe I	3917.181	0.990	-2.155	36.40	4.68	-0.262	-0.001	0.028	0.263
Fe I	3920.258	0.120	-1.750	63.90	4.06	-0.312	0.042	0.104	0.332
Fe I	3922.912	0.050	-1.650	79.60	4.36	-0.341	0.106	0.144	0.385
Fe I	3927.920	0.110	-1.522	69.70	3.40	-0.319	0.063	0.123	0.348
Fe I	3930.297	0.090	-1.491	101.40	4.80	-0.393	0.204	0.126	0.460
Fe I	3997.392	2.730	-0.400	15.10	4.13	-0.186	-0.013	0.008	0.187
Fe I	4005.242	1.560	-0.610	55.00	4.13	-0.248	0.028	0.065	0.258
Fe I	4045.812	1.480	0.280	93.70	4.14	-0.320	0.173	0.114	0.381
Fe I	4063.594	1.560	0.070	91.50	4.37	-0.313	0.166	0.115	0.372
Fe I	4071.738	1.610	-0.020	51.00	3.49	-0.244	0.019	0.054	0.251
Fe I	4132.058	1.610	-0.670	58.10	4.30	-0.251	0.035	0.072	0.263
Fe I	4143.415	3.050	-0.204	15.70	4.26	-0.175	-0.011	0.007	0.175
Fe I	4143.868	1.560	-0.460	64.60	4.20	-0.260	0.054	0.090	0.280
Fe I	4187.039	2.450	-0.550	20.60	4.15	-0.202	-0.003	0.010	0.202
Fe I	4187.795	2.420	-0.550	23.40	4.19	-0.204	-0.001	0.012	0.204
Fe I	4198.304	2.400	-0.719	23.00	4.33	-0.204	-0.001	0.012	0.204
Fe I	4202.029	1.480	-0.700	48.40	3.96	-0.248	0.014	0.048	0.253
Fe I	4227.427	3.330	0.230	26.60	4.41	-0.167	-0.002	0.014	0.168
Fe I	4250.119	2.470	-0.400	29.00	4.22	-0.204	0.005	0.016	0.205

Table 5.6 – continued from previous page

Element	λ	χ	log(gf)	Equivalent width	A(x)	abund δ T	abund δ log g	abund $\delta\xi$	σ
		(eV)		m	dex	$\pm$ 250 K	$\pm$ 0.5	$\pm$ 0.2 km/s	$\pm$
Fe I	4250.787	1.560	-0.714	51.60	4.12	-0.248	0.020	0.055	0.255
Fe I	4260.474	2.400	-0.020	47.00	4.15	-0.218	0.033	0.037	0.224
Fe I	4271.761	1.480	-0.160	72.60	4.01	-0.277	0.082	0.108	0.308
Fe I	4282.403	2.170	-0.820	30.20	4.38	-0.213	-0.007	0.020	0.214
Fe I	4325.762	1.610	-0.010	62.40	3.72	-0.257	0.047	0.082	0.274
Fe I	4375.930	0.000	-3.030	25.50	4.22	-0.305	-0.002	0.015	0.305
Fe I	4383.545	1.480	0.200	87.50	4.01	-0.307	0.144	0.121	0.360
Fe I	4404.750	1.560	-0.140	68.20	3.93	-0.268	0.065	0.096	0.292
Fe I	4415.123	1.610	-0.610	44.20	3.88	-0.244	0.009	0.037	0.247
Fe I	4427.310	0.050	-2.924	31.90	4.31	-0.304	0.000	0.022	0.305
Fe I	4528.614	2.180	-0.820	21.60	4.14	-0.214	-0.004	0.011	0.214
Fe I	4890.755	2.880	-0.394	18.70	4.32	-0.188	-0.002	0.008	0.188
Fe I	4891.492	2.850	-0.110	21.70	4.09	-0.190	0.001	0.010	0.190
Fe I	4920.503	2.830	0.070	34.90	4.19	-0.197	0.016	0.020	0.199
Fe I	5171.596	1.490	-1.793	19.50	4.30	-0.246	-0.002	0.010	0.246
Fe I	5227.190	1.560	-1.228	31.40	4.10	-0.246	0.004	0.020	0.247
Fe I	5269.537	0.860	-1.320	60.80	4.12	-0.293	0.040	0.074	0.305
Fe I	5270.356	1.610	-1.339	30.00	4.23	-0.244	0.003	0.018	0.245
Fe I	5328.039	0.920	-1.470	53.90	4.16	-0.284	0.027	0.057	0.291
Fe I	5328.532	1.560	-1.850	19.70	4.43	-0.243	-0.001	0.010	0.243
Fe I	5371.490	0.960	-1.650	47.70	4.25	-0.278	0.018	0.043	0.282
Fe I	5397.128	0.920	-1.990	34.20	4.26	-0.274	0.005	0.023	0.275
Fe I	5405.775	0.990	-1.840	38.20	4.26	-0.272	0.008	0.028	0.274
Fe I	5429.697	0.960	-1.880	37.90	4.27	-0.274	0.008	0.027	0.275
Fe I	5434.524	1.010	-2.120	27.20	4.32	-0.268	0.002	0.016	0.268
Fe I	5446.917	0.990	-1.910	31.50	4.19	-0.270	0.004	0.020	0.271

Table 5.6 – continued from previous page

Element	λ	χ	log(gf)	Equivalent width	A(x)	abund δ T	abund δ log g	abund $\delta\xi$	σ
		(eV)		m	dex	$\pm$ 250 K	$\pm$ 0.5	$\pm$ 0.2 km/s	$\pm$
Fe II	4233.172	2.580	-1.900	21.50	4.36	-0.049	-0.181	0.012	0.188
Fe II	4923.927	2.890	-1.320	23.50	4.10	-0.040	-0.177	0.013	0.182
Fe II	5018.440	2.890	-1.220	39.20	4.35	-0.045	-0.171	0.029	0.179
Fe II	5169.033	2.890	-1.303	45.50	4.56	-0.048	-0.165	0.038	0.176
Ni I	3783.524	0.420	-1.310	41.70	3.09	-0.273	-0.007	0.041	0.276
*Ni I	3807.138	0.420	-1.180	54.00	3.25	-0.280	0.014	0.072	0.289
Ni I	3858.292	0.420	-0.970	55.80	3.08	-0.281	0.018	0.077	0.292
Sr II	4077.709	0.000	0.167	56.60	-0.76	-0.178	-0.127	0.099	0.240
Sr II	4215.519	0.000	-0.145	33.70	-1.05	-0.165	-0.160	0.030	0.232

* Refers to those lines which are not used for calculating the mean abundance of the respective elements.

Chapter 6

HESP-TIRSPEC synergy

6.1 Introduction

Spectroscopic studies of metal poor stars identified from large surveys like Hamburg/ESO survey and HK survey brought out the fact that a significant fraction of Galactic halo stars with [Fe/H] $<$ -2.0 exhibit strong enhancement in carbon with [C/Fe] $>$+1.0. The fraction of so called carbon enhanced metal poor [CEMP] stars increases with decreasing metallicity. These CEMP stars also show peculiar elemental abundance pattern along with the strong over abundance in Carbon. Based on the over abundance of neutron capture elements, CEMP stars are broadly classified into two category, one shows over abundance of neutron capture elements (CEMP-s,CEMP-r, CEMP-r/s) and other does not show any enhancement in neutron capture elements (CEMP-no).

Various mechanisms have been proposed to explain the high carbon abundance in these CEMP subclasses. Carbon in CEMP-s stars are likely to be produced from

the AGB companion and transferred the carbon rich material to the presently observed star. Whereas origin of carbon in other CEMP classes are not fully understood. Various theories suggest that the massive, rapidly rotating, zero metallicity progenitor stars which produce large amount of C,N,O due to internal nuclear burning and mixing episodes, might have experienced significant mass loss of this CNO enhanced material via strong winds. Another explanation is the association of faint supernovae with the first generation of stars, which experience extensive mixing and fallback during their explosions and eject huge amount of C,N and O to the ISM. The low $^{12}C/^{13}C$ ratio of CEMP-no stars is an indicator of the significant mixing during the nuclear burning process in their progenitors.

In order to fully understand the connection of CEMP stars with their progenitors and the nature of s- process in AGB stars we require measurements of important elements like C, N and O for a large sample of CEMP stars. Carbon and nitrogen abundance can be determined from medium resolution optical spectra of CEMP stars using the CH, C_2 and CN features, while O requires high resolution spectroscopy. Use of the O I λ7774 triplet lines which are strongly affected by NLTE effects. The only reliable abundance measurements come from the forbidden [O I] line at λ6300, which is very weak at lower metallicities and it requires several hours of exposures even with 8 m class telescopes to detect the feature. The near-infrared first-overtone ro-vibrational bands of CO at 2.3 μm give the best alternate for this problem because of their visibility even at lower resolution. The carbon abundance in CEMP stars exceeds the O abundance. So essentially all the oxygen would be locked up in CO molecules and these lines will provide a sensitive probe for the oxygen abundance in CEMP stars.

The isotope ratio $^{12}C/^{13}C$ is usually derived from the optical spectra using the $^{12}C_2$ band head at 4736 Å and the $^{12}C^{13}C$ band head at 4745Å . But in cool stars the $^{12}C_2$

band head at 4736 Å is saturated and leads to a large derived $^{12}C/^{13}C$ ratio. This problem can be resolved by looking at the CO features at 2.3 μm where the ^{13}CO lines are largely separated from the ^{12}CO lines. So it provides an accurate and better estimates of the mixing diagnostic $^{12}C/^{13}C$ ratio than deriving it from the optical spectra.

High frequency of CEMP stars at low metallicity indicates the presence of large amount of carbon at early evolutionary stages of the Galaxy. This early carbon production can have a significant influence on the chemical evolution of the galaxy and the universe. This indicates that IMF in the early universe included fairly large number of intermediate to high mass stars than the present day universe. In order to draw conclusions about the IMF and to constrain the models of the progenitors and various nucleosynthetic mechanisms existed at early times, observations of large number of CEMP stars are needed.

In this chapter, the observations of a few CEMP stars are reported. In order for the study to complete, a large set of CEMP stars are required which would be beyond the thesis time. So this chapter has been restricted for a few objects. The primary motivation is to validate the oxygen abundances derived from NIR spectra with that of [OI]6300 line in optical. The chapter is organized as follows: In section 2, sample selection and observation have been mentioned. Section 3 describes about stellar parameters and abundance analysis. In section 4, the results are briefed with individual stars and in section 6, the mechanisms contributing for the abundance have been discussed and the chapter is concluded by section 7.

star	Vmag	Kmag	RA	DEC	RV(kms^{-1})
HD 5223	8.47	5.57	00 54 13.60922	+24 04 01.5142	-214
HE 0314-0143	11.63	8.00	03 17 22.178	-01 32 36.51	-300
HE 0017+0055	11.66	8.5	00 20 21.608	+01 12 06.83	- 320
HE 1152-0355	11.43	8.43	11 55 06.057	-04 12 24.71	-387

6.2 Sample selection, observation and data reduction

Since the original intention of this study is to measure the CNO abundance, and compare the oxygen abundance from CO features in the near infra red regime and oxygen from [OI] at 6300 Å when available, The requirements of the sample selection include high carbon abundance, low effective temperature ($T_{eff} < 5000K$) and samples which are bright in V and K magnitude. It is because the first overtone vibration rotation band of CO forms at a cooler temperature at 2.29 μm - 2.5 μm. In such a cooler temperature, when C/O > 1, all the oxygen will be locked up as CO than forming ZrO, TiO and VO etc. So the samples were chosen from literature where the carbon has been previously measured which has low effective temperature. The forbidden line [OI] at 6300 Å requires longer exposures for a good detection of the line, so samples included in the study are brighter than K_s= 10 and V= 13.00 in order to ensure sufficient SNR to detect the CO features in NIR and the forbidden oxygen line [OI] at 6300 Å line.

The targets were observed using the near infrared spectrograph TIRSPEC to capture the CO band at 2.3 μm and using HESP for the optical observations.

The NIR spectra has been taken in the cross dispersed mode using short slit S3 (width is 1.97") to match with the seeing. The spectra in the H and K windows have been simultaneously achieved covering a wavelength of 1.50 - 1.84 & 1.95

- 2.45 μm at a resolution R= 1200. Dithering along the slit has been performed to for accurate background subtraction, avoid bad pixel affecting the spectra also to reduce any systematic noise. A0 type stars at the same air mass were also observed along with the targets to correct the telluric lines in the spectra. In order to avoid the counts reaching the non linearity regime of the detector, the observations were done as multiple exposures of 500sec which gave an SNR of 30. The NIR data reduction has been performed using semi automated pipeline developed by Ninan et al 2014 in which the bias correction, flat fielding, background subtraction, spectrum extraction, wavelength calibration, telluric line correction and continuum fitting were performed using codes in python which made use of standard modules like astropy, numpy, matplotlib and PyRAF[1].

The optical observations of the objects were taken during the test run period of the instrument in the low resolution mode (R=30000). The objects were observed for multiple frames of 45 minute exposure frames depending on the brightness. The object were observed in star-sky mode of the which enabled the sky to be subtracted from the object fibre. ThAr spectrum was taken along with each object spectra for the wavelength calibration. The spectra reduction included, trimming, bias subtraction, aperture extraction and wavelength calibration. Theses steps were performed using PyRAF. Each frames were then normalized and coadded. The final spectrum covers a wavelength from 3800-10500 Å .

[1]PyRAF is a product of the Space Telescope Science Institute, which is operated by AURA for NASA

6.3 Stellar parameters

All the samples except HE 0017+0055 have optical high resolution observations along with the NIR spectrum. So the stellar parameters are derived using conventional methods. The spectrum of all the objects are dominated by molecular features because of high carbon abundance and low effective temperature. This hinders getting clean lines of Fe for estimating the stellar parameters. So a full spectrum synthesis was performed to understand the degree of dominance of the molecular features on the atomic lines. So the abundance analysis and deriving the stellar parameters were performed using spectral synthesis method.

The effective temperature is calculated by fitting the H_α and H_β profiles and from the V-K color using the Alonso relations (Alonso et al., 1996, 1999). The log g is derived by fitting the wings of Mg I triplet around 5172 Å for various values of log g with a step size of 0.25 dex and the best fit value is found by goodness of the fit and chosen as the final log g.The metallicity is also derived using the same method by fitting the iron features in the spectra region where the molecular features have less influence on the continuum. Finally, a Microturbulent velocity (ξ) of 2.2 kms^{-1} has been adopted as a representative value for cool CEMP stars (Hansen et al., 2016b). The stellar parameters are listed in the table 6.1

star name	teff	logg	metallicity	micro vel
HD 5223	4500	1.0	-2.1	2.2
HE 0314-0143	4200	0.22	-1.3	2.2
HE 1152-0355	3900	0.1	-2.1	2.2
HE 0017+0055	4250	1.0	-2.4	2.2

Table 6.1: Stellar parameters for the samples used in this study.

6.4 Results

6.4.1 HD 5223

This star is CEMP star with high carbon abundance. Various studies have reported the high resolution abundance analysis as well as radial velocity follow up to understand the nature of the origin of carbon enhancement and other s-process enhancement (Goswami et al., 2006, Lucatello et al., 2011). But no studies have reported the nitrogen and oxygen abundance from optical observations. Lucatello et al. (2011) reported the N and O abundance from the NIR spectrum. So high resolution spectrum of the sample has been taken and performed an independent abundance analysis in order to derive the N and O abundance from optical spectrum and compare them with the NIR and literature values. The stellar parameters and the carbon abundance are converging to the literature values (Goswami et al., 2006) whereas the nitrogen abundance derived from the optical (this study) and NIR (Lucatello et al., 2011) has a difference of 0.4 dex. The oxygen abundance derived from CO lines in this study as well as Lucatello et al. (2011) are matching within a difference of 0.27 which is falling with in the error quoted. Goswami et al. (2006) also reported a high Ba and other s-process elements enhanced. The Ba line in the spectrum has

been fitted to derive the Ba abundance and the value found to be [Ba/Fe]=1.8 The fitted CO feature whose plot is shown in the figure 6.4

6.4.2 HE 1152-0355

Similar to HD 5223, this star is also found to have no oxygen and nitrogen abundance reported from optical studies. Lucatello et al. (2011) derived the nitrogen and oxygen abundance from NIR spectrum of the sample using the literature stellar parameters and carbon abundance. The Ba lines were fitted to derive the abundance and the value obtained to be [Ba/Fe]=1.4. In this study, the stellar parameters and carbon abundance have independently derived using the high resolution spectrum and found to have a deviation from the values from the literature especially for the log g and metallicity. In order to see the goodness of the fit, spectrum has been synthesized for the model parameters in the literature and fitted with the observed spectrum which is shown in the figure 6.1 The estimated stellar parameters and the abundance of key elements are given in the tables 6.2 and the best fit for CO and [OI] lines are shown in the figure 6.5.

6.4.3 HE 0314-0143

Kennedy et al. (2011) have reported the NIR oxygen abundance of this star. No high resolution observation is available for this object till date. So this star has been observed and derived the carbon abundance and atmospheric parameters. The star also found to show enhancement in s-process elements. The abundance of barium is derived using spectral fitting method and found to be [Ba/Fe]= 0.7. The forbidden [OI] lines are not visible in the optical spectra, so the oxygen abundance from the optical was derived from the oxygen triplet at 7771 Å . These lines are largely

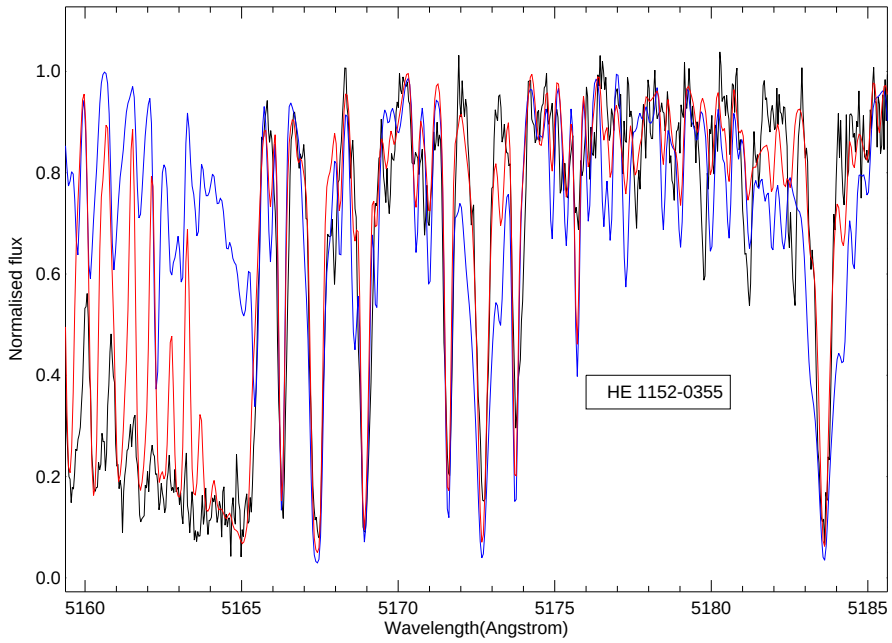

Figure 6.1: The spectrum of HE 1152-0355 has been fitted near the Mg I triplet at 5172 ÅṪhe blue fit is obtained from the model parameters opted from literature values whereas the red fit is obtained from the model parameter derived from this study. Mg I triplet is found to be fitting for the log g derived from this study.

affected by NLTE effects. The oxygen abundance was also measured from the NIR CO lines, given in the table 6.2. The abundance derived by Kennedy et al. (2011) from NIR CO lines differs from this study still the value found to be lying within the error quoted by those authors. T The best fit is shown here.

6.4.4 HE 0017+0055

High resolution analysis as well as long term radial velocity monitoring of the object has been reported by (Jorissen et al., 2016) and found that the star has high carbon abundance ([C/Fe] = +2.16) and radial velocity variation of 384 days. The nitrogen abundance also has been measured ([N/Fe] = +2.46). The oxygen abundance reported in Jorissen et al. (2016) is from figure 18 of Masseron et al. (2010) and overall fit of the observed spectrum. Kennedy et al. (2011) also reported the oxygen abundance of the sample from NIR CO bands. But stellar parameters reported by Kennedy et al. (2011) is from low resolution optical spectrum of the sample. Though a deviation has been observed in the literature abundances as well as stellar parameters, the sample could not be independently observed using HESP because of the low airmass , shorter availability and the turbulent sky conditions. Since there is a significant difference in the stellar parameters reported by (Jorissen et al., 2016) and Kennedy et al. (2011), the stellar parameters and carbon abundance from (Jorissen et al., 2016) have been adopted where the reported values are from high resolution estimates. So the difference in oxygen abundance reported from NIR studies for this object cannot be compared. But it is observed that deviation in the oxygen abundance from optical as well as NIR samples have been identified which is given in the table 6.2. In order to understand this difference, the observation in the optical regime is required.

Table 6.2: The carbon nitrogen and oxygen abundance of the sample. For the object HE 0017+0055, the subscript lit is mentioned which denote the literature value.

star name	[C/Fe]	[N/Fe]	[O/Fe]$_{NIR}$	[O/Fe]$_{optical}$	^{12}C/^{13}C	[Ba/Fe]
HD5223	+1.7	1.1	0.34	0.54	9.0	1.8
HE 0314-0143	0.9	0.8	0.3	0.6	6.7	0.7
HE 1152-0355	1.0	0.6	0.4	0.4	5.6	1.4
HE 0017+0055	2.08$_{lit}$	2.33$_{lit}$	0.0	+0.8$_{lit}$	4	–

6.5 Discussion

The CNO abundances of 4 CEMP stars are measured from optical spectra and the value of oxygen abundance is compared with that from NIR CO lines. It can be seen that the derived oxygen abundance from optical and NIR studies are matching within an error of 0.3 dex which is reasonable when the resolution of the NIR spectra is considered. For the case of HE 0314-0143, the oxygen abundance could not be measured from from 6300 Å and 6363 Å due to non-detection of the lines. So the triplet around 7771 Å though they are affected by NLTE effects, is used to derive the oxygen abundance in the optical regime. The match between oxygen abundance derived from optical and NIR is shown in the figure 6.2. These stars also show enhancement in both heavy and light s-process elements. The radial velocity when compared with the literature values, show variations. The enhancement in s-process elements and radial velocity variation favors the concept of the presence of a binary companion which was an AGB star and transferred its carbon and s-process rich material to the surface of the star through mass transfer mechanisms. A close examination of the abundance of C,N and O, one can see that the abundance of these

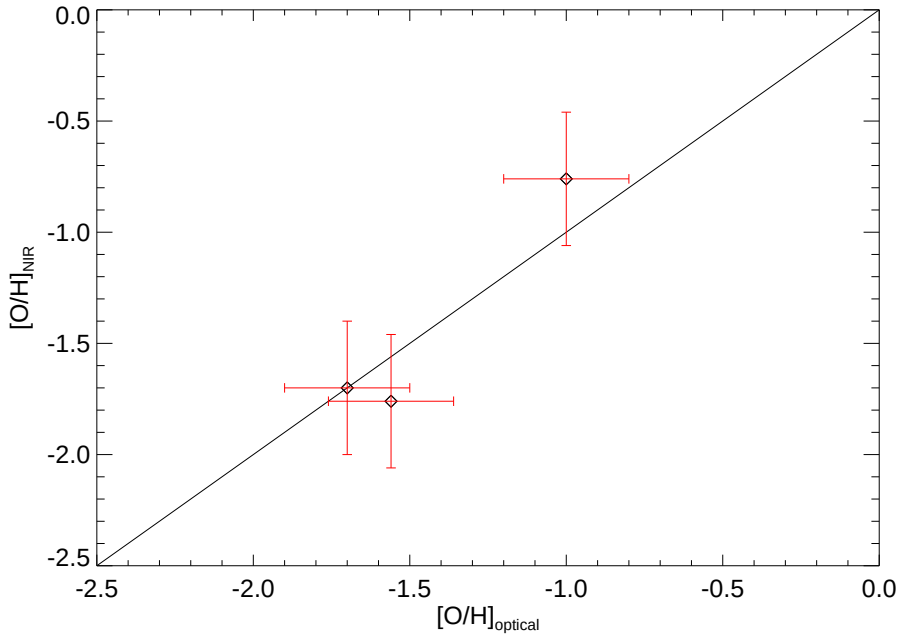

Figure 6.2: The oxygen abundance derived from optical [OI] lines and NIR CO lines are compared. In this plot, the oxygen abundance of HE 0017+0055 has been omitted because only oxygen abundance measured is from the NIR CO band. The star could not be observed in high resolution and the available value in literature is from theoretical consideration, the details for which is given in the text.

elements, increases with decrease in metallicity. Also the abundance pattern of these elements, when compared with the pattern produced by models of AGB stars, shows resemblance with that of the low mass AGB stars than higher mass AGBs (refer figure 6.3). Though the carbon and oxygen abundance are found to be following the same trend suggested by the models, there is a disagreement in the nitrogen abundance from the observed value and the value predicted from the theoretical models. A similar discrepancy is found in the $^{12}C/^{13}C$ values. According to low mass AGB models, the $^{12}C/^{13}C$ should be very high (Fishlock et al., 2014) that all ^{12}C observed in the CEMP star is considered to be the resultant of mass transfer scenario. It means that very few ^{13}C is transferred with respect to ^{12}C. At the same time, more massive models ($M>3M_{\odot}$) produce low carbon isotopic ratio through Hot Bottom Burning (HBB), a process happens at the bottom of the convective envelope which convert the carbon to nitrogen when the temperature is sufficient for the CN cycle. The values thus obtained is similar to the values observed in CEMP stars. However, such massive companion stars also produce high nitrogen abundance resulting in [C/N]<0 which is not found in any of the stars studied here. This makes HBB an unlikely contributor for the observed low carbon isotopic ratios.

The models, which produced high carbon isotopic ratios, did not consider any abundance of carbon and ^{13}C isotope on the surface of the accreting star. All the samples in this study are giants and they undergo several mixing episodes during first dredge-up, extra mixing for the RGB bump etc. This changes the surface composition of the carbon and carbon isotopes. So it is reasonable to assume that the accreted material get affected by the mixing episodes in the presently observed star and might resulted in the observed intermediate nitrogen enhancement (still [C/N]>0.1) as well as the low isotopic ratio (Denissenkov and Pinsonneault, 2008). The lower panel of figure 6 in Lucatello et al. (2011) shows the model fitted to the observed $^{12}C/^{13}C$ when

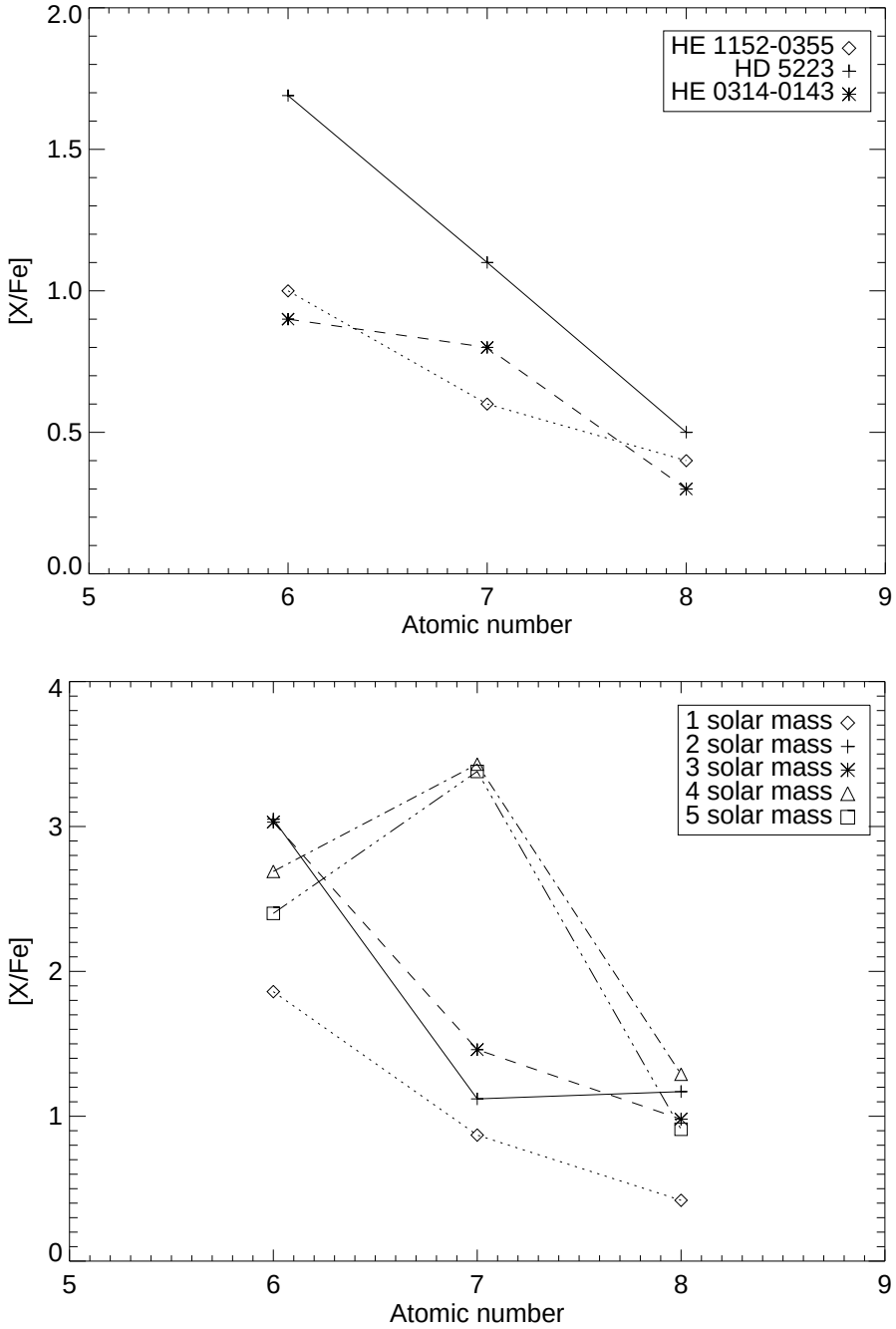

Figure 6.3: The CNO abundance of the sample stars. The lower figure is the abundance pattern observed in the standard AGB models with different masses (Lugaro et al., 2012). It can be seen that the abundance pattern of the observed stars matches with that of low mass AGB stars ($M \leqslant 3M_{\odot}$)

they consider the original isotopic ratio and carbon abundance in the observed star. The concept of Cool Bottom Processing (CBP) can also be invoked to explain the moderately high nitrogen abundance and low ^{12}C/^{13}C. In CBP, the material from the base of the convective envelope is circulated into the radiative region located on top of the H-burning shell where the material captures protons and then brings back to the envelope thereby leaving CN processed materials at the surface of the star (Wasserburg et al., 1995). This process is found to occur in the RGB phase of stars having M $\leqslant 2.5M_{\odot}$ (Charbonnel, 1995) and in AGB stars where an extra mixing happens at the bottom of the AGB envelope, and a part of the envelope material turns carbon into nitrogen through CN cycle (Nollett et al., 2003). Though the physical mechanism causing the CBP is unclear, many hypothesis have been put forward to explain this mixing phenomena, which include the instabilities generated due to the molecular weight inversion induced by ^{3}He burning (Eggleton et al., 2008) and the magnetic buoyancy induced by a stellar dynamo (Busso et al., 2007, Palmerini et al., 2008). Nitrogen as well as ^{13}C are products of CN cycle. A complete CN cycle produces ^{12}C/^{13}C ≈ 4 and [C/N] ≈ -1.3. Thus the observed low ^{12}C/^{13}C and [C/N] value can be obtained when the carbon is partially processed possibly in the H-burning shell before reaching the convective envelope. This supports the concept of CBP contributing for the moderately high nitrogen abundance and low carbon isotopic ratio observed in CEMP-s stars.

Oxygen is another important element to constrain the nature of AGB companion. Low metallicity AGB stars are expected to produce an elevated oxygen abundance from ^{12}C(α, γ)^{16}O reaction activated due to the hotter conditions in the helium burning shell. But the oxygen yields predicted by different models do not agree with each other. Herwig (2004) finds that the oxygen abundance decreases with mass of the

AGB star due to the dilution in the AGB envelope. Though the dredge up matter brings more oxygen to the surface the dilution dominates the dredge up when the mass increases. Karakas and Lattanzio (2007) found a contradicting scenario. According to Karakas and Lattanzio (2007) as the mass increases, the dilution is dominated by the hotter conditions for the $^{12}C(\alpha, \gamma)^{16}O$ and around $3M_{\odot}$ maximum oxygen abundance is predicted. All the models assume a solar scaled abundance for the key elements to start with. The amount of the elements produced during AGB evolution is high that the initial assumptions do not affect the final composition. In contrary, the oxygen is produced in the scale of [O/Fe]$\sim$0.5 in metal poor stars (Lucatello et al., 2011) which is greatly influenced by the initial composition.

Another scenario which can account for observed CNO abundance, especially the low carbon isotopic ratio and moderately high nitrogen abundance, is the Proton Ingestion Episodes (PIE). At the beginning of the thermally pulsating phase of low mass metal poor models, the convective envelope extends up to the base of the the H-rich envelope and the protons get mixed to in the convective shell and captured by ^{12}C and produces ^{13}C and ^{14}N through various reactions which results in a deep-Third Dredge Up. After the deep TDU, the model follows the standard evolution. Each thermal pulses bring the synthesized material to the surface of the stellar envelope resulting in constantly varying the surface composition. The observed low ^{12}C /^{13}C is also produced in the PIE. The final abundance pattern at each TDU phases resemble to the CNO abundance pattern exhibited by the stars in this study (refer figure 6 in Cristallo et al. (2009) Regardless of the abundance pattern exhibited, certain uncertainties are also associated with the PIE. Enhancement in the alpha elements can suppress the PIE as the proton ingestion requires lower CNO abundance to break the entropy barrier. Also the mixing and nucleosynthetic mechanisms in the convective regions does not account for the assumptions of mixing length theory

and one dimensional spherically symmetric evolution (Cristallo et al., 2009, Herwig et al., 2011). Nevertheless, the PIE with a few TDU contributing to the observed CNO abundance and low isotopic ratio in CEMP stars can be acknowledged.

6.6 Conclusion

The CNO abundance of a small subset of CEMP stars have been derived using optical and NIR spectra. The oxygen abundance derived from [OI] lines are reasonably matching with the oxygen abundance derived from NIR CO lines. This indicate that NIR medium resolution spectroscopic studies can be used to derive the oxygen abundance of cool CEMP stars. This can save considerable amount of observing time required to capture the [OI] lines in the optical spectroscopy.

All the observed stars are showing a radial velocity variation indicating the presence of a binary companion. These stars are also showing an enhancement in the s-process elements. The origin of carbon and the s-process elements found in the CEMP stars can be associated with the companion star, possibly a white dwarf now, during its AGB phase transferred its carbon rich materials through some mass transfer mechanisms. The abundance pattern exhibited by C,N and O matches with those produced by models of AGB stars having M $\leqslant$ 2.5M$\odot$ and metallicity -2.3. The observed abundance pattern of carbon and oxygen is found to be matching with the model predicted shape, whereas the nitrogen is found to have an elevated value than the model prediction. The models also failed to reproduce the lower carbon isotopic ratio observed in these CEMP stars. Among the various scenarios invoked, Cool-Bottom Processing and Proton-Ingestion Episodes are two likely scenarios which can support the observed nitrogen abundance and the low carbon isotopic ratio. Though there are various uncertainties associated with each of these scenario,

one cannot rule out the possibility of either of them contributing to the observed abundance pattern of CNO in the CEMP stars.

6.7 Appendix

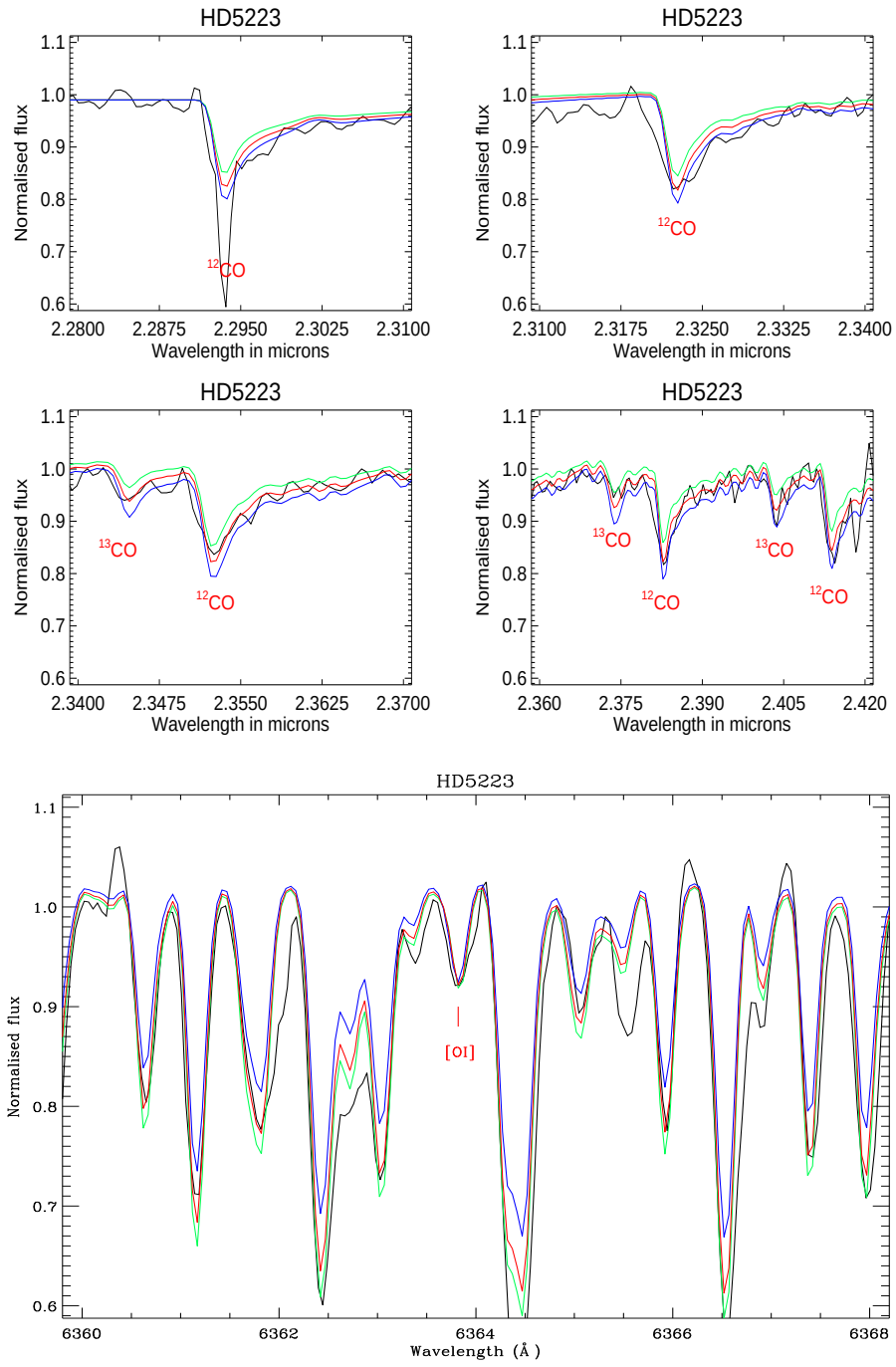

Figure 6.4: CO molecular band and [OI] line at 6363 is plotted for HD 5223. The The best fit is shown in red color and the errors quoted are ± 0.3 of the best fit value.

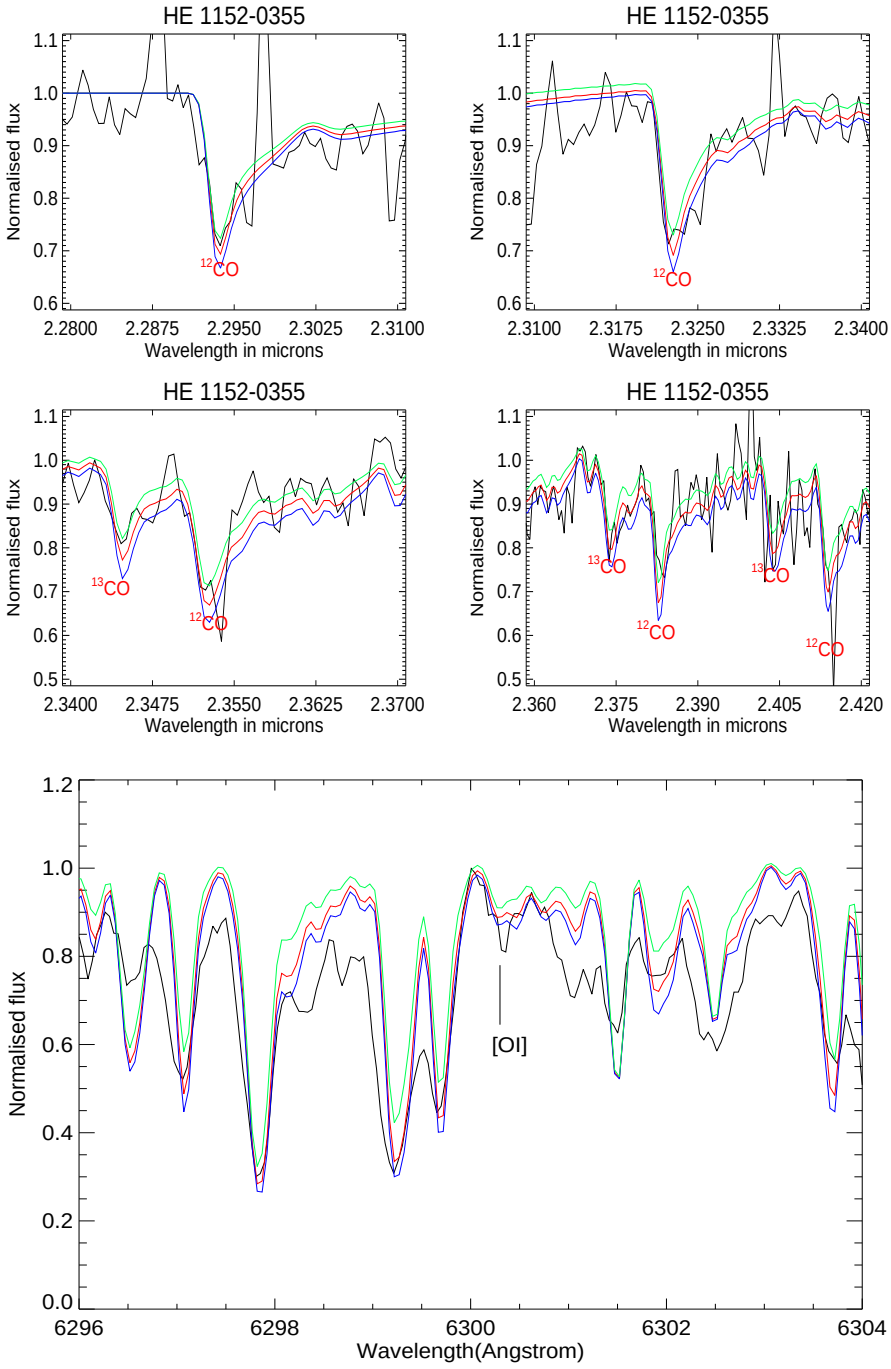

Figure 6.5: CO lines and [OI] line fitted with best synthetic models. The best fitted spectra is in red. The values are given in the table 6.2. The colors used are similar to that of figure 6.4

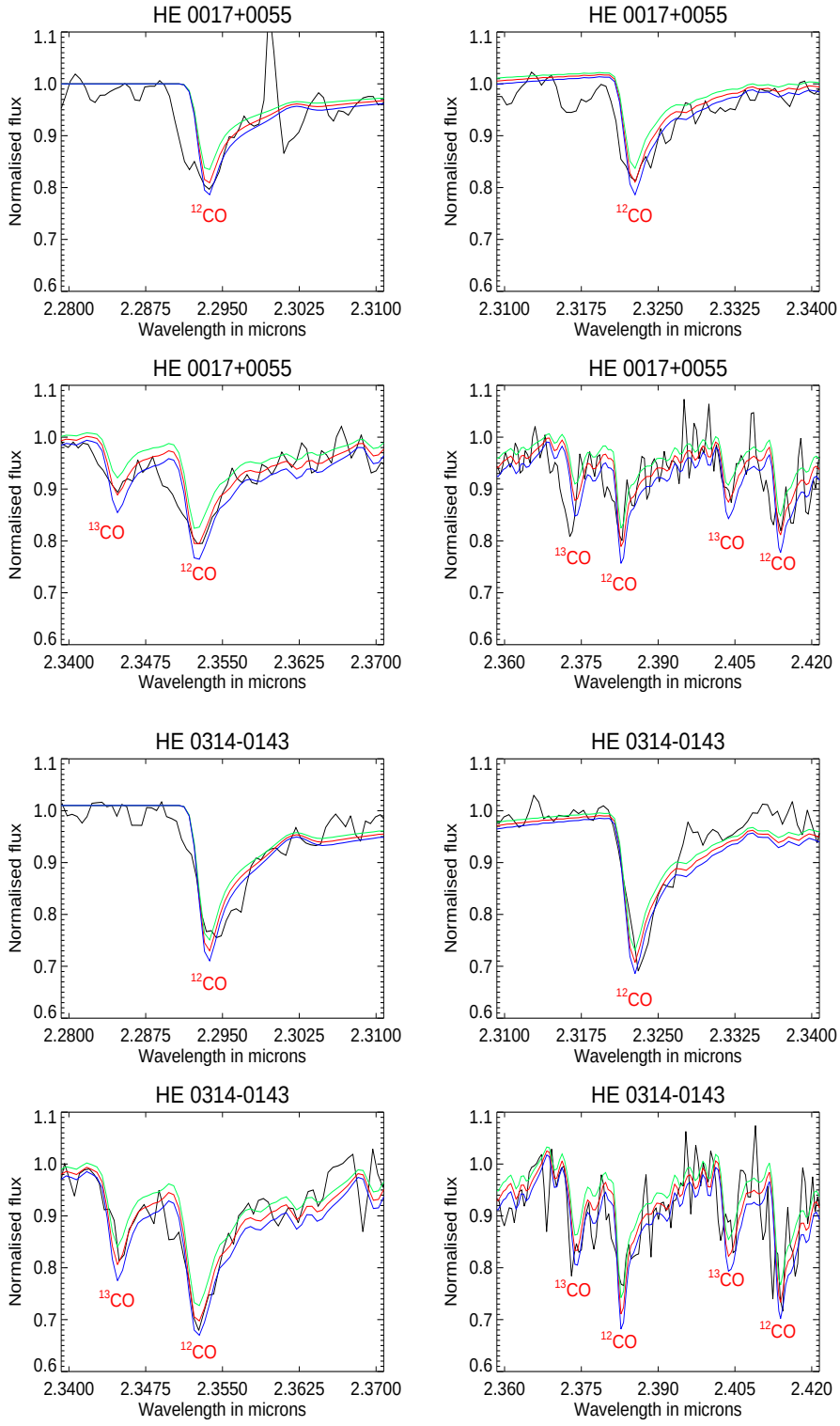
HE 0017+0055
Normalised flux
Wavelength in microns
^{12}CO
HE 0017+0055
Normalised flux
Wavelength in microns
^{12}CO
HE 0017+0055
Normalised flux
Wavelength in microns
^{13}CO
^{12}CO
HE 0017+0055
Normalised flux
Wavelength in microns
^{13}CO
^{12}CO
^{13}CO
^{12}CO
HE 0314-0143
Normalised flux
Wavelength in microns
^{12}CO
HE 0314-0143
Normalised flux
Wavelength in microns
^{12}CO
HE 0314-0143
Normalised flux
Wavelength in microns
^{13}CO
^{12}CO
HE 0314-0143
Normalised flux
Wavelength in microns
^{13}CO
^{12}CO
^{13}CO
^{12}CO

Chapter 7

Summary and future works

7.1 Summary

In this thesis, chemical properties of metal poor stars from the Galaxy and the satellite galaxies of the Milkyway have been studied using low and high resolution optical and NIR spectroscopic data to understand the common origin of them in the context of Galaxy formation. It can be seen that the stars in the Milkyway halo has contributions from sub halos of different masses for the formation of extremely metal poor stars(EMP). Low mass subhalos contribute to the formation of EMP stars with low [Sr/Ba]. The Ultra faint dwarf satellites of the Milkyway are low mass subsystems and observed to have consistently lower [Sr/Ba] ratio. This observational match in the ratio of neutron capture elements for a subset of EMP stars in the halo and stars in the UFDs supports the scenario of UFDs being contributing to the formation of the Milkyway halo. The presence of carbon normal and carbon rich population in the low metallicity regime in the halo and the satellite can be attributed to different supernovae contributing to the ISM from where the two

different populations evolved. The results from individual projects are summerised below.

- In chapter 3, details of slitless spectroscopic survey of satellite galaxies of the Milkyway have been explained. During the survey new members have been identified in the field of Ursa major II and Segue II ultra faint dwarf satellites. Uma-II, many of the new members are spatially distributed outside the half light radius. However, recent deep optical observations by Muñoz et al. (2010), has shown the galaxy is more extended than it was original thought. This shows great potential of slitless spectroscopy even with smaller telescopes, in probing the evolved bright stars, that helps to understand the spatial distribution and morphology. Extended distribution of such these stars in Uma-II further reinstates that these satellites underwent tidal disruption events and there might be many more members outside the half light radius which can be probed with better sensitivity instruments.

  Two chemically peculiar members were also identified in the field of UMa II UFD. We have initiated followup studies of these candidates, which will be part of my future work. The identified new members in many of these satellites are populating the intermediate metallicity range. This may indicate extended star formation in these satellite galaxies. Detailed spectroscopic studies are needed to understand origin and chemical evolution.

- In chapter 4, the results of high resolution abundance analysis of two CEMP stars (ALW-1 and ALW-8) from Carina dwarf spheroidal galaxy is included. One of the CEMP star (ALW-8) found to be showing no enhancement in neutron capture elements thus classified as CEMP-no star which is the first

CEMP-no star being reported from the Carina dwarf spheroidal galaxy. ALW-1 show enhancement in s-process elements along with radial velocity variation thus classified as CEMP-s star. The radial velocity variation together with enhancement in s-process elements indicate that, the carbon and s-process rich material was transferred from a binary companion which was once in its AGB phase, probably a white dwarf now. The companion AGB star, during the third dredge up episodes, convectively transferred the carbon and s-process materials to the surface from the interior which later transferred to the presently observable star through some mass transfer mechanism.

The abundance analysis of ALW-8 indicate that the star was born from a medium which was enriched by a mixture of faint supernovae and/or fast rotating massive star with a low metallicity SNe II. The abundance of neutron capture elements in ALW-8 is in excellent agreement with the only CEMP-no star in the Sculptor dSph and the weak-r process star HD 122563. This suggests that, whichever process was responsible for the heavy element production must be an ubiquitous source to pollute the CEMP-no stars, acting independently of the environment, such as in the halo or in dSphs.

- In chapter 5, the results of high resolution abundance analysis of an extremely metal poor star (SDSS J134338.67+484426.6) from the Milkyway halo is provided. The abundance pattern of this star is similar to the other carbon normal EMP star except for the low $\alpha-$ element abundance. The low $\alpha-$ element abundance indicates that the star was born from a medium where the star formation rate was low or from an inhomogeneously mixed medium. Contributions from Pop III intermediate-mass stars, along with later Pop II contributions with a low star formation rate (similar to dwarf spheroidal galaxies),

may explain the abundance patterns seen in this star. The abundance distribution of neutron capture elements in EMP stars in the Milkyway halo shows that subhalos of different masses contributed for the formation of EMP stars.

- Chapter 6 explains the CNO abundance of CEMP stars from the Milkyway using optical and NIR observations to derive the origin of the CNO abundance. The oxygen abundance derived from [OI] lines in the optical spectra and the oxygen abundance derived from NIR CO lines are found to be reasonably matching. This illustrates that the NIR medium resolution spectroscopic observations of CO lines can be used to derive oxygen abundance of cool CEMP stars. All the observed samples are showing radial velocity variation and enhancement in s-process elements. The origin of carbon and the s-process elements found in the CEMP stars can be associated with the companion star, possibly a white dwarf now, during its AGB phase transferred its carbon rich materials through some mass transfer mechanisms. The abundance pattern exhibited by C,N and O matches with those produced by models of AGB stars having M $\leqslant$2.5M$_{\odot}$ and metallicity ~ -2.3. The low carbon isotopic ratio and observed nitrogen abundance can be attributed to the additional CN cycles experienced by the companion star during its AGB phase and can be explained either by Cool Bottom Processing (CBP) or Proton Ingestion Episodes (PIE).

7.2 Future works

- We are planning to perform deep observations of satellite galaxy fields using slitless spectroscopy. So far we have observed each frame for a period of one hour with which we probed upto V$_{mag}$ = 16. An increase in the exposure time

by triple times may enable us to probe one magnitude deeper, this would help to find new members in the field.

- The follow up studies of newly identified members from slitless spectroscopic survey is planned. The detailed studies of these intermediate metallicity stars gives details about their origin and nature of various supernovae contributed for their formation.

Bibliography

C. Abia, P. de Laverny, and R. Wahlin. Chemical analysis of carbon stars in the Local Group. II. The Carina dwarf spheroidal galaxy. A&A, 481:161–168, Apr. 2008. doi: 10.1051/0004-6361:20079114.

M. Afşar, C. Sneden, A. Frebel, H. Kim, G. N. Mace, K. F. Kaplan, H.-I. Lee, H. Oh, J. Sok Oh, S. Pak, C. Park, M. D. Pavel, I.-S. Yuk, and D. T. Jaffe. The Chemical Compositions of Very Metal-poor Stars HD 122563 and HD 140283: A View from the Infrared. ApJ, 819:103, Mar. 2016. doi: 10.3847/0004-637X/819/2/103.

A. Alonso, S. Arribas, and C. Martinez-Roger. The empirical scale of temperatures of the low main sequence (F0V-K5V). A&A, 313:873–890, Sept. 1996.

A. Alonso, S. Arribas, and C. Martínez-Roger. The effective temperature scale of giant stars (F0-K5). I. The effective temperature determination by means of the IRFM. A&AS, 139:335–358, Oct. 1999. doi: 10.1051/aas:1999506.

R. Alvarez and B. Plez. Near-infrared narrow-band photometry of M-giant and Mira stars: models meet observations. A&A, 330:1109–1119, Feb. 1998.

S. M. Andrievsky, M. Spite, S. A. Korotin, F. Spite, P. Bonifacio, R. Cayrel, P. François, and V. Hill. Non-LTE abundances of Mg and K in extremely metal-poor stars and the evolution of [O/Mg], [Na/Mg], [Al/Mg], and [K/Mg] in the Milky Way. A&A, 509:A88, Jan. 2010. doi: 10.1051/0004-6361/200913223.

S. M. Andrievsky, F. Spite, S. A. Korotin, P. François, M. Spite, P. Bonifacio, R. Cayrel, and V. Hill. NLTE strontium abundance in a sample of extremely metal poor stars and the Sr/Ba ratio in the early Galaxy. A&A, 530:A105, June 2011. doi: 10.1051/0004-6361/201116591.

W. Aoki, T. C. Beers, N. Christlieb, J. E. Norris, S. G. Ryan, and S. Tsangarides. Carbon-enhanced Metal-poor Stars. I. Chemical Compositions of 26 Stars. ApJ, 655:492–521, Jan. 2007. doi: 10.1086/509817.

W. Aoki, N. Arimoto, K. Sadakane, E. Tolstoy, G. Battaglia, P. Jablonka, M. Shetrone, B. Letarte, M. Irwin, V. Hill, P. Francois, K. Venn, F. Primas, A. Helmi, A. Kaufer, M. Tafelmeyer, T. Szeifert, and C. Babusiaux. Chemical composition of extremely metal-poor stars in the Sextans dwarf spheroidal galaxy. A&A, 502:569–578, Aug. 2009. doi: 10.1051/0004-6361/200911959.

A. Arcones and F. Montes. Production of Light-element Primary Process Nuclei in Neutrino-driven Winds. ApJ, 731:5, Apr. 2011. doi: 10.1088/0004-637X/731/1/5.

M. Asplund. New Light on Stellar Abundance Analyses: Departures from LTE and Homogeneity. ARA&A, 43:481–530, Sept. 2005. doi: 10.1146/annurev.astro.42.053102.134001.

M. Asplund, N. Grevesse, A. J. Sauval, and P. Scott. The Chemical Composition

of the Sun. ARA&A, 47:481–522, Sept. 2009. doi: 10.1146/annurev.astro.46.060407.145222.

M. Azzopardi, J. Lequeux, and B. E. Westerlund. New carbon stars in spheroidal galaxies. II - Draco, Ursa Minor and new data on Sculptor, Carina, and Leo I. A&A, 161:232–236, June 1986.

J. Bagchi, M. Vivek, V. Vikram, A. Hota, K. G. Biju, S. K. Sirothia, R. Srianand, Gopal-Krishna, and J. Jacob. Megaparsec Relativistic Jets Launched from an Accreting Supermassive Black Hole in an Extreme Spiral Galaxy. ApJ, 788:174, June 2014. doi: 10.1088/0004-637X/788/2/174.

B. Barbuy, J. Meléndez, M. Spite, F. Spite, E. Depagne, V. Hill, R. Cayrel, P. Bonifacio, A. Damineli, and C. A. O. Torres. Oxygen Abundance in the Template Halo Giant HD 122563. ApJ, 588:1072–1081, May 2003. doi: 10.1086/374312.

B. Barbuy, M. Spite, F. Spite, V. Hill, R. Cayrel, B. Plez, and P. Petitjean. New analysis of the two carbon-rich stars CS 22948-27 and CS 29497-34: Binarity and neutron capture elements. A&A, 429:1031–1042, Jan. 2005. doi: 10.1051/0004-6361:20040415.

P. S. Barklem, N. Christlieb, T. C. Beers, V. Hill, M. S. Bessell, J. Holmberg, B. Marsteller, S. Rossi, F.-J. Zickgraf, and D. Reimers. The Hamburg/ESO R-process enhanced star survey (HERES). II. Spectroscopic analysis of the survey sample. A&A, 439:129–151, Aug. 2005. doi: 10.1051/0004-6361:20052967.

G. Battaglia, M. Irwin, E. Tolstoy, V. Hill, A. Helmi, B. Letarte, and P. Jablonka. Analysis and calibration of CaII triplet spectroscopy of red giant branch stars

from VLT/FLAMES observations. MNRAS, 383:183–199, Jan. 2008. doi: 10.1111/j.1365-2966.2007.12532.x.

C. Battistini and T. Bensby. The origin and evolution of r- and s-process elements in the Milky Way stellar disk. A&A, 586:A49, Feb. 2016. doi: 10.1051/0004-6361/201527385.

D. Baumueller and T. Gehren. Aluminium in metal-poor stars. A&A, 325:1088–1098, Sept. 1997.

D. Baumueller, K. Butler, and T. Gehren. Sodium in the Sun and in metal-poor stars. A&A, 338:637–650, Oct. 1998.

T. C. Beers and N. Christlieb. The Discovery and Analysis of Very Metal-Poor Stars in the Galaxy. ARA&A, 43:531–580, Sept. 2005. doi: 10.1146/annurev.astro.42.053102.134057.

T. C. Beers, J. E. Norris, V. M. Placco, Y. S. Lee, S. Rossi, D. Carollo, and T. Masseron. Population Studies. XIII. A New Analysis of the Bidelman-MacConnell "Weak-metal" StarsConfirmation of Metal-poor Stars in the Thick Disk of the Galaxy. ApJ, 794:58, Oct. 2014. doi: 10.1088/0004-637X/794/1/58.

V. Belokurov, D. B. Zucker, N. W. Evans, G. Gilmore, S. Vidrih, D. M. Bramich, H. J. Newberg, R. F. G. Wyse, M. J. Irwin, M. Fellhauer, P. C. Hewett, N. A. Walton, M. I. Wilkinson, N. Cole, B. Yanny, C. M. Rockosi, T. C. Beers, E. F. Bell, J. Brinkmann, Ž. Ivezić, and R. Lupton. The Field of Streams: Sagittarius and Its Siblings. ApJ, 642:L137–L140, May 2006a. doi: 10.1086/504797.

V. Belokurov, D. B. Zucker, N. W. Evans, M. I. Wilkinson, M. J. Irwin, S. Hodgkin,

D. M. Bramich, J. M. Irwin, G. Gilmore, B. Willman, S. Vidrih, H. J. Newberg, R. F. G. Wyse, M. Fellhauer, P. C. Hewett, N. Cole, E. F. Bell, T. C. Beers, C. M. Rockosi, B. Yanny, E. K. Grebel, D. P. Schneider, R. Lupton, J. C. Barentine, H. Brewington, J. Brinkmann, M. Harvanek, S. J. Kleinman, J. Krzesinski, D. Long, A. Nitta, J. A. Smith, and S. A. Snedden. A Faint New Milky Way Satellite in Bootes. ApJ, 647:L111–L114, Aug. 2006b. doi: 10.1086/507324.

V. Belokurov, N. W. Evans, M. J. Irwin, D. Lynden-Bell, B. Yanny, S. Vidrih, G. Gilmore, G. Seabroke, D. B. Zucker, M. I. Wilkinson, P. C. Hewett, D. M. Bramich, M. Fellhauer, H. J. Newberg, R. F. G. Wyse, T. C. Beers, E. F. Bell, J. C. Barentine, J. Brinkmann, N. Cole, K. Pan, and D. G. York. An Orphan in the "Field of Streams". ApJ, 658:337–344, Mar. 2007a. doi: 10.1086/511302.

V. Belokurov, D. B. Zucker, N. W. Evans, J. T. Kleyna, S. Koposov, S. T. Hodgkin, M. J. Irwin, G. Gilmore, M. I. Wilkinson, M. Fellhauer, D. M. Bramich, P. C. Hewett, S. Vidrih, J. T. A. De Jong, J. A. Smith, H.-W. Rix, E. F. Bell, R. F. G. Wyse, H. J. Newberg, P. A. Mayeur, B. Yanny, C. M. Rockosi, O. Y. Gnedin, D. P. Schneider, T. C. Beers, J. C. Barentine, H. Brewington, J. Brinkmann, M. Harvanek, S. J. Kleinman, J. Krzesinski, D. Long, A. Nitta, and S. A. Snedden. Cats and Dogs, Hair and a Hero: A Quintet of New Milky Way Companions. ApJ, 654:897–906, Jan. 2007b. doi: 10.1086/509718.

V. Belokurov, M. G. Walker, N. W. Evans, G. Gilmore, M. J. Irwin, M. Mateo, L. Mayer, E. Olszewski, J. Bechtold, and T. Pickering. The discovery of Segue 2: a prototype of the population of satellites of satellites. MNRAS, 397:1748–1755, Aug. 2009. doi: 10.1111/j.1365-2966.2009.15106.x.

V. Belokurov, M. G. Walker, N. W. Evans, G. Gilmore, M. J. Irwin, D. Just, S. Koposov, M. Mateo, E. Olszewski, L. Watkins, and L. Wyrzykowski. Big Fish, Little Fish: Two New Ultra-faint Satellites of the Milky Way. ApJ, 712:L103–L106, Mar. 2010. doi: 10.1088/2041-8205/712/1/L103.

T. Bensby, S. Feltzing, and M. S. Oey. Exploring the Milky Way stellar disk. A detailed elemental abundance study of 714 F and G dwarf stars in the solar neighbourhood. A&A, 562:A71, Feb. 2014. doi: 10.1051/0004-6361/201322631.

P. Bonifacio, M. Spite, R. Cayrel, V. Hill, F. Spite, P. François, B. Plez, H.-G. Ludwig, E. Caffau, P. Molaro, E. Depagne, J. Andersen, B. Barbuy, T. C. Beers, B. Nordström, and F. Primas. First stars XII. Abundances in extremely metal-poor turnoff stars, and comparison with the giants. A&A, 501:519–530, July 2009. doi: 10.1051/0004-6361/200810610.

P. Bonifacio, E. Caffau, M. Spite, M. Limongi, A. Chieffi, R. S. Klessen, P. François, P. Molaro, H.-G. Ludwig, S. Zaggia, F. Spite, B. Plez, R. Cayrel, N. Christlieb, P. C. Clark, S. C. O. Glover, F. Hammer, A. Koch, L. Monaco, L. Sbordone, and M. Steffen. TOPoS . II. On the bimodality of carbon abundance in CEMP stars Implications on the early chemical evolution of galaxies. A&A, 579:A28, July 2015. doi: 10.1051/0004-6361/201425266.

V. Bromm and N. Yoshida. The First Galaxies. ARA&A, 49:373–407, Sept. 2011. doi: 10.1146/annurev-astro-081710-102608.

V. Bromm, N. Yoshida, and L. Hernquist. The First Supernova Explosions in the Universe. ApJ, 596:L135–L138, Oct. 2003. doi: 10.1086/379359.

V. Bromm, N. Yoshida, L. Hernquist, and C. F. McKee. The formation of the first stars and galaxies. Nature, 459:49–54, May 2009. doi: 10.1038/nature07990.

T. M. Brown, J. Tumlinson, M. Geha, E. N. Kirby, D. A. VandenBerg, R. R. Muñoz, J. S. Kalirai, J. D. Simon, R. J. Avila, P. Guhathakurta, A. Renzini, and H. C. Ferguson. The Primeval Populations of the Ultra-faint Dwarf Galaxies. ApJ, 753: L21, July 2012. doi: 10.1088/2041-8205/753/1/L21.

T. M. Brown, J. Tumlinson, M. Geha, J. D. Simon, L. C. Vargas, D. A. VandenBerg, E. N. Kirby, J. S. Kalirai, R. J. Avila, M. Gennaro, H. C. Ferguson, R. R. Muñoz, P. Guhathakurta, and A. Renzini. The Quenching of the Ultra-faint Dwarf Galaxies in the Reionization Era. ApJ, 796:91, Dec. 2014. doi: 10.1088/0004-637X/796/2/91.

J. S. Bullock and K. V. Johnston. Tracing Galaxy Formation with Stellar Halos. I. Methods. ApJ, 635:931–949, Dec. 2005. doi: 10.1086/497422.

M. Busso, G. J. Wasserburg, K. M. Nollett, and A. Calandra. Can Extra Mixing in RGB and AGB Stars Be Attributed to Magnetic Mechanisms? ApJ, 671:802–810, Dec. 2007. doi: 10.1086/522616.

E. Caffau, P. Bonifacio, P. François, L. Sbordone, M. Spite, L. Monaco, B. Plez, F. Spite, S. Zaggia, H.-G. Ludwig, R. Cayrel, P. Molaro, S. Randich, F. Hammer, and V. Hill. X-shooter GTO: evidence for a population of extremely metal-poor, alpha-poor stars. A&A, 560:A15, Dec. 2013. doi: 10.1051/0004-6361/201322213.

J. L. Carlin, C. J. Grillmair, R. R. Muñoz, D. L. Nidever, and S. R. Majewski. Kinematics and Metallicities in the Boötes III Stellar Overdensity: A Disrupted

Dwarf Galaxy? ApJ, 702:L9–L13, Sept. 2009. doi: 10.1088/0004-637X/702/1/L9.

B. W. Carney, J. S. Wright, C. Sneden, J. B. Laird, L. A. Aguilar, and D. W. Latham. Discovery of an "alpha" Element-Poor Halo Star in a Search for Very Low- Metallicity Disk Stars. AJ, 114:363–375, July 1997. doi: 10.1086/118480.

D. Carollo, T. C. Beers, Y. S. Lee, M. Chiba, J. E. Norris, R. Wilhelm, T. Sivarani, B. Marsteller, J. A. Munn, C. A. L. Bailer-Jones, P. R. Fiorentin, and D. G. York. Two stellar components in the halo of the Milky Way. Nature, 450:1020–1025, Dec. 2007. doi: 10.1038/nature06460.

D. Carollo, T. C. Beers, M. Chiba, J. E. Norris, K. C. Freeman, Y. S. Lee, Ž. Ivezić, C. M. Rockosi, and B. Yanny. Structure and Kinematics of the Stellar Halos and Thick Disks of the Milky Way Based on Calibration Stars from Sloan Digital Sky Survey DR7. ApJ, 712:692–727, Mar. 2010. doi: 10.1088/0004-637X/712/1/692.

D. Carollo, K. Freeman, T. C. Beers, V. M. Placco, J. Tumlinson, and S. L. Martell. Carbon-enhanced Metal-poor Stars: CEMP-s and CEMP-no Subclasses in the Halo System of the Milky Way. ApJ, 788:180, June 2014. doi: 10.1088/0004-637X/788/2/180.

F. Castelli and R. L. Kurucz. New Grids of ATLAS9 Model Atmospheres. *ArXiv Astrophysics e-prints*, May 2004.

R. Cayrel, E. Depagne, M. Spite, V. Hill, F. Spite, P. François, B. Plez, T. Beers, F. Primas, J. Andersen, B. Barbuy, P. Bonifacio, P. Molaro, and B. Nordström. First stars V - Abundance patterns from C to Zn and supernova yields in the early Galaxy. A&A, 416:1117–1138, Mar. 2004. doi: 10.1051/0004-6361:20034074.

G. Cayrel de Strobel and M. Spite, editors. *The impact of very high S/N spectroscopy on stellar physics: proceedings of the 132nd Symposium of the International Astronomical Union held in Paris, France, June 29-July 3, 1987.*, volume 132 of *IAU Symposium*, 1988.

C. Charbonnel. A Consistent Explanation for 12C/ 13C, 7Li and 3He Anomalies in Red Giant Stars. ApJ, 453:L41, Nov. 1995. doi: 10.1086/309744.

C. Charbonnel, J. A. Brown, and G. Wallerstein. Mixing processes during the evolution of red giants with moderate metal deficiencies: the role of molecular-weight barriers. A&A, 332:204–214, Apr. 1998.

J. G. Cohen, N. Christlieb, Y.-Z. Qian, and G. J. Wasserburg. Abundance Analysis of HE 2148-1247, A Star with Extremely Enhanced Neutron Capture Elements. ApJ, 588:1082–1098, May 2003. doi: 10.1086/374269.

J. G. Cohen, N. Christlieb, A. McWilliam, S. Shectman, I. Thompson, G. J. Wasserburg, I. Ivans, M. Dehn, T. Karlsson, and J. Melendez. Abundances In Very Metal-Poor Dwarf Stars. ApJ, 612:1107–1135, Sept. 2004. doi: 10.1086/422576.

J. G. Cohen, N. Christlieb, I. Thompson, A. McWilliam, S. Shectman, D. Reimers, L. Wisotzki, and E. Kirby. Normal and Outlying Populations of the Milky Way Stellar Halo at [Fe/H] -2. ApJ, 778:56, Nov. 2013. doi: 10.1088/0004-637X/778/1/56.

A. P. Cooper, R. D'Souza, G. Kauffmann, J. Wang, M. Boylan-Kolchin, Q. Guo, C. S. Frenk, and S. D. M. White. Galactic accretion and the outer structure of galaxies in the CDM model. MNRAS, 434:3348–3367, Oct. 2013. doi: 10.1093/mnras/stt1245.

S. Cristallo, L. Piersanti, O. Straniero, R. Gallino, I. Domínguez, and F. Käppeler. Asymptotic-Giant-Branch Models at Very Low Metallicity. PASA, 26:139–144, Aug. 2009. doi: 10.1071/AS09003.

W. Y. Cui, T. Sivarani, and N. Christlieb. The Hamburg/ESO R-process Enhanced Star survey (HERES). VIII. The r+s star HE 1405-0822. A&A, 558:A36, Oct. 2013. doi: 10.1051/0004-6361/201321597.

R. M. Cutri, M. F. Skrutskie, S. van Dyk, C. A. Beichman, J. M. Carpenter, T. Chester, L. Cambresy, T. Evans, J. Fowler, J. Gizis, E. Howard, J. Huchra, T. Jarrett, E. L. Kopan, J. D. Kirkpatrick, R. M. Light, K. A. Marsh, H. McCallon, S. Schneider, R. Stiening, M. Sykes, M. Weinberg, W. A. Wheaton, S. Wheelock, and N. Zacarias. VizieR Online Data Catalog: 2MASS All-Sky Catalog of Point Sources (Cutri+ 2003). *VizieR Online Data Catalog*, 2246:0, June 2003.

P. de Laverny, C. Abia, I. Domínguez, B. Plez, O. Straniero, R. Wahlin, K. Eriksson, and U. G. Jørgensen. Chemical analysis of carbon stars in the Local Group. A&A, 446:1107–1118, Feb. 2006. doi: 10.1051/0004-6361:20053423.

P. Demarque, J.-H. Woo, Y.-C. Kim, and S. K. Yi. Y^2 Isochrones with an Improved Core Overshoot Treatment. ApJS, 155:667–674, Dec. 2004. doi: 10.1086/424966.

P. A. Denissenkov and M. Pinsonneault. The Impact of Carbon Enhancement on Extra Mixing in Metal-poor Stars. ApJ, 679:1541-1548, June 2008. doi: 10.1086/587681.

J. Diemand, M. Kuhlen, P. Madau, M. Zemp, B. Moore, D. Potter, and J. Stadel.

Clumps and streams in the local dark matter distribution. Nature, 454:735–738, Aug. 2008. doi: 10.1038/nature07153.

O. J. Eggen, D. Lynden-Bell, and A. R. Sandage. Evidence from the motions of old stars that the Galaxy collapsed. ApJ, 136:748, Nov. 1962. doi: 10.1086/147433.

P. P. Eggleton, D. S. P. Dearborn, and J. C. Lattanzio. Compulsory Deep Mixing of ^{3}He and CNO Isotopes in the Envelopes of Low-Mass Red Giants. ApJ, 677: 581-592, Apr. 2008. doi: 10.1086/529024.

M. Fabrizio, M. Nonino, G. Bono, F. Primas, F. Thévenin, P. B. Stetson, S. Cassisi, R. Buonanno, G. Coppola, R. O. da Silva, M. Dall'Ora, I. Ferraro, K. Genovali, R. Gilmozzi, G. Iannicola, M. Marconi, M. Monelli, M. Romaniello, and A. R. Walker. The Carina Project. VIII. The α-element abundances. A&A, 580:A18, Aug. 2015. doi: 10.1051/0004-6361/201525753.

R. Fadely, B. Willman, M. Geha, S. Walsh, R. R. Muñoz, H. Jerjen, L. C. Vargas, and G. S. Da Costa. Segue 3: An Old, Extremely Low Luminosity Star Cluster in the Milky Way's Halo. AJ, 142:88, Sept. 2011. doi: 10.1088/0004-6256/142/3/88.

M. Fellhauer, N. W. Evans, V. Belokurov, D. B. Zucker, B. Yanny, M. I. Wilkinson, G. Gilmore, M. J. Irwin, D. M. Bramich, S. Vidrih, P. Hewett, and T. Beers. Is Ursa Major II the progenitor of the Orphan Stream? MNRAS, 375:1171–1179, Mar. 2007. doi: 10.1111/j.1365-2966.2006.11404.x.

C. K. Fishlock, A. I. Karakas, M. Lugaro, and D. Yong. Evolution and Nucleosynthesis of Asymptotic Giant Branch Stellar Models of Low Metallicity. ApJ, 797: 44, Dec. 2014. doi: 10.1088/0004-637X/797/1/44.

P. François, E. Depagne, V. Hill, M. Spite, F. Spite, B. Plez, T. C. Beers, J. Andersen, G. James, B. Barbuy, R. Cayrel, P. Bonifacio, P. Molaro, B. Nordström, and F. Primas. First stars. VIII. Enrichment of the neutron-capture elements in the early Galaxy. A&A, 476:935–950, Dec. 2007. doi: 10.1051/0004-6361:20077706.

A. Frebel and V. Bromm. Chemical Signatures of the First Galaxies: Criteria for One-shot Enrichment. ApJ, 759:115, Nov. 2012. doi: 10.1088/0004-637X/759/2/115.

A. Frebel and J. E. Norris. Near-Field Cosmology with Metal-Poor Stars. *ArXiv e-prints*, Jan. 2015.

A. Frebel, E. N. Kirby, and J. D. Simon. Linking dwarf galaxies to halo building blocks with the most metal-poor star in Sculptor. Nature, 464:72–75, Mar. 2010a. doi: 10.1038/nature08772.

A. Frebel, J. D. Simon, M. Geha, and B. Willman. High-Resolution Spectroscopy of Extremely Metal-Poor Stars in the Least Evolved Galaxies: Ursa Major II and Coma Berenices. ApJ, 708:560–583, Jan. 2010b. doi: 10.1088/0004-637X/708/1/560.

A. Frebel, J. D. Simon, and E. N. Kirby. Segue 1: An Unevolved Fossil Galaxy from the Early Universe. ApJ, 786:74, May 2014. doi: 10.1088/0004-637X/786/1/74.

U. Frischknecht, R. Hirschi, M. Pignatari, A. Maeder, G. Meynet, C. Chiappini, F.-K. Thielemann, T. Rauscher, C. Georgy, and S. Ekström. s-process production in rotating massive stars at solar and low metallicities. MNRAS, 456:1803–1825, Feb. 2016. doi: 10.1093/mnras/stv2723.

R. Gallino, C. Arlandini, M. Busso, M. Lugaro, C. Travaglio, O. Straniero, A. Chieffi, and M. Limongi. Evolution and Nucleosynthesis in Low-Mass Asymptotic Giant Branch Stars. II. Neutron Capture and the S-Process. ApJ, 497:388–403, Apr. 1998. doi: 10.1086/305437.

R. Gallino, M. Busso, M. Lugaro, O. Straniero, F. Käppeler, and C. Arlandini. How many s-process components from realistic models of asymptotic giant branch stars? Mem. Soc. Astron. Italiana, 71:771, 2000.

J. Ge, S. Mahadevan, B. Lee, X. Wan, B. Zhao, J. van Eyken, S. Kane, P. Guo, E. Ford, S. Fleming, J. Crepp, R. Cohen, J. Groot, M. C. Galvez, J. Liu, E. Agol, S. Gaudi, H. Ford, D. Schneider, S. Seager, D. Weinberg, and D. Eisenstein. The Multi-object APO Radial-Velocity Exoplanet Large-area Survey (MARVELS). In D. Fischer, F. A. Rasio, S. E. Thorsett, and A. Wolszczan, editors, *Extreme Solar Systems*, volume 398 of *Astronomical Society of the Pacific Conference Series*, page 449, 2008.

M. Geha, B. Willman, J. D. Simon, L. E. Strigari, E. N. Kirby, D. R. Law, and J. Strader. The Least-Luminous Galaxy: Spectroscopy of the Milky Way Satellite Segue 1. ApJ, 692:1464–1475, Feb. 2009. doi: 10.1088/0004-637X/692/2/1464.

D. Geisler, V. V. Smith, G. Wallerstein, G. Gonzalez, and C. Charbonnel. "Sculptoring" the Galaxy? The Chemical Compositions of Red Giants in the Sculptor Dwarf Spheroidal Galaxy. AJ, 129:1428–1442, Mar. 2005. doi: 10.1086/427540.

D. Geisler, G. Wallerstein, V. V. Smith, and D. I. Casetti-Dinescu. Chemical Abundances and Kinematics in Globular Clusters and Local Group Dwarf Galaxies and Their Implications for Formation Theories of the Galactic Halo. PASP, 119: 939–961, Sept. 2007. doi: 10.1086/521990.

A. Goswami, W. Aoki, T. C. Beers, N. Christlieb, J. E. Norris, S. G. Ryan, and S. Tsangarides. A high-resolution spectral analysis of three carbon-enhanced metal-poor stars. MNRAS, 372:343–356, Oct. 2006. doi: 10.1111/j.1365-2966.2006.10877.x.

R. G. Gratton, E. Carretta, K. Eriksson, and B. Gustafsson. Abundances of light elements in metal-poor stars. II. Non-LTE abundance corrections. A&A, 350: 955–969, Oct. 1999.

R. G. Gratton, C. Sneden, E. Carretta, and A. Bragaglia. Mixing along the red giant branch in metal-poor field stars. A&A, 354:169–187, Feb. 2000.

E. K. Grebel. Star Formation Histories of Local Group Dwarf Galaxies. (Ludwig Biermann Award Lecture 1996). In R. E. Schielicke, editor, *Reviews in Modern Astronomy*, volume 10 of *Reviews in Modern Astronomy*, pages 29–60, 1997.

N. Grevesse and A. J. Sauval. Standard Solar Composition. Space Sci. Rev., 85: 161–174, May 1998. doi: 10.1023/A:1005161325181.

C. J. Grillmair. Four New Stellar Debris Streams in the Galactic Halo. ApJ, 693: 1118–1127, Mar. 2009. doi: 10.1088/0004-637X/693/2/1118.

J. E. Gunn, W. A. Siegmund, E. J. Mannery, R. E. Owen, C. L. Hull, R. F. Leger, L. N. Carey, G. R. Knapp, D. G. York, W. N. Boroski, S. M. Kent, R. H. Lupton, C. M. Rockosi, M. L. Evans, P. Waddell, J. E. Anderson, J. Annis, J. C. Barentine, L. M. Bartoszek, S. Bastian, S. B. Bracker, H. J. Brewington, C. I. Briegel, J. Brinkmann, Y. J. Brown, M. A. Carr, P. C. Czarapata, C. C. Drennan, T. Dombeck, G. R. Federwitz, B. A. Gillespie, C. Gonzales, S. U. Hansen, M. Harvanek, J. Hayes, W. Jordan, E. Kinney, M. Klaene, S. J. Kleinman, R. G.

Kron, J. Kresinski, G. Lee, S. Limmongkol, C. W. Lindenmeyer, D. C. Long, C. L. Loomis, P. M. McGehee, P. M. Mantsch, E. H. Neilsen, Jr., R. M. Neswold, P. R. Newman, A. Nitta, J. Peoples, Jr., J. R. Pier, P. S. Prieto, A. Prosapio, C. Rivetta, D. P. Schneider, S. Snedden, and S.-i. Wang. The 2.5 m Telescope of the Sloan Digital Sky Survey. AJ, 131:2332–2359, Apr. 2006. doi: 10.1086/500975.

M. Hanke, A. Koch, C. J. Hansen, and A. McWilliam. Insights into the chemical composition of the metal-poor Milky Way halo globular cluster NGC 6426. A&A, 599:97–110, Dec. 2017.

C. J. Hansen, B. Nordström, P. Bonifacio, M. Spite, J. Andersen, T. C. Beers, R. Cayrel, F. Spite, P. Molaro, B. Barbuy, E. Depagne, P. François, V. Hill, B. Plez, and T. Sivarani. First stars. XIII. Two extremely metal-poor RR Lyrae stars. A&A, 527:A65, Mar. 2011. doi: 10.1051/0004-6361/201015076.

C. J. Hansen, F. Montes, and A. Arcones. How Many Nucleosynthesis Processes Exist at Low Metallicity? ApJ, 797:123, Dec. 2014. doi: 10.1088/0004-637X/797/2/123.

C. J. Hansen, H.-G. Ludwig, W. Seifert, A. Koch, W. Xu, E. Caffau, N. Christlieb, A. J. Korn, K. Lind, L. Sbordone, G. Ruchti, S. Feltzing, R. S. de Jong, and S. Barden. Stellar science from a blue wavelength range. A possible design for the blue arm of 4MOST. *Astronomische Nachrichten*, 336:665, Sept. 2015. doi: 10.1002/asna.201512206.

C. J. Hansen, P. Jofre, A. Koch, A. McWilliam, and C. S. Sneden. Something borrowed, something blue: The nature of blue metal-poor stars inferred from their colours and chemical abundances. *ArXiv e-prints*, Nov. 2016a.

C. J. Hansen, B. Nordström, T. T. Hansen, C. R. Kennedy, V. M. Placco, T. C. Beers, J. Andersen, G. Cescutti, and C. Chiappini. Abundances of carbon-enhanced metal-poor stars as constraints on their formation. A&A, 588:A37, Apr. 2016b. doi: 10.1051/0004-6361/201526895.

T. T. Hansen, J. Andersen, B. Nordström, T. C. Beers, V. M. Placco, J. Yoon, and L. A. Buchhave. The role of binaries in the enrichment of the early Galactic halo. II. Carbon-enhanced metal-poor stars: CEMP-no stars. A&A, 586:A160, Feb. 2016c. doi: 10.1051/0004-6361/201527235.

T. T. Hansen, J. Andersen, B. Nordström, T. C. Beers, V. M. Placco, J. Yoon, and L. A. Buchhave. The role of binaries in the enrichment of the early Galactic halo. III. Carbon-enhanced metal-poor stars - CEMP-s stars. A&A, 588:A3, Apr. 2016d. doi: 10.1051/0004-6361/201527409.

A. A. Henden, S. Levine, D. Terrell, and D. L. Welch. APASS - The Latest Data Release. In *American Astronomical Society Meeting Abstracts*, volume 225 of *American Astronomical Society Meeting Abstracts*, page 336.16, Jan. 2015.

F. Herwig. Evolution and Yields of Extremely Metal-poor Intermediate-Mass Stars. ApJS, 155:651–666, Dec. 2004. doi: 10.1086/425419.

F. Herwig. Evolution of Asymptotic Giant Branch Stars. ARA&A, 43:435–479, Sept. 2005. doi: 10.1146/annurev.astro.43.072103.150600.

F. Herwig, M. Pignatari, P. R. Woodward, D. H. Porter, G. Rockefeller, C. L. Fryer, M. Bennett, and R. Hirschi. Convective-reactive Proton-^{12}C Combustion in Sakurai's Object (V4334 Sagittarii) and Implications for the Evolution

and Yields from the First Generations of Stars. ApJ, 727:89, Feb. 2011. doi: 10.1088/0004-637X/727/2/89.

S. Honda, W. Aoki, Y. Ishimaru, S. Wanajo, and S. G. Ryan. Neutron-Capture Elements in the Very Metal Poor Star HD 122563. ApJ, 643:1180–1189, June 2006. doi: 10.1086/503195.

S. Honda, W. Aoki, N. Arimoto, and K. Sadakane. Enrichment of Heavy Elements in the Red Giant S 15-19 in the Sextans Dwarf Spheroidal Galaxy. PASJ, 63: 523–529, Mar. 2011. doi: 10.1093/pasj/63.sp2.S523.

R. A. Ibata, G. Gilmore, and M. J. Irwin. Sagittarius: the nearest dwarf galaxy. MNRAS, 277:781–800, Dec. 1995. doi: 10.1093/mnras/277.3.781.

T. Idiart and F. Thévenin. Non-LTE Abundances and Consequences for the Evolution of the α-Elements in the Galaxy. ApJ, 541:207–217, Sept. 2000. doi: 10.1086/309416.

M. N. Ishigaki, N. Tominaga, C. Kobayashi, and K. Nomoto. Faint Population III Supernovae as the Origin of the Most Iron-poor Stars. ApJ, 792:L32, Sept. 2014. doi: 10.1088/2041-8205/792/2/L32.

I. I. Ivans, C. Sneden, C. R. James, G. W. Preston, J. P. Fulbright, P. A. Höflich, B. W. Carney, and J. C. Wheeler. Chemical Substructure in the Milky Way Halo: A New Population of Old Stars. ApJ, 592:906–934, Aug. 2003. doi: 10.1086/375812.

I. I. Ivans, C. Sneden, R. Gallino, J. J. Cowan, and G. W. Preston. Near-Ultraviolet Observations of CS 29497-030: New Constraints on Neutron-Capture Nucleosynthesis Processes. ApJ, 627:L145–L148, July 2005. doi: 10.1086/432465.

A. P. Ji, A. Frebel, R. Ezzeddine, and A. R. Casey. Chemical Diversity in the Ultra-faint Dwarf Galaxy Tucana II. ApJ, 832:L3, Nov. 2016a. doi: 10.3847/2041-8205/832/1/L3.

A. P. Ji, A. Frebel, J. D. Simon, and A. Chiti. Complete Element Abundances of Nine Stars in the r-process Galaxy Reticulum II. ApJ, 830:93, Oct. 2016b. doi: 10.3847/0004-637X/830/2/93.

J. A. Johnson, F. Herwig, T. C. Beers, and N. Christlieb. A Search for Nitrogen-enhanced Metal-poor Stars. ApJ, 658:1203–1216, Apr. 2007. doi: 10.1086/510114.

K. Jonsell, P. S. Barklem, B. Gustafsson, N. Christlieb, V. Hill, T. C. Beers, and J. Holmberg. The Hamburg/ESO R-process enhanced star survey (HERES). III. HE 0338-3945 and the formation of the r + s stars. A&A, 451:651–670, May 2006. doi: 10.1051/0004-6361:20054470.

A. Jorissen, T. Hansen, S. Van Eck, J. Andersen, B. Nordström, L. Siess, G. Torres, T. Masseron, and H. Van Winckel. HE 0017+0055: A probable pulsating CEMP-rs star and long-period binary. A&A, 586:A159, Feb. 2016. doi: 10.1051/0004-6361/201526993.

A. Karakas and J. C. Lattanzio. Stellar Models and Yields of Asymptotic Giant Branch Stars. PASA, 24:103–117, Oct. 2007. doi: 10.1071/AS07021.

A. I. Karakas. Updated stellar yields from asymptotic giant branch models. MNRAS, 403:1413–1425, Apr. 2010. doi: 10.1111/j.1365-2966.2009.16198.x.

S. C. Keller, M. S. Bessell, A. Frebel, A. R. Casey, M. Asplund, H. R. Jacobson, K. Lind, J. E. Norris, D. Yong, A. Heger, Z. Magic, G. S. da Costa, B. P. Schmidt,

and P. Tisserand. A single low-energy, iron-poor supernova as the source of metals in the star SMSS J031300.36-670839.3. Nature, 506:463–466, Feb. 2014. doi: 10.1038/nature12990.

C. R. Kennedy, T. Sivarani, T. C. Beers, Y. S. Lee, V. M. Placco, S. Rossi, N. Christlieb, F. Herwig, and B. Plez. [O/Fe] Estimates for Carbon-enhanced Metal-poor Stars from Near-infrared Spectroscopy. AJ, 141:102, Mar. 2011. doi: 10.1088/0004-6256/141/3/102.

J. R. King. Abundance Ratios in a Common Proper Motion Pair: Chemical Evidence of Accreted Substructure in the Halo Field? AJ, 113:2302, June 1997. doi: 10.1086/118440.

E. N. Kirby and J. G. Cohen. Detailed Abundances of Two Very Metal-poor Stars in Dwarf Galaxies. AJ, 144:168, Dec. 2012. doi: 10.1088/0004-6256/144/6/168.

E. N. Kirby, G. A. Lanfranchi, J. D. Simon, J. G. Cohen, and P. Guhathakurta. Multi-element Abundance Measurements from Medium-resolution Spectra. III. Metallicity Distributions of Milky Way Dwarf Satellite Galaxies. ApJ, 727:78, Feb. 2011. doi: 10.1088/0004-637X/727/2/78.

E. N. Kirby, M. Boylan-Kolchin, J. G. Cohen, M. Geha, J. S. Bullock, and M. Kaplinghat. Segue 2: The Least Massive Galaxy. ApJ, 770:16, June 2013. doi: 10.1088/0004-637X/770/1/16.

C. Kobayashi, H. Umeda, K. Nomoto, N. Tominaga, and T. Ohkubo. Galactic Chemical Evolution: Carbon through Zinc. ApJ, 653:1145–1171, Dec. 2006. doi: 10.1086/508914.

C. Kobayashi, N. Tominaga, and K. Nomoto. Chemical Enrichment in the Carbon-enhanced Damped Lyα System by Population III Supernovae. ApJ, 730:L14, Apr. 2011. doi: 10.1088/2041-8205/730/2/L14.

C. Kobayashi, M. N. Ishigaki, N. Tominaga, and K. Nomoto. The Origin of Low [α/Fe] Ratios in Extremely Metal-poor Stars. ApJ, 785:L5, Apr. 2014. doi: 10.1088/2041-8205/785/1/L5.

A. Koch and B. Edvardsson. Europium abundances in F and G disk dwarfs. A&A, 381:500–506, Jan. 2002. doi: 10.1051/0004-6361:20011578.

A. Koch, E. K. Grebel, R. F. G. Wyse, J. T. Kleyna, M. I. Wilkinson, D. R. Harbeck, G. F. Gilmore, and N. W. Evans. Complexity on Small Scales: The Metallicity Distribution of the Carina Dwarf Spheroidal Galaxy. AJ, 131:895–911, Feb. 2006. doi: 10.1086/499490.

A. Koch, E. K. Grebel, G. F. Gilmore, R. F. G. Wyse, J. T. Kleyna, D. R. Harbeck, M. I. Wilkinson, and N. Wyn Evans. Complexity on Small Scales. III. Iron and α Element Abundances in the Carina Dwarf Spheroidal Galaxy. AJ, 135:1580–1597, Apr. 2008. doi: 10.1088/0004-6256/135/4/1580.

A. Koch, K. Lind, and R. M. Rich. Discovery of a Super-Li-rich Turnoff Star in the Metal-poor Globular Cluster NGC 6397. ApJ, 738:L29, Sept. 2011. doi: 10.1088/2041-8205/738/2/L29.

A. Koch, A. McWilliam, G. W. Preston, and I. B. Thompson. Metal-poor stars towards the Galactic bulge: A population potpourri. A&A, 587:A124, Mar. 2016. doi: 10.1051/0004-6361/201527413.

F. Kupka, N. Piskunov, T. A. Ryabchikova, H. C. Stempels, and W. W. Weiss. VALD-2: Progress of the Vienna Atomic Line Data Base. A&AS, 138:119–133, July 1999. doi: 10.1051/aas:1999267.

R. Kurucz. ATLAS9 Stellar Atmosphere Programs and 2 km/s grid. *ATLAS9 Stellar Atmosphere Programs and 2 km/s grid. Kurucz CD-ROM No. 13. Cambridge, Mass.: Smithsonian Astrophysical Observatory, 1993.*, 13, 1993.

D. K. Lai, M. Bolte, J. A. Johnson, S. Lucatello, A. Heger, and S. E. Woosley. Detailed Abundances for 28 Metal-poor Stars: Stellar Relics in the Milky Way. ApJ, 681:1524–1556, July 2008. doi: 10.1086/588811.

D. K. Lai, C. M. Rockosi, M. Bolte, J. A. Johnson, T. C. Beers, Y. S. Lee, C. Allende Prieto, and B. Yanny. A Unique Star in the Outer Halo of the Milky Way. ApJ, 697:L63–L67, May 2009. doi: 10.1088/0004-637X/697/1/L63.

D. K. Lai, Y. S. Lee, M. Bolte, S. Lucatello, T. C. Beers, J. A. Johnson, T. Sivarani, and C. M. Rockosi. The [Fe/H], [C/Fe], and [α/Fe] Distributions of the Boötes I Dwarf Spheroidal Galaxy. ApJ, 738:51, Sept. 2011. doi: 10.1088/0004-637X/738/1/51.

Y. S. Lee, T. C. Beers, T. Sivarani, J. A. Johnson, D. An, R. Wilhelm, C. Allende Prieto, L. Koesterke, P. Re Fiorentin, C. A. L. Bailer-Jones, J. E. Norris, B. Yanny, C. Rockosi, H. J. Newberg, K. M. Cudworth, and K. Pan. The SEGUE Stellar Parameter Pipeline. II. Validation with Galactic Globular and Open Clusters. AJ, 136:2050–2069, Nov. 2008. doi: 10.1088/0004-6256/136/5/2050.

Y. S. Lee, T. C. Beers, Y. K. Kim, V. Placco, J. Yoon, D. Carollo, T. Masseron, and

J. Jung. Chemical Cartography. I. A Carbonicity Map of the Galactic Halo. ApJ, 836:91, Feb. 2017. doi: 10.3847/1538-4357/836/1/91.

B. Lemasle, V. Hill, E. Tolstoy, K. A. Venn, M. D. Shetrone, M. J. Irwin, T. J. L. de Boer, E. Starkenburg, and S. Salvadori. VLT/FLAMES spectroscopy of red giant branch stars in the Carina dwarf spheroidal galaxy. A&A, 538:A100, Feb. 2012. doi: 10.1051/0004-6361/201118132.

K. Lind, F. Primas, C. Charbonnel, F. Grundahl, and M. Asplund. Signatures of intrinsic Li depletion and Li-Na anti-correlation in the metal-poor globular cluster NGC 6397. A&A, 503:545–557, Aug. 2009. doi: 10.1051/0004-6361/200912524.

K. Lind, M. Asplund, P. S. Barklem, and A. K. Belyaev. Non-LTE calculations for neutral Na in late-type stars using improved atomic data. A&A, 528:A103, Apr. 2011. doi: 10.1051/0004-6361/201016095.

S. Lucatello, T. C. Beers, N. Christlieb, P. S. Barklem, S. Rossi, B. Marsteller, T. Sivarani, and Y. S. Lee. The Frequency of Carbon-enhanced Metal-poor Stars in the Galaxy from the HERES Sample. ApJ, 652:L37–L40, Nov. 2006. doi: 10.1086/509780.

S. Lucatello, T. Masseron, J. A. Johnson, M. Pignatari, and F. Herwig. Fluorine and Sodium in C-rich Low-metallicity Stars. ApJ, 729:40, Mar. 2011. doi: 10.1088/0004-637X/729/1/40.

M. Lugaro, A. I. Karakas, R. J. Stancliffe, and C. Rijs. The s-process in Asymptotic Giant Branch Stars of Low Metallicity and the Composition of Carbon-enhanced Metal-poor Stars. ApJ, 747:2, Mar. 2012. doi: 10.1088/0004-637X/747/1/2.

S. R. Majewski, M. F. Skrutskie, M. D. Weinberg, and J. C. Ostheimer. A Two Micron All Sky Survey View of the Sagittarius Dwarf Galaxy. I. Morphology of the Sagittarius Core and Tidal Arms. ApJ, 599:1082–1115, Dec. 2003. doi: 10.1086/379504.

N. F. Martin, R. A. Ibata, S. C. Chapman, M. Irwin, and G. F. Lewis. A Keck/DEIMOS spectroscopic survey of faint Galactic satellites: searching for the least massive dwarf galaxies. MNRAS, 380:281–300, Sept. 2007. doi: 10.1111/j.1365-2966.2007.12055.x.

N. F. Martin, J. T. A. de Jong, and H.-W. Rix. A Comprehensive Maximum Likelihood Analysis of the Structural Properties of Faint Milky Way Satellites. ApJ, 684:1075-1092, Sept. 2008. doi: 10.1086/590336.

L. Mashonkina, A. J. Korn, and N. Przybilla. A non-LTE study of neutral and singly-ionized calcium in late-type stars. A&A, 461:261–275, Jan. 2007. doi: 10.1051/0004-6361:20065999.

T. Masseron, J. A. Johnson, B. Plez, S. van Eck, F. Primas, S. Goriely, and A. Jorissen. A holistic approach to carbon-enhanced metal-poor stars. A&A, 509:A93, Jan. 2010. doi: 10.1051/0004-6361/200911744.

T. Masseron, J. A. Johnson, S. Lucatello, A. Karakas, B. Plez, T. C. Beers, and N. Christlieb. Lithium Abundances in Carbon-enhanced Metal-poor Stars. ApJ, 751:14, May 2012. doi: 10.1088/0004-637X/751/1/14.

A. McWilliam, G. W. Preston, C. Sneden, and L. Searle. Spectroscopic Analysis of 33 of the Most Metal Poor Stars. II. AJ, 109:2757, June 1995. doi: 10.1086/117486.

S. Mészáros, C. Allende Prieto, B. Edvardsson, F. Castelli, A. E. García Pérez, B. Gustafsson, S. R. Majewski, B. Plez, R. Schiavon, M. Shetrone, and A. de Vicente. New ATLAS9 and MARCS Model Atmosphere Grids for the Apache Point Observatory Galactic Evolution Experiment (APOGEE). AJ, 144:120, Oct. 2012. doi: 10.1088/0004-6256/144/4/120.

G. Meynet, S. Ekström, and A. Maeder. The early star generations: the dominant effect of rotation on the CNO yields. A&A, 447:623–639, Feb. 2006. doi: 10.1051/0004-6361:20053070.

A. Miceli, A. Rest, C. W. Stubbs, S. L. Hawley, K. H. Cook, E. A. Magnier, K. Krisciunas, E. Bowell, and B. Koehn. Evidence for Distinct Components of the Galactic Stellar Halo from 838 RR Lyrae Stars Discovered in the LONEOS-I Survey. ApJ, 678:865-887, May 2008. doi: 10.1086/533484.

A. Modigliani, G. Mulas, I. Porceddu, B. Wolff, F. Damiani, and B. K. Banse. The FLAMES-UVES Pipeline. *The Messenger*, 118:8–10, Dec. 2004.

M. Monelli, L. Pulone, C. E. Corsi, M. Castellani, G. Bono, A. R. Walker, E. Brocato, R. Buonanno, F. Caputo, V. Castellani, M. Dall'Ora, M. Marconi, M. Nonino, V. Ripepi, and H. A. Smith. The Carina Project. II. Stellar Populations. AJ, 126:218–236, July 2003. doi: 10.1086/375457.

F. Montes, T. C. Beers, J. Cowan, T. Elliot, K. Farouqi, R. Gallino, M. Heil, K.-L. Kratz, B. Pfeiffer, M. Pignatari, and H. Schatz. Nucleosynthesis in the Early Galaxy. ApJ, 671:1685–1695, Dec. 2007. doi: 10.1086/523084.

J. Mould and M. Aaronson. The Carina dwarf spheroidal - an intermediate age galaxy. ApJ, 273:530–538, Oct. 1983. doi: 10.1086/161389.

R. R. Muñoz, M. Geha, and B. Willman. Turning the Tides on the Ultra-faint Dwarf Spheroidal Galaxies: Coma Berenices and Ursa Major II. AJ, 140:138–151, July 2010. doi: 10.1088/0004-6256/140/1/138.

J. F. Navarro, C. S. Frenk, and S. D. M. White. A Universal Density Profile from Hierarchical Clustering. ApJ, 490:493–508, Dec. 1997. doi: 10.1086/304888.

H. J. Newberg, B. Yanny, C. Rockosi, E. K. Grebel, H.-W. Rix, J. Brinkmann, I. Csabai, G. Hennessy, R. B. Hindsley, R. Ibata, Z. Ivezić, D. Lamb, E. T. Nash, M. Odenkirchen, H. A. Rave, D. P. Schneider, J. A. Smith, A. Stolte, and D. G. York. The Ghost of Sagittarius and Lumps in the Halo of the Milky Way. ApJ, 569:245–274, Apr. 2002. doi: 10.1086/338983.

J. P. Ninan, D. K. Ojha, S. K. Ghosh, S. L. A. D'Costa, M. B. Naik, S. S. Poojary, P. R. Sandimani, G. S. Meshram, R. B. Jadhav, S. B. Bhagat, S. M. Gharat, C. B. Bakalkar, T. P. Prabhu, G. C. Anupama, and D. W. Toomey. TIRSPEC: TIFR Near Infrared Spectrometer and Imager. *Journal of Astronomical Instrumentation*, 3:1450006, 2014. doi: 10.1142/S2251171714500068.

K. M. Nollett, M. Busso, and G. J. Wasserburg. Cool Bottom Processes on the Thermally Pulsing Asymptotic Giant Branch and the Isotopic Composition of Circumstellar Dust Grains. ApJ, 582:1036–1058, Jan. 2003. doi: 10.1086/344817.

M. Nonino, E. Bertin, L. da Costa, E. Deul, T. Erben, L. Olsen, I. Prandoni, M. Scodeggio, A. Wicenec, R. Wichmann, C. Benoist, W. Freudling, M. D. Guarnieri, I. Hook, R. Hook, R. Mendez, S. Savaglio, D. Silva, and R. Slijkhuis. ESO Imaging Survey. I. Description of the survey, data reduction and reliability of the data. A&AS, 137:51–74, May 1999. doi: 10.1051/aas:1999473.

J. E. Norris, G. Gilmore, R. F. G. Wyse, D. Yong, and A. Frebel. An Extremely Carbon-rich, Extremely Metal-poor Star in the Segue 1 System. ApJ, 722:L104–L109, Oct. 2010a. doi: 10.1088/2041-8205/722/1/L104.

J. E. Norris, R. F. G. Wyse, G. Gilmore, D. Yong, A. Frebel, M. I. Wilkinson, V. Belokurov, and D. B. Zucker. Chemical Enrichment in the Faintest Galaxies: The Carbon and Iron Abundance Spreads in the Boötes I Dwarf Spheroidal Galaxy and the Segue 1 System. ApJ, 723:1632–1650, Nov. 2010b. doi: 10.1088/0004-637X/723/2/1632.

K. Otsuki, S. Honda, W. Aoki, T. Kajino, and G. J. Mathews. Neutron-Capture Elements in the Metal-poor Globular Cluster M15. ApJ, 641:L117–L120, Apr. 2006. doi: 10.1086/504106.

S. Palmerini, K. Nollett, and M. Busso. Magnetically-driven Cool Bottom Processing. In *Nuclei in the Cosmos (NIC X)*, 2008.

A. Pietrinferni, S. Cassisi, M. Salaris, and F. Castelli. A Large Stellar Evolution Database for Population Synthesis Studies. II. Stellar Models and Isochrones for an α-enhanced Metal Distribution. ApJ, 642:797–812, May 2006. doi: 10.1086/501344.

V. M. Placco, A. Frebel, T. C. Beers, and R. J. Stancliffe. Carbon-enhanced Metal-poor Star Frequencies in the Galaxy: Corrections for the Effect of Evolutionary Status on Carbon Abundances. ApJ, 797:21, Dec. 2014. doi: 10.1088/0004-637X/797/1/21.

B. Plez. Turbospectrum: Code for spectral synthesis. Astrophysics Source Code Library, May 2012.

B. Plez and J. G. Cohen. Analysis of the carbon-rich very metal-poor dwarf G77-61. A&A, 434:1117–1124, May 2005. doi: 10.1051/0004-6361:20042082.

B. Plez, J. M. Brett, and Å. Nordlund. Spherical opacity samples of model atmospheres for M giants and supergiants. In C. de Jager and H. Nieuwenhuijzen, editors, *Instabilities in Evolved Super- and Hypergiants*, page 119, 1992.

B. Plez, V. V. Smith, and D. L. Lambert. Lithium Abundances and Other Clues to Envelope Burning in Small Magellanic Cloud Asymptotic Giant Branch Stars. ApJ, 418:812, Dec. 1993. doi: 10.1086/173438.

G. W. Preston. CS 22873-139: A very metal-poor main-sequence spectroscopic binary with colors indicative of intermediate age. AJ, 108:2267–2272, Dec. 1994. doi: 10.1086/117239.

G. Ramsay and K. Wu. A search for stellar X-ray sources in the Sagittarius and Carina dwarf galaxies. I. X-ray observations. A&A, 459:777–781, Dec. 2006. doi: 10.1051/0004-6361:20065959.

I. U. Roederer, G. W. Preston, I. B. Thompson, S. A. Shectman, C. Sneden, G. S. Burley, and D. D. Kelson. A Search for Stars of Very Low Metal Abundance. VI. Detailed Abundances of 313 Metal-poor Stars. AJ, 147:136, June 2014a. doi: 10.1088/0004-6256/147/6/136.

I. U. Roederer, G. W. Preston, I. B. Thompson, S. A. Shectman, C. Sneden, G. S. Burley, and D. D. Kelson. A Search for Stars of Very Low Metal Abundance. VI. Detailed Abundances of 313 Metal-poor Stars. AJ, 147:136, June 2014b. doi: 10.1088/0004-6256/147/6/136.

S. G. Ryan and C. P. Deliyannis. Lithium in Short-Period Tidally Locked Binaries: A Test of Rotationally Induced Mixing. ApJ, 453:819, Nov. 1995. doi: 10.1086/176444.

C. Salgado, G. S. Da Costa, D. Yong, and J. E. Norris. Scl-1013644: a CEMP-s star in the Sculptor dwarf spheroidal galaxy. MNRAS, 463:598–603, Nov. 2016. doi: 10.1093/mnras/stw1986.

S. Salvadori, Á. Skúladóttir, and E. Tolstoy. Carbon-enhanced metal-poor stars in dwarf galaxies. MNRAS, 454:1320–1331, Dec. 2015. doi: 10.1093/mnras/stv1969.

L. Sbordone, P. Bonifacio, E. Caffau, H.-G. Ludwig, N. T. Behara, J. I. González Hernández, M. Steffen, R. Cayrel, B. Freytag, C. van't Veer, P. Molaro, B. Plez, T. Sivarani, M. Spite, F. Spite, T. C. Beers, N. Christlieb, P. François, and V. Hill. The metal-poor end of the Spite plateau. I. Stellar parameters, metallicities, and lithium abundances. A&A, 522:A26, Nov. 2010a. doi: 10.1051/0004-6361/200913282.

L. Sbordone, P. Bonifacio, E. Caffau, H.-G. Ludwig, N. T. Behara, J. I. González Hernández, M. Steffen, R. Cayrel, B. Freytag, C. van't Veer, P. Molaro, B. Plez, T. Sivarani, M. Spite, F. Spite, T. C. Beers, N. Christlieb, P. François, and V. Hill. The metal-poor end of the Spite plateau. I. Stellar parameters, metallicities, and lithium abundances. A&A, 522:A26, Nov. 2010b. doi: 10.1051/0004-6361/200913282.

D. J. Schlegel, D. P. Finkbeiner, and M. Davis. Maps of Dust Infrared Emission for Use in Estimation of Reddening and Cosmic Microwave Background Radiation Foregrounds. ApJ, 500:525–553, June 1998a. doi: 10.1086/305772.

D. J. Schlegel, D. P. Finkbeiner, and M. Davis. Maps of Dust Infrared Emission for Use in Estimation of Reddening and Cosmic Microwave Background Radiation Foregrounds. ApJ, 500:525–553, June 1998b. doi: 10.1086/305772.

L. Searle and R. Zinn. Compositions of halo clusters and the formation of the galactic halo. ApJ, 225:357–379, Oct. 1978a. doi: 10.1086/156499.

L. Searle and R. Zinn. Compositions of halo clusters and the formation of the galactic halo. ApJ, 225:357–379, Oct. 1978b. doi: 10.1086/156499.

M. Shetrone, K. A. Venn, E. Tolstoy, F. Primas, V. Hill, and A. Kaufer. VLT/UVES Abundances in Four Nearby Dwarf Spheroidal Galaxies. I. Nucleosynthesis and Abundance Ratios. AJ, 125:684–706, Feb. 2003. doi: 10.1086/345966.

J. Simmerer, C. Sneden, J. J. Cowan, J. Collier, V. M. Woolf, and J. E. Lawler. The Rise of the s-Process in the Galaxy. ApJ, 617:1091–1114, Dec. 2004. doi: 10.1086/424504.

J. D. Simon and M. Geha. The Kinematics of the Ultra-faint Milky Way Satellites: Solving the Missing Satellite Problem. ApJ, 670:313–331, Nov. 2007. doi: 10.1086/521816.

T. Sivarani, T. C. Beers, P. Bonifacio, P. Molaro, R. Cayrel, F. Herwig, M. Spite, F. Spite, B. Plez, J. Andersen, B. Barbuy, E. Depagne, V. Hill, P. François, B. Nordström, and F. Primas. First stars X. The nature of three unevolved carbon-enhanced metal-poor stars. A&A, 459:125–135, Nov. 2006. doi: 10.1051/0004-6361:20065440.

Á. Skúladóttir, E. Tolstoy, S. Salvadori, V. Hill, M. Pettini, M. D. Shetrone, and

E. Starkenburg. The first carbon-enhanced metal-poor star found in the Sculptor dwarf spheroidal. A&A, 574:A129, Feb. 2015. doi: 10.1051/0004-6361/201424782.

T. A. Smecker-Hane, P. B. Stetson, J. E. Hesser, and M. D. Lehnert. The stellar populations of the Carina dwarf spheroidal Galaxy. 1: A new color-magnitude diagram for the giant and horizontal branches. AJ, 108:507–513, Aug. 1994. doi: 10.1086/117087.

C. Sneden, J. J. Cowan, J. E. Lawler, I. I. Ivans, S. Burles, T. C. Beers, F. Primas, V. Hill, J. W. Truran, G. M. Fuller, B. Pfeiffer, and K.-L. Kratz. The Extremely Metal-poor, Neutron Capture-rich Star CS 22892-052: A Comprehensive Abundance Analysis. ApJ, 591:936–953, July 2003. doi: 10.1086/375491.

C. Sneden, J. J. Cowan, and R. Gallino. Neutron-Capture Elements in the Early Galaxy. ARA&A, 46:241–288, Sept. 2008. doi: 10.1146/annurev.astro.46.060407.145207.

M. Spite and F. Spite. Lithium abundance at the formation of the Galaxy. Nature, 297:483–485, June 1982. doi: 10.1038/297483a0.

M. Spite, R. Cayrel, B. Plez, V. Hill, F. Spite, E. Depagne, P. François, P. Bonifacio, B. Barbuy, T. Beers, J. Andersen, P. Molaro, B. Nordström, and F. Primas. First stars VI - Abundances of C, N, O, Li, and mixing in extremely metal-poor giants. Galactic evolution of the light elements. A&A, 430:655–668, Feb. 2005. doi: 10.1051/0004-6361:20041274.

M. Spite, R. Cayrel, V. Hill, F. Spite, P. François, B. Plez, P. Bonifacio, P. Molaro, E. Depagne, J. Andersen, B. Barbuy, T. C. Beers, B. Nordström, and F. Primas.

First stars IX - Mixing in extremely metal-poor giants. Variation of the $^{12}C/^{13}C$, [Na/Mg] and [Al/Mg] ratios. A&A, 455:291–301, Aug. 2006. doi: 10.1051/0004-6361:20065209.

M. Spite, S. M. Andrievsky, F. Spite, E. Caffau, S. A. Korotin, P. Bonifacio, H.-G. Ludwig, P. François, and R. Cayrel. NLTE determination of the calcium abundance and 3D corrections in extremely metal-poor stars. A&A, 541:A143, May 2012. doi: 10.1051/0004-6361/201218773.

E. Starkenburg, M. D. Shetrone, A. W. McConnachie, and K. A. Venn. Binarity in carbon-enhanced metal-poor stars. MNRAS, 441:1217–1229, June 2014. doi: 10.1093/mnras/stu623.

O. Straniero, R. Gallino, M. Busso, A. Chiefei, C. M. Raiteri, M. Limongi, and M. Salaris. Radiative C-13 burning in asymptotic giant branch stars and s-processing. ApJ, 440:L85–L87, Feb. 1995. doi: 10.1086/187767.

T. Suda, Y. Katsuta, S. Yamada, T. Suwa, C. Ishizuka, Y. Komiya, K. Sorai, M. Aikawa, and M. Y. Fujimoto. Stellar Abundances for the Galactic Archeology (SAGA) Database — Compilation of the Characteristics of Known Extremely Metal-Poor Stars. PASJ, 60:1159–, Oct. 2008. doi: 10.1093/pasj/60.5.1159.

M. Tafelmeyer, P. Jablonka, V. Hill, M. Shetrone, E. Tolstoy, M. J. Irwin, G. Battaglia, A. Helmi, E. Starkenburg, K. A. Venn, T. Abel, P. Francois, A. Kaufer, P. North, F. Primas, and T. Szeifert. Extremely metal-poor stars in classical dwarf spheroidal galaxies: Fornax, Sculptor, and Sextans. A&A, 524: A58, Dec. 2010. doi: 10.1051/0004-6361/201014733.

I. B. Thompson, I. I. Ivans, S. Bisterzo, C. Sneden, R. Gallino, S. Vauclair, G. S.

Burley, S. A. Shectman, and G. W. Preston. CS 22964-161: A Double-Lined Carbon- and s-Process-Enhanced Metal-Poor Binary Star. ApJ, 677:556-571, Apr. 2008. doi: 10.1086/529016.

F. X. Timmes, S. E. Woosley, and T. A. Weaver. Galactic chemical evolution: Hydrogen through zinc. ApJS, 98:617–658, June 1995. doi: 10.1086/192172.

E. Tolstoy, K. A. Venn, M. Shetrone, F. Primas, V. Hill, A. Kaufer, and T. Szeifert. VLT/UVES Abundances in Four Nearby Dwarf Spheroidal Galaxies. II. Implications for Understanding Galaxy Evolution. AJ, 125:707–726, Feb. 2003. doi: 10.1086/345967.

E. Tolstoy, V. Hill, and M. Tosi. Star-Formation Histories, Abundances, and Kinematics of Dwarf Galaxies in the Local Group. ARA&A, 47:371–425, Sept. 2009. doi: 10.1146/annurev-astro-082708-101650.

N. Tominaga, H. Umeda, and K. Nomoto. Supernova Nucleosynthesis in Population III 13-50 M_{solar} Stars and Abundance Patterns of Extremely Metal-poor Stars. ApJ, 660:516–540, May 2007. doi: 10.1086/513063.

C. Travaglio, R. Gallino, E. Arnone, J. Cowan, F. Jordan, and C. Sneden. Galactic Evolution of Sr, Y, And Zr: A Multiplicity of Nucleosynthetic Processes. ApJ, 601:864–884, Feb. 2004. doi: 10.1086/380507.

H. Umeda and K. Nomoto. First-generation black-hole-forming supernovae and the metal abundance pattern of a very iron-poor star. Nature, 422:871–873, Apr. 2003. doi: 10.1038/nature01571.

E. Vangioni. Cosmic chemical evolution with intermediate mass pop III stars.

Journal of Physics Conference Series, 337(1):012074, Feb. 2012. doi: 10.1088/1742-6596/337/1/012074.

E. Vangioni, S. Goriely, F. Daigne, P. Francois, and K. Belczynski. Early Cosmic Evolution of Europium from Core Collapse Supernovae and/or Neutron Star Mergers. *ArXiv e-prints*, Jan. 2015.

H. A. T. Vanhala and A. G. W. Cameron. Numerical Simulations of Triggered Star Formation. I. Collapse of Dense Molecular Cloud Cores. ApJ, 508:291–307, Nov. 1998. doi: 10.1086/306396.

L. C. Vargas, M. Geha, E. N. Kirby, and J. D. Simon. The Distribution of Alpha Elements in Ultra-faint Dwarf Galaxies. ApJ, 767:134, Apr. 2013. doi: 10.1088/0004-637X/767/2/134.

K. A. Venn, M. D. Shetrone, M. J. Irwin, V. Hill, P. Jablonka, E. Tolstoy, B. Lemasle, M. Divell, E. Starkenburg, B. Letarte, C. Baldner, G. Battaglia, A. Helmi, A. Kaufer, and F. Primas. Nucleosynthesis and the Inhomogeneous Chemical Evolution of the Carina Dwarf Galaxy. ApJ, 751:102, June 2012. doi: 10.1088/0004-637X/751/2/102.

M. G. Walker, M. Mateo, and E. W. Olszewski. Stellar Velocities in the Carina, Fornax, Sculptor, and Sextans dSph Galaxies: Data From the Magellan/MMFS Survey. AJ, 137:3100–3108, Feb. 2009. doi: 10.1088/0004-6256/137/2/3100.

S. M. Walsh, H. Jerjen, and B. Willman. A Pair of Boötes: A New Milky Way Satellite. ApJ, 662:L83–L86, June 2007. doi: 10.1086/519684.

S. M. Walsh, B. Willman, D. Sand, J. Harris, A. Seth, D. Zaritsky, and H. Jerjen. Boötes II ReBoöted: An MMT/MegaCam Study of an Ultrafaint Milky Way Satellite. ApJ, 688:245-253, Nov. 2008. doi: 10.1086/592076.

G. J. Wasserburg, A. I. Boothroyd, and I.-J. Sackmann. Deep Circulation in Red Giant Stars: A Solution to the Carbon and Oxygen Isotope Puzzles? ApJ, 447: L37, July 1995. doi: 10.1086/309555.

D. Webster, A. Frebel, and J. Bland-Hawthorn. Segue 1 – A Compressed Star Formation History before Reionization. ApJ, 818:80, Feb. 2016. doi: 10.3847/0004-637X/818/1/80.

B. Willman, J. J. Dalcanton, D. Martinez-Delgado, A. A. West, M. R. Blanton, D. W. Hogg, J. C. Barentine, H. J. Brewington, M. Harvanek, S. J. Kleinman, J. Krzesinski, D. Long, E. H. Neilsen, Jr., A. Nitta, and S. A. Snedden. A New Milky Way Dwarf Galaxy in Ursa Major. ApJ, 626:L85–L88, June 2005. doi: 10.1086/431760.

E. L. Wright, P. R. M. Eisenhardt, A. K. Mainzer, M. E. Ressler, R. M. Cutri, T. Jarrett, J. D. Kirkpatrick, D. Padgett, R. S. McMillan, M. Skrutskie, S. A. Stanford, M. Cohen, R. G. Walker, J. C. Mather, D. Leisawitz, T. N. Gautier, III, I. McLean, D. Benford, C. J. Lonsdale, A. Blain, B. Mendez, W. R. Irace, V. Duval, F. Liu, D. Royer, I. Heinrichsen, J. Howard, M. Shannon, M. Kendall, A. L. Walsh, M. Larsen, J. G. Cardon, S. Schick, M. Schwalm, M. Abid, B. Fabinsky, L. Naes, and C.-W. Tsai. The Wide-field Infrared Survey Explorer (WISE): Mission Description and Initial On-orbit Performance. AJ, 140:1868, Dec. 2010. doi: 10.1088/0004-6256/140/6/1868.

J. T. Wright and A. W. Howard. Efficient Fitting of Multiplanet Keplerian Models to Radial Velocity and Astrometry Data. ApJS, 182:205, May 2009. doi: 10.1088/0067-0049/182/1/205.

B. Yanny, H. J. Newberg, E. K. Grebel, S. Kent, M. Odenkirchen, C. M. Rockosi, D. Schlegel, M. Subbarao, J. Brinkmann, M. Fukugita, Ž. Ivezic, D. Q. Lamb, D. P. Schneider, and D. G. York. A Low-Latitude Halo Stream around the Milky Way. ApJ, 588:824–841, May 2003. doi: 10.1086/374220.

D. Yong, J. E. Norris, M. S. Bessell, N. Christlieb, M. Asplund, T. C. Beers, P. S. Barklem, A. Frebel, and S. G. Ryan. The Most Metal-poor Stars. II. Chemical Abundances of 190 Metal-poor Stars Including 10 New Stars with [Fe/H] = -3.5. ApJ, 762:26, Jan. 2013. doi: 10.1088/0004-637X/762/1/26.

J. Yoon, T. C. Beers, V. M. Placco, K. C. Rasmussen, D. Carollo, S. He, T. T. Hansen, I. U. Roederer, and J. Zeanah. Observational Constraints on First-star Nucleosynthesis. I. Evidence for Multiple Progenitors of CEMP-No Stars. ApJ, 833:20, Dec. 2016. doi: 10.3847/0004-637X/833/1/20.

D. B. Zucker, V. Belokurov, N. W. Evans, J. T. Kleyna, M. J. Irwin, M. I. Wilkinson, M. Fellhauer, D. M. Bramich, G. Gilmore, H. J. Newberg, B. Yanny, J. A. Smith, P. C. Hewett, E. F. Bell, H.-W. Rix, O. Y. Gnedin, S. Vidrih, R. F. G. Wyse, B. Willman, E. K. Grebel, D. P. Schneider, T. C. Beers, A. Y. Kniazev, J. C. Barentine, H. Brewington, J. Brinkmann, M. Harvanek, S. J. Kleinman, J. Krzesinski, D. Long, A. Nitta, and S. A. Snedden. A Curious Milky Way Satellite in Ursa Major. ApJ, 650:L41–L44, Oct. 2006a. doi: 10.1086/508628.

D. B. Zucker, V. Belokurov, N. W. Evans, M. I. Wilkinson, M. J. Irwin, T. Sivarani, S. Hodgkin, D. M. Bramich, J. M. Irwin, G. Gilmore, B. Willman, S. Vidrih,

M. Fellhauer, P. C. Hewett, T. C. Beers, E. F. Bell, E. K. Grebel, D. P. Schneider, H. J. Newberg, R. F. G. Wyse, C. M. Rockosi, B. Yanny, R. Lupton, J. A. Smith, J. C. Barentine, H. Brewington, J. Brinkmann, M. Harvanek, S. J. Kleinman, J. Krzesinski, D. Long, A. Nitta, and S. A. Snedden. A New Milky Way Dwarf Satellite in Canes Venatici. ApJ, 643:L103–L106, June 2006b. doi: 10.1086/505216.